MASARYKOVA UNIVERZITA
Přírodovědecká fakulta
Ústav fyziky kondenzovaných látek

Ph.D. thesis

Brno 2017 Dominique Geffroy

MASARYKOVA
UNIVERZITA
Přírodovědecká fakulta
Ústav fyziky kondenzovaných látek

Theoretical study of electronic properties of high-T_c superconductors and other materials with strongly correlated electrons

Ph.D. thesis

Dominique Geffroy

Supervisor: Doc. Mgr. Dominik Munzar, Dr. **Brno 2017**

Bibliografický záznam

Autor:	Mgr. Dominique Geffroy Přírodovědecká fakulta, Masarykova univerzita Ústav fyziky kondenzovaných látek
Název práce:	Teoretické studium elektronové struktury vysokoteplotních supravodičů a jiných materiálů se silně korelovanými elektrony
Studijní program:	PřF D-FY4 Fyzika
Studijní obor:	PřF KOND Fyzika kondenzovaných látek
Vedoucí práce:	Doc. Mgr. Dominik Munzar, Dr.
Akademický rok:	2016/2017
Počet stran:	x + 156
Klíčová slova:	vysokoteplotní supravodiče; kupráty; Hubbardův model; excitonová kondenzace; dynamická teorie středního pole

Bibliographic Entry

Author:	Mgr. Dominique Geffroy Faculty of Science, Masaryk University Department of Condensed Matter Physics
Title of Thesis:	Theoretical study of electronic properties of high-T_c superconductors and other materials with strongly correlated electrons
Degree Programme:	PřF D-FY4 Physics
Field of Study:	PřF KOND Condensed Matter Physics
Supervisor:	Doc. Mgr. Dominik Munzar, Dr.
Academic Year:	2016/2017
Number of Pages:	x + 156
Keywords:	High-temperature superconductors; Cuprates; Hubbard model; Excitonic condensation; Dynamical Mean Field Theory

Abstrakt

V první části této práce (kapitoly 1 až 7) jsou stručně představeny oblasti našeho výzkumu a některé nástroje používané při studiu elektronové struktury systémů se silně korelovanými elektrony. V kapitolách 8 a 9 pak pojednáváme o našich hlavních výsledcích z oblasti elektronové struktury kuprátových supravodičů s vysokou hodnotou teploty supravodivého přechodu T_c, a z oblasti excitonové kondenzace v rámci Hubbardova modelu.

Dispersní relace fermionových excitací ve vysokoteplotních supravodičích byla studována s využitím selfkonsistentní varianty fenomenologického modelu, kde nabité kvazičástice interagují se spinovými fluktuacemi. Vstupy pro výpočty - pásová struktura a spinová susceptibilita χ - byly získány fitováním fotoemisních a neutronových dat v předchozí práci Thomase Dahma a spolupracovníků [T. Dahm et al., Nature Physics. 5, 217 (2009)]. Naše hlavní výsledky jsou tyto: (i) Potvrdili jsme zjištění T. Dahma a spolupracovníků, že hlavní zlom ("kink") v dispersní relaci podél hlavní diagonály Brillouinovy zóny je - pro dané hodnoty vstupních parametrů - určen tzv. horní větví přesypacích hodin ve spektru spinové susceptibility χ. (ii) Vliv na fermionovou dispersní relaci tzv. rezonančního módu ve spektru χ silně závisí na jeho čtvrtém standardizovaném momentu (anglicky "kurtosis") v prostoru kvazihybností. Nízká (vysoká) hodnota momentu má za následek zanedbatelný (významný) vliv módu na dispersní relaci podél hlavní diagonály Brillouinovy zóny. (iii) Energie zlomu klesá s rostoucím úhlem mezi řezem Fermiho plochy a hlavní diagonálou Brillouinovy zóny, v kvalitativním souladu s nedávno získanými experimentálními poznatky. Tento trend je objasněn, zároveň předpovězeny určité vlastnosti úhlové závislosti zlomu.

Objevili jsme mechanismus, který vede ke vzniku spinové textury v $\mathbf{k}$ prostoru v rámci nedegenerovaného dvojpásového Hubbardova modelu, daný spontánním narušením symetrie způsobeným elektronovými korelacemi. S využitím dynamické teorie středního pole ukazujeme, že dopování tripletního excitonového izolantu může vést ke vzniku nových termodynamických fází s jedinečnými vlastnostmi. Numerické výsledky jsou interpretovány s využitím nástrojů analogických těm, které jsou používány v kontextu teorie tzv. dvojné výměny. Spinové textury v $\mathbf{k}$ prostoru jsou zajímavé z toho důvodu, že mají řadu aplikací v oblasti spintroniky. Náš výsledek je významný tím, že ukazuje, jak mohou spinové textury vzniknout bez přispění spin-orbitální interakce.

Abstract

In the first part of the thesis (chapters 1 to 7), we briefly introduce the topics of our research and we summarize some important tools used in studies of strongly correlated electron systems. Next (in chapters 8 and 9) we report on our main results concerning the electronic structure of the high-T_c cuprate superconductors, and the excitonic condensation in the Hubbard model, respectively.

The electronic dispersion of the high-T_c cuprate superconductors has been investigated using the fully self-consistent version of the phenomenological model, where charge quasiparticles are coupled to spin fluctuations. The inputs we use —the underlying (bare) band structure and the spin susceptibility χ— are extracted from fits of angle resolved photoemission and inelastic neutron scattering data of underdoped $YBa_2Cu_3O_{6.6}$ reported by T. Dahm and coworkers [T. Dahm *et al.*, Nat. Phys. **5**, 217 (2009)]. Our main results are: (i) We have confirmed the finding by T. Dahm and coworkers that the main nodal kink is, for the present values of the input parameters, determined by the upper branch of the hour-glass of χ. We demonstrate that the properties of the kink depend qualitatively on the strength of the charge-spin coupling. (ii) The effect of the resonance mode of χ on the electronic dispersion strongly depends on its kurtosis in the quasimomentum space. A low (high) kurtosis implies a negligible (considerable) effect of the mode on the dispersion in the near-nodal region. (iii) The energy of the kink decreases as a function of the angle θ between the Fermi surface cut and the nodal direction, in qualitative agreement with recent experimental observations. We clarify the trend and make a specific prediction concerning the angular dependence of the kink energy in underdoped $YBa_2Cu_3O_{6.6}$.

We have discovered a mechanism that leads to the appearance of a $\boldsymbol{k}$-space spin texture in the non-degenerate two-band Hubbard model, due to a spontaneous symmetry breaking driven by electronic correlations. Using dynamical mean-field theory, we show that doping a spin-triplet excitonic insulator provides a means of creating new thermodynamic phases with unique properties. The numerical results are interpreted using analytic calculations within a generalized double-exchange framework. Spin textures in $\boldsymbol{k}$-space are of particular interest because they find numerous applications in spintronics. Our result represents a significant step forward, insofar as it shows that such patterns can be generated even in the absence of spin-orbit coupling.

Acknowledgments

I am extremely grateful to my supervisor doc. Dominik Munzar, for accepting my application as a PhD candidate in spite of my unusual profile, for his guidance through the complexities of many-body physics, his continuous support and numerous advice. I am very indebted to Ass. Prof. Jan Kuneš, who accepted to teach me the intricacies of dynamical mean field theory, and helped me acquire a working proficiency with this technique. I wish to thank Prof. Dr. Thomas Dahm, whose input was essential in reaching convincing results in our work on high temperature superconductors. I am thankful to the heads of the Institute of Condensed Matter Physics, Prof. Josef Humlíček and doc. Dominik Munzar, as well as to all the staff, for promoting and developing a pleasant and stimulating working atmosphere. In particular, I would like to thank Mgr. Jiří Chaloupka, Ph.D., for numerous enriching conversations on theoretical physics and for proofreading a substantial part of this thesis, and Mgr. Petr Klenovský, Ph.D., for a fruitful cooperation.

It is my pleasure to acknowledge the wonderful support I have received during these four years, from a number of people in science. Mgr. Pierre Chary was the first to inspire me to come back to physics after some time spent in the banking industry. My former professors, Distinguished Teaching Prof. Harold Metcalf, Prof. Emeritus Joseph Zyss, and Mgr. Stéphane Olivier approved of my decision and encouraged me. I have also enjoyed the interactions with and advice from my friends and fellow academics Ass. Prof. Charlotte Truchet, Ass. Prof. Camille Coti, Dr Setareh Chong, Ass. Prof. David Abergel, Dr. Baptiste Gault, Ass. Prof. Mix Lamalice, Ass. Prof. Francois-Xavier Coudert, Ass. Prof Eric-Olivier Le Bigot. Their input was priceless, and helped me ease into the research community, at a point when I found many reasons to question my adequacy to the task.

Finally, I want to thank my family: my parents, my wife Sylva for her unfaltering support and unwavering patience, and last but not least our four kids who have been the unsuspecting driving force to get this work started.

Prohlášení

Prohlašuji, že jsem svoji práci vypracoval samostatně s využitím informačních zdrojů, které jsou v práci citovány.

Brno 12. Duben 2017 .....

Dominique Geffroy

Contents

1 Introduction **1**

2 From Cooper to excitonic pairing **3**
2.1 Cooper pairing in high-temperature superconductors 3
2.1.1 Cuprate superconductors 3
2.1.2 Kinks in the electronic dispersion 5
2.1.3 The main kink in the electronic dispersion of cuprates 8
2.1.4 Angular dependence of the kink 14
2.2 Excitonic instability 17
2.2.1 A thought experiment: Mott's insight 17
2.2.2 Nature of the order parameter and phase diagram 20
2.2.3 Excitonic ferromagnetism 22
2.2.4 Experimental results 23

3 Models of strongly correlated electron systems **25**
3.1 The Hubbard model 25
3.1.1 SU(2) symmetry 26
3.1.2 U(1) symmetry 26
3.1.3 Particle-hole symmetry 26
3.2 The single impurity Anderson model 28
3.2.1 Anderson Hamiltonian 28
3.2.2 Hartree-Fock treatment of the interaction term 29

4 Excitonic condensation within the Hubbard model **34**
4.1 The two-band Hubbard model 34
4.2 Weak coupling limit formalism 35
4.3 Strong coupling limit formalism 37
4.3.1 Ultralocal regime 37
4.3.2 Strong-coupling limit 39
4.3.3 Effective Hamiltonian approach 40
4.3.4 Pseudospin formulation 41
4.4 Intermediate coupling 42
4.4.1 Half-filling case 42
4.4.2 Impact of doping 43

5 Coherent states and the functional integral formalism **46**
5.1 Coherent states for fermions 46

5.1.1 The basis of coherent states . . . 46
5.1.2 Grassmann algebra . . . 47
5.1.3 Coherent states for fermionic systems . . . 48
5.1.4 Algebraic properties of the fermion coherent state basis . . . 50
5.2 Functional integral formalism . . . 52
5.2.1 Time evolution operator . . . 52
5.2.2 Partition function for a many-body fermion system . . . 54
5.3 Stationary phase approximation for the Hubbard model . . . 55
5.3.1 Partition function for the Hubbard model . . . 55
5.3.2 From the Hubbard model to the spin-fermion model . . . 58

6 Dynamical Mean Field Theory . . . 61
6.1 Introduction . . . 61
6.2 Lagrangian expression for selected models . . . 62
6.2.1 Non-interacting system . . . 62
6.2.2 Single impurity Anderson model . . . 65
6.2.3 Hubbard model . . . 66
6.3 Self-consistency loop . . . 71

7 Quantum impurity solvers . . . 74
7.1 Introduction . . . 74
7.2 Monte Carlo sampling of partition functions . . . 74
7.2.1 Monte Carlo basics . . . 74
7.2.2 Importance sampling . . . 76
7.2.3 Metropolis algorithm . . . 77
7.3 Monte Carlo approach to the impurity problem . . . 78
7.3.1 Sampling the partition function to finite order . . . 79
7.3.2 Sampling the partition function to infinite order . . . 80
7.4 The hybridization expansion continuous-time solver . . . 81
7.4.1 Expansion of the partition function . . . 81
7.4.2 Case of density-density interactions . . . 83
7.4.3 Updates . . . 84
7.4.4 Accumulation formulas: Green's function . . . 85

8 Main kink in the electronic dispersion of cuprate superconductors . . . 89
8.1 Introduction . . . 89
8.2 Spin-fermion model based calculations . . . 90
8.3 The kink in the dispersion relation along the nodal axis . . . 93
8.3.1 Role of the upper branch of χ'' . . . 93
8.3.2 Impact of the magnitude of the coupling constant . . . 95
8.4 The kink in the dispersion relation away from the nodal axis . . . 97
8.4.1 Effective self-energy approach . . . 98
8.4.2 Relation between the kink and the features of the quasiparticle self-energy . . . 99

8.5 Comparison with experimental data . . . 103

9 Spontaneous Spin Textures in Multiorbital Mott Systems . . . 107
9.1 Introduction . . . 107
9.2 Model . . . 108
9.2.1 Computational details . . . 108
9.2.2 Results of calculations . . . 108
9.3 Interpretation: double-exchange mechanism . . . 110
9.3.1 The undoped case . . . 112
9.3.2 The doped case . . . 112
9.4 Realization . . . 116
9.5 Spin-galvanic effect . . . 118
9.5.1 Algorithm . . . 119
9.5.2 Updates . . . 121
9.5.3 Sampling . . . 122

10 Summary and outlook . . . 124

A Gaussian integrals over the Grassmann algebra . . . 127

B Link between cavity and full Green's function in DMFT . . . 130

C Fast update formulas . . . 132
C.1 Segment insertion . . . 132
C.2 Segment removal . . . 135
C.3 Segment shift . . . 135
C.3.1 Shift of a creation time . . . 135
C.3.2 Shift of an annihilation time . . . 136

D High-frequency expansion formulas . . . 137
D.1 Green's function . . . 137
D.1.1 Analytic expressions for the tails . . . 137
D.1.2 Coefficients of the high-frequency expansion . . . 139
D.2 Self-energy . . . 141
D.3 Hybridization function . . . 142

Publications . . . 155

Conference presentations . . . 156

Chapter 1

Introduction

The explanation, by Sir Nevill F. Mott, of the subtle ways in which strong electronic correlations can dramatically affect the macroscopic physical properties of materials [1] was a groundbreaking work which earned him the 1977 Nobel prize in physics. It was a major milestone in the development of what is now known as the theory of strongly correlated electron systems. The ways in which strong correlations affect a system are numerous and varied, the Mott metal to insulator transition being only one of them. The present work focuses on two different but related manifestations of strong correlations in condensed matter systems.

The first phenomenon we investigate is high-temperature superconductivity in cuprates. For more than thirty years, it has remained an outstanding unsolved problem in the field of condensed matter theory. In spite of intense efforts by the community, no consensus has been reached as to the precise underlying microscopic mechanism. Instead, the mystery deepened with the discovery of new compounds which also exhibit an unconventional superconducting phase, in particular iron arsenides and iron selenides discovered in 2008 [2–5]. Recently a conventional superconductivity setting on at 203 K has been reported to occur in a high-pressure phase in the sulfure hydride system [6, 7]. A large part of the present work is dedicated to a theoretical investigation of the interaction mechanism involved in the high-temperature superconductivity of cuprate superconductors.

A number of experimental probes have been employed to shed light on the origin of superconductivity. Among those, angular resolved photoemission spectroscopy (ARPES) has raised a lot of interest, insofar as it allows access to details of the underlying fermionic physics with an unprecedented precision. One of the most direct ways, in which ARPES can be used, consists in measuring the dispersion of fermions. The profiles may exhibit signatures of the dominant interactions in the system, and thus give precious clues as to which aspects of the underlying physics need to be taken into account in a theoretical approach.

In this thesis we concentrate on a heavily discussed feature of the fermionic dispersion in cuprates, called the main kink. It is a sudden change in the slope of the dispersion, which has been observed in many classes of cuprates ca. 70 meV below the Fermi level. This is most naturally interpreted as a consequence of an interaction between the fermions, and a bosonic mode in the system. We rely on a theoretical model called the spin-fermion model, which involves the interaction of the fermions with spin fluctuations, i.e. bosonic collective modes of the fermionic system itself. A critical input for this model is the spectrum of the magnetic excitations of the material. Our aim is to compare the results of the model calculations and the experimental data of the momentum dependence of the main kink, and

thus contribute to the identification of the essential ingredients of the pairing mechanism.

This work then addresses a different phase transition observed in condensed matter, namely that towards an excitonic condensate. While this transition manifests itself in a very different way than superconductivity, the phenomena are formally similar, insofar as both transitions involve the pairing of fermions into bosonic entities. In the case of superconductivity, Cooper pairs, consisting of two electrons, are formed, while in the case of excitonic condensation, an electron and a hole are paired to form an exciton. We carry out our study of this condensation within the framework of a time-honed model for strongly correlated systems: the Hubbard model [8].

The possibility of excitonic condensation in the Hubbard model is not a recent finding, since it had been proposed already by Mott [9], but the development of new powerful numerical techniques such as the Dynamical Mean Field Theory (DMFT) [10] has recently allowed to obtain new insights into the physics of this transition. In the present work we use DMFT to study the two-band Hubbard model in a region of the phase diagram where Hund's coupling and the crystal field splitting are in competition, so that the system is close to a transition between a low-spin and a high-spin configuration. This allows us to detect a spin texture in the ordered phase, and explain its emergence using a strong-coupling model.

The structure of the thesis is as follows: in the second chapter we provide an overview of the experimental findings relevant to our work on cuprates, and the theoretical foundations of the field of excitonic condensation. The chapters which follow introduce the tools which were used in our research: essential features of a number of models employed in studies of strongly correlated systems are introduced in Chapter 3, and the specific case of the strong-coupling approach to excitonic condensation in the Hubbard model is addressed in Chapter 4. In Chapter 5, the path-integral formalism in the coherent state representation is introduced, which provides a formal justification for the spin-fermion model. The two following chapters introduce the tools used in the study of the excitonic condensation. In Chapter 6, we derive the self-consistent system of equations of DMFT. The following chapter (Chapter 7), presents the details of the most demanding part of the numerical calculations, the continuous-time hybridization expansion impurity solver [11]. Our results related to the physics of cuprates are presented in Chapter 8, while those connected to excitonic condensation are given in Chapter 9. The final chapter contains a summary of our work and outlines several possible extensions.

Chapter 2

From Cooper to excitonic pairing

2.1 Cooper pairing in high-temperature superconductors

The Bardeen, Cooper, and Schrieffer (BCS) theory of superconductivity in conventional superconductorsof [12, 13] was confirmed by many experiments based on the isotope effect, on manifestations of the electron-phonon spectral density $\alpha^2F(\Omega)$ in tunneling data, etc. On the other hand, the discovery of high-temperature superconductivity by Bednorz and Müller [14] triggered a flurry of experimental and theoretical work, but no consensus has been reached concerning the exact underlying mechanism for the emergence of superconductivity, to this day. In particular, while the "bosonic glue" is provided by phonons in the BCS theory, the very existence of such a glue for high-temperature superconductivity has been questioned [15]. Several important theories, however, involve a glue connected either with the lattice or with spin fluctuations. In order to settle the related questions, the identification of an electron-boson spectrum which would be consistent with the experimental data is a crucial step. One of the ways this can be done is by the quantitative study of the kinks present in the electronic dispersion.

2.1.1 Cuprate superconductors

Here we summarize the essential properties of cuprate superconductors that are relevant to our research, following the work by J. Bok [16]. For extensive reviews on the subject see refs [17–21].

Structure and doping

All the high-temperature cuprates are layered materials, and possess copper oxygen planes (CuO_2 planes). Figure 2.1 illustrates the layered nature of the cuprates, and highlights the orbital hybridization that takes place in the CuO_2 planes. The unit cell of the well known material $YBa_2Cu_3O_{7-\delta}$ (YBCO) is illustrated in Fig. 2.2. In this material, δ can be tuned, which allows one to control the density p of mobile charge carriers (holes). For $\delta = 1$, $p = 0$, the compound is insulating and exhibits antiferromagnetic order with a Néel temperature of approximately 300 K. With decreasing δ, p increases, the material is doped with holes, the antiferromagnetic order is rapidly suppressed, and disappears for $p \simeq 0.03$ (see the schematic phase diagram in Fig. 2.3). A superconducting phase with critical temperature T_c appears for $p \simeq 0.05$. The critical temperature exhibits a maximum, as a function of doping, for $p \equiv p_o \simeq 0.17$ (optimum doping).

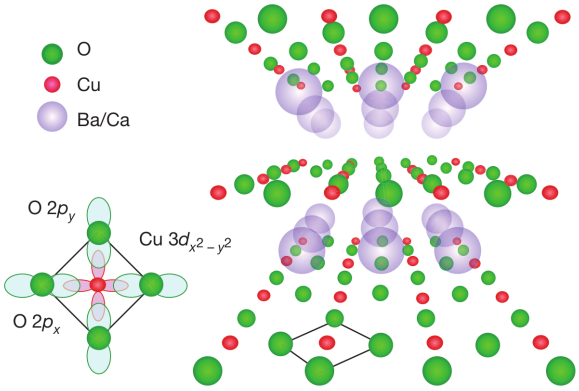

Figure 2.1: Layered copper oxides are composed of CuO_2 planes, typically separated by insulating spacer layers. The electronic structure of the planes is determined involves primarily the hybridization of Cu $3d_{x^2-y^2}$ orbitals with planar-coordinated $2p_x$ and $2p_y$ oxygen orbitals. Reprinted figure with permission from Ref. [17].

Phase diagram

The schematic phase diagram of copper oxides in Fig. 2.3 displays a number of different phases, as well as the associated critical and onset temperatures. We will now briefly introduce the essential features of the diagram.

Above T_c in the normal state, three regions may be distinguished:

- The underdoped region, where $p < p_o$. In this region, we observe the so-called pseudogap, whose origin has not yet been clarified.
- The region around $p \simeq p_o$, where the compound is a bad metal with unusual properties, referred to as the "strange metal" region.
- The overdoped region, for $p > p_o$, where the conduction electrons exhibit the properties of a Fermi liquid and the system behaves like a usual metal.

Experiments have shown [18, 19, 22] that in the superconducting phase, electrons are paired in a spin singlet state. The coherence length is quite short compared to that observed in conventional superconductors. Besides, the symmetry of the pair-wave function and of the related superconducting gap Δ_k is $d_{x^2-y^2}$, in contrast to the full (s-wave) symmetry occurring in conventional superconductors.

Electronic structure

It is straightforward to execute a single particle calculation of the electronic structure, assuming the compound is represented by a regular two-dimensional lattice[18, 23, 24]. Figure 2.3, panels (b) and (c), shows the result of such a calculation. One can show that a topological transition occurs for a critical value of doping of ca. $p_c = 0.21$ hole per Cu atom. The Fermi surface is hole-like (electron-like) for $p < p_c$ ($p > p_c$).

This approach is not valid in the low doping region. The strong Coulomb repulsion U between electrons on the same site triggers the appearance of long range magnetic order. This means that strong correlations have to be taken into account. Even when the long range antiferromagnetic order is suppressed by doping, antiferromagnetic fluctuations

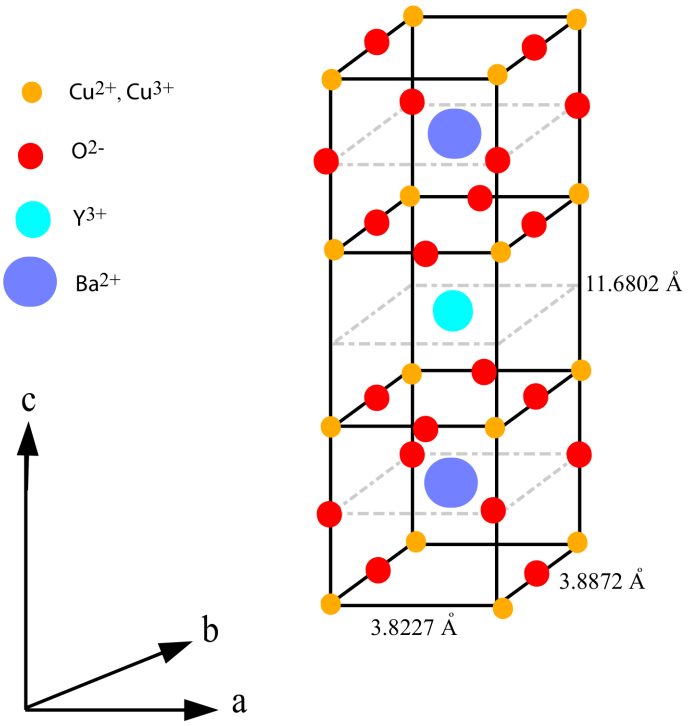

Figure 2.2: Structure of $YBa_2Cu_3O_{7-\delta}$. Reprinted figure from Ref. [16].

remain present, and need to be considered, for doping levels at least up to optimal doping. The valid approach in this context is that of a doped Mott insulator, as confirmed by results of angular resolved photoemission spectroscopy (ARPES) experiments on heavily underdoped cuprates [25]. For moderately underdoped cuprates, some segments of the Fermi surface disappear upon the formation of the pseudogap as illustrated in Fig. 2.4.

2.1.2 Kinks in the electronic dispersion

Many properties of condensed matter are determined by single-particle and collective excitations, and their interactions. These excitations are characterized by their energy and momentum, themselves related via the dispersion relation, labeled as $\epsilon_{\boldsymbol{k}}$ for the single particle case. The coupling between excitations can bring about sudden changes in the profile of the dispersion (kinks). The study of kinks therefore provides an important information on the latter coupling.

Kinks occur already within the simplest models, such as that of non-interacting electrons coupled to phonons [26]. More generally, any boson coupled to the electrons has the potential to generate a kink in $\epsilon_{\boldsymbol{k}}$, and this phenomenon is expected to be quite ubiquitous in interacting systems.

A surprising insight was recently reported by Byczuk and coworkers [27], who demonstrated that kinks can be observed in strongly correlated electronic systems, even in the absence of an explicit coupling to any excitation. They can be observed for any strongly correlated metal whose spectral function exhibits three well separated peaks: a central peak and two well separated Hubbard sub-bands.

The development of angular ARPES (see Ref. [25] for a review of the technique) marked a turning point in the experimental study of strongly correlated systems, as it allowed for a

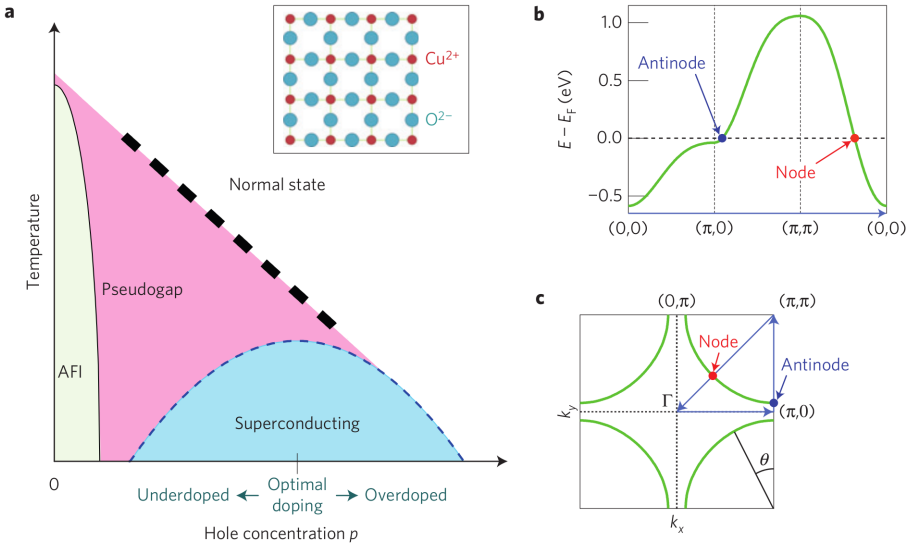

Figure 2.3: Panel (a): schematic phase diagram of high-temperature superconductors. The inset shows the crystal structure of the CuO_2 planes. Panel (b): schematic representation of the band dispersion for cuprates along the high-symmetry cuts, as shown in blue in panel (c). Panel (c): schematic representation of the Fermi surface, where the nodal and antinodal momenta and the angle θ are defined. Reprinted figure with permission from Ref. [21].

precise measurement of the electronic dispersion in these materials. In order to understand the origin of ARPES signals, the so-called three-step model has been developed [25]. This model assumes that the photoemission process can be divided into three independent and sequential steps:

- Optical excitation of the electron in the bulk,
- Travel of the excited electron to the surface,
- Escape of the photoelectron into vacuum,

which allows one to evaluate the total photoemission intensity as a product of three independent terms: the total probability for the optical transition, the scattering probability for the traveling electrons, and the probability of transmission through the surface potential barrier. The other important assumption has to do with the fate of the excited electrons while the travel to the surface. In all generality, the possibility for them to relax before they have the possibility to escape into the vacuum should be evaluated. Nevertheless, the sudden approximation is usually employed. In this limit, which is in all rigor applicable only to high-energy electrons, the photoemission process is assumed to be sudden, with no interaction between the excited photoelectron and the system left behind. Under these assumptions, one can show that the ARPES signal is proportional to $A(\boldsymbol{k},\omega)n_F(\omega)$, where $A(\boldsymbol{k},\omega)$ is the spectral function

$$A(\boldsymbol{k},\omega) = -\frac{1}{\pi}\frac{\mathrm{Im}\{\Sigma(\boldsymbol{k},\omega)\}}{\left[\omega - \epsilon_{\boldsymbol{k}} - \mathrm{Re}\{\Sigma(\boldsymbol{k},\omega)\}\right]^2 + \mathrm{Im}\{\Sigma(\boldsymbol{k},\omega)\}^2}, \tag{2.1}$$

so that precise measurement of the ARPES profiles provides an insight into the structure of the self-energy $\Sigma(\boldsymbol{k},\omega)$. In particular, it is possible to interpret a kink in an ARPES signal

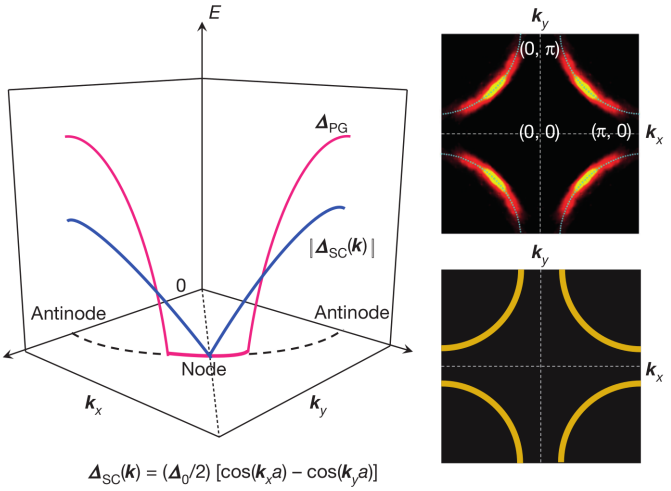

Figure 2.4: The large Fermi surface predicted by band theory is observed by ARPES and STS for overdoped compounds (bottom right). Conversely, once the pseudogap sets in, the antinodal regions of the Fermi surface near the Brillouin zone edge are gapped out, giving rise to Fermi arcs (top right). This is reflected (left) in the angle dependence of the energies of the superconducting gap Δ_{SC} (blue line) and of the pseudogap Δ_{PG} (red line) as functions of the momenta k_x and k_y in one quadrant of the Brillouin zone around the underlying large Fermi surface (dashed curve). Reprinted figure with permission from Ref. [17].

in terms of the energy dependence of the self-energy: by inspection of Eq. (2.1), it can be seen that any kink in the ARPES signal, that does not originate from the bare dispersion $\epsilon_{\boldsymbol{k}}$, must be caused by a slope change in $\mathrm{Re}\,\Sigma(\boldsymbol{k}, \omega)$. Therefore, the analysis of the ARPES signal offers a precious insight into the structure of the self-energy of the studied system. The features of the self-energy can then be confronted with predictions based on models involving electron-boson coupling. If and when a relevant bosonic mode is identified, and the importance of its coupling to electrons thus demonstrated, its role in connection with other electronic properties of the material such as superconductivity can be examined. The kink is most easily measured by extrapolating the linear fermionic dispersion at low energy. At higher energies, the experimental profile diverges from the linear extrapolation. The energy of the point where the slope suddenly changes is a good estimate for the energy of the kink. Alternatively, a reference dispersion can be constructed, which connects the Fermi level crossing to the high-energy dispersion. The difference between the actual dispersion, and this reference line can be interpreted as an effective self-energy, which is zero by construction at low and high energies, and thus exhibits a peak at an intermediate energy. The energy of the peak in this effective self-energy provides another estimate for the energy of the kink. More details on these approaches, as well as an alternative method, based on a theoretical framework rather than on experimental data, are given in Sec. 8.

A drawback of the ARPES technique is that, due to its sensitivity to the quality of the surface of the sample, it cannot be used for all compounds for all dopings. Its limitations are illustrated in Fig. 2.5. This can make it difficult to relate the results of ARPES with those obtained using other techniques, such as neutron diffraction.

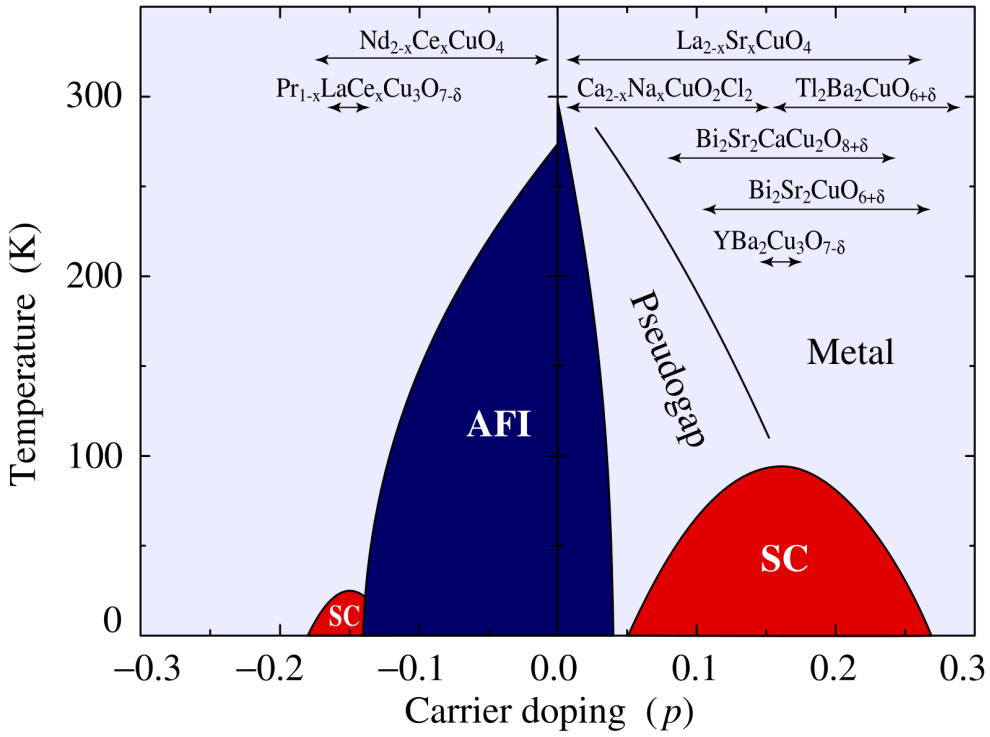

Figure 2.5: Schematic phase diagram of the cuprates in the doping versus temperature plane. Positive (negative) values of the doping p correspond to hole (electron) doping. The arrows indicate which regions of the phase diagram can be studied by ARPES, for each species of cuprate. Used under CC BY-NC-SA version 3.0 license, from Ref. [28].

2.1.3 The main kink in the electronic dispersion of cuprates

The first experimental observation of a kink in the electronic dispersion of cuprates along the Brillouin zone diagonal is due to Valla et al. [29], who studied the quantum critical behavior of the doped cuprate $Bi_2Sr_2CaCu_2O_{8+\delta}$. They observed that the dispersion along the nodal axis was not modified by the transition to the superconducting state, and deduced that the nodal states, i.e. those with $\boldsymbol{k}$ along the diagonal of the Brillouin zone, are not involved in the emergence of superconductivity. The profile which they obtained is displayed in Fig. 2.6. It clearly shows the presence of a kink around an energy of 80 meV. This feature was intensively investigated after the publication of this work, and became known as the main kink in the dispersion.

The discovery of this kink sparked a theoretical effort to trace back its origin to other known properties of the material. Among the potential origins of the kink, a phonon mode [30] was considered, as well as coupling to collective spin excitations. The latter speculation was inspired in part by previous observations of spin excitations in cuprates, using inelastic neutron scattering. As early as 1991, Rossat-Mignod et al. reported a sharp peak in the measured magnetic susceptibility of $YBa_2Cu_3O_{6.51}$ [31], known as the "magnetic mode". Their result is shown in Fig. 2.7. They concluded that hole doping has a strong effect on the antiferromagnetic order of the parent compound. They also showed that dynamical antiferromagnetic correlations persist in the metallic state, and that the superconducting samples exhibit an energy gap in the spin excitation spectrum at low temperature.

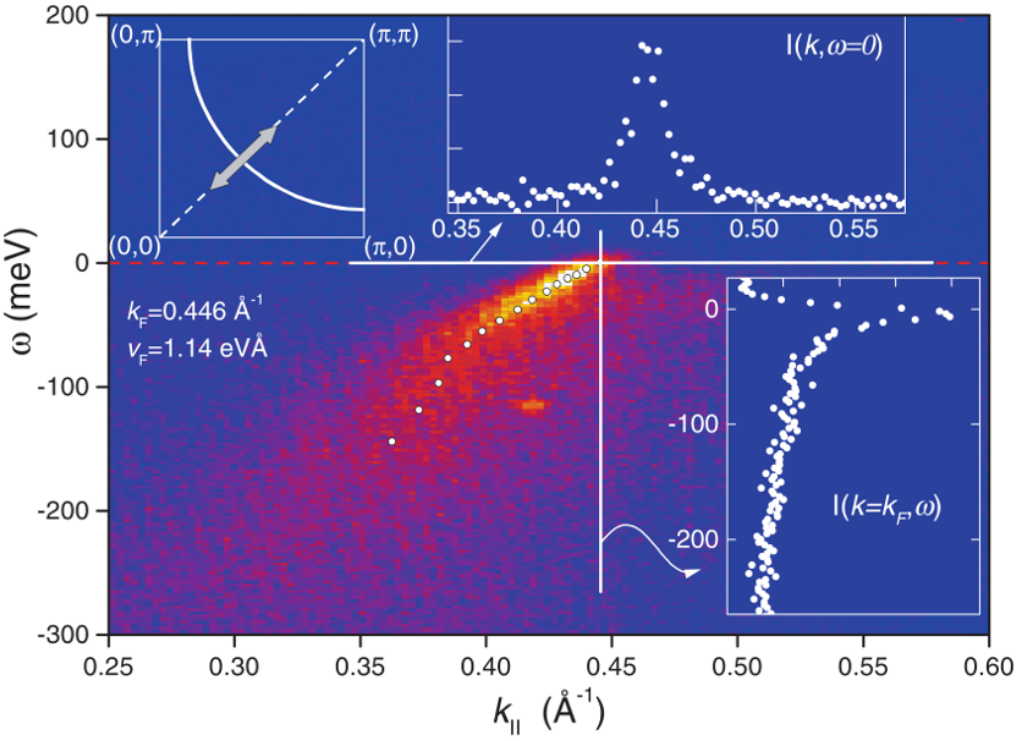

Figure 2.6: (Main panel) ARPES profile of the electronic dispersion along the nodal axis for $Bi_2Sr_2CaCu_2O_{8+\delta}$. (Upper left panel) Schematic representation of the Brillouin zone, with an arrow showing the position of the experimental cut. (Upper right panel) Cross section of the data for constant energy $\omega = 0$, as a function of momentum k. (Lower right panel) Cross section of the data for constant momentum $k = k_F$, as a function of energy ω. Reprinted with permission from AAAS, from Ref. [29].

The role that such a magnetic mode could play in superconductivity has been considered by many authors, for reviews, see Ref. [32, 33] . One notable effort in this direction was that by Eschrig, Norman, Abanov, Chubukov and coworkers [34, 35]. They argued that even though the spectral weight of the resonance in the magnetic spectrum is small, it can generate a large fermionic self-energy and strongly affect the electronic properties of the cuprates below T_c. The spin-fermion model, presented in detail in Sec. 5 and used in Sec. 8, was extensively used in this context.

The debate on whether the kink is of a phononic or of a magnetic origin, and on its ties with superconductivity, has not been firmly settled in the community yet. Our work brings new insights in this context, which show some of the strengths of the magnetic scenario. Before introducing our results in Chapter 8, we review here some earlier studies which support either the phonon or the magnetic scenario.

The case for the phonon scenario

In this paragraph and the following, we highlight some earlier experimental results which we find to be most relevant for the determination of the origin of the kink, and in relation to our own results. Extensive reviews of the subject are available in Refs. [17, 33, 36]. An important result was published by Lanzara et al. in 2001 [30]. They used ARPES to probe three different kinds of cuprates: $La_{2-x}Sr_xCuO_4$ (LSCO), $Bi_2Sr_2CaCu_2O_8$ (Bi2212), and

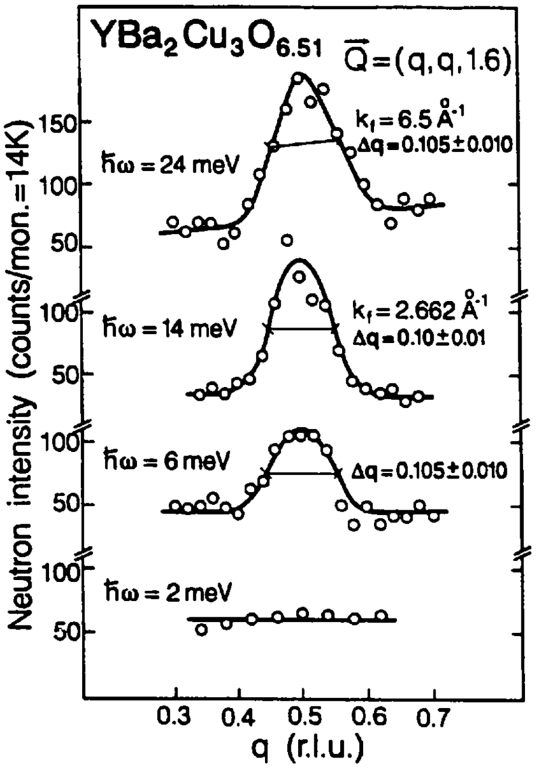

Figure 2.7: Experimental profile of the magnetic susceptibility in $YBa_2Cu_3O_{6.51}$. Measurements were carried out for fixed energy levels equal to 24 meV, 14 meV, 6 meV, and 2 meV, from top to bottom. Reprinted figure with permission from Ref. [31].

Pb-doped $Bi_2Sr_2CuO_6$ (Bi2201). Their main result is shown in Fig. 2.8. The obtained dispersion relations display a kink in a narrow range of energy 50 meV–80 meV, which coincides with the energy range of certain phonons in these systems. For instance, the red arrow in panel (a) corresponds to the energy of the zone boundary in-plane oxygen-stretching longitudinal optical phonon, identified by neutrons as being strongly coupled to charge [37, 38].

They also pointed out that the kink is present in the normal state as well as in the superconducting state, while the magnetic mode is (for optimally doped cuprates) present only in the superconducting state. Their conclusion is that the phonons must play a crucial role in the emergence of superconductivity in these systems.

The role of phonons in high-temperature superconductivity was also investigated by Iwasawa et al. [39]. They used ARPES to study a sample of Bi2212, together with a sample of the same material where ^{16}O has been replaced by ^{18}O, in order to study the isotope shift in the energy of the kink. Their results are reported in Fig. 2.9, and show that the magnitude (a few meV) and the direction of the shift follow those expected from the isotope shift of the phonon frequency. Thus, they argued that oxygen phonons are dominant players in cuprates.

The case for a magnetic scenario

The progress of ARPES soon allowed the investigation of the electronic dispersion away from the nodal axis. Kaminski et al. reported their results for the angular dependence

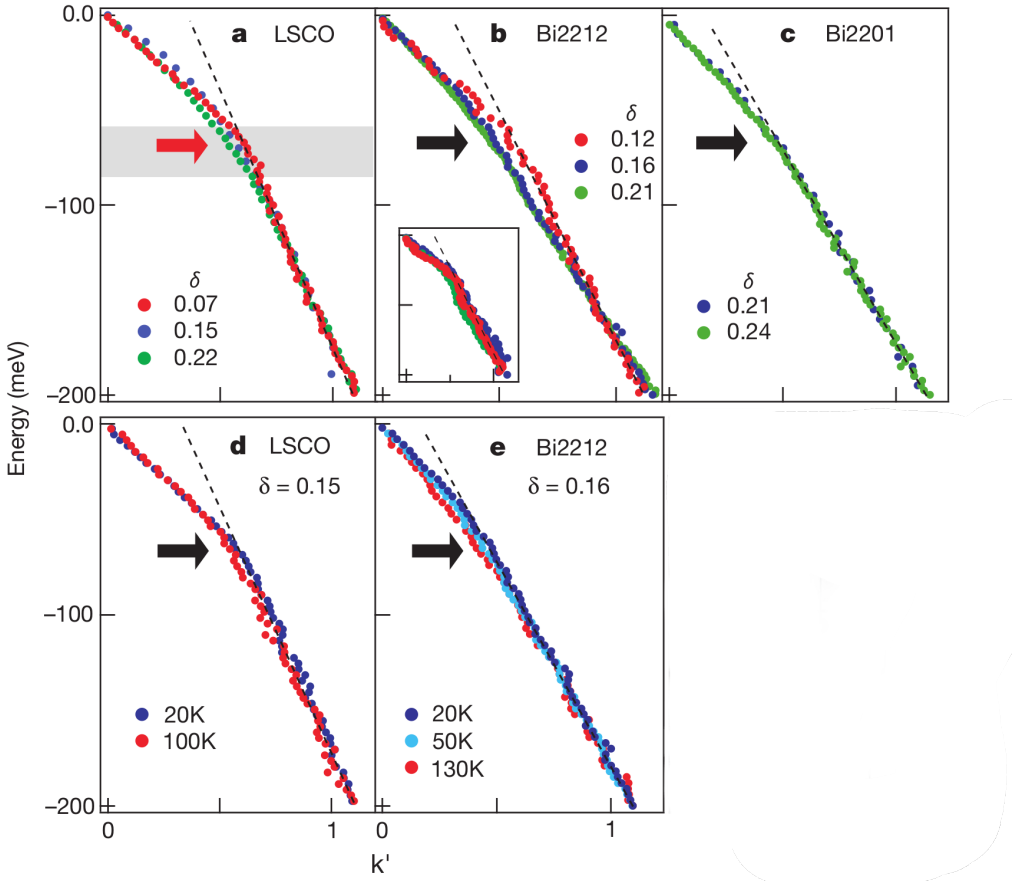

Figure 2.8: Top panels: electronic dispersions along the Brillouin zone diagonal, as a function of doping δ, for $La_{2-x}Sr_xCuO_4$ (LSCO), $Bi_2Sr_2CaCu_2O_8$ (Bi2212) (both in the superconducting state, 20 K), and Pb-doped $Bi_2Sr_2CuO_6$ (Bi2201) (in the normal state, 30 K). The energy of the kink in panel (a) is compared with that of the energy of the $q = (\pi, 0)$ oxygen stretching phonon (thick red arrow). The inset of panel (b) shows the sharpening of the kink feature for a cut away from the nodal axis. Panels (d) and (e) illustrate the temperature dependence of the dispersions for optimally doped LSCO and Bi2212. Reprinted figure with permission from Ref. [30].

of the electronic dispersion in $Bi_2Sr_2CaCu_2O_{8+\delta}$, for the normal and the superconducting states [40]. They confirmed the previous results related to the main kink along the nodal axis, and showed that as one moves closer to the $(\pi, 0)$ point, the kink evolves into a spectral dip. Their main results are presented in Fig. 2.10. It can be seen that the kink strongly depends on the state of the material (normal or superconducting), which may be consistent with the magnetic scenario. Their results also show that the profile of the kink is strongly dependent on the position of the cut in the Brillouin zone, along which the dispersion is measured. This dependence should be met by any theoretical model of the main kink.

A few years later, Borisenko et al. applied a new-generation ARPES methodology, which allowed them to study $YBa_2Cu_3O_{6+x}$. They observed features similar to those previously reported for Bi2212. In particular, they showed that there is a clear shift in energy of the kink to higher binding energies upon doping. They also identified a secondary kink, at

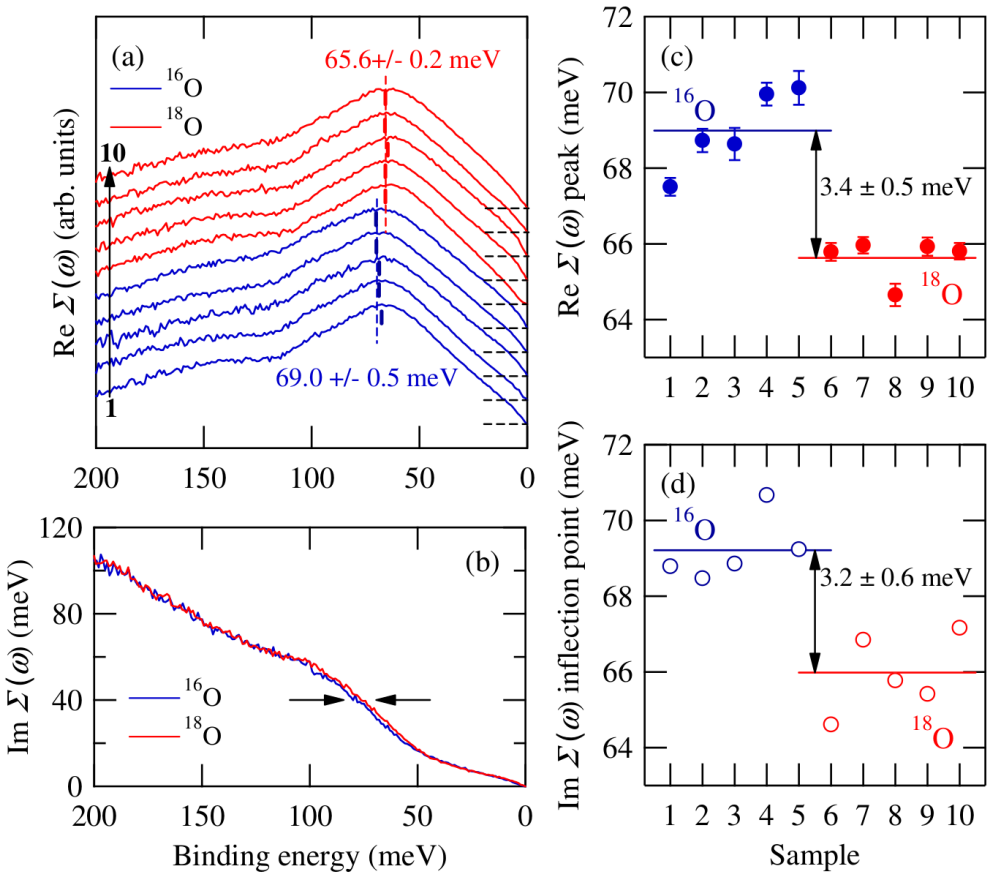

Figure 2.9: Panel (a): real part of the self-energy $\mathrm{Re}\,\Sigma(\omega)$ for five samples containing ^{16}O (blue lines) and five samples containing ^{18}O (red lines), for a cut along the Brillouin zone diagonal. The profiles are offset for clarity. Panel (b): imaginary part of the self-energy $\mathrm{Im}\,\Sigma(\omega)$. Panels (c) and (d): Kink energy versus sample index. Reprinted figure with permission from Ref. [39].

an energy higher than that of the main kink. On the basis of these results, they claimed that these features are universal among cuprates, and could be essential in the search for the mechanism of superconductivity [41]. Given the correlations between the energy of the kinks in these different systems, and the energies of the resonant mode in their magnetic spectra, these observations are supportive of the magnetic scenario. The profiles of the kinks obtained by Borisenko et al. are given in Fig 2.11.

Bridging the gap

Improvements in high-resolution ARPES techniques allowed the finer measurement of electronic dispersion. This allowed to obtain more reliable experimental results away from the nodal axis, as well as data with a much improved resolution in energy. Gromko et al. reported the first high-quality data of the electronic dispersion in Bi2212, close to the antinodal point $k = (\pi, 0)$ [42]. This allowed them to observe the presence of a kink, at an energy lower than that reported for the nodal kink (around 40 meV, as can be seen Fig. 2.12). More importantly, they observed that this antinodal kink was absent in the normal state, contradicting earlier observations of the nodal kink. This important piece

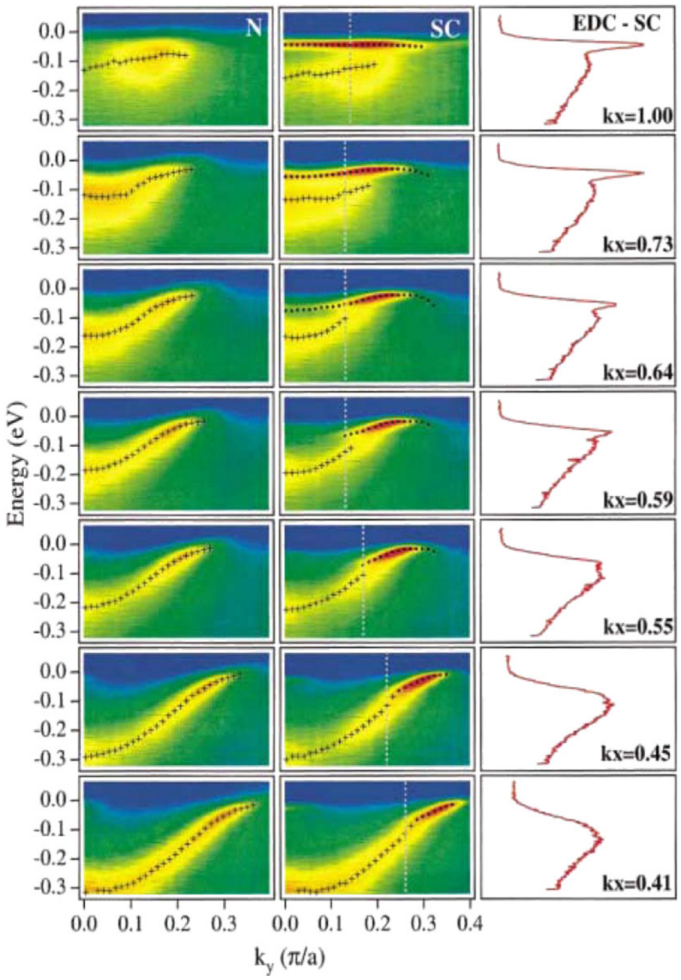

Figure 2.10: ARPES intensity along selected cuts in the Brillouin zone. Left panels: normal state (T=140 K). Middle panels: superconducting state (T=40 K). Right panels: energy dispersion curves (cuts for constant values of momentum k) corresponding to the cuts indicated by the dashed lines in the middle panel. Reprinted figure with permission from Ref. [40].

of information established that not only the slope of the kink, but also its temperature dependence is strongly momentum dependent. This was interpreted as a support for the magnetic origin of the kink, but it could also be consistent with a mixed interpretation, according to which the nodal and the antinodal kinks do not necessarily obey the same mechanism.

Another result came to support a possible mixed origin of the kinks, when Sato et al. [43] used high-resolution ARPES to study and compare single-layered and multilayered samples of $Bi_2Sr_2Ca_{n-1}Cu_nO_{2n+4}$, $(n = 1, \ldots, 3)$. Their analysis showed that in the multilayered compounds, the antinodal kink is pronounced, while it is absent in single-layered ones. The nodal kink, on the other hand, is clearly seen also in the single-layer compound, and remains present in the normal state. This allowed them to speculate that the magnetic mode is the dominant factor in the superconducting state for multilayered cuprates, while another mechanism prevails in the single layered compounds. Their results shown in Fig. 2.13, demonstrate the dependence of the kinks (and their temperature dependence)

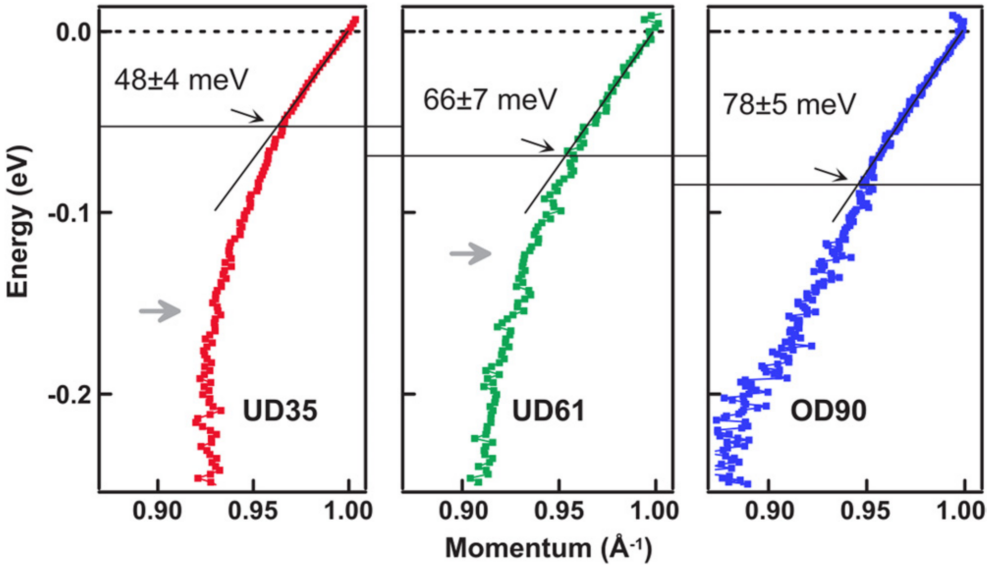

Figure 2.11: Dispersion in $YBa_2Cu_3O_{6+x}$ along the nodal axis, as a function of doping. Horizontal lines mark the energies of the kink; the energy of the kink is defined as the energy where the profile departs from the linear extrapolation from the low energies. Gray arrows show the position of the secondary kink, at higher energy. The energy of the kink displays a high degree of correlation with the energy of the resonance in the magnetic spectra of the materials, obtained by inelastic neutron scattering. Reprinted figure with permission from Ref. [41].

on the number of layers.

2.1.4 Angular dependence of the kink

Up to this point, the nodal and antinodal points of the Brillouin zone were assessed and compared with respect to the kink behavior. A few years of further improvements in ARPES technique were necessary before the resolution in momentum became fine enough and allowed the momentum dependence of the energy of the kink to be measured. Two important works have shed light on this issue. The first one, carried out by He et al. [44], addressed the electronic dispersion in the superconducting state for Bi2212. It revealed the coexistence of two distinct energy scales over a large range of momentum values, starting from the nodal axis, and moving away from it. Not only are these energy scales distinct, but they follow a very different dependence on momentum. The energy of one of them (the higher energy feature) remains approximately constant over the whole range of momentum, while the energy of the other one goes from a value of around 40 meV near the antinodal region to 75 meV on the nodal axis. This comes as a confirmation of the previously observed variety in the kink features, and confirms their different sensitivities to the angle ϕ from the nodal axis.

Their main result is presented in Fig. 2.14. In the left panel, the red arrows point at the low-energy kink, while the black arrows indicate the higher-energy kink. The different colored profiles, labeled cut 1 to cut 4, correspond to different cuts in the Brillouin zone, illustrated in the upper right panel. The lower right panel presents the evolution of the energies of the features, with the same color coding, as a function of the angle ϕ of the cut, measured from the boundary of the Brillouin zone (the nodal axis corresponds to $\phi = 45°$).

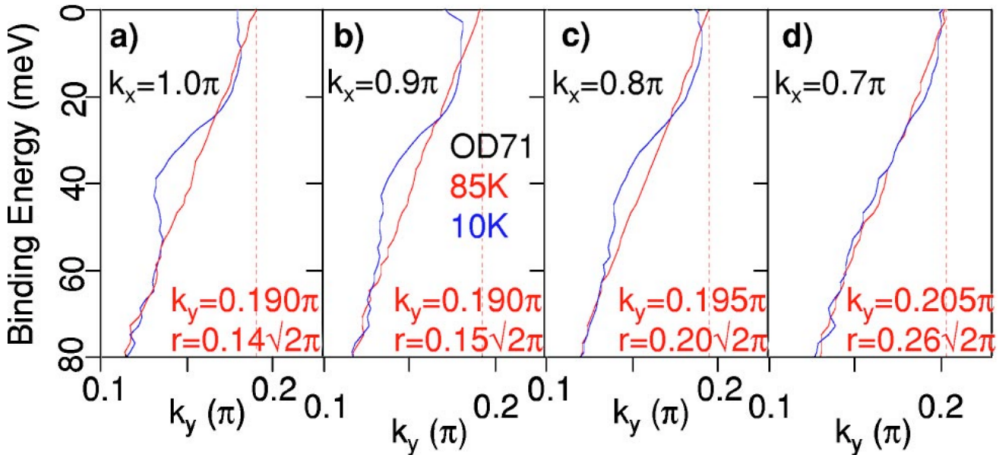

Figure 2.12: Electronic dispersion close to the antinodal point for Bi2212, in the normal and the superconducting states. A low-energy kink is clearly visible. This kink is not present in the normal state, but only in the superconducting state. Reprinted figure with permission from from Ref. [42].

The cut labeled 1 is along the nodal axis. Along this cut, the two features are barely distinguishable, see the left panel. Correspondingly, they share almost the same energy in the right panel, around 70 meV. As the cut moves away from the nodal axis, from cut 1 to cut 4, the two features clearly separate, due to the distinct behavior of their energy as a function of the angle ϕ: the energy of the lower-energy kink is a monotonous, strictly increasing function of ϕ, while the energy of the high-energy kink is constant.

This breakthrough comes as a very new input for the theories of the kink, as it reveals two phenomena which may have a different origin, given their different qualitative behavior. It is worth noting in this context that the feature referred to as the main kink up to this point in history and in this work, is the lower energy kink, which displays a pronounced dependence on ϕ.

The conclusions of the work by He et al. were confirmed by Plumb et al. [45]. They used ultrahigh resolution ARPES to study the same material, Bi2212. They did not identify two distinct features, and focused on the main kink. Their main result is illustrated in Fig. 2.15. The profile of the kink is shown, for two representative cuts, in the panel (b). From these raw data, it is difficult to compare the energies of the kinks, but it can be seen that the feature is much sharper for cut (ii), i.e. away from the nodal axis. Panel (d) illustrates clearly the method used by the authors to determine the position of the kink: they constructed a quantity called effective self-energy $\Sigma_{\text{eff}}(\theta, \omega)$, and identified the position of the kink with that of the maximum of $\Sigma'_{\text{eff}}(\theta, \omega) \equiv \text{Re}\,\Sigma_{\text{eff}}(\theta, \omega)$ [see Eq. (2.1)] and the related discussion for a definition and justification of the concept of effective self-energy). While the validity of this concept of effective self-energy can be discussed, it is a reasonable approach for the the analysis of experimental data. This point is discussed in further details in Sec. 8. Panel (d) shows that the Kramers-Kronig relation between the two components of the self-energy is verified, and clearly shows a sharp maximum in the profile of the real part of the self-energy (black curve), which allows a precise determination of the energy of the kink, Ω_{kink}. The evolution of Ω_{kink} with θ, the angle of the cut measured, this time, from the nodal axis, is presented in panel (e) and shows a very clear trend. The absolute value of the energy of the kink decreases with increasing θ, in agreement with the

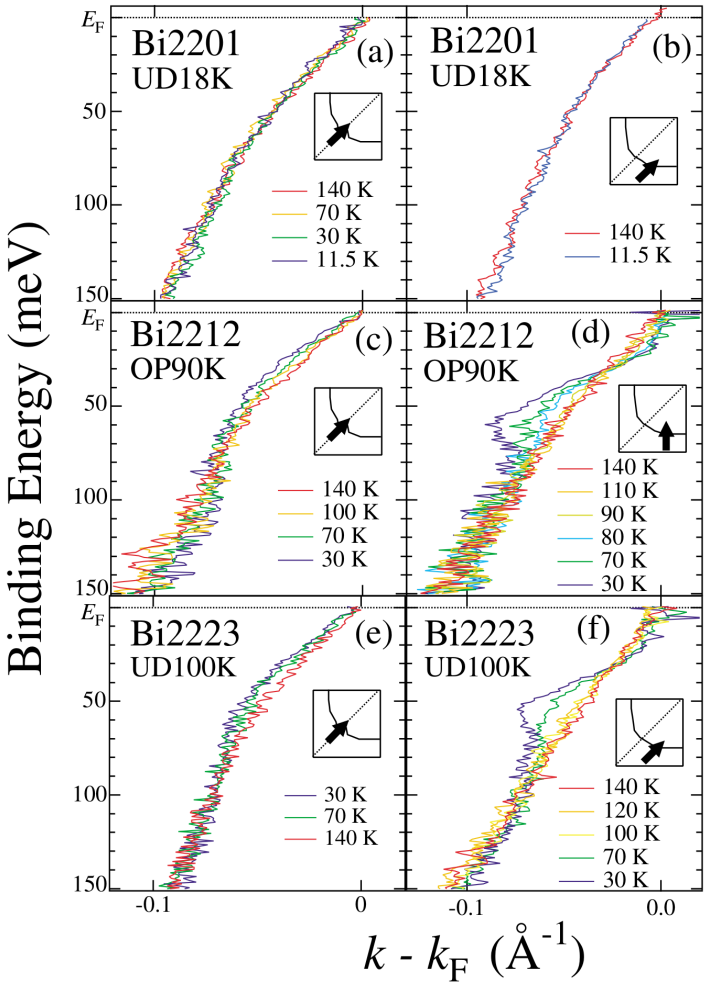

Figure 2.13: Electronic dispersion close to the nodal axis (left panels), and close to the antinode (right panels), for different compounds of BISCO: single-layer Bi2201, bilayer Bi2212, and trilayer Bi2223. The data for the single-layered sample Bi2201 are shown in the top panels, and those of the multi-layered compounds in the middle and bottom panels. Reprinted figure with permission from from Ref. [43].

results published by He et al.

The authors further studied the influence of some bosonic modes on the angular dependence of the kink, which could be connected to the profile presented in panel (e), in particular certain phonon and magnetic modes. Their model calculations lead to the conclusion that the best agreement occurs for the case of electrons coupled to spin excitations of the upper branch of the hour glass. Their study did not, however rule out a role of phonons. Instead, their conclusion was that a phonon branch could have a finite (even if relatively small) contribution to the total self-energy, or that the dispersion might be influenced by a coupling between spin and lattice degrees of freedom.

We shall be investigating in depth the dependence of Ω_{kink} on θ in Chapter 8. In particular, our goal will be to assess quantitatively, on the basis of a precise experimental magnetic spectrum, the profile of Ω_{kink}, under the hypothesis of a coupling between spin fluctuations and fermions.

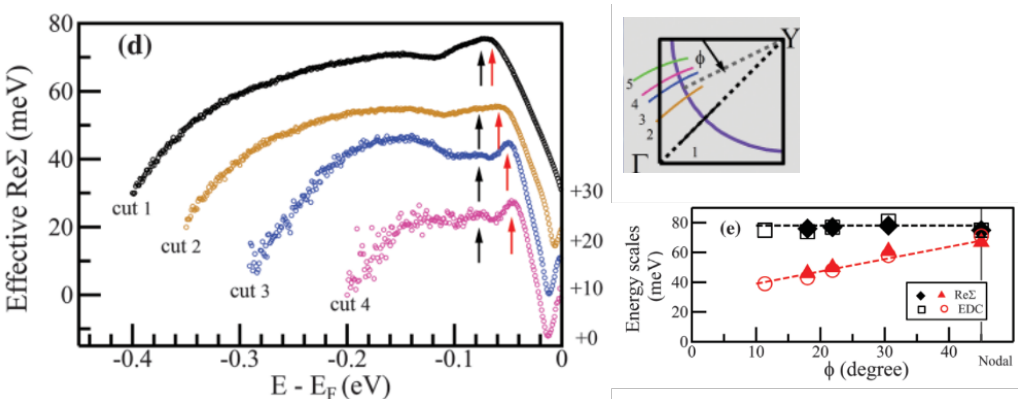

Figure 2.14: Momentum dependence of the two kinks in Bi2212 (overdoped sample, $T_c = 82\,K$). Left panel: real part of the electron effective self-energy for cuts 1 through 4, as shown in the upper right panel. The profiles are offset for clarity, as indicated on the right-side axis. Lower right panel: momentum dependence of the main and secondary kinks. The ϕ angle represents the angle of the cut as measured from the antinode, so that the nodal cut corresponds to $\phi = 45°$, as illustrated in the upper right panel. Reprinted figure with permission from Ref. [44].

2.2 Excitonic instability

2.2.1 A thought experiment: Mott's insight

The formation and condensation of excitons in small band-overlap semimetals, as well as in small band-gap semiconductors, was predicted in the 1960s [9, 46–48], building upon techniques and ideas developed in the context of the BCS theory [12, 13]. Indeed, the occurrence of excitonic condensation in weak-coupling models of semimetals bears some similarity with that of BCS superconductivity in models of metals. On the other hand, the appearance of this phase in semiconducting systems can be discussed in terms of Bose-Einstein condensation (BEC) of preformed excitons. Mott was the first to distinguish the physics of the Mott transition in odd-valency systems from that in even-valency systems [9]. He made some cunning observations in the specific case of even-valency systems, on which we will now focus, following the exposure in Ref. [48].

Fig. 2.16 illustrates the simplest case of a divalent electronic system in the presence of an indirect band gap. The lower energy band (a) is full, while the upper b band is empty at zero temperature. The bands are separated by a finite energy gap E_G. We may now consider a thought experiment, in which some external perturbation is applied to the system, such that E_G varies continuously, decreasing and passing through zero. In such case, in the framework of the one-electron approximation, the system is insulating for $E_G > 0$, and metallic for $E_G < 0$. In this picture, no anomaly is present, and the density of free electrons and holes increases in a monotonous and continuous manner from its value of zero, reached for large values of E_G.

Mott [9] observed that this behavior is not realistic for small values of $|E_G|$; as E_G crosses zero downwards, the density of free electrons is small, so that the screening of the Coulomb interaction can be neglected. In this situation, the attractive Coulomb potential has the long range form $-\dfrac{e^2}{\epsilon r}$, where ϵ is the dielectric constant. It is well known that such a potential leads to the presence of bound electron-hole states [49], such that the

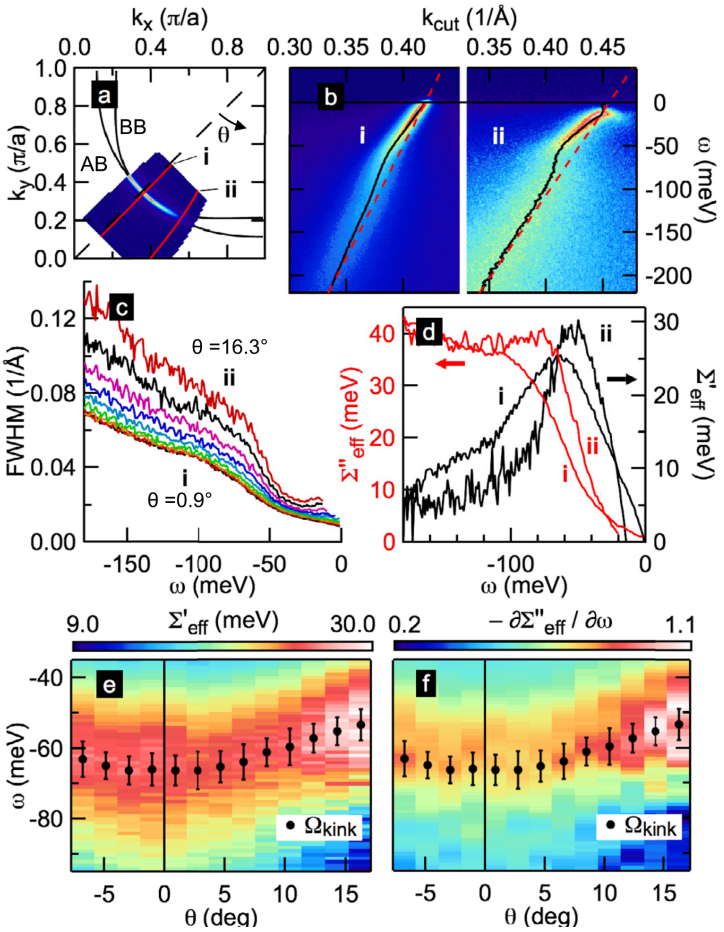

Figure 2.15: Panel (a): Fermi surface of Bi2212, with two representative cuts labeled (i) and (ii) (red curves). Panel (b): raw ARPES data along the representative cuts (i) and (ii). Panel (c): width of the momentum dispersion curves, for cuts progressing away from the node. Panel (d): Real (black) and imaginary (red) components of the self-energy for cuts (i) and (ii). Panels (e) and (f): Real part of the self-energy (Σ'_{eff}), and derivative of its imaginary part ($-\partial\Sigma''_{\text{eff}}/\partial\omega$), as functions of θ and ω. Used under CC BY-NC-SA version 3.0 license, from Ref. [45].

system is non-conducting. This means that in some finite range of strictly negatives values for E_G, the system remains insulating. With decreasing E_G, the density of free carriers further increases, and so does the efficiency of screening, until it is strong enough, and the potential can be described by a Yukawa type formula. When this happens, the pair binding energy decreases and the conductivity can become finite. This insight led Mott to argue that the number of free carriers should vary *discontinuously* as a function of E_G.

We may consider the same thought experiment, starting this time from a semi metallic, rather than semiconducting, configuration. A similar conclusion can be drawn: if no hybridization between the lower and upper bands is allowed, then the bands are allowed to cross, as shown in the left panel of Fig. 2.17. However, if hybridization is finite, then an anti-crossing occurs, which leads to the appearance of a gap. The profile in the right panel of Fig. 2.17 is then expected.

The very first studies of excitonic condensation focused on the weak coupling regime,

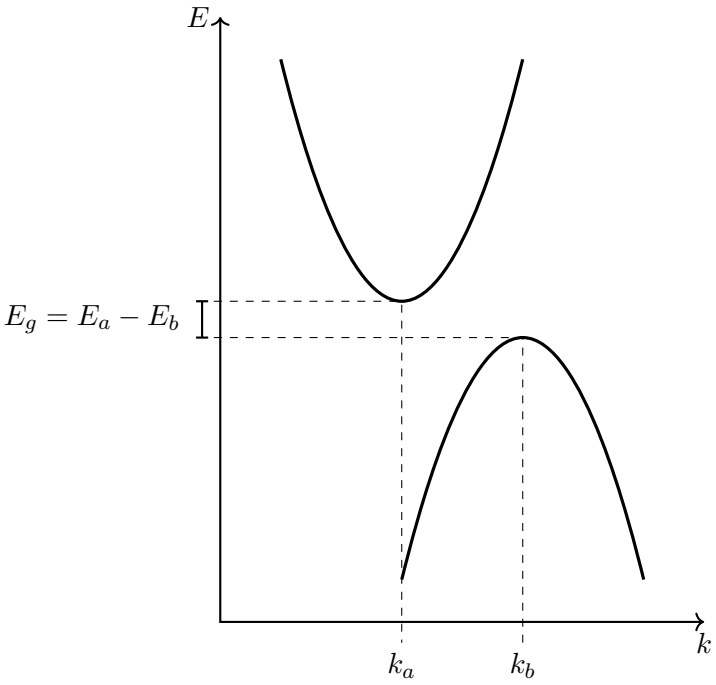

Figure 2.16: Schematic representation of a divalent system possessing an indirect band gap. Band a is empty, while band b is full.

where Coulomb repulsion is small compared to kinetic energy. In this limit, the formation and the condensation of excitons occur at the same temperature, as in the BCS mechanism. The decoupling of the interaction term of the Hamiltonian can be achieved using a Hartree-Fock approach. The key feature in this context is the existence of nesting between the Fermi surface sheets of the valence and conduction bands. The pairing is driven by the long range part of the Coulomb interaction.

Knox [50] studied the transition in these systems, starting from the insulating limit. He observed that the Coulomb interaction should lead to the formation of an exciton. Moreover, if the binding energy of this exciton is larger than the band gap, then the usual insulating ground state is unstable against the formation of pairs, triggering a phase transition. The analogy with the instability of the Fermi sea in the BCS theory is apparent at this phenomenological stage.

This concept motivated more detailed theoretical studies of electronic systems in the vicinity of this predicted phase transition. The first work on this subject was carried out by des Cloizeaux [51], with the Hartree-Fock approximation. In the normal state, assuming a large enough long-wavelength dielectric constant, the excitons are loosely bound: the radius of the excitons is large compared to the interatomic distance, and the binding energy of the excitons is small compared to the energy difference between the conduction and valence band states. Des Cloizeaux showed that in the limit of a vanishing band gap, the binding energy of the excitons could exceed the band gap. In such a case, an instability occurs in the system, and a new Hartree-Fock approximation must be built. The new approximation is obtained by applying a unitary transformation to the normal state basis states. This transformation mixes the one-electron states at the top of the valence band with those at the bottom of the conduction band. This mixing can induce a breaking of the symmetry of the crystal, and the induced long range order is determined by the wave-vector associated

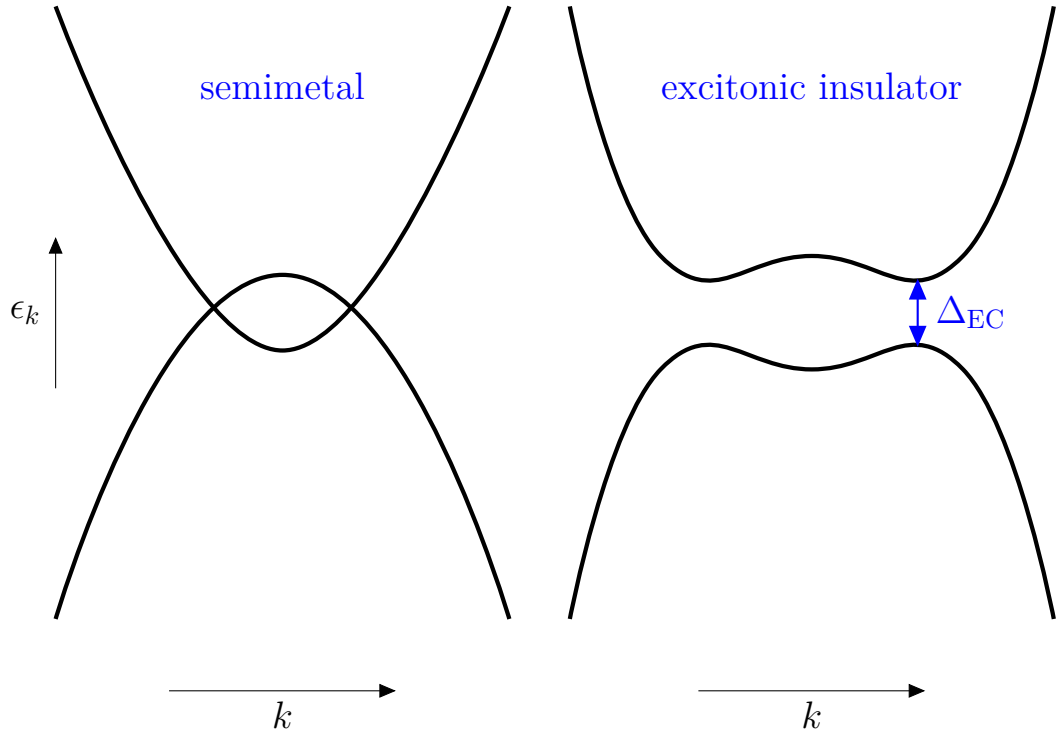

Figure 2.17: Schematic illustration of excitonic condensation in a semimetal. Left: the band structure of a semimetal with overlapping bands and no inter-band hybridization. Right: The band structure of an excitonic insulator.

with the band gap.

2.2.2 Nature of the order parameter and phase diagram

Halperin and Rice studied a two-band model where there is one valence band maximum and one conduction band minimum in the normal state. They argued that in this case, the wave-vector difference $\boldsymbol{w}$ between the extrema of the bands must be one-half of a reciprocal lattice vector. They made substantial headway in the field, describing for the first time a rich phase diagram [47, 48]. Furthermore, they used the screened Hartree-Fock approximation, which is similar to ordinary Hartree-Fock, except that the exchange part of the electron-electron interaction is screened by the dielectric response of the medium. Their variational study showed that the ground-state energy is minimized by a large manifold of degenerate excitonic states. Due to this degeneracy, small and usually neglected interaction terms can play a crucial role.

The degenerate ground-state subspace is spanned by states which can be divided into four different classes. These classes are characterized by charge-density wave order (CDW), spin-density wave order (SDW), charge-current-density wave (CCDW), and spin-current-density wave (SCDW), respectively. Once the degeneracy is lifted, by including further terms in the model Hamiltonian, the CDW order is found to possess a higher energy than the SDW order. Halperin and Rice also find that the current and spin-current orders possess higher energies than the SDW order. This classification is mirrored in the structure and symmetry of the order parameter, which we now discuss. Halperin and Rice argue that in the limit of a small band gap, $E_G < E_B$, with E_B the binding energy of the

excitons, the Hartree-Fock approximation is roughly equivalent to treating the excitons as a weakly repulsive Bose gas. Excitons thus form, until their repulsive potential equals the energy E_B associated with the creation of an exciton. Furthermore, they show that the excitons present in the system form a Bose condensate in the exciton state of minimum energy, which is a state with wave vector $\boldsymbol{w} \equiv \boldsymbol{G}/2$, where $\boldsymbol{G}$ is a reciprocal lattice vector, identical to the wave vector which connects the band extrema.

The creation operator for such an exciton can be written as

$$A^{\dagger\,\nu}_{\boldsymbol{w}} = \sum_{\boldsymbol{k}\sigma\sigma'} f_{\sigma\sigma'}(\boldsymbol{k}) b^{\dagger}_{\boldsymbol{k}+\boldsymbol{w}\,\sigma} a_{\boldsymbol{k}\sigma'} \tau^{\nu}_{\sigma\,\sigma'}$$

where $f_{\sigma\sigma'}(\boldsymbol{k})$ is an envelope wavefunction peaked near $\boldsymbol{k} = 0$, $a^{\dagger}_{\boldsymbol{q}\,\sigma}$ and $b^{\dagger}_{\boldsymbol{q}\,\sigma}$ are the creation operators for the valence and conduction bands, respectively, and $\boldsymbol{\tau}^{\nu}$, $\nu \in \{0,1,2,3\}$ are the Pauli matrices.

A Bose condensate of excitons is observed if $\left\langle \boldsymbol{A}^{\dagger}_{\boldsymbol{w}} \right\rangle \neq 0$, i.e. $\left\langle b^{\dagger}_{\boldsymbol{k}+\boldsymbol{w}\,\sigma} a_{\boldsymbol{k}\,\sigma'} \right\rangle \neq 0$ for some choice of σ and σ'. This defines the order parameter for the phase transition. The $A^{\dagger}_0$ operator creates a singlet exciton, while the operators $A^{\dagger}_{\nu}$, $\nu = 1,2,3$ create triplet excitons in the quantum states $S_x = 0$, $S_y = 0$, $S_z = 0$, respectively. The nature of the symmetry breaking depends on whether the expectation value $\left\langle \boldsymbol{A}^{\dagger}_{\boldsymbol{w}} \right\rangle$ is real or imaginary, and also on whether the macroscopically occupied exciton state is a singlet or a triplet. Halperin and Rice thus introduced four possible classes of states (in the absence of spin-orbit coupling [47]), given in this table:

Table 2.1: The four classes of states identified by Halperin and Rice [47]

Class I	$\langle A_0 \rangle$ real	$\left\langle A_{\nu\|\nu\in\{1,2,3\}} \right\rangle = 0$	Singlet, real phase
Class II	$\langle A_0 \rangle = 0$	$\left\langle A_{\nu\|\nu\in\{1,2,3\}} \right\rangle$ real	Triplet, real phase
Class III	$\langle A_0 \rangle$ imaginary	$\left\langle A_{\nu\|\nu\in\{1,2,3\}} \right\rangle = 0$	Singlet, imaginary phase
Class IV	$\langle A_0 \rangle = 0$	$\left\langle A_{\nu\|\nu\in\{1,2,3\}} \right\rangle$ imaginary	Triplet, imaginary phase

These four classes correspond to the CDW, SDW, CCDW, and SCDW orders discussed above, respectively. As Tugushev explicitly stresses [52], the SCDW and CCDW states of matter are not associated with any mesoscopic charge or spin currents in the ground state. Instead, they correspond to spatial modulations of stationary distributions of charge or spin currents on the scale of the unit cell.

Finally, Halperin and Rice discussed the stability of the excitonic condensate for different values of the densities of holes and electrons, and different values of the ratio of their effective masses. They concluded that for roughly isotropic bands, and for a mass ratio close enough to 1, the excitonic condensate should exist, rather than a condensate of excitonic molecules, or a combination of a crystalline structure of the heavier particles, together with a uniform background of the lighter ones. Their considerations remained qualitative, but they can be compared to the recent results by Kuneš and Augustinský [53], who studied the stability of the excitonic condensate as a function of electron and hole band asymmetry.

The symmetries of the ordered phase were later studied by Volkov and Kopaev [54], while Tugushev [52] elaborated further the study of the SCDW order, using an insightful analytic approach based on the Landau functional theory. He focused on a two-band model for a metallic system, with intraband interactions of density-density type, and interband interactions of two types: density-density interactions, and interactions related to the interband transitions of pairs of particles. The phase diagram he obtained is reproduced in Fig. 2.18. It bears a striking qualitative resemblance with the results which we will report in Sec. 9, in particular in Fig. 9.1.

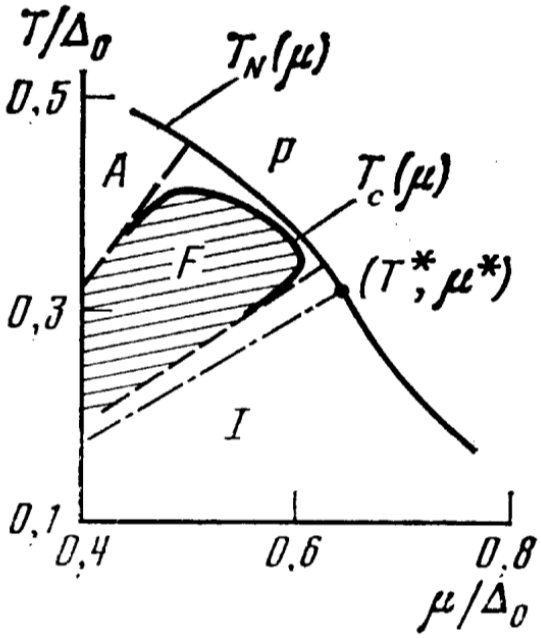

Figure 2.18: Phase diagram for the two-band model studied in Ref. [52]. P denotes the paramagnetic phase, A denotes the antiferromagnetic phase, F the ferromagnetic phase, and I the incommensurate phase. Δ_0 is an energy constant which depends on the parameters of the Landau functional for the model. μ is the chemical potential. Excerpt from Ref. [52].

2.2.3 Excitonic ferromagnetism

Volkov and Kopaev [55] developed the theory of excitonic condensation further, and proposed a theory of the so-called excitonic ferromagnetism. In the more usual case of ferromagnetism, qualitatively described by the Stoner model, a criterion for the emergence of long range order can be identified, e.g. the gain in exchange energy should compensate for the increase of the effective kinetic energy. In contrast, the model considered by Volkov, Kopaev, and Rusinov [56] leads to ferromagnetic order, regardless of the magnitude of the electron-electron interaction, but under assumptions related to the band structure of the unperturbed system. Semiconductors with a band gap smaller than the exciton binding energy figure among the potential candidates. They find out that this system is unstable against the formation of excitons. The singlet instability corresponds to the CDW state, while the triplet instability corresponds to the SDW state. Furthermore, in case of coexistence of the CDW and SDW orders, the spin degeneracy of the electron and hole bands is lifted, leading to ferromagnetism, if the chemical potential lies outside the energy gap of the perturbed band structure. They coined the term excitonic ferromagnetism to designate this effect, whose existence is therefore tantamount to the coexistence of singlet and triplet pairing in the presence of a difference between the electron and hole concentration. The corresponding profile of the band structure in the presence of such order is displayed in Fig. 2.19. Note in particular the splittings of the bands connected to the spin polarization.

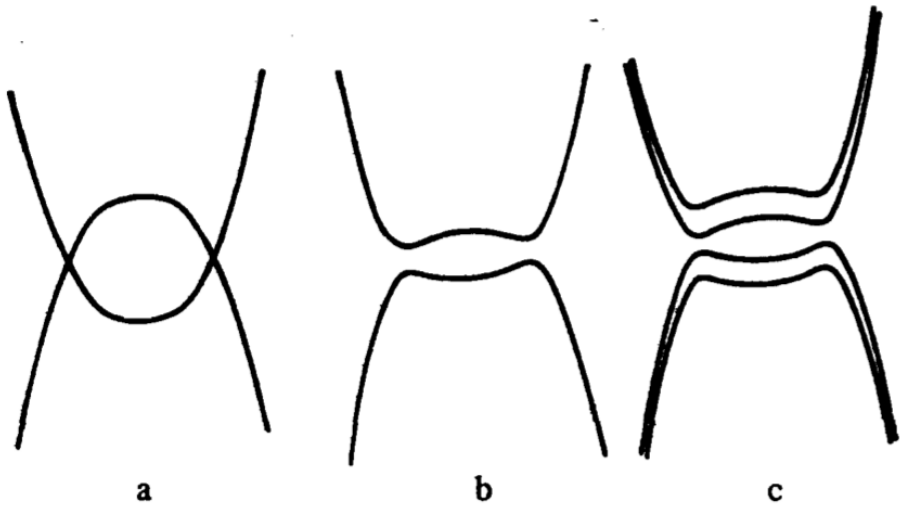

Figure 2.19: Band structure in the presence of various phases. (a) Unperturbed semimetal band structure. (b) Band structure of the excitonic insulator phase. (c) Band structure of the system after the spin degeneracy is lifted, in the ferromagnetic state. Schematic from Ref. [56]

2.2.4 Experimental results

For a long time, experimental confirmation of the presence of an excitonic condensate in matter remained elusive. More recently, a number of candidate materials have been put forward. These include compounds such as $TmSe_xTe_{1-x}$, whose increased electrical resistivity and thermal diffusivity was argued to be an experimental evidence for the presence of a pressure-induced excitonic instability [57, 58]. The experimental discovery of high-T_c itinerant ferromagnetism in lightly doped hexaborides ($Ca_{1-x}La_xB_6$) was also attributed to the presence of a polarized excitonic condensate in the lightly doped material, whose parent compound is a semimetal [59–63]. These materials are ferromagnetic in spite of the absence of partially filled d or f orbitals, and have a very high Curie temperature, $T_c > 600\,K$. The value of T_c is also strongly dependent on doping. In another compound, 1T-$TiSe_2$, charge density wave order was observed, and an excitonic origin was put forward [64–73].

The layered chalcogenide Ta_2NiSe_5, was studied by ARPES. The observed evolution of the band structure with temperature was argued to be consistent with excitonic condensation of the BEC kind [74–79]. The quasi-one-dimensional structure of Ta_2NiSe_5, as well as a sketch of the BEC-BCS crossover for excitonic condensates, are given in Fig. 2.20.

The origin of the SDW state of Chromium was attributed to excitonic condensation [80–83]. Excitonic condensates were also shown to possibly arise in cobalt oxides, facilitated by the proximity in energy of the high-spin and low-spin configurations [84–87].

Excitonic condensation has also attracted strong interest in the context of the so-called bilayer systems, two-dimensional [88, 89] as well as one-dimensional [90]. In this context, several schemes based on the excitonic pairing have been proposed for the design of new logic devices [90, 91], as well as for the design of devices with greatly enhanced thermoelectric efficiency [92].

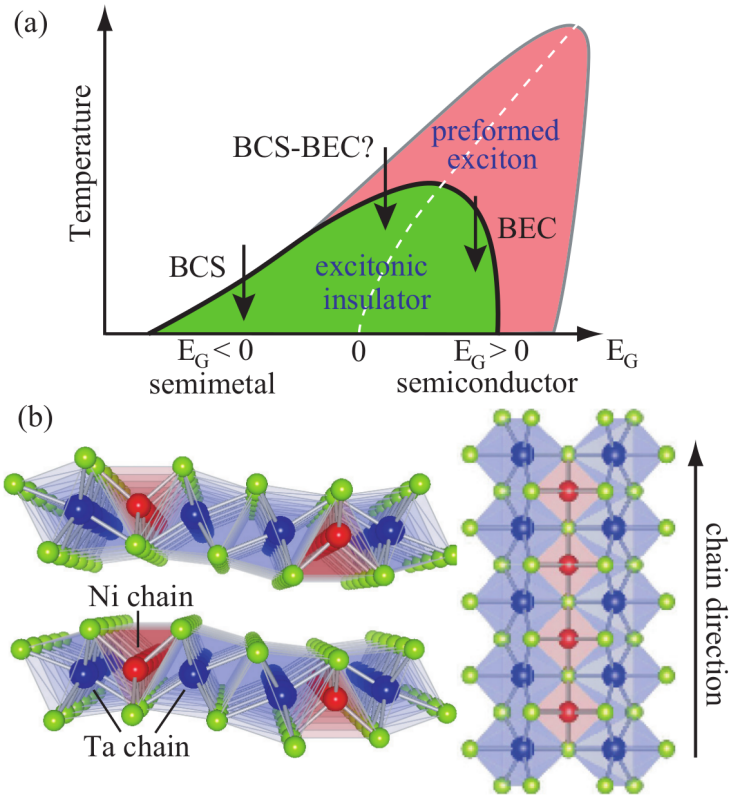

Figure 2.20: Schematic phase diagram of an excitonic insulator as a function of temperature and band gap E_G. The white dashed curve indicates the boundary between semimetal and semiconductor regions, which roughly correspond to the BCS-BEC crossover. (b) Sketch of the quasi-1D crystal structure of Ta_2NiSe_5. The excitons are formed between the electrons in the Ta chains, and the holes in the Ni chains. Ta_2NiSe_5 belongs in the right hand side (i.e. the BEC region) of the upper panel phase diagram. Reprinted figure with permission from Ref. [76].

Chapter 3

Models of strongly correlated electron systems

In this chapter, we discuss the model Hamiltonians commonly used to describe strongly correlated electron systems. We first recall some general features of the one-band Hubbard model [93–95].

3.1 The Hubbard model

The Hubbard model is ubiquitous in the universe of strongly correlated electron systems. In this model, electrons interact via a purely repulsive Coulomb interaction, and the electron-phonon interaction is not included. This model has been extensively used in the theory of magnetism. On the other hand, since the discovery of the BCS theory, superconductivity has usually been interpreted as emerging from an instability of the ground state, driven by an effective, typically electron-phonon interaction based, attractive interaction. This was the common approach before the publication of the seminal paper by Anderson [96], in which the concept of superconductivity occurring in a doped insulating system, described using the one-band Hubbard model, was developed for the first time.

The second quantized form of the simplest one-band Hamiltonian for electrons on a lattice reads

$$H = -\sum_{ij,\sigma} t_{ij} c^\dagger_{i\sigma} c_{j\sigma} + \sum_{ijkl,\sigma\sigma'} U_{ijkl} c^\dagger_{i\sigma} c^\dagger_{j\sigma'} c_{l\sigma'} c_{k\sigma} \equiv H_t + H_{int}, \tag{3.1}$$

where $c^\dagger_{i\sigma}$ is the creation operator corresponding to the Wannier orbital $\phi_i(\boldsymbol{r})$ centered at site i with spin σ, $\hat{n}_{i\sigma} = c^\dagger_{i\sigma} c_{j\sigma}$ is the particle number operator, t_{ij} is the hopping matrix element between sites i and j, and the matrix element U_{ijkl} of the screened Coulomb interaction is given as

$$U_{ijkl} = \int d\boldsymbol{r}_1 d\boldsymbol{r}_2 \phi^*_i(\boldsymbol{r}_1) \phi^*_j(\boldsymbol{r}_2) \tilde{V}(\boldsymbol{r}_1 - \boldsymbol{r}_2) \phi_k(\boldsymbol{r}_1) \phi_l(\boldsymbol{r}_2).$$

The screened interaction $\tilde{V}$ decreases fast with increasing distance between the sites, so that the largest matrix element is the on-site one $U_{ii,ii} \equiv U$. If the hopping is restricted to the nearest-neighbors, and only U is conserved, the Hamiltonian becomes

$$H = -t \sum_{\langle ij \rangle,\sigma} \left(c^\dagger_{i\sigma} c_{j\sigma} + \text{H. c.} \right) + U \sum_i \hat{n}_{i\uparrow} \hat{n}_{i\downarrow}, \tag{3.2}$$

where $\langle ij \rangle$ means that the sum is restricted to pairs of nearest neighbors. This is the well-known one-band Hubbard model. Next, we address some of the symmetries of this particular model.

3.1.1 SU(2) symmetry

The terms of the Hamiltonian describe the effective kinetic energy, as well as the most important component of the Coulomb interaction. The latter depends only on the distance between the electrons. As a consequence, we expect the Hubbard Hamiltonian to be invariant under rotations of the spin quantization axis. While not apparent in the form on the right hand side of Eq. (3.2), this symmetry is respected by the Hamiltonian as we demonstrate below.

The kinetic energy term obviously respects this spin-rotational invariance, but it is not so clear for the interaction term. The expression $\hat{n}_{i\uparrow}\hat{n}_{i\downarrow}$ of the latter can be rewritten as

$$\hat{n}_{i\uparrow}\hat{n}_{i\downarrow} = c^\dagger_{i\uparrow}c_{i\uparrow}\Big(1 - c_{i\downarrow}c^\dagger_{i\downarrow}\Big) = \hat{n}_{i\uparrow} - c^\dagger_{i\uparrow}c_{i\downarrow}c^\dagger_{i\downarrow}c_{i\uparrow} = \hat{n}_{i\uparrow} - S^+_i S^-_i,$$

and similarly we can show that $\hat{n}_{i\uparrow}\hat{n}_{i\downarrow} = \hat{n}_{i\downarrow} - S^-_i S^+_i$. Noting that $(S^z_i)^2 = \frac{1}{4}(\hat{n}_{i\uparrow} - \hat{n}_{i\downarrow})^2 = \frac{1}{4}\hat{n}_i - \frac{1}{2}\hat{n}_{i\uparrow}\hat{n}_{i\downarrow}$, where $\hat{n}_i \equiv \hat{n}_{i\uparrow} + \hat{n}_{i\downarrow}$, we finally obtain

$$\begin{aligned} \hat{n}_{i\uparrow}\hat{n}_{i\downarrow} &= \frac{\hat{n}_i}{2} - \frac{2}{3}\boldsymbol{S}^2_i \\ \Rightarrow H_{int} &= \frac{UN}{2} - \frac{2U}{3}\sum_i \boldsymbol{S}^2_i \end{aligned} \tag{3.3}$$

which demonstrates the spin-rotational invariance of the interaction term.

3.1.2 U(1) symmetry

We are free to change the phase of the one-particle operator: $c_{i\sigma} \to c'_{i\sigma} = e^{i\theta}c_{i\sigma}$, where $e^{i\theta}$ is an element of the $U(1)$ group, equipped with the product law $e^{i\theta}e^{i\theta'} = e^{i(\theta+\theta')}$. Hamiltonian 3.1 is clearly invariant under such a transformation applied simultaneously to all sites. This invariance expresses charge conservation in the system; it is easy to check that terms which do not conserve charge do not respect this U(1) symmetry, e.g. $c^\dagger_{i\sigma}c^\dagger_{j-\sigma}$, which transforms as $c^\dagger_{i\sigma}c^\dagger_{j-\sigma} \to e^{-2i\theta}c^\dagger_{i\sigma}c^\dagger_{j-\sigma}$.

3.1.3 Particle-hole symmetry

We follow Ref. [94], and rewrite the interaction term as

$$H_{int} = U\sum_i \left(\hat{n}_{i\uparrow} - \frac{1}{2}\right)\left(\hat{n}_{i\downarrow} - \frac{1}{2}\right) + \frac{UN}{2} - \frac{UL}{4}, \tag{3.4}$$

where L is the number of lattice sites in the system, and N the total number of electrons. The canonical transformation $\hat{c}^\dagger_{i\sigma} \to \hat{c}_{i\sigma}, \hat{c}_{i\sigma} \to \hat{c}^\dagger_{i\sigma}$ turns an electron with spin σ into a hole with the same spin, and vice versa. The occupation number operators transform as $\hat{n}_{i\sigma} \to 1 - \hat{n}_{i\sigma}$, and the total number of electrons N becomes $2L - N$. Under this transformation, the

interaction term is unchanged, except for a shift by a constant: $H_{int} \to H_{int} - U(N - L)$. The kinetic energy term on the other hand is transformed as follows:

$$t_{ij}\hat{c}^\dagger_{i\sigma}\hat{c}_{j\sigma} + t^*_{ij}\hat{c}^\dagger_{j\sigma}\hat{c}_{i\sigma} \to -t^*_{ij}\hat{c}^\dagger_{i\sigma}\hat{c}_{j\sigma} - t_{ij}\hat{c}^\dagger_{j\sigma}\hat{c}_{i\sigma}, \tag{3.5}$$

where we have introduced the dependence of the hopping term on site indices, for the sake of generality. This differs from the the initial expression for H_t, and shows that the one-band Hubbard model does not possess electron-hole symmetry in the general case. There is, however, an important special case in which this symmetry is respected: bipartite lattices in the absence of magnetic field.

In the absence of magnetic field, and considering the special case of nearest-neighbor hopping for simplicity, we may choose t real. The bipartite nature of the lattice, on the other hand, means that we can define two sublattices A and B, such that $t \neq 0$ if and only if the sites i and j belong to different sublattices. In this case, it is possible to change the sign of t by the following transformation:

$$c_{i\sigma} \to \begin{cases} c_{i\sigma} \text{ if } i \in A \\ -c_{i\sigma} \text{ if } i \in B \end{cases}$$

Under this transformation, the kinetic energy term changes sign, while the interaction term is conserved. It is therefore natural to use this property in order to compensate the undesired sign change highlighted above, and define the particle-hole transformation as follows:

$$\begin{matrix} \hat{c}^\dagger_{i\sigma} \to \eta_i \hat{c}_{i\sigma} \\ \hat{c}_{i\sigma} \to \eta_i \hat{c}^\dagger_{i\sigma} \end{matrix} \quad \text{with} \quad \eta_i = \begin{cases} 1 \text{ if } i \in A \\ -1 \text{ if } i \in B \end{cases}$$

Under this transformation, H_t is unchanged, and the total Hamiltonian transforms as

$$H(N) \to H(2L - N) - U(N - L).$$

Since these two expressions differ only by an additive constant, it follows that the excitation energies are identical in systems with L electrons and in systems with $2L - N$ electrons, and that the phase diagram of the Hubbard model is symmetrical about half-filling.

We may consider additional transformations, such as the following partial particle-hole transformation [93]:

$$\begin{aligned} c_{i\uparrow} &\to d_{i\uparrow} \\ c_{i\downarrow} &\to \begin{cases} d^\dagger_{i\downarrow} \text{ if } i \in A \\ -d^\dagger_{i\downarrow} \text{ if } i \in B \end{cases} \end{aligned}$$

Under this transformation, the kinetic energy term is conserved. Furthermore, we get

$$\begin{aligned} \hat{n}_{i\uparrow} + \hat{n}_{i\downarrow} &= c^\dagger_{i\uparrow}c_{i\uparrow} + c^\dagger_{i\downarrow}c_{i\downarrow} = d^\dagger_{i\uparrow}d_{i\uparrow} - d^\dagger_{i\downarrow}d_{i\downarrow} + 1 \\ \hat{n}_{i\uparrow} - \hat{n}_{i\downarrow} &= c^\dagger_{i\uparrow}c_{i\uparrow} - c^\dagger_{i\downarrow}c_{i\downarrow} = d^\dagger_{i\uparrow}d_{i\uparrow} + d^\dagger_{i\downarrow}d_{i\downarrow} - 1. \end{aligned}$$

Thus, the total number of up spins is conserved. The interaction term becomes $H_{int}(-U) + UN_\uparrow$, therefore the Hamiltonian (3.2) turns into $H(t, -U) + UN_\uparrow$, where $N_\uparrow$ is the total number of electrons with up spin. The above relations also show that the total charge Q and the component S_z of the total spin transform as follows:

$$\begin{aligned} Q &\to S_z + 1, \\ S_z &\to Q - 1. \end{aligned}$$

Therefore, overall, this transformation maps the attractive version of the Hubbard Hamiltonian onto the repulsive one, while at the same time, spin is mapped onto charge (and vice versa).

3.2 The single impurity Anderson model

In the present section, we turn our attention to the problem of a magnetic impurity (e.g., a transition metal or rare earth element atom) embedded in a nonmagnetic metallic host. We follow the presentations by Doniach [97], and by Jones and March [98].

3.2.1 Anderson Hamiltonian

In order to discuss the formation of localized magnetic states in compounds involving magnetic impurities, Anderson [99] proposed a model Hamiltonian which turns out to be very closely related to the Hubbard Hamiltonian. The models share some essential features. The first one is the existence of a localized state (which turns into a narrow band in the extended system described by the Hubbard Hamiltonian), connected with the Fermi sea of conduction electrons. In the impurity case, Anderson's Hamiltonian describes the connection in terms of matrix elements $V_{\boldsymbol{k}d}$ between a localized d-like orbital of the impurity and the Bloch states of the host. The single-particle part of the Hamiltonian reads

$$H_0 = \sum_{\boldsymbol{k}} \epsilon_{\boldsymbol{k}} a^\dagger_{\boldsymbol{k}} a_{\boldsymbol{k}} + \epsilon_d a^\dagger_d a_d + \sum_{\boldsymbol{k}} V_{\boldsymbol{k}d}\Big(a^\dagger_{\boldsymbol{k}} a_d + a^\dagger_d a_{\boldsymbol{k}}\Big). \tag{3.6}$$

The second distinct feature shared by these models is the on-site electron-electron repulsion. In the Anderson model, this interaction is limited to the electrons occupying the localized d-like orbital. This leads to the following form of the interaction term:

$$H_1 = U n_{d\downarrow} n_{d\uparrow}. \tag{3.7}$$

First, we consider the non-interacting limit of this model to get a feeling for its behavior and an overview of the method for its solution. In the absence of interaction, the one-electron Green's function may be obtained in closed form. Using the equation of motion approach, we obtain a pair of coupled equations for $G_{\boldsymbol{k},\boldsymbol{k'}}$, the Green's function for the conduction electrons, and $G^\sigma_{dd}(t) \equiv -i\theta(t)\left\langle\left[\tilde{a}_{d\sigma}(t), \tilde{a}^\dagger_{d\sigma}(0)\right]\right\rangle$, the retarded Green's function of the impurity. Here $\tilde{a}_{d\sigma}(t)$ is a Heisenberg operator. The equation of motion is:

$$i\frac{\partial G^\sigma_{dd}(t)}{\partial t} = \delta(t) - i\theta(t)\left\langle\left[[\tilde{a}_{d\sigma}(t), H], \tilde{a}^\dagger_{d\sigma}(0)\right]\right\rangle. \tag{3.8}$$

The commutator in Eq. (3.8) provides a coupling between $G^\sigma_{dd}(t)$ and a mixed propagator defined as $G^\sigma_{\boldsymbol{k}d}(t) \equiv -i\theta(t)\left\langle\left[\tilde{a}_{\boldsymbol{k}\sigma}(t), \tilde{a}^\dagger_{d\sigma}(0)\right]\right\rangle$, via the equation

$$i\frac{\partial G^\sigma_{dd}(t)}{\partial t} = \delta(t) + \epsilon_d G^\sigma_{dd}(t) + \sum_{\boldsymbol{k}} V_{\boldsymbol{k}d} G^\sigma_{\boldsymbol{k}d}(t). \tag{3.9}$$

Using the equation of motion for $G^\sigma_{\boldsymbol{k}d}(t)$, we similarly obtain

$$(\omega - \epsilon_{\boldsymbol{k}}) G^\sigma_{\boldsymbol{k}d}(\omega) - V_{\boldsymbol{k}d} G^\sigma_{dd}(\omega) = 0. \tag{3.10}$$

We can eliminate $G^{\sigma}_{\boldsymbol{k}d}$ and obtain

$$G^{\sigma}_{dd}(\omega) = \frac{1}{\omega - \epsilon_d - \Sigma_d(\omega)}, \tag{3.11}$$

where

$$\begin{aligned} \Sigma_d(\omega) &= \sum_{\boldsymbol{k}} \frac{|V_{\boldsymbol{k}d}|^2}{\omega - \epsilon_{\boldsymbol{k}} + i\eta} \\ &= \sum_{\boldsymbol{k}} \mathcal{P}\frac{|V_{\boldsymbol{k}d}|^2}{\omega - \epsilon_{\boldsymbol{k}}} - i\pi \sum_{\boldsymbol{k}} |V_{\boldsymbol{k}d}|^2 \delta(\omega - \epsilon_{\boldsymbol{k}}) \\ &\equiv \Lambda_d(\omega) - i\Delta_d(\omega). \end{aligned} \tag{3.12}$$

Here η is a positive infinitesimal inserted so that G^{σ}_{dd} is a retarded function. In this case $\Lambda_d(\omega)$ may be absorbed as a constant shift in the unperturbed energy ϵ_d [99]. Moreover, if we neglect the $\boldsymbol{k}$-dependence of $V_{\boldsymbol{k}d}$ (which is approximately justified in case of short range impurity-host hoppings only), we have $\Delta_d(\omega) = \pi|V|^2\mathcal{N}(\omega)$, where $\mathcal{N}(\omega)$ is the band density of states, that can be approximated by a constant $D(E_F)$.

3.2.2 Hartree-Fock treatment of the interaction term

In the non-interacting framework, $G^{\sigma}_{dd}(\omega)$ does not depend on σ, and there is no magnetic instability. The interaction term H_1 changes the situation. The impact of this term may be treated using a Hartree-Fock approximation scheme. Anderson [99] explains the principle of the approach as follows: assuming that a localized moment exists, then one of the d-shell states of the impurity is full, for example the spin up state, while this very state with spin down is empty. Considering the interaction energy within the d-shell of the model, only an electron with down spin is perturbed by the repulsion term. Thus, if the energy of the spin up state lies a distance E below the Fermi level, the energy of the spin down state is $-E + U$, and must lie above the Fermi level, consistent with the fact that this state is empty. The effect of the hybridization captured by $V_{\boldsymbol{k}d}$ is to reduce this imbalance between spin up and spin down. For sufficiently high values of the magnitude of $V_{\boldsymbol{k}d}$, the local moment vanishes.

The equation of motion including H_1 reads

$$i\frac{\partial G^{\sigma}_{dd}(t)}{\partial t} = \delta(t) + \epsilon_d G^{\sigma}_{dd}(t) + U\Gamma^{\sigma}_{dd}(t) + \sum_{\boldsymbol{k}} V_{\boldsymbol{k}d} G^{\sigma}_{\boldsymbol{k}d}(t), \tag{3.13}$$

where $\Gamma^{\sigma}_{dd}(t) = -i\theta(t)\left\langle \left[\tilde{n}_{d,-\sigma}(t)\tilde{a}_{d\sigma}(t), \tilde{a}^{\dagger}_{d\sigma}(0)\right]\right\rangle$. The related equation of motion for $\Gamma^{\sigma}_{dd}(t)$ involves additional higher order Green's functions, so that the system of equations does not close up, and needs an approximation to be solved. The Hartree-Fock scheme can be used for this purpose: in the expression for $\Gamma^{\sigma}_{dd}(t)$, $\tilde{n}_{d,-\sigma}(t)$ is replaced by its expectation value $\langle n_{d,-\sigma}\rangle$. We obtain

$$\Gamma^{\sigma}_{dd}(\omega) = \langle n_{d,-\sigma}\rangle\, G^{\sigma}_{dd}(\omega),$$

and the system of equations is formally identical to that of the non-interacting case, with modified, spin-dependent terms for ϵ_d and $G^{\sigma}_{dd}(\omega)$:

$$\begin{aligned} G^{\sigma}_{dd}(\omega) &= \frac{1}{\omega - \tilde{\epsilon}_{d\sigma} - \Sigma_d(\omega)}, \\ \tilde{\epsilon}_{d\sigma} &= \epsilon_d + U\langle n_{d,-\sigma}\rangle\,. \end{aligned} \tag{3.14}$$

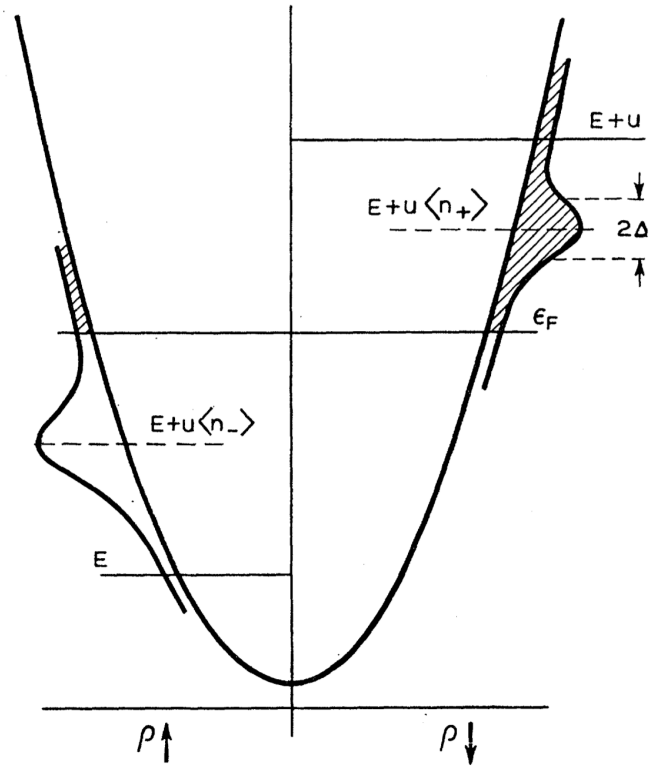

Figure 3.1: Schematic representation of the densities of states in a magnetic case, see Eq. (3.14). The humps at $E + U\,\langle n_{d,\downarrow}\rangle / E + U\,\langle n_{d,\uparrow}\rangle$ are the virtual d-levels described in the text. The numbers of electrons $\langle n_{d,\downarrow}\rangle / \langle n_{d,\downarrow}\rangle$ occupying them are to be computed from the areas of the unshaded portions, located below the Fermi energy. Reprinted figure with permission from Ref. [99].

The densities of states are given by

$$\rho_{d\sigma}(\omega) = \frac{1}{\pi} \frac{\Delta}{\left(\omega - \tilde{\epsilon}_{d\sigma}\right)^2 + \Delta^2}. \tag{3.15}$$

They are illustrated in Fig. 3.1.

Thus, G^{σ}_{dd} behaves exactly as if there were a virtual state at $E = \tilde{\epsilon}_{d\sigma} + i\Delta$, with Δ directly determining the width of the resonance. Equipped with these expressions, one can now determine self-consistently $\langle n_{d,\sigma}\rangle$, using the definition of G^{σ}_{dd}:

$$\begin{aligned}
\langle n_{d,\sigma}\rangle &= \int_{-\infty}^{\epsilon_f} \rho^{\sigma}_{d}(\omega) d\omega = -\frac{1}{\pi} \int_{-\infty}^{\epsilon_f} \mathrm{Im}\, G^{\sigma}_{dd}(\omega) \\
&= \frac{1}{\pi} \int_{-\infty}^{\epsilon_f} \frac{\Delta_d}{\left[\omega - \tilde{\epsilon}_{d\sigma}\right]^2 + \Delta_d^2} d\omega \\
&= \frac{1}{\pi}\, \mathrm{arccotan} \left(\frac{\epsilon_d + U\,\langle n_{d,-\sigma}\rangle - \epsilon_f}{\Delta} \right).
\end{aligned}$$

This is equivalent to the following two equations that should hold simultaneously:

$$\begin{aligned} \langle n_{d,\uparrow} \rangle &= \frac{1}{\pi} \operatorname{arccotan} \left(\frac{\epsilon_d + U \langle n_{d,\downarrow} \rangle - \epsilon_f}{\Delta} \right), \\ \langle n_{d,\downarrow} \rangle &= \frac{1}{\pi} \operatorname{arccotan} \left(\frac{\epsilon_d + U \langle n_{d,\uparrow} \rangle - \epsilon_f}{\Delta} \right). \end{aligned} \tag{3.16}$$

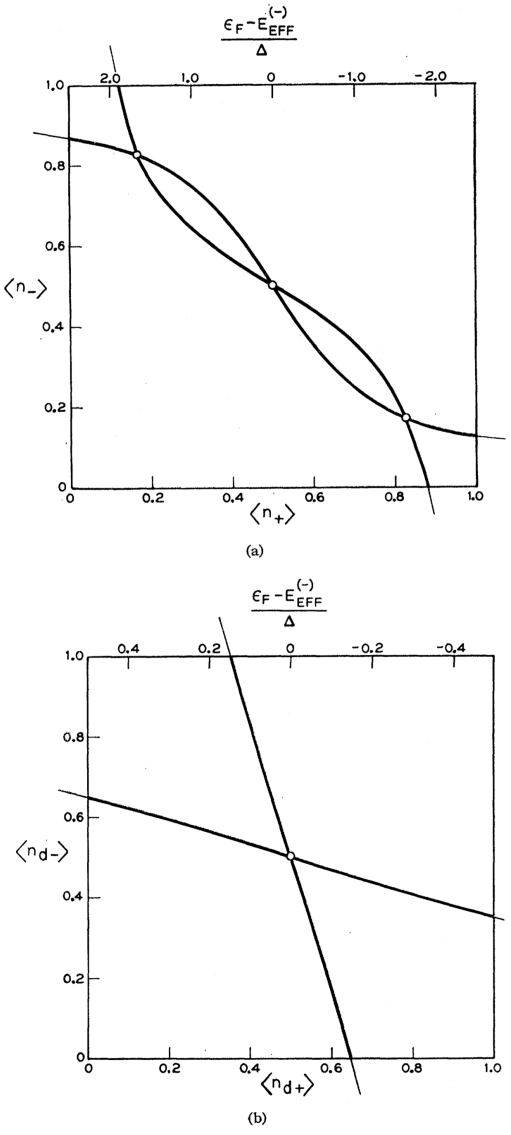

Figure 3.2: Graphical solution of Eqs. (3.17) for n_1 and n_2 in two typical cases. Panel (a): magnetic case, with $y = U/\Delta = 5$, $x = (\epsilon_F - \epsilon_d)/U = 0.5$, exhibiting three possible solutions. Panel (b): non-magnetic case, with $y = 1$, $x = 0.5$, leaving only one possible solution in the admissible range of values for n_1, n_2. Reprinted figure with permission from Ref. [99].

It is convenient to introduce the following notations:

$$\begin{aligned} y &= \frac{U}{\Delta}, \\ x &= \frac{\epsilon_F - \epsilon_d}{U}, \\ n_1 &= \langle n_{d,\uparrow} \rangle , \\ n_2 &= \langle n_{d,\downarrow} \rangle . \end{aligned} \tag{3.17}$$

A graphical representation of the expressions on the right hand side of Eq. (3.16) is shown in Fig. 3.2, for two specific pairs of values of the parameters x and y: $x = 0.5$ and $y = 5$ for the upper panel; $x = 0.5$ and $y = 1$ for the bottom panel. In the lower panel, U/Δ is small, so that only one self-consistent solution appears. As U increases, the maximum slope of the arccotan curve becomes steeper, so that magnetic solutions become possible for $U > U_c$, as shown in the upper panel. Note that $x = 0$ means that the empty d state is right at the Fermi level, while $x = 1$ means that $\epsilon_d + U$ is at the Fermi level. $x = 1/2$ corresponds to the case where ϵ_d and $\epsilon_d + U$ lie in symmetric positions with respect to the Fermi level. This is the most favorable case for magnetism, which only happens for $0 \leq x \leq 1$. It is also possible to plot the phase diagram in the $x - (1/y)$ plane, as shown in Fig. 3.3.

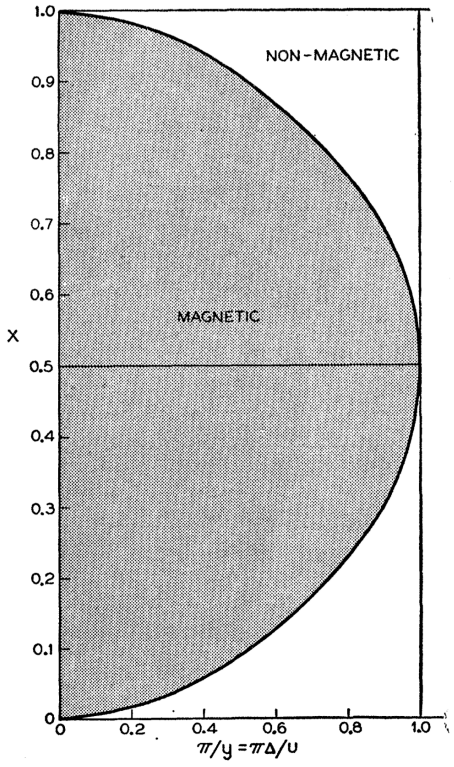

Figure 3.3: Phase diagram showing the magnetic and non-magnetic regions in the x-$1/y$ plane. Reprinted figure with permission from Ref. [99].

This approach gave for the first time a quantitative theoretical explanation for the complex phenomena which had been experimentally observed in these systems. In spite of its qualitative success, this is still very rough. A fundamental deficiency of the Hartree-Fock treatment is that it leads to a broken symmetry solution which cannot persist in

the thermodynamic limit: a single impurity cannot lead to a magnetic solution in an infinite system. This model has been the subject of intense scrutiny since it was first examined, and it will be the focus of Sec. 7 to examine the recent advances in the numerical approaches using Monte Carlo techniques for solving this problem, the so-called quantum impurity solvers. Before that, we will introduce, in Sec. 6, the observation by Georges and Kotliar [100], of a mapping between the Hubbard model in infinite dimensions and the single impurity Anderson model. This correspondence led to the emergence of a new technique for investigating the Hubbard model: the Dynamical Mean-Field Theory (DMFT).

Chapter 4

Excitonic condensation within the Hubbard model

In this chapter, we review the formalism used in previous studies, show how excitonic condensation emerges in the weak and the strong coupling limits of the Hubbard Hamiltonian, and present some considerations on the intermediate coupling regime. For an exhaustive overview of the theoretical results in the field, the reader is referred to the topical review by Kuneš [101], which we loosely follow in this short summary of the subject.

4.1 The two-band Hubbard model

In order to understand excitonic condensation in the Hubbard model, it is necessary to use two bands. In this case, and considering a square two-dimensional lattice, the Hubbard Hamiltonian takes the following form

$$\begin{aligned}
H_{2BH} &= H_t + H_{\mathrm{loc}} \\
H_t &= \sum_{\langle \mathbf{ij} \rangle} H_t^{(\mathbf{i},\mathbf{j})} \\
H_{\mathrm{t}}^{(\mathbf{i},\mathbf{i}+\mathbf{e}_\nu)} &= \sum_{\sigma} \left(t_a a^\dagger_{\mathbf{i}+\mathbf{e}_\nu\sigma} a_{\mathbf{i}\sigma} + t_b b^\dagger_{\mathbf{i}+\mathbf{e}_\nu\sigma} b_{\mathbf{i}\sigma} \right) + \mathrm{H.c.} \\
&\quad + \sum_{\sigma} \left(V_1 a^\dagger_{\mathbf{i}+\mathbf{e}_\nu\sigma} b_{\mathbf{i}\sigma} + V_2 b^\dagger_{\mathbf{i}+\mathbf{e}_\nu\sigma} a_{\mathbf{i}\sigma} \right) + \mathrm{H.c.} \\
H_{\mathrm{loc}} &= \frac{\Delta}{2} \sum_{\mathbf{i}\sigma} \left(n^a_{\mathbf{i}\,\sigma} - n^b_{\mathbf{i}\,\sigma} \right) + \sum_{\mathbf{i}} H^{(\mathbf{i})}_{\mathrm{int}} \\
H^{(\mathbf{i})}_{\mathrm{int}} &= +U \left(n^a_{\mathbf{i}\uparrow} n^a_{\mathbf{i}\downarrow} + n^b_{\mathbf{i}\uparrow} n^b_{\mathbf{i}\downarrow} \right) + U' \sum_{\sigma\sigma'} n^a_{\mathbf{i}\sigma} n^b_{\mathbf{i}\sigma'} \\
&\quad - J \sum_{\sigma} \left(n^a_{\mathbf{i}\sigma} n^b_{\mathbf{i}\sigma} + \gamma a^\dagger_{\mathbf{i}\sigma} a_{\mathbf{i}-\sigma} b^\dagger_{\mathbf{i}-\sigma} b_{\mathbf{i}\sigma} \right).
\end{aligned} \tag{4.1}$$

Each lattice site hosts two orbitals, a and b. Here $a^\dagger_{i\sigma}$ ($a_{i\sigma}$) is the operator creating (annihilating) a fermion in orbital a on lattice site $\mathbf{i}$, with spin $\sigma = \uparrow, \downarrow$. Further, $n^a_{\mathbf{i}\,\sigma} = a^\dagger_{\mathbf{i}\,\sigma} a_{\mathbf{i}\,\sigma}$ is the corresponding particle number operator, and equivalently for the b fermions. The sum $\sum_{\langle \mathbf{ij} \rangle}$ runs over the nearest neighbor (nn) bonds. The symbol $\mathbf{e}_\nu$ stands for the lattice vector of the 2D square lattice. The local part of the Hamiltonian contains the

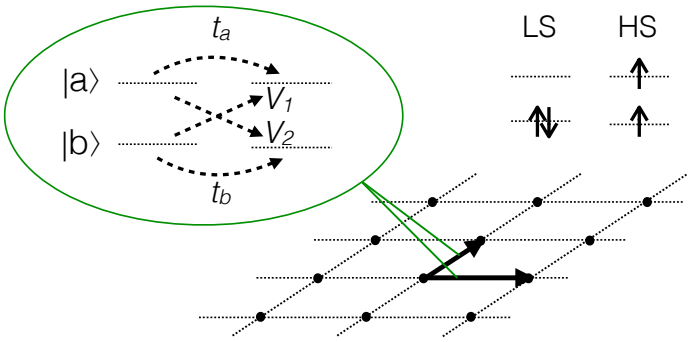

Figure 4.1: The hopping processes with corresponding amplitudes on the square lattice. The values of the parameters used in the calculations presented in Sec. 9 are: $t_a = 0.4118$, $t_b = -0.1882$, $V_1 = \pm V_2 = 0.05$, $\Delta = 3.4$, $U = 4$, $U' = 2$, and $J = 1$ in the units of eV. Reprinted figure with permission from Ref. [102].

crystal-field splitting Δ between the orbitals labeled a and b and the Hubbard repulsion with ferromagnetic Hund's exchange J. The parameter U' is defined as $U' \equiv U - 2J$. The kinetic part H_t involves the nearest-neighbor hoppings on the square lattice between orbitals of the same flavor (t_a and t_b terms), as well as cross-hoppings between orbitals of different flavors (V_1 and V_2 terms), see Fig. 4.1.

4.2 Weak coupling limit formalism

We now briefly review the Hartree-Fock theory of excitonic magnetism, in the simplest case of uniform excitonic condensation (EC) order ($t_a t_b < 0$ in Hamiltonian 4.1). The mean-field decoupling of the interaction term leads to the following expression for the Hamiltonian:

$$\begin{aligned} H = &\sum_{\boldsymbol{k},\sigma\sigma'} \left(\epsilon_{\boldsymbol{k}a}\delta_{\sigma\sigma'} - \boldsymbol{h}_a \cdot \boldsymbol{\tau}_{\sigma\sigma'} a^\dagger_{\boldsymbol{k}\sigma} a_{\boldsymbol{k}\sigma'} \right) \\ &+ \sum_{\boldsymbol{k},\sigma\sigma'} \left(\epsilon_{\boldsymbol{k}b}\delta_{\sigma\sigma'} - \boldsymbol{h}_b \cdot \boldsymbol{\tau}_{\sigma\sigma'} b^\dagger_{\boldsymbol{k}\sigma} b_{\boldsymbol{k}\sigma'} \right) \\ &- \left((\Delta_s \delta_{\sigma\sigma'} + \boldsymbol{\Delta}_t \cdot \boldsymbol{\tau}_{\sigma\sigma'}) b^\dagger_{\boldsymbol{k}\sigma} a_{\boldsymbol{k}\sigma'} + \text{H.c.} \right). \end{aligned} \tag{4.2}$$

Here, $a_{\boldsymbol{k}\sigma}$, $b_{\boldsymbol{k}\sigma}$ are the Fourier transforms of $a_{i\sigma}$ and $b_{i\sigma}$, respectively. The crystal-field splitting and the spin-independent parts of the self-energy from Eq. (4.1) are absorbed in the band dispersions $\epsilon_{\boldsymbol{k}a}$, $\epsilon_{\boldsymbol{k}b}$. Following the historical usage in the excitonic condensation literature, the a (b) band is referred to as the conduction (valence) band. The Weiss fields considered in this mean-field expression are $\boldsymbol{h}_a$, $\boldsymbol{h}_b$, Δ_s, $\boldsymbol{\Delta}_t$, given by:

$$\begin{aligned} \boldsymbol{h}_a &= \boldsymbol{h} + \frac{U}{2N} \sum_{\boldsymbol{k},\sigma\sigma'} \left\langle a^\dagger_{\boldsymbol{k}\sigma} a_{\boldsymbol{k}\sigma'} \right\rangle \boldsymbol{\tau}_{\sigma\sigma'}, \quad \text{and similarly for } \boldsymbol{h}_b, \\ \Delta_s &= \frac{U'}{2N} \sum_{\boldsymbol{k},\sigma\sigma'} \left\langle a^\dagger_{\boldsymbol{k}\sigma} b_{\boldsymbol{k}\sigma'} \right\rangle \delta_{\sigma\sigma'} \\ \boldsymbol{\Delta}_t &= \frac{U'}{2N} \sum_{\boldsymbol{k},\sigma\sigma'} \left\langle a^\dagger_{\boldsymbol{k}\sigma} b_{\boldsymbol{k}\sigma'} \right\rangle \boldsymbol{\tau}_{\sigma\sigma'}, \end{aligned} \tag{4.3}$$

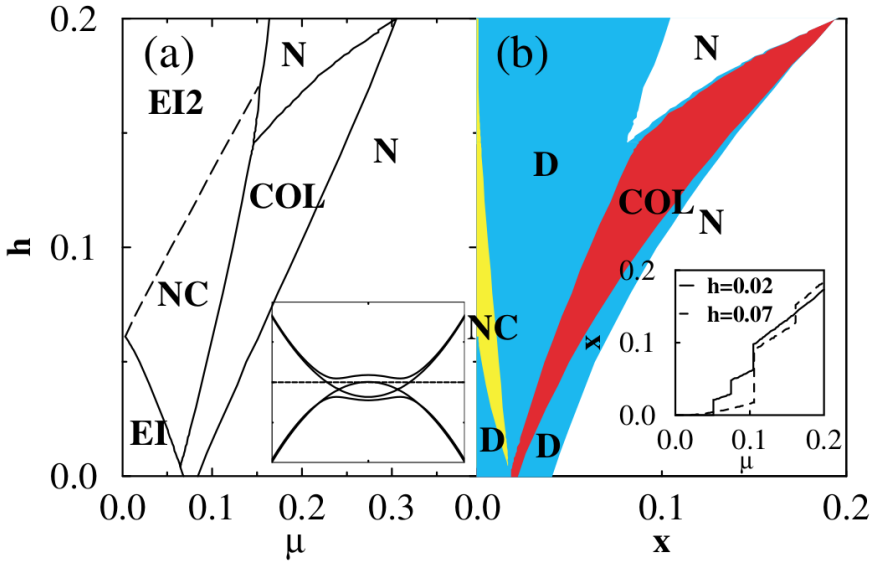

Figure 4.2: The mean-field phase diagram of the doped two-band Hubbard model, as a function of the external magnetic field $\boldsymbol{h}$, and as a function of the chemical potential μ (left panel), as well as of doping x (right panel). $\mu = 0$ in the left panel corresponds to the half-filled situation, i.e. $x = 0$ in the right panel. The light blue areas in the right panel represent phase coexistence regions (marked as D). The meaning of the different phases is described in the text. The two separate panels allow the distinction of these phase coexistence zones, for which the value of doping is not uniquely determined by the chemical potential. The inset in (a) is a sketch of the Hartree-Fock quasiparticle bands in the ferromagnetic state. The inset in (b) shows the dependence of doping on the chemical potential. Reprinted figure with permission from Ref. [103].

where $\boldsymbol{h}$ is the external magnetic field. The field $\boldsymbol{h}_b$ is defined similarly, with orbital flavor b replacing a. The Weiss fields do not depend on $\boldsymbol{k}$, since the Hubbard model only includes local interactions.

Bascones and coworkers [103] considered the model introduced in Eq. (4.2), and studied its ground state as a function of doping and external magnetic field at zero temperature. The phase diagram they found is displayed in Fig. 4.2. Four phases are identified: the normal phase N, the excitonic insulator phase EI, and two metallic phases with a ferromagnetic excitonic condensation order: NC (non-collinear) and COL (collinear). The figure is most easily read by considering the tensor form of the order parameter $\Delta_{\sigma\sigma'} = \frac{1}{2}(\Delta_s \delta_{\sigma\sigma'} + \boldsymbol{\Delta}_t \cdot \boldsymbol{\tau}_{\sigma\sigma'})$. In the EI phase, for $\boldsymbol{h} = 0$, the singlet and triplet excitonic orders are degenerate. The finite field (assumed to possess a positive component along the z axis), lifts this degeneracy. The undoped system first enters a triplet state, $\Delta_s = 0$, and $|\Delta_{\uparrow\downarrow}| > |\Delta_{\downarrow\uparrow}|$ (EI). For $|h_z|$ larger than some critical value, the EI2 phase is reached, in which $\Delta_{\downarrow\uparrow} = 0$. The order parameter in the NC phase is purely triplet, while in the COL phase, the only finite component of the order parameter is $\Delta_{\downarrow\downarrow} \neq 0$. This corresponds to the case of the excitonic ferromagnet predicted by Volkov and collaborators [56], and illustrated in panel (c) of Fig 2.19, with singlet and triplet order parameters mixing with equal weight ($\Delta_s = -\Delta_t^z$).

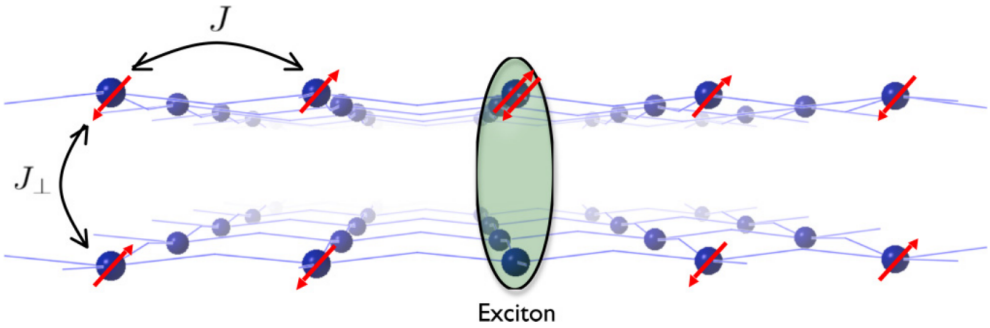

Figure 4.3: Side view of a strongly correlated electron bilayer with an exciton present. The red arrows denote the spins of the localized electrons. The exciton is a bound state of a double occupied and an empty site. Reprinted figure with permission from Ref [89].

4.3 Strong coupling limit formalism

After the first period of interest for the excitonic condensation, this subject was brought back to the forefront by the experimental study of weak ferromagnetism in the hexaborides [59]. Balents [104], performed an extensive study of the strong-coupling limit of the model. One of his goals was to determine whether excitonic ferromagnetism can exist under less restrictive conditions than those required by the weak-coupling theories. We will follow his exposition in the following.

4.3.1 Ultralocal regime

The strong coupling limit corresponds to the situation where the interaction energy (H_{int} in Eq. (4.1) dominates the kinetic energy. A tight-binding based approach, in which the conduction and valence bands of the continuum theory are represented by localized a and b orbitals, is suitable for the description of such a situation. This offers a picture dramatically different from that illustrated by Fig. 2.16: instead of the electron-hole pairs consisting of an electron in the conduction band and a hole in the valence band, an exciton now consists of a doubly occupied site and a vacant site bound together, as shown in Fig. 4.3. In this framework, the analog of the band gap in the continuum model is the level splitting $E_G = E_a - E_b > 0$, and the order parameter is a matrix in spin-space, which reads:

$$\Delta_{\alpha\beta} = \left\langle a_\alpha^\dagger b_\beta \right\rangle .$$

Excitonically ordered states thus exhibit some partial occupation of the nominally excited a states.

We first consider the most minimal model able to display the emergence of excitonic order, with two orbitals per unit cell, but no hopping between adjacent cells: only the local interactions within the unit cell are considered, bringing about the following "ultralocal" Hamiltonian [104]:

$$\begin{aligned} H_{\text{UL}} = \frac{E_G}{2} \sum_{i,\sigma} \left(a_{i\sigma}^\dagger a_{i\sigma} - b_{i\sigma}^\dagger b_{i\sigma} \right) - \mu \sum_{i,\sigma} \left(a_{i\sigma}^\dagger a_{i\sigma} + b_{i\sigma}^\dagger b_{i\sigma} \right) \\ + U \sum_i \left(a_{i\uparrow}^\dagger a_{i\uparrow} a_{i\downarrow}^\dagger a_{i\downarrow} + b_{i\uparrow}^\dagger b_{i\uparrow} b_{i\downarrow}^\dagger b_{i\downarrow} \right) + V \sum_{i,\sigma\,\sigma'} a_{i\sigma}^\dagger a_{i\sigma} b_{i\sigma'}^\dagger b_{i\sigma'}, \end{aligned}$$

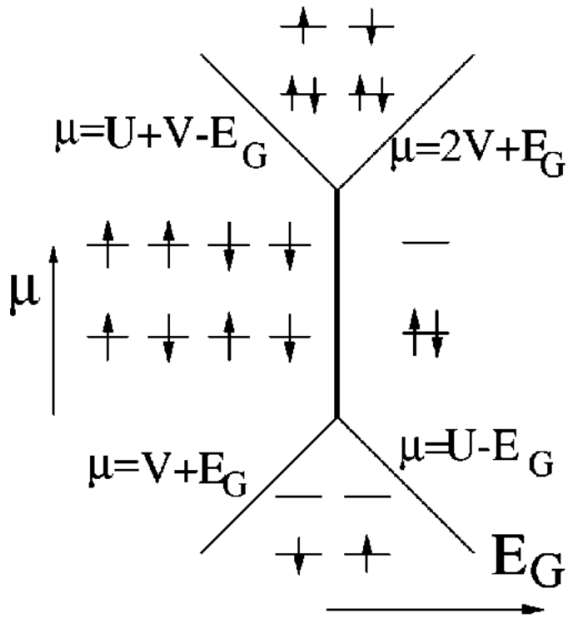

Figure 4.4: Strong-coupling (ultralocal) phase diagram in the $E_G - \mu$ plane, neglecting exchange and all inter-cell hoppings and interactions. Regions with zero and four electrons per unit cell are not shown. For each phase, the lowest-energy states are pictured. The a orbital sits above the b orbital. Reprinted figure with permission from Ref. [104].

where the a and b annihilation operators correspond to the conduction and valence states respectively, indices i, j denote lattice sites, E_G is the orbital energy difference, μ is the chemical potential, U is the Hubbard parameter, and V is the parameter describing repulsion between electrons located in different orbitals. An exchange interaction is also allowed by symmetry in this model, giving rise to a perturbation $H_1 = -J_H \sum_i \boldsymbol{S}_{ia} \cdot \boldsymbol{S}_{ib}$, where $\boldsymbol{S}_{ia} = \frac{1}{2} a_i^\dagger \boldsymbol{\sigma} a_i$, $\boldsymbol{S}_{ib} = \frac{1}{2} b_i^\dagger \boldsymbol{\sigma} b_i$.

In the absence of hopping between adjacent cells, the occupation of each orbital is a good quantum number for the on-site Hamiltonian $H_{\mathrm{UL}} + H_1$. This allows for a simple enumeration of the possible states. The schematic phase diagram represented in Fig. 4.4 is obtained, for $E_G > V > 0$, and a variable concentration centered around half-filling. It is clear that the dependence of the ground state on doping depends crucially on the relative magnitudes of E_G and U.

For $2E_G > U - V$, the lowest state with two electrons per unit cell is that where both electrons occupy the b orbital. This corresponds to a band insulator. Conversely, for $2E_G < U - V$, the ground state is one where each of the a, b orbitals is occupied by one electron. This corresponds to the local version of a Mott insulator. It is important to note that none of these two states exhibits excitonic order, as can be seen by computing $\langle a^\dagger b \rangle = 0$ in each configuration. The $a^\dagger b$ and $b^\dagger a$ operators actually transform one phase into the other.

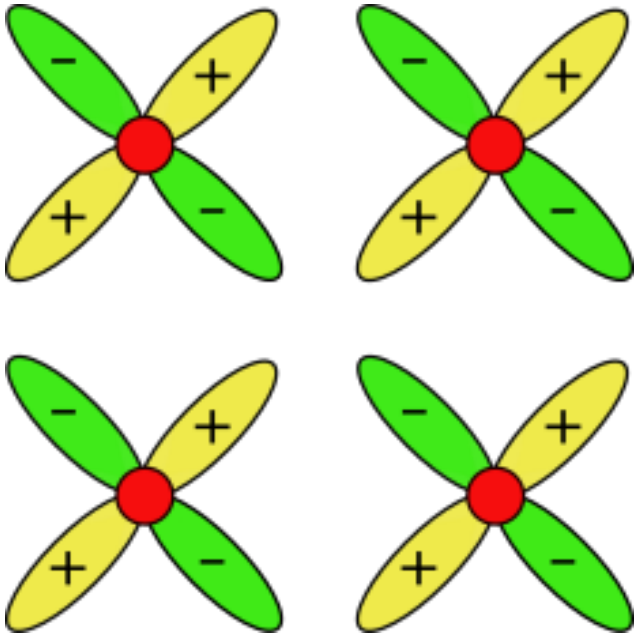

Figure 4.5: Illustration of the model for which the tight-binding description employed phenomenologically in Ref. [104] directly applies. Red circles and yellow plus green crosses represent s and d_{xy} orbitals, respectively.

4.3.2 Strong-coupling limit

The proper strong-coupling regime is obtained if hopping between adjacent cells is restored, via the term

$$H' = \sum_{\langle ij\rangle,\sigma} t\Big(a^\dagger_{i,\sigma}a_{j,\sigma} + b^\dagger_{i,\sigma}b_{j,\sigma} + \text{H.c.}\Big),$$

where $\langle ij\rangle$ indicates that the sum is over nearest-neighbor pairs. Balents also considered cross-hopping, i.e. direct hopping between the different orbitals a and b. He considered orbitals with s and d_{xy} symmetry, as shown in Fig. 4.5, in which case this cross-hopping is restricted to next-nearest neighbors and takes the following form:

$$H'' = \sum_{\langle\langle ij\rangle\rangle,\sigma} t_{ab}\,\mathrm{sgn}\Big[(x_{i,\sigma}-x_{j,\sigma})(y_{i,\sigma}-y_{j,\sigma})\Big]\Big(a^\dagger_{i,\sigma}b_{j,\sigma} + \text{H.c.}\Big),$$

where $\langle\langle ij\rangle\rangle$ indicates that the sum is over next nearest neighbor pairs. The term H'' is a small term which may be treated perturbatively, but plays an important role since it reduces the symmetry of the Hamiltonian: while all the terms in $H_{\text{UL}}+H_1+H'$ conserve the number of a and b particles separately, H'' does not. Upon introduction of this additional term, the symmetry of the model therefore goes from SU(2) × U(1) × U(1), corresponding to the conservation of spin, and a and b charges, to a lower SU(2) × U(1) symmetry, corresponding to the conservation of spin and total charge.

We may address the phase diagram sketched in Fig 4.4, and discuss the influence of H' and H''. In the central region along the vertical axis, i.e. for $(U+V)/2 < \mu < (U+3V)/2$, all sites are doubly occupied in the strong coupling limit. Moreover, to the left of the thick vertical line, the low-energy states are highly degenerate: each orbital is singly occupied, allowing for two spin-1/2 degrees of freedom in each unit cell. In the infinite coupling limit,

these are completely free, but they are not independent once H' and H'' are introduced. Conversely, to the right of the vertical line, there is a unique low-energy state consisting in one doubly occupied b orbital in each unit cell, and hopping does not qualitatively impact this picture. When the system is close enough to the limit between these two extremes, interesting phenomena occur, as interactions involving all five low-energy states are involved. This is the situation where excitonic order appears. Overall, the analytic study of this system by Balents is in qualitative agreement with the conclusions of Halperin and Rice [47], presented in Sec. 2.2.2.

4.3.3 Effective Hamiltonian approach

An effective Hamiltonian approach can be employed in order to investigate the problem given by Hamiltonian 4.1. The strong-coupling limit is characterized by the low spin and high-spin states being separated from the remaining atomic states by an energy $E_i - E_{HS/LS} \gg |t_{a/b}|, |V_{1/2}|$. In this case, an effective model without charge fluctuations can be obtained using the Schrieffer-Wolff transformation [105], providing a simplified picture of the low-energy physics. The resulting effective Hamiltonian with hopping treated to the second order is derived in Ref [53], and takes the following form (only the density-density terms of the Coulomb interaction have been considered):

$$\begin{aligned} H_{\text{eff}}^{\text{dd}} = &\sum_i \mu n_i + K_\perp \sum_{ij,s} d_{i,s}^\dagger d_{j,s} + \sum_{\langle ij\rangle} \left(K_\parallel n_i n_j + K_0 S_i^z S_j^z\right) \\ &+ K_1 \sum_{\langle ij\rangle,s} \left(d_{i,s}^\dagger d_{j,-s}^\dagger + d_{i,s} d_{j,-s}\right). \end{aligned} \tag{4.4}$$

This actually describes bosons of two flavors, with $s = \pm 1$, and the hard-core constraint $n_i = \sum_s d_{i,s}^\dagger d_{i,s} \leq 1$. These correspond to high-spin states created by $d_1^\dagger = a_\uparrow^\dagger b_\downarrow$ and $d_{-1}^\dagger = a_\downarrow^\dagger b_\uparrow$, from the low-spin state considered as the vacuum. Neglecting the cross-hopping term, the coupling constants are given by formulas derived in Ref. [53]: $\mu = \Delta - 3J - Z\dfrac{t_a^2 + t_b^2}{U - 2J}$, $K_\perp = \dfrac{2t_a t_b}{U - 2J}$, $K_\parallel = \left(t_a^2 + t_b^2\right)\dfrac{U + 4J}{(U - 2J)(U + J)}$, and $K_0 = \dfrac{t_a^2 + t_b^2}{U + J}$, where $Z = 4$ is the number of nearest-neighbor sites. The last term appears only for finite cross-hopping: $K_1 = -2V_{ab}V_{ba}\dfrac{U - 2J}{(U + J - \Delta)(U - 5J + \Delta)}$.

When the spin-flip and pair-hopping terms of the Coulomb interaction are considered as well, (restoring the SU(2) symmetry of the Hamiltonian), a richer effective Hamiltonian is obtained:

$$\begin{aligned} H_{\text{eff}} = &\sum_i \mu n_i + K_\perp \sum_{ij} \boldsymbol{d}_i^\dagger \cdot \boldsymbol{d}_j + \sum_{\langle ij\rangle} \left(K_\parallel n_i n_j + K_0 \boldsymbol{S}_i \cdot \boldsymbol{S}_j\right) \\ &- K_1 \sum_{\langle ij\rangle} \left(\boldsymbol{d}_i^\dagger \cdot \boldsymbol{d}_j^\dagger + \boldsymbol{d}_i \cdot \boldsymbol{d}_j\right) + K_2 \sum_{i,j} \left(\boldsymbol{d}_i + \boldsymbol{d}_i^\dagger\right) \cdot \boldsymbol{S}_j, \end{aligned} \tag{4.5}$$

where the symbol $\boldsymbol{d}$ stands for $\begin{pmatrix} \dfrac{1}{\sqrt{2}}(d_{-1} - d_1) \\ \dfrac{1}{i\sqrt{2}}(d_{-1} + d_1) \\ d_0 \end{pmatrix}$, $(\boldsymbol{S_i})_\alpha = \sum_{ss'} d_{i,s}^\dagger S_{ss'}^\alpha d_{i,s'}$, and $n_i = \sum_s d_{i,s}^\dagger d_{i,s}$. Here, $s = 0, \pm 1$ and $S_{ss'}^\alpha$ are the spin $S = 1$ matrices and d_0 corresponds

to a third kind of boson, $d_0^\dagger = \dfrac{a_\uparrow^\dagger b_\uparrow - a_\downarrow^\dagger b_\downarrow}{\sqrt{2}}$. The hard-core constraint $n_i \leq 1$ is assumed. The full expressions for the coupling constants are available in Ref. [53].

4.3.4 Pseudospin formulation

An effective Hamiltonian such as that in Eq. (4.5) is conveniently interpreted using pseudospin variables [101, 104]. These can be introduced by the use of the on-site standard-basis operators [106]. These are the T_i^{mn} operators, with matrix elements in the local basis given by

$$\left\langle m' \middle| T^{mn} \middle| n' \right\rangle = \delta_{mm'}\delta_{nn'}.$$

We now follow the presentation by Kuneš [101], which is valid in the large J case. The general situation is examined by Balents [104] within the same formalism. In the large J case, the low-energy Hilbert space can be constructed from the atomic high-spin and low-spin states (note that in the below, $|\text{vac}\rangle$ denotes the vacuum with no spin present, not to be confused with the low-spin vacuum employed elsewhere in this work):

$$\left| \begin{array}{l|l} |1\rangle = a_\uparrow^\dagger b_\uparrow^\dagger |\text{vac}\rangle & |0\rangle = \dfrac{1}{\sqrt{2}}\Big(a_\uparrow^\dagger b_\downarrow^\dagger + a_\downarrow^\dagger b_\uparrow^\dagger\Big)|\text{vac}\rangle \\ |-1\rangle = a_\downarrow^\dagger b_\downarrow^\dagger |\text{vac}\rangle & |\varnothing\rangle = b_\uparrow^\dagger b_\downarrow^\dagger |\text{vac}\rangle \end{array} \right|$$

If an easy axis anisotropy is assumed, the local Hilbert space is further reduced and the state $|0\rangle$ may be dropped. In such a case, only the density-density part of the Hund's interaction contributes, which is an approximation often used in numerical simulations of the Anderson impurity model with the quantum Monte-Carlo approach, such as that used in Sec. 9. Under this approximation, the effective Hamiltonian reads

$$\begin{aligned} H_{\text{eff}}^{(J)} = \epsilon \sum_{i,s} T_i^{ss} + K_\perp \sum_{\langle ij\rangle,s} \Big(T_i^{s\varnothing} T_j^{\varnothing s} + i \leftrightarrow j \Big) \\ + \sum_{\langle ij\rangle,s,s'} \Big(K_\parallel + (-1)^{ss'} K_0 \Big) T_i^{ss} T_j^{s's'} \\ + K_1 \sum_{\langle ij\rangle,s} \Big(T_i^{s\varnothing} T_j^{\bar{s}\varnothing} + T_i^{\varnothing s} T_j^{\varnothing \bar{s}} \Big), \end{aligned} \tag{4.6}$$

where $s = \pm 1$ and $\bar{s} = -s$. The expressions for the coupling constants can be found in Ref. [53]. This formalism allows a direct interpretation of the Hamiltonian in terms of elementary processes, which are illustrated in Fig. 4.6. Process (i), corresponding to the first term of $H_{\text{eff}}^{(J)}$, involves states with high-spin, and lowers the energy of a high-spin low-spin pair on a nearest-neighbor bond. In other terms, it reduces the energy ϵ of a single high-spin state in an otherwise low-spin background, down from the atomic value $E_{\text{HS}} - E_{\text{LS}}$. Conversely, the third term of the Hamiltonian induces a repulsive interaction between nearest neighbor pairs of high-spin states, via the term $K_\parallel T_i^{ss} T_j^{s's'}$. Process (ii), illustrative of the second term of Eq. (4.6), exchanges high-spin and low-spin configurations on nearest-neighbor bonds, corresponding to quantum fluctuations. The last term of Eq. (4.6) corresponds to the conversion of a low-spin low-spin pair on a nearest-neighbor bond, into a high-spin high-spin pair. Such a process exists only if cross-hopping is finite, and is illustrated by the diagram (iii) in Fig. 4.6.

The form 4.6 can be further expressed in the language of hard-core bosons, and with the introduction of Schwinger-like bosons, so that the hard-core constraint of one boson per

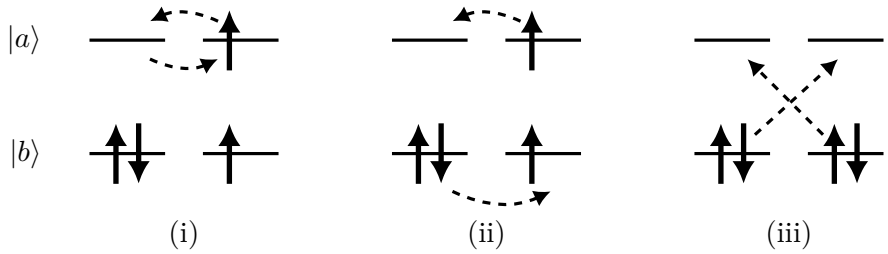

Figure 4.6: Schematic representation of the hopping processes contributing to the Hamiltonian of Eq. (4.6).

site is more easily managed. Once this transformation is done, the correspondence between this Hamiltonian, and other well studied bosonic Hamiltonians can be established. Among these, the Blume-Emmery-Griffiths model, the bosonic t-J model, or the bi-layer Heisenberg model are all special cases whose results can be interpreted back in the framework of excitonic condensation [101].

4.4 Intermediate coupling

In the intermediate coupling regime, it is not possible to identify a small parameter, so that the best results have been obtained using numerical simulations for finite systems, namely exact diagonalization, quantum Monte-Carlo, or embedded cluster methods such as dynamical mean-field theory (DMFT) [10], variational cluster approximation [107], or cluster DMFT [108]. The dynamical mean field theory has been particularly valuable for the study of the Hubbard model in recent years, but most applications of DMFT have been limited to studies of one-particle quantities, and the normal state. The studies of the linear response, aimed at identifying the instabilities of the model, have been limited to one- [109] and two-band models [110, 111], with the exception of Ref. [112]. The phase diagram of the two- and three-band Hubbard models remains a subject of active research, as the most recent results on superconductivity [113–116] or excitonic condensation [117] in this model, obtained using DMFT, demonstrate.

4.4.1 Half-filling case

The basic physical properties of the excitonic condensate in the context of the two-band Hubbard model, at half-filling and in the vicinity of the high-spin low-spin state transition have been investigated by Kuneš and Augustinský [118]. The excitonic condensation order parameter is divided into its spin-singlet and spin-triplet components:

$$\begin{aligned} F^{\sigma\sigma'} &= \frac{1}{2}\left(\phi^s \delta_{\sigma\sigma'} + \boldsymbol{\phi}^t \cdot \boldsymbol{\tau}^*_{\sigma\sigma'}\right), \\ \phi^s &= \sum_\sigma \left\langle a^\dagger_\sigma b_\sigma \right\rangle, \\ \boldsymbol{\phi}^t &= \sum_{\sigma\sigma'} \left\langle a^\dagger_\sigma b_{\sigma'} \right\rangle \boldsymbol{\tau}_{\sigma\sigma'}, \end{aligned} \tag{4.7}$$

where $\boldsymbol{\tau}$ are the Pauli matrices and * denotes complex conjugation. In the following, we drop the triplet index, and denote $\boldsymbol{\phi} \equiv \boldsymbol{\phi}^t$.

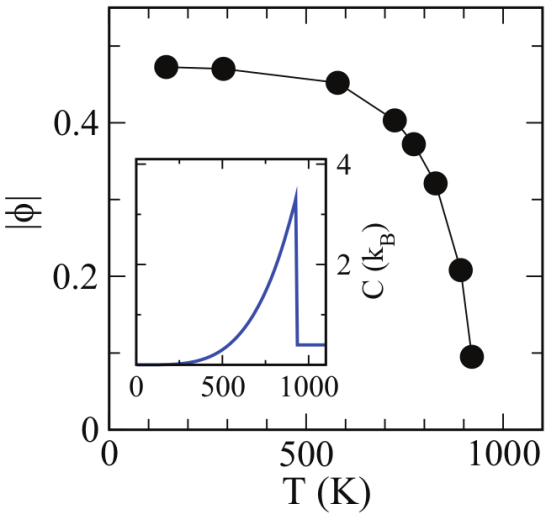

Figure 4.7: The magnitude of the order parameter $|\boldsymbol{\phi}(\boldsymbol{T})|$, as the critical temperature is crossed, obtained from a DMFT calculation, in the two-band Hubbard model. The specific heat per site is also shown in the inset. Reprinted figure with permission from Ref. [118].

Figure 4.7 illustrates the dependence of the magnitude of the order parameter $|\boldsymbol{\phi}|$ on temperature, which exhibits the form $(1 - T/T_c)^{1/2}$, typical of mean-field approaches. In this instance, the order parameter was chosen to point in the x direction. The existence of a finite x component of $\boldsymbol{\phi}$ is linked to the presence of a finite anomalous (spin off-diagonal) matrix element of the self-energy, which also triggers the opening of a gap in the one-particle spectrum (see panels (a) and (b) of Fig. 4.8). This is in line with the formal analogy with superconductivity mentioned earlier in Sec. 2. The charge-neutral excitons do not contribute to charge transport, so that the gap opening in the one-particle spectra is reflected in the opening of an optical gap, illustrated in panel (e) of Fig. 4.8, together with the suppression of the Drude peak below T_c. The dc resistivity, represented in the inset of panel (e), grows exponentially upon cooling.

4.4.2 Impact of doping

Kuneš [119] used DMFT to study the impact of doping on the two-band Hamiltonian presented above (note in particular the absence of cross hopping). The resulting phase diagram, shown in Fig. 4.9, includes the normal phase, and three distinct excitonic phases. In order to discuss these phases, it is convenient to introduce

$$\begin{aligned} \phi^+ &= \frac{\phi_x + i\phi_y}{2}, \\ \phi^- &= \frac{\phi_x - i\phi_y}{2}. \end{aligned} \tag{4.8}$$

The symmetry of the model is such that a variation in the phase of either ϕ^+ or ϕ^- leads to degenerate states, so that only the amplitudes of ϕ^+ and ϕ^- need to be considered.

The normal phase (N) corresponds to the case $|\phi^+| = |\phi^-| = 0$. The linear excitonic phase (L) is characterized by $|\phi^+| = |\phi^-| \neq 0$, the circular excitonic phase (C) by $|\phi^+| = 0$, $|\phi^-| \neq 0$, and the elliptic excitonic phase by $0 \neq |\phi^+| \neq |\phi^-| \neq 0$. The phase labeled EI

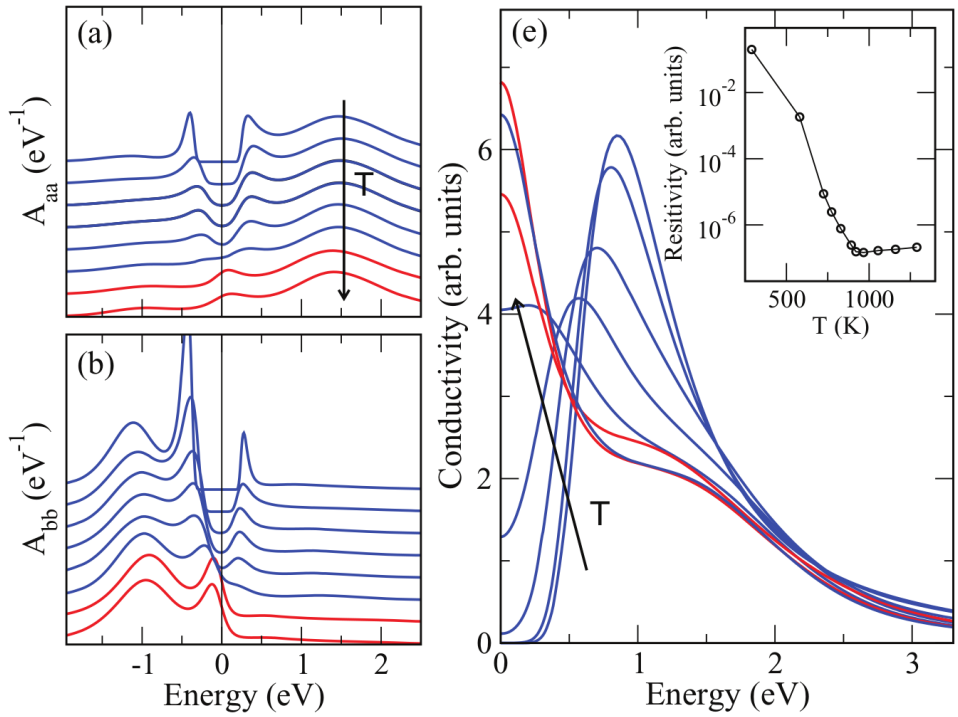

Figure 4.8: Left panel: The evolution of the one-particle spectral function (diagonal elements) with temperature T, for $T = 1160, 968, 921, 892, 829, 725, 580$, and $290\,\mathrm{K}$. Right panel: The corresponding optical conductivity, and the T-dependence of the *dc* resistivity, shown in the inset. Data obtained in the same framework as those shown in Fig. 4.7. Reprinted figure with permission from Ref. [118].

in Fig. 4.2 in the half-filling case corresponds to the linear excitonic (L) phase, and extends in the finite doping region.

In the (C) and (E) phases, we observe a finite uniform magnetization

$$m_z = \left\langle a^\dagger_{i\uparrow} a_{i\uparrow} + b^\dagger_{i\uparrow} b_{i\uparrow} - a^\dagger_{i\downarrow} a_{i\downarrow} - b^\dagger_{i\downarrow} b_{i\downarrow} \right\rangle .$$

Conversely, the (L) phase does not possess any ordered moment, which translates into $\boldsymbol{\phi}^* \times \boldsymbol{\phi} = \mathbf{0}$ [101, 104], so that $\boldsymbol{\phi}$ may be factorized into a real vector and a phase factor. The arbitrariness of the phase factor is related to the absence of cross-hopping (and pair-hopping) terms in the model. In Sec. 9, we will discuss in detail the physics of excitonic condensation in the presence of a finite cross-hopping term.

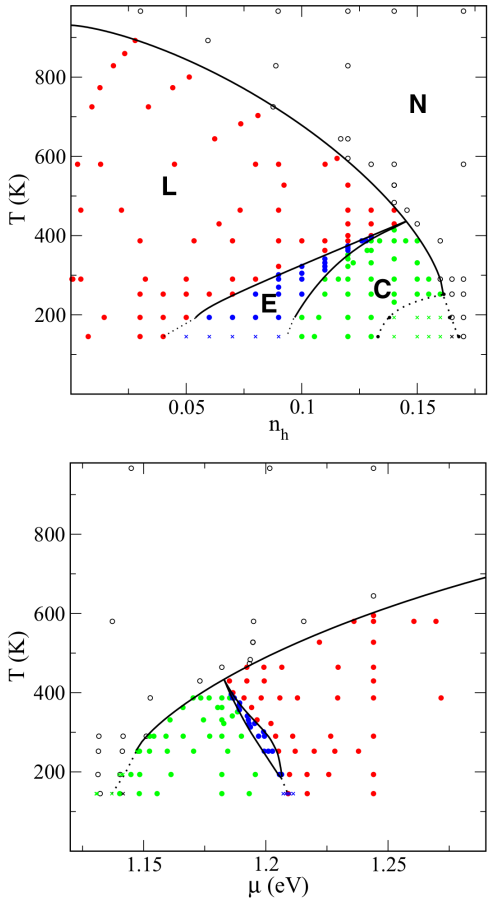

Figure 4.9: Top panel: the phase diagram in the density-temperature ($n_h - T$) plane. The symbols correspond to the parameters where actual calculations were performed. The circles mark stable solutions, while the crosses mark the thermodynamically unstable ones. The colors code the thermodynamic phases: N (open circles), L (red), E (blue), and C (green). The lines mark the estimated phase boundaries corresponding to continuous transitions (solid) and the phase separation region (dotted). Bottom panel: the corresponding phase diagram in the $\mu - T$ plane. The solid lines mark the continuous transitions, while the dotted lines mark the first-order ones. Reprinted figure with permission from Ref. [119].

Chapter 5

Coherent states and the functional integral formalism

In this chapter we establish the theoretical ground for the spin-fermion model. We first introduce the path integral representation of many-body fermion systems, following the lines of Ref. [120]. We then apply the formalism to the Hubbard model, and derive a mean-field theory in this framework[121]. Its merits as a justification for the spin-fermion model are discussed. The properties of this model, and its ability to reproduce the dispersion anomalies in cuprates, are addressed in detail in Sec. 8.

5.1 Coherent states for fermions

The simplest possible mean-field approach to the Hubbard model is based on the assumption that the fluctuations of the density of electrons on a site are small compared to the value of the average. This allows the interaction term to be transformed from a quartic form to a quadratic form, and provides some useful insights into the physics of the model. A deeper insight can be gained in a more natural and concise way by using the path-integral formalism, which we will now introduce. Once this formalism is introduced, we will use it to derive an alternative mean-field approach to the one-band Hubbard model, which will provide the so-called spin-fermion model. The material in this section follows closely the derivations provided in Ref. [120]

5.1.1 The basis of coherent states

When dealing with many-body fermionic systems, it is frequent to make use of Slater determinants in order to obtain a set of suitably symmetrized states forming a basis of the Fock space. Another extremely useful basis of the Fock space is the basis of coherent states[120]. Although it is not an orthonormal basis, it spans the whole Fock space. Just as the states $|\boldsymbol{r}\rangle$ are defined as eigenstates of the position operator $\hat{\boldsymbol{r}}$, the coherent states are defined as eigenstates of the annihilation operators. It is instructive to examine why annihilation operators, rather than creation operators, are considered for this purpose. Let us consider a general vector of the Fock space $|\phi\rangle$ and expand it in the occupation number basis:

$$|\phi\rangle = \sum_{n=0}^{\infty} \sum_{\alpha_1 \ldots \alpha_n} \phi_{\alpha_1 \alpha_n} |\alpha_1 \ldots \alpha_n\rangle \,, \tag{5.1}$$

where $|\alpha_1 \dots \alpha_n\rangle$ is a many-particle state where single-particle states $\alpha_1, \dots \alpha_n$ are occupied. Now, consider the infinite but countable set made up of the positive numbers of particles in each of the components of $|\phi\rangle$. This set being countable, made up of integer numbers greater than or equal to 0, it possesses a smallest element. Application of a creation operator increases the value of this smallest element in the obtained ket by one, and therefore the image ket cannot be a multiple of $|\phi\rangle$: a creation operator cannot have an eigenstate. On the other hand, this set does not necessarily possess a largest element: physically, $|\phi\rangle$ may contain components with all particle numbers. As a consequence, application of an annihilation operator does not preclude the image ket to be proportional to $|\phi\rangle$. In other terms, nothing forbids the ket $|\phi\rangle$ to be an eigenstate.

Assuming such an eigenstate $|\phi\rangle$ of the annihilation operators a_α has been found, then

$$a_\alpha |\phi\rangle = \phi_\alpha |\phi\rangle .$$

The commutation (anticommutation) relations of the creation and annihilation operators for bosons (fermions) then have an interesting consequence for the eigenvalues ϕ_α. For bosons, the eigenvalues commute, and can therefore be ordinary complex numbers. For fermions though, the eigenvalues anticommute, $\phi_\beta \phi_\alpha = -\phi_\alpha \phi_\beta$. This requires the introduction of anticommuting variables, called Grassmann numbers, which we will now focus on.

5.1.2 Grassmann algebra

Algebras of anticommuting numbers are called Grassmann algebras. For our purpose, it will be sufficient to view the rules of Grassmann algebra as a clever mathematical construct, which takes care of all the minus signs related to the necessary symmetrization of fermionic states, in the same way as second quantization does it. For a more thorough mathematical treatment of these algebras, we refer the reader to Ref. [122]. A Grassmann algebra is defined by a set of generators $\{\xi_\alpha\}$, $\alpha = 1, \dots, n$. Such generators anticommute, $\xi_\beta \xi_\alpha + \xi_\alpha \xi_\beta = 0$, so that $\xi_\alpha^2 = 0$. The set of all distinct products of the generators makes up a basis of the algebra: any number in the Grassmann algebra is a linear combination with complex coefficients of the numbers from the set $\{1, \xi_{\alpha_1}, \dots, \xi_{\alpha_1}\xi_{\alpha_2}, \dots, \xi_{\alpha_1}\xi_{\alpha_2} \dots \xi_{\alpha_n}\}$ where by convention the indices are ordered: $\alpha_1 < \alpha_2 < \dots < \alpha_n$. The dimension of the algebra is therefore 2^n.

In an algebra with an even set $n = 2p$ of generators, conjugation is defined as follows: a set of p generators is selected, and to each of these ξ_α, a different generator among the other p is associated, and denoted ξ_α^*. The following properties then define conjugation in the Grassmann algebra:

$$\begin{aligned} (\xi_\alpha)^* &= \xi_\alpha^* \\ (\xi_\alpha^*)^* &= \xi_\alpha \\ \forall \lambda \in \mathbb{C},\ (\lambda \xi_\alpha)^* &= \lambda^* \xi_\alpha^* \\ (\xi_{\alpha_1}\xi_{\alpha_2} \dots \xi_{\alpha_n})^* &= \xi_{\alpha_n}^* \dots \xi_{\alpha_2}^* \xi_{\alpha_1}^* . \end{aligned}$$

In the following, we focus for clarity on a Grassmann algebra possessing two generators. As a consequence of $\xi^2 = 0$, we find that any analytic function f on this algebra is a linear function, and that a function A of two Grassmann variables ξ and ξ^* has the following form:

$$\begin{aligned} f(\xi) &= f_0 + f_1 \xi \\ A(\xi, \xi^*) &= a_0 + a_1 \xi + \overline{a_1} \xi^* + a_{12} \xi^* \xi . \end{aligned}$$

Note that a_1 and $\overline{a_1}$ are not necessarily complex conjugates of each other.

A derivative on these functions may be defined, as it is for ordinary complex functions, only in this case, the variable ξ has to be anticommuted through, until adjacent to the relevant $\dfrac{\partial}{\partial\xi}$, e.g.:

$$\frac{\partial}{\partial\xi}(\xi^*\xi) = -\frac{\partial}{\partial\xi}(\xi\xi^*) = -\xi^*.$$

Note that with this definition, the operators $\dfrac{\partial}{\partial\xi}$ and $\dfrac{\partial}{\partial\xi^*}$ anticommute.

For integration, there is no analog to the familiar Riemann integral construction for ordinary variables. Instead, integration over Grassmann variables is defined as a linear mapping which respects the fundamental property that the integral of an exact differential form is zero. With this, considering that 1 is the derivative of ξ, while ξ is not a derivative, we find the following rules, which define integration:

$$\int d\xi\xi = 1$$
$$\int d\xi 1 = 0.$$

Note that in these expressions, $d\xi$ does not represent an infinitesimal Grassmann number, but is only a notational convenience, and that an expression such as $\int d\xi^*\xi$ does not make sense. A convenient way to remember these definitions is to remark that integration and differentiation are identical on the Grassmann algebra.

Finally, we may equip the space of functions over the Grassmann algebra with a scalar product, e.g. for $f \equiv f_0 + f_1\xi$ and $g(\xi) \equiv g_0 + g_1\xi$:

$$\begin{aligned}\langle f|g\rangle &\equiv \int d\xi^*\, d\xi\, e^{-\xi^*\xi}\, f^*(\xi)\, g(\xi^*) \\ &= \int d\xi^*\, d\xi\, (1-\xi^*\,\xi)(f_0^* + f_1^*\xi)(g_0 + g_1\xi^*) \\ &= -\int d\xi^*\, d\xi\, \xi^*\,\xi f_0^* g_0 + \int d\xi^*\, d\xi\, \xi\,\xi^*\, f_1^* g_1 \\ &= f_0^* g_0 + f_1^* g_1.\end{aligned}$$

It can be shown that with this definition of the product, functions of Grassmann variables form a Hilbert space.

5.1.3 Coherent states for fermionic systems

In this section, we will give an explicit expression for the fermion coherent states. As illustrated above, any relevant expansion – of the kind Eq. (5.1) – must involve Grassmann numbers as coefficients. Therefore, any attempt at an expression for the fermion coherent states requires that the Fock space be enlarged. To this end, a Grassmann algebra $\mathcal{G}$ is defined, by associating a generator ξ_α (ξ_α^*) to each annihilation (creation) operator a_α ($a_\alpha^\dagger$). The generalized Fock space is then constructed as the set of linear combinations of elements of the Fock space $\mathcal{F}$, with coefficients in the Grassmann algebra $\mathcal{G}$:

$$|\psi\rangle = \sum_\alpha \chi_\alpha\, |\phi_\alpha\rangle\,,$$

where $\chi_\alpha \in \mathcal{G}$, and $|\phi_\alpha\rangle \in \mathcal{F}$. Finally, we require the following relations between elements of $\mathcal{G}$ and the creation/annihilation operators:

$$\begin{aligned}\left[\tilde{\xi}, \tilde{a}\right]_+ &= 0 \\ \left(\tilde{\xi}\tilde{a}\right)^\dagger &= \tilde{a}^\dagger \tilde{\xi}^*,\end{aligned}$$

where $\tilde{\xi}$ is any Grassmann variable in $\{\xi_\alpha, \xi_\alpha^*\}$, and $\tilde{a}$ any operator in $\left\{a_\alpha, a_\alpha^\dagger\right\}$.

We are now in a position to introduce the fermion coherent state (this definition closely follows that used in the bosonic case):

$$|\xi\rangle = e^{-\sum_\alpha \xi_\alpha a_\alpha^\dagger} |0\rangle = \prod_\alpha \left(1 - \xi_\alpha a_\alpha^\dagger\right) |0\rangle ,$$

where we have used the fact that $\xi_\alpha a_\alpha^\dagger$ and $\xi_\beta a_\beta^\dagger$ commute. For any state α, we have

$$\begin{aligned} a_\alpha \left(1 - \xi_\alpha a_\alpha^\dagger\right) |0\rangle = \xi_\alpha |0\rangle &= \xi_\alpha \left(1 - \xi_\alpha a_\alpha^\dagger\right) |0\rangle \\ \Rightarrow a_\alpha |\xi\rangle &= \prod_{\beta\neq\alpha} \left(1 - \xi_\beta a_\beta^\dagger\right) a_\alpha \left(1 - \xi_\alpha a_\alpha^\dagger\right) |0\rangle \\ &= \prod_{\beta\neq\alpha} \left(1 - \xi_\beta a_\beta^\dagger\right) \xi_\alpha \left(1 - \xi_\alpha a_\alpha^\dagger\right) |0\rangle \\ &= \xi_\alpha \prod_\beta \left(1 - \xi_\beta a_\beta^\dagger\right) |0\rangle = \xi_\alpha |\xi\rangle . \end{aligned} \tag{5.2}$$

The action of $a_\alpha^\dagger$ on a coherent state is as follows:

$$\begin{aligned} a_\alpha^\dagger |\xi\rangle &= a_\alpha^\dagger \left(1 - \xi_\alpha a_\alpha^\dagger\right) \prod_{\beta\neq\alpha} \left(1 - \xi_\beta a_\beta^\dagger\right) |0\rangle \\ &= a_\alpha^\dagger \prod_{\beta\neq\alpha} \left(1 - \xi_\beta a_\beta^\dagger\right) |0\rangle \\ &= -\frac{\partial}{\partial \xi_\alpha} \left(1 - \xi_\alpha a_\alpha^\dagger\right) \prod_{\beta\neq\alpha} \left(1 - \xi_\beta a_\beta^\dagger\right) |0\rangle = -\frac{\partial}{\partial \xi_\alpha} |\xi\rangle \end{aligned}$$

Similarly, the adjoint of the coherent state is

$$\langle\xi| = \langle 0| e^{-\sum_\alpha a_\alpha \xi_\alpha^*} = \langle 0| e^{\sum_\alpha \xi_\alpha^* a_\alpha},$$

with $\langle\xi| a_\alpha^\dagger = \langle\xi| \xi_\alpha^*$, and one can verify that

$$\langle\xi| a_\alpha = \frac{\partial}{\partial \xi_\alpha^*} \langle\xi| . \tag{5.3}$$

5.1.4 Algebraic properties of the fermion coherent state basis

The overlap between coherent states is given by:

$$\begin{aligned}\langle\xi|\xi'\rangle &= \langle 0|\prod_{\alpha}(1+\xi_\alpha^* a_\alpha)\prod_{\beta}\left(1-\xi'_\beta a_\beta^\dagger\right)|0\rangle \\ &= \langle 0|\prod_{\alpha,\beta}(1+\xi_\alpha^* a_\alpha)\left(1-\xi'_\beta a_\beta^\dagger\right)|0\rangle \\ &= \prod_{\alpha}\left(1+\xi_\alpha^*\xi'_\alpha\right) \\ &= e^{\sum_\alpha \xi_\alpha^*\xi'_\alpha},\end{aligned} \tag{5.4}$$

which shows that coherent states are not orthogonal.

Whenever dealing with (over)complete basis of the Fock space, the closure relation is an essential ingredient. We will now establish its form for coherent states. Let us define the operator

$$A = \int \prod_\alpha d\xi_\alpha^*\, d\xi_\alpha\, e^{-\sum_\alpha \xi_\alpha^*\,\xi_\alpha}\,|\xi\rangle\langle\xi|\,.$$

Using the eigenvalue property of the coherent states, we have

$$\begin{aligned}\langle\alpha_1\ldots\alpha_n|\xi\rangle &= \langle 0|a_{\alpha_1}\ldots a_{\alpha_n}|\xi\rangle \\ &= \langle 0|\xi_{\alpha_1}\ldots\xi_{\alpha_n}|\xi\rangle \\ &= \langle 0|\xi_{\alpha_1}\ldots\xi_{\alpha_n}\prod_\alpha\left(1-\xi_\alpha a_\alpha^\dagger\right)|0\rangle \\ &= \xi_{\alpha_1}\ldots\xi_{\alpha_n},\end{aligned}$$

and the similar adjoint equation. Thus, for any vectors $|\alpha_1\ldots\alpha_n\rangle$ and $|\beta_1\ldots\beta_m\rangle$ of the basis of the Fock space,

$$\begin{aligned}\langle\alpha_1\ldots\alpha_n|A|\beta_1\ldots\beta_m\rangle &= \int\prod_\alpha d\xi_\alpha^*\, d\xi_\alpha e^{-\sum_\alpha\xi_\alpha^*\,\xi_\alpha}\,\langle\alpha_1\ldots\alpha_n|\xi\rangle\,\langle\xi|\beta_1\ldots\beta_m\rangle \\ &= \int\prod_\alpha d\xi_\alpha^*\, d\xi_\alpha\prod_\alpha(1-\xi_\alpha^*\,\xi_\alpha)\xi_{\alpha_1}\ldots\xi_{\alpha_n}\xi_{\beta_1}^*\ldots\xi_{\beta_m}^*.\end{aligned} \tag{5.5}$$

We can now consider the kinds of integrals which may appear, for a specific state γ:

$$\int d\xi_\gamma^*\, d\xi_\gamma\left(1-\xi_\gamma^*\,\xi_\gamma\right)\left\{\begin{array}{c}\xi_\gamma\,\xi_\gamma^* \\ \xi_\gamma \\ \xi_\gamma^* \\ 1\end{array}\right\} = \left\{\begin{array}{c}1\\0\\0\\1\end{array}\right\}, \tag{5.6}$$

which shows that the only γ-terms that contribute are those where the γ state is either occupied or unoccupied in both $|\alpha_1\ldots\alpha_n\rangle$ and $|\beta_1\ldots\beta_m\rangle$ simultaneously. This means that $m=n$, and that $\{\alpha_1\ldots\alpha_n\}$ is some permutation P of $\{\beta_1\ldots\beta_n\}$. As a consequence, $\xi_{\alpha_1}\ldots\xi_{\alpha_n}\xi_{\beta_1}^*\ldots\xi_{\beta_m}^* = (-1)^P\xi_{\alpha_1}\ldots\xi_{\alpha_n}\xi_{\alpha_1}^*\ldots\xi_{\alpha_m}^*$. Observing that an even number of pair exchanges is required to bring the product in Eq. (5.5) to the form in Eq. (5.6), we find that each transformation contributes a factor of 1, and the final value of the expression is $(-1)^P$. It is a known result of second quantization that this is exactly the value of the

overlap between the two considered many-particle states: $(-1)^P = \langle\alpha_1 \dots \alpha_n|\beta_1 \dots \beta_n\rangle$. This proves the key equality:

$$\langle\alpha_1 \dots \alpha_n|A|\beta_1 \dots \beta_n\rangle = \langle\alpha_1 \dots \alpha_n|\beta_1 \dots \beta_n\rangle\,,$$

for any two vectors $|\alpha_1 \dots \alpha_n\rangle$ and $|\beta_1 \dots \beta_m\rangle$ of the basis of the Fock space. This is nothing other than a proof of the following closure relation for fermions in the coherent state representation:

$$\int \prod_\alpha d\xi^*_\alpha\, d\xi_\alpha\, e^{-\sum_\alpha \xi^*_\alpha \xi_\alpha}\, |\xi\rangle\langle\xi| = 1. \tag{5.7}$$

This completeness relation in turn provides us with a very useful expression for the trace of operators: Considering that matrix elements between vectors of the Fock space and coherent states involve Grassmann numbers, we know that $\langle\psi_i|\xi\rangle\,\langle\xi|\psi_j\rangle = \langle -\xi|\psi_j\rangle\,\langle\psi_i|\xi\rangle$. Using this, and considering a complete set $\{|n\rangle\}$ of states in the Fock space, we may express the trace of an operator A as follows:

$$\begin{aligned}
\mathrm{Tr}\{A\} &= \sum_n \langle n|A|n\rangle \\
&= \int \prod_\alpha d\xi^*_\alpha\, d\xi_\alpha\, e^{-\sum_\alpha \xi^*_\alpha \xi_\alpha} \sum_n \langle n|\xi\rangle\ \langle\xi|A|n\rangle \\
&= \int \prod_\alpha d\xi^*_\alpha\, d\xi_\alpha\, e^{-\sum_\alpha \xi^*_\alpha \xi_\alpha}\, \langle -\xi|A \sum_n |n\rangle\,\langle n|\xi\rangle \\
&= \int \prod_\alpha d\xi^*_\alpha\, d\xi_\alpha\, e^{-\sum_\alpha \xi^*_\alpha \xi_\alpha}\, \langle -\xi|A|\xi\rangle\,.
\end{aligned} \tag{5.8}$$

The completeness relation Eq. (5.7) also provides us with an elegant Grassmann coherent state representation of any ket $|\psi\rangle$: defining $\psi(\xi^*) \equiv \langle\xi|\psi\rangle$, we get

$$|\psi\rangle = \int \prod_\alpha d\xi^*_\alpha\, d\xi_\alpha\, e^{-\sum_\alpha \xi^*_\alpha \xi_\alpha} \psi(\xi^*)\, |\xi\rangle\,. \tag{5.9}$$

Just as it is useful to know how the operators $\hat{x}$ and $\hat{p}$ act in coordinate representation, it is useful to have a clear idea of how the creation and annihilation operators act in the coherent state representation. We can apply relations (5.2) and (5.3) to the above expression, in order to obtain directly:

$$\begin{aligned}
\langle\xi|a_\alpha|\psi\rangle &= \frac{\partial}{\partial\xi^*_\alpha}\psi(\xi^*) \\
\langle\xi|a^\dagger_\alpha|\psi\rangle &= \xi^*_\alpha\psi(\xi^*).
\end{aligned} \tag{5.10}$$

In other words, the operators a_α and $a^\dagger_\alpha$ are represented by $\dfrac{\partial}{\partial\xi^*_\alpha}$ and ξ^*_α respectively.

Finally, let us note that the expression for the matrix element of a normal-ordered operator A (i.e., an operator written in such a way that all creation operators are to the left of the annihilation operators), takes a particularly simple form: using again relations (5.2) and (5.3), together with the expression for the overlap between coherent states (5.4), we immediately find

$$\langle\xi|A\Big(a^\dagger_\alpha, a_\alpha\Big)|\xi'\rangle = e^{\sum_\alpha \xi^*_\alpha \xi'_\alpha} A\big(\xi^*_\alpha, \xi'_\alpha\big). \tag{5.11}$$

For example, the expectation value of the number of particles in a state $|\xi\rangle$ is

$$\begin{aligned}\left\langle \hat{N} \right\rangle &= \frac{\langle \xi | \hat{N} | \xi \rangle}{\langle \xi | \xi \rangle} \\ &= \sum_{\alpha} \frac{\langle \xi | a_{\alpha}^{\dagger} a_{\alpha} | \xi \rangle}{\langle \xi | \xi \rangle} \\ &= \sum_{\alpha} \xi_{\alpha}^{*} \xi_{\alpha},\end{aligned}$$

which is not a fixed number, but more surprisingly, is not a real number either.

We conclude this section with a short comment on the concept of fermionic coherent states. Coherent states for bosons are usually identified as those which correspond to the classical limit of quantum mechanics (e.g. in the harmonic oscillator system). Fermion coherent states do not lend themselves to this interpretation: they are not part of the fermion Fock space, are not physically observable, and do not correspond to any form of classical field. Nevertheless, as sometimes occurs in other branches of physics, they are a useful and efficient formal tool, in this case for unifying many-fermion and many-boson problems. One notable consequence of this difference in nature between bosonic and fermionic coherent states appears when one applies the stationary phase approximation. This approximation applied to a bosonic expression yields an expansion around a physical classical field configuration. There is no such thing for fermions, and this means that in order to make such an approximation useful, one has to integrate out explicitly the fermionic degrees of freedom. We will demonstrate how this is done in the derivation of the spin-fermion model which follows in Sec. 5.3.2, and in the derivation of the hybridization expansion algorithm for continuous-time quantum Monte-Carlo algorithms in Sec. 6.

5.2 Functional integral formalism

The functional integral representation of many-particle systems dates back to the seminal work of Dirac[123], extensively developed by Feynman[124–126]. Its appeal lies partially in the fact that the partition function can be expressed as an integral over field configurations. This in turn lends itself readily to useful physical approximations, and a very intuitive description of the system. We will now consider the extension of this approach to a general many-particle system described using the second quantization formalism, and use the coherent states in place of the momentum and position eigenstates, which lead to the standard derivation of the Feynman path integral expressions. The derivations follow the textbook by Negele and Orland [120].

5.2.1 Time evolution operator

An intuitive way to introduce this functional integral representation is to calculate the matrix element of the evolution operator between one initial coherent state $|\phi_i\rangle$ at time t_i, with components $\phi_{\alpha,i}$ – in terms of the expansion described in Eq. (5.1) –, and a final state $\langle\phi_f|$ at time t_f, with components $\phi^*_{\alpha,f}$. Formally, for a time-independent Hamiltonian H, we have:

$$\mathcal{U}\left(\phi^*_{\alpha,f}, t_f; \phi_{\alpha,i}, t_i\right) = \langle \phi_f | e^{-\frac{i}{\hbar} H \left(t_f - t_i\right)} | \phi_i \rangle \tag{5.12}$$

We may, with no loss of generality, assume the Hamiltonian to be normal-ordered. In

that case, it can be seen that

$$\exp\left(-i\frac{\epsilon}{\hbar}H\left(a^\dagger,a\right)\right) =: \exp\left(-i\frac{\epsilon}{\hbar}H\left(a^\dagger,a\right)\right) : +\mathcal{O}(\epsilon^2),$$

where $: A :$ denotes the normal-ordered form of operator A.

We may split the time interval into M intervals of length $\epsilon = \dfrac{t_f - t_i}{M}$, of the form $[t_k, t_{k+1}]$. To this end, we introduce $t_k = t_i + k\epsilon$, for $k \in [0, \ldots, M]$. With these definitions, $t_0 = t_i$ and $t_M = t_f$. The closure relation Eq.(5.7), can then be used at each internal time step t_k, $k \in [1, \ldots, M-1]$:

$$\int \prod_\alpha d\phi^*_{\alpha,k}\, d\phi_{\alpha,k}\, e^{-\sum_\alpha \phi^*_{\alpha,k}\,\phi_{\alpha,k}}\, |\phi_k\rangle\langle\phi_k| = 1,$$

For notational convenience, we define $\phi_{\alpha,0} \equiv \phi_{\alpha,i}$ and $\phi_{\alpha,f} \equiv \phi_{\alpha,M}$. With these, we obtain:

$$\begin{aligned}
&\mathcal{U}\left(\phi^*_{\alpha,f}, t_f; \phi_{\alpha,i}, t_i\right) = \langle\phi_f| e^{-\frac{i}{\hbar}H(t_f - t_i)} |\phi_i\rangle \\
&= \lim_{M\to\infty} \int \prod_{k=1}^{M-1} \prod_\alpha d\phi^*_{\alpha,k}\, d\phi_{\alpha,k}\, e^{-\sum_{k=1}^{k=M-1}\sum_\alpha \phi^*_{\alpha,k}\,\phi_{\alpha,k}} \\
&\times \prod_{k=1}^{M} \langle\phi_k| : \exp\left(-i\frac{\epsilon}{\hbar}H\left(a^\dagger,a\right)\right) : +\mathcal{O}\left(\epsilon^2\right)|\phi_{k-1}\rangle \\
&= \lim_{M\to\infty} \int \prod_{k=1}^{M-1} \prod_\alpha d\phi^*_{\alpha,k}\, d\phi_{\alpha,k}\, e^{-\sum_{k=1}^{k=M-1}\sum_\alpha \phi^*_{\alpha,k}\,\phi_{\alpha,k}} \\
&\times \exp\left[\sum_{k=1}^{M}\left(\sum_\alpha \phi^*_{\alpha,\,k}\phi_{\alpha,\,k-1} - \frac{i\epsilon}{\hbar}H\left(\phi^*_{\alpha,\,k},\, \phi_{\alpha,\,k-1}\right)\right)\right],
\end{aligned} \tag{5.13}$$

where the crucial expression Eq. (5.11) was used to obtain the last line.

By analogy with the Feynman path integral formalism, which defines trajectories in real space, it is convenient to introduce the concept of a trajectory $\phi_\alpha(t)$ in the space of coherent states, as the limit, as $M \to \infty$, of the set $\{\phi_{\alpha,0}, \ldots, \phi_{\alpha,M}\}$. This naturally induces us to switch to a continuous notation, in which the following definitions are used:

$$\begin{aligned}
\phi_{\alpha,\,k} &\equiv \phi_\alpha(t) \\
\frac{\phi_{\alpha,\,k} - \phi_{\alpha,\,k-1}}{\epsilon} &\equiv \frac{\partial}{\partial t}\phi_\alpha(t) \\
H\left(\phi^*_{\alpha,\,k},\, \phi_{\alpha,\,k-1}\right) &\equiv H(\phi^*_\alpha(t),\, \phi_\alpha(t))
\end{aligned}$$

With this notation, the exponent of the integrand in the last line of Eq. (5.13) becomes

$$\begin{aligned}
&\sum_\alpha \phi^*_{\alpha,\,M}\phi_{\alpha,\,M-1} - \frac{i\epsilon}{\hbar}H\left(\phi^*_{\alpha,\,M},\, \phi_{\alpha,\,M-1}\right) \\
&+ i\epsilon \sum_{k=1}^{M-1}\left(i\sum_\alpha \phi^*_{\alpha,\,k}\left(\frac{\phi_{\alpha,\,k} - \phi_{\alpha,\,k-1}}{\epsilon}\right) - \frac{1}{\hbar}H\left(\phi^*_{\alpha,\,k},\, \phi_{\alpha,\,k-1}\right)\right) \\
&\underset{\epsilon\to 0}{=} \sum_\alpha \phi^*_\alpha(t_f)\phi_\alpha(t_f) + \frac{i}{\hbar}\int_{t_i}^{t_f} dt\left[\sum_\alpha i\hbar\phi^*_\alpha(t)\frac{\partial}{\partial t}\phi_\alpha(t) - H(\phi^*_\alpha(t),\, \phi_\alpha(t))\right] \\
&= \sum_\alpha \phi^*_\alpha(t_f)\phi_\alpha(t_f) + \frac{i}{\hbar}\int_{t_i}^{t_f} dt L(\phi^*_\alpha(t),\, \phi_\alpha(t)),
\end{aligned} \tag{5.14}$$

where L stands for the Lagrangian operator: $L \equiv i\hbar\dfrac{\partial}{\partial t} - H$.

As a conclusion, we have obtained the functional integral representation of the matrix element of the evolution operator in the coherent state representation:

$$\begin{aligned}\mathcal{U}\big(\phi^*_{\alpha,f}, t_f; \phi_{\alpha,i}, t_i\big) = &\int\limits_{\phi_\alpha(t_i)\equiv\phi_{\alpha,\,i}}^{\phi^*_\alpha(t_f)\equiv\phi^*_{\alpha,\,f}} \mathcal{D}[\phi^*_\alpha(t),\, \phi_\alpha(t)] e^{\sum\limits_\alpha \phi^*_\alpha(t_f)\phi_\alpha(t_f)} \\ &\times \exp\left\{\frac{i}{\hbar}\int\limits_{t_i}^{t_f} dt\left[\sum_\alpha i\hbar\phi^*_\alpha(t)\frac{\partial}{\partial t}\phi_\alpha(t) - H(\phi^*_\alpha(t),\, \phi_\alpha(t))\right]\right\},\end{aligned} \tag{5.15}$$

where

$$\int\limits_{\phi_\alpha(t_i)\equiv\phi_{\alpha,\,i}}^{\phi^*_\alpha(t_f)\equiv\phi^*_{\alpha,\,f}} \mathcal{D}[\phi^*_\alpha(t),\, \phi_\alpha(t)] \equiv \lim_{M\to\infty}\int \prod_{k=1}^{M-1}\prod_\alpha d\phi^*_{\alpha,\,k},\, d\phi_{\alpha,\,k}.$$

A few remarks are in order at this point with regards to this final expression Eq. (5.15). First, in the discrete expression, $\phi_{\alpha,0}$ and $\phi^*_{\alpha,M}$ are present, as the states for which the matrix element of the evolution operator is calculated, but neither $\phi^*_{\alpha,0}$ nor $\phi_{\alpha,M}$ appear. Moreover, all variables of the type $\phi^*_{\alpha,k}$ and $\phi_{\alpha,k}$ for $k \in \{1,\ldots,M-1\}$ are integrated over. When considering the trajectory notation, note that $\phi^*_\alpha(t)$ is associated to $\phi^*_{\alpha,\,k}$, while $\phi_\alpha(t)$ is associated to $\phi^*_{\alpha,\,k-1}$. Therefore, carried over to the trajectory notation, the previous observation means that $\phi^*_\alpha(t_f)$ and $\phi_\alpha(t_i)$ are specified by the matrix element we wish to calculate, i.e., the boundary conditions of the trajectory, while $\phi^*_\alpha(t_i)$ and $\phi_\alpha(t_f)$ are internal variables over which integration is carried out.

Second, if one considers the corresponding derivation applied for a single particle in the coordinate basis, one obtains the Feynman path integral:

$$\mathcal{U}(x_f, t_f;\, x_i, t_i) = \int\limits_{(x_i,t_i)}^{(x_f,t_f)} \mathcal{D}[x(t)][p(t)] \exp\left\{\frac{i}{\hbar}\int\limits_{t_i}^{t_f} dt\Big[p(t)\frac{\partial}{\partial t}x(t) - H(p(t),\, x(t))\Big]\right\},$$

which, in spite of a strong formal similarity with Eq .(5.15), contains a very important difference: in the Feynman path integral expression, the factor $\dfrac{1}{\hbar}$ appears as a constant factor in front of the entire exponent. As a result, the stationary phase approximation corresponds to the classical limit. In the present formalism of Eq. (5.15), a factor $\hbar$ appears inside the expression for the Lagrangian itself, in addition to the same global $\dfrac{1}{\hbar}$ factor, so that the same stationary phase approximation leads to a result which differs from the classical limit.

5.2.2 Partition function for a many-body fermion system

The partition function for a many-particle system is given by[127]

$$\begin{aligned}Z = \operatorname{Tr} e^{-\beta\left(\hat{H}-\mu\hat{N}\right)} &= \int dx\, \langle x|e^{-\beta\left(\hat{H}-\mu\hat{N}\right)}|x\rangle \\ &= \int \prod_\alpha d\phi^*_\alpha\, d\phi_\alpha\, e^{-\sum_\alpha \phi^*_\alpha\,\phi_\alpha}\, \langle -\phi|e^{-\beta\left(\hat{H}-\mu\hat{N}\right)}|\phi\rangle\,,\end{aligned} \tag{5.16}$$

where the last line of Eq. (5.8) was used, with A replaced by the Hamiltonian in the grand canonical ensemble.

This relation may be seen as the sum of the diagonal matrix elements of the time evolution operator, after a Wick rotation to imaginary time has been applied. Under this transformation, the integration domain becomes the imaginary time interval $\tau_f - \tau_i = \beta\hbar$. With this picture in mind, it is clear that all the steps in the derivation of Eq. (5.15) may be repeated, using imaginary time variables, by replacing t with the variable $-i\tau$, with τ imaginary time. If this is done, then Eq. (5.15) becomes (replace dt by $-id\tau$, and $\frac{\partial}{\partial t}$ by $i\frac{\partial}{\partial \tau}$):

$$\begin{aligned} Z = & \int\limits_{\phi_\alpha(\beta)=-\phi_\alpha(0)} \mathcal{D}[\phi^*_\alpha(\tau),\, \phi_\alpha(\tau)] \\ & \exp\left\{ -\int\limits_0^\beta d\tau \left[\sum_\alpha \phi^*_\alpha(\tau) \left(\frac{\partial}{\partial \tau} - \mu \right) \phi_\alpha(\tau) + H(\phi^*_\alpha(\tau),\, \phi_\alpha(\tau)) \right] \right\}, \end{aligned} \tag{5.17}$$

where the boundary term $e^{\sum\limits_\alpha \phi^*_\alpha(t_f)\phi_\alpha(t_f)}$ (a number) has been dropped for simplicity, with no loss of generality, and units where $\hbar = 1$ have been used (and will be used throughout the rest of this section). This expression allows us to introduce the action in this representation as

$$\begin{aligned} S[\phi^*_\alpha(\tau),\, \phi_\alpha(\tau)] &\equiv \int\limits_0^\beta d\tau \left[\sum_\alpha \phi^*_\alpha(\tau) \left(\frac{\partial}{\partial \tau} - \mu \right) \phi_\alpha(\tau) + H(\phi^*_\alpha(\tau),\, \phi_\alpha(\tau)) \right] \\ &= \int\limits_0^\beta d\tau\, L(\phi^*_\alpha(\tau),\, \phi_\alpha(\tau)), \end{aligned} \tag{5.18}$$

where $L(\phi^*_\alpha(\tau),\, \phi_\alpha(\tau))$ is the imaginary time Lagrangian for the problem at hand.

Note that in expression (5.17), the integration is done over trajectories satisfying antiperiodic boundary conditions for the Grassmann variables. The problem has thus been formally reduced to a quadrature, and the last remaining step in order to apply this result consists in developing techniques which allow the evaluation of the expression (5.17).

Many approaches may be employed for the treatment of this problem, and in the following we will expose two of them. In the next paragraph, we will introduce the stationary phase approximation applied to the Hubbard Hamiltonian, which justifies the spin-fermion model approach. Further, in Sec. 7, we shall examine the single impurity Anderson model and the expansion of expression (5.17) in powers of the hybridization. This will provide us with a very efficient algorithm for solving the impurity problem.

5.3 Stationary phase approximation for the Hubbard model

5.3.1 Partition function for the Hubbard model

In this section, we show how the spin-fermion model may be justified as a stationary phase approximation of the Hubbard model. We follow the derivation by Fradkin [93]. Other approaches based on the Hubbard model, and leading to models of the spin-fermion type are reviewed in Ref. [33].

The one-band Hubbard model is introduced and discussed in Sec. 3.1. In order to use the framework presented above for the treatment of this specific model, we need to consider a lattice version of this formalism. This is done by attaching the Grassmann variables to the lattice sites, in the same way as quasiparticle operators are attached to the sites. We will also place ourselves at zero temperature, so that real times may be used.

Using the definition for the Lagrangian operator $\left(L \equiv i\hbar\dfrac{\partial}{\partial t} - H\right)$, and expression (3.3) for the interaction term of the Hamiltonian of the Hubbard model, we find that the Lagrangian density $\mathcal{L}$ takes the form (summation over repeated indices is now assumed here and throughout the rest of this section):

$$\begin{aligned}\mathcal{L}(\phi^*_\alpha(\boldsymbol{r},r),\,\phi_\alpha(\boldsymbol{r},t)) = \phi^*_\alpha(\boldsymbol{r},t)\left(i\frac{\partial}{\partial t}+\mu\right)\phi_\alpha(\boldsymbol{r},t)\\ + t\sum_{j=1,2}\left(\phi^*_\alpha(\boldsymbol{r},t)\,\phi_\alpha(\boldsymbol{r}+\boldsymbol{e_j},t)+\phi^*_\alpha(\boldsymbol{r},t)\,\phi_\alpha(\boldsymbol{r}-\boldsymbol{e_j},t)+\text{H.c.}\right)\\ + \frac{U}{6}(\phi^*_\alpha(\boldsymbol{r},t)\,\tau_{\alpha\,\beta}\,\phi_\beta(\boldsymbol{r},t))^2,\end{aligned} \tag{5.19}$$

As stated earlier, the problem has been essentially reduced to that of the calculation of a quadrature. As shown in Appendix A, such evaluation is simple in the case where the integrand involves quadratic terms. Here though, H_{int} induces quartic terms, which we need to handle differently. In such cases, the Hubbard-Stratonovich transformation [128] can be useful. This transformation is based on the analytic expression for the Gaussian integral given in Eq.(A.1), which can be written in the form:

$$e^{i\frac{1}{2}\lambda^2(\Psi\boldsymbol{\tau}\psi)^2} \propto \int d\boldsymbol{\chi} e^{-i(\frac{1}{2}\boldsymbol{\chi}^2+\lambda\boldsymbol{\chi}\cdot\Psi\boldsymbol{\tau}\Psi)} \tag{5.20}$$

where $\boldsymbol{\chi}(\boldsymbol{r},t)$ is a bosonic field. This transformation allows the mapping of an interacting fermion system to that of non interacting fermions coupled to an external fluctuating field $\boldsymbol{\chi}(\boldsymbol{r},t)$.

We may apply Eq. (5.20) to the system described by Eq. (5.19), using $\lambda = \sqrt{\dfrac{U}{3}}$. In this way, the left hand side exponential of Eq. (5.20) can be identified with the term corresponding to an interaction, in Eq. (3.3). We thus obtain the following expression for the Lagrangian density (note that the corresponding complete expression for the action also involves an integration over the bosonic field $\boldsymbol{\chi}(\boldsymbol{r},t)$, not present in Eq. (5.19)):

$$\begin{aligned}\mathcal{L}'(\phi^*_\alpha(\boldsymbol{r},r),\,\phi_\alpha(\boldsymbol{r},t),\boldsymbol{\chi}(\boldsymbol{r},t)) = \phi^*_\alpha(\boldsymbol{r},t)\left(i\frac{\partial}{\partial t}+\mu\right)\phi_\alpha(\boldsymbol{r},t)\\ + t\sum_{j=1,2}\left(\phi^*_\alpha(\boldsymbol{r},t)\,\phi_\alpha(\boldsymbol{r}+\boldsymbol{e_j},t)+\phi^*_\alpha(\boldsymbol{r},t)\,\phi_\alpha(\boldsymbol{r}-\boldsymbol{e_j},t)+\text{H.c.}\right)\\ - \sqrt{\frac{U}{3}}\boldsymbol{\chi}(\boldsymbol{r},t)\cdot(\phi^*_\alpha(\boldsymbol{r},t)\,\tau_{\alpha\,\beta}\,\phi_\beta(\boldsymbol{r},t)) - \frac{1}{2}\boldsymbol{\chi}(\boldsymbol{r},t)^2.\end{aligned} \tag{5.21}$$

This expression is bilinear in the fermion fields, so that they can be analytically integrated, using Eq.(A.1). We thus obtain an effective Lagrangian density, providing us with an effective action, where the quartic terms coming from the interacting fermions are replaced by

terms representing the coupling of the fermions with the bosonic field $\boldsymbol{\chi}(\boldsymbol{r},t)$. Integrating out the fermionic degrees of freedom goes as follows:

$$\begin{aligned}
Z &= \int\limits_{\phi_\alpha(\beta)=-\phi_\alpha(0)} \mathcal{D}[\phi_\alpha(\boldsymbol{r},t),\phi^*_\alpha(\boldsymbol{r},t),\boldsymbol{\chi}(\boldsymbol{r},t)] e^{iS(\phi_\alpha(\boldsymbol{r},t),\phi^*_\alpha(\boldsymbol{r},t),\boldsymbol{\chi}(\boldsymbol{r},t))} \\
&= \int\limits_{\phi_\alpha(\beta)=-\phi_\alpha(0)} \mathcal{D}[\phi_\alpha(\boldsymbol{r},t),\phi^*_\alpha(\boldsymbol{r},t),\boldsymbol{\chi}(\boldsymbol{r},t)] e^{i\int dt \sum\limits_{\boldsymbol{r}} \mathcal{L}'(\phi^*_\alpha(\boldsymbol{r},r),\,\phi_\alpha(\boldsymbol{r},t),\boldsymbol{\chi}(\boldsymbol{r},t))} \\
&= \int\limits_{\phi_\alpha(\beta)=-\phi_\alpha(0)} \mathcal{D}[\phi_\alpha(\boldsymbol{r},t),\phi^*_\alpha(\boldsymbol{r},t),\boldsymbol{\chi}(\boldsymbol{r},t)] \exp\left[-i\int dt \sum_{\boldsymbol{r}} \frac{1}{2}\boldsymbol{\chi}(\boldsymbol{r},t)^2\right] \\
&\times \exp\left\{ i\int dt \sum_{\boldsymbol{r}} \phi^*_\alpha(\boldsymbol{r},t)\left[\delta_{\alpha\beta}\delta_{\boldsymbol{r}\boldsymbol{r}'}\delta_{tt'}\left(i\frac{\partial}{\partial t}+\mu\right)\right]\phi_\beta(\boldsymbol{r}',t')\right\} \\
&\times \exp\Bigg\{ i\int dt \sum_{\boldsymbol{r}} \phi^*_\alpha(\boldsymbol{r},t) \\
&\qquad \cdot \left[2\mathrm{t}\,\delta_{\alpha\beta}\,\delta_{tt'}\sum_{j=1,2}(\delta_{\boldsymbol{r}',\,\boldsymbol{r}+\boldsymbol{e_j}}+\delta_{\boldsymbol{r}',\,\boldsymbol{r}-\boldsymbol{e_j}}) - \sqrt{\frac{U}{3}}\delta_{\boldsymbol{r}\boldsymbol{r}'}\,\delta_{tt'}\,\boldsymbol{\chi}(\boldsymbol{r},t)\cdot\tau_{\alpha\,\beta}\right]\phi_\beta(\boldsymbol{r}',t')\Bigg\}.
\end{aligned} \tag{5.22}$$

Therefore, we have

$$\begin{aligned}
Z &\propto \int \mathcal{D}[\boldsymbol{\chi}(\boldsymbol{r},t)] \exp\left[-i\int dt\sum_{\boldsymbol{r}}\frac{1}{2}\boldsymbol{\chi}(\boldsymbol{r},t)^2\right] \times \det\left[\left(i\frac{\partial}{\partial t}+\mu\right)\mathbb{I} - \boldsymbol{M}(\boldsymbol{\chi}(\boldsymbol{r},t))\right] \\
&= \int \mathcal{D}[\boldsymbol{\chi}(\boldsymbol{r},t)] \exp i\left[-\int dt\sum_{\boldsymbol{r}}\frac{1}{2}\boldsymbol{\chi}(\boldsymbol{r},t)^2 - i\ln\det\left[\left(i\frac{\partial}{\partial t}+\mu\right)\mathbb{I} - \boldsymbol{M}(\boldsymbol{\chi}(\boldsymbol{r},t))\right]\right],
\end{aligned} \tag{5.23}$$

where Eq. (A.3) was used to integrate out the fermionic degrees of freedom. $\mathbb{I}$ is the identity matrix, and $M(\boldsymbol{\chi}(\boldsymbol{r},t))$ is the matrix defined on the $|\boldsymbol{r}\,t\alpha\rangle$ basis by the following matrix elements:

$$\left\langle \boldsymbol{r}\,t\alpha\right| M(\boldsymbol{\chi})\left|\boldsymbol{r}'\,t'\beta\right\rangle = -2\mathrm{t}\,\delta_{\alpha\,\beta}\,\delta_{t\,t'}\sum_{j=1,2}\left(\delta_{\boldsymbol{r}',\,\boldsymbol{r}+\boldsymbol{e_j}} - \delta_{\boldsymbol{r}',\,\boldsymbol{r}-\boldsymbol{e_j}}\right) + \sqrt{\frac{U}{3}}\delta_{t\,t'}\delta_{\boldsymbol{r},\,\boldsymbol{r}'}\boldsymbol{\chi}(\boldsymbol{r},t)\cdot\tau_{\alpha\,\beta}. \tag{5.24}$$

Identifying the last line of Eq. (5.23) with the expression for the partition function in terms of a functional of the (effective) action,

$$Z = \int \mathcal{D}[\boldsymbol{\chi}] e^{iS_{\mathrm{eff}}(\boldsymbol{\chi})}, \tag{5.25}$$

we obtain the expression for the effective action:

$$S_{\mathrm{eff}}(\boldsymbol{\chi}) = -\int dt\sum_{\boldsymbol{r}}\frac{1}{2}\boldsymbol{\chi}(\boldsymbol{r},t)^2 - i\ln\det\left(i\frac{\partial}{\partial t}+\mu - M(\boldsymbol{\chi})\right), \tag{5.26}$$

5.3.2 From the Hubbard model to the spin-fermion model

One way to implement a mean-field approach in this framework consists in using the stationary-phase approximation. The stationary-phase condition reads:

$$\begin{aligned}
0 = \frac{\delta S_{\text{eff}}}{\delta \chi_a(\boldsymbol{r},t)} &= -\chi_a(\boldsymbol{r},t) - i\frac{\delta}{\delta\chi_a(\boldsymbol{r},t)} \ln\det\left(i\frac{\partial}{\partial t} + \mu - M(\chi)\right) \\
\Leftrightarrow \chi_a(\boldsymbol{r},t) &= -i\frac{\delta}{\delta\chi_a(\boldsymbol{r},t)} \operatorname{Tr}\left[\ln\left(i\frac{\partial}{\partial t} + \mu - M(\boldsymbol{\chi})\right)\right] \\
&= i \operatorname{Tr}\left[\frac{1}{i\dfrac{\partial}{\partial t} + \mu - M(\boldsymbol{\chi})}\frac{\delta M(\chi)}{\delta\chi_a(\boldsymbol{r},t)}\right] \\
&= i\,\langle \boldsymbol{r}\,t\alpha|\frac{1}{i\dfrac{\partial}{\partial t} + \mu - M(\boldsymbol{\chi})}\frac{\delta M(\chi)}{\delta\chi_a(\boldsymbol{r},t)}|\boldsymbol{r}\,t\alpha\rangle \\
&= i\,\langle \boldsymbol{r}\,t\alpha|\frac{1}{i\dfrac{\partial}{\partial t} + \mu - M(\boldsymbol{\chi})}|\boldsymbol{r}\,t\beta\rangle\ \langle \boldsymbol{r}\,t\beta|\frac{\delta M(\chi)}{\delta\chi_a(\boldsymbol{r},t)}|\boldsymbol{r}\,t\alpha\rangle \\
&= i\sqrt{\frac{U}{3}}\,\langle \boldsymbol{r}\,t\alpha|\frac{1}{i\dfrac{\partial}{\partial t} + \mu - M(\boldsymbol{\chi})}|\boldsymbol{r}\,t\beta\rangle\,\tau^a_{\beta\,\alpha}
\end{aligned} \tag{5.27}$$

Where use was made of the identity $\ln\det(A) = \operatorname{Tr}\ln(A)$, valid for any matrix whose logarithm is defined, and of Eq. (5.24).

This equation describes the nature of the bosonic field interacting with the fermions in the saddle-point approximation. It is possible to get a better physical insight into the nature of this field with the following observation. The expression $\langle \boldsymbol{r}\,t\alpha|\frac{1}{i\frac{\partial}{\partial t} + \mu - M(\boldsymbol{\chi})}|\boldsymbol{r}\,t\beta\rangle$ from Eq. (5.27) can be recognized as the expression for the matrix element of the one-particle Green's function for fermions interacting with a background field $\boldsymbol{\chi}(\boldsymbol{r},t)$:

$$G_{\alpha\,\beta}(\boldsymbol{r}\,t;\boldsymbol{r'}\,t';\boldsymbol{\chi}) \equiv -i\,\langle \boldsymbol{r}\,t\alpha|\frac{1}{i\frac{\partial}{\partial t} + \mu - M(\boldsymbol{\chi})}|\boldsymbol{r'}\,t'\,\beta\rangle\,.$$

In such a system, the local magnetic moment at point $\boldsymbol{r}$ and time t is given by

$$\langle \boldsymbol{m}(\boldsymbol{r},\,t)\rangle = G_{\alpha\,\beta}(\boldsymbol{r}\,t;\boldsymbol{r}\,t;\boldsymbol{\chi})\frac{\boldsymbol{\tau}_{\alpha\,\beta}}{2}.$$

The condition in Eq. (5.27) may therefore be written as

$$\boldsymbol{\chi}(\boldsymbol{r},t) = -\sqrt{\frac{4U}{3}}\,\langle \boldsymbol{m}(\boldsymbol{r},\,t)\rangle\,.$$

This allows us to physically identify the bosonic field introduced via the Hubbard-Stratonovich transformation with the local magnetic moment. It must be noted though that in the context of the one-band Hubbard model, this approach cannot be quantitatively justified, insofar as it is not controlled by any small parameter other than $\hbar$, which makes it essentially a semi-classical approximation. Moreover, one has to keep in mind that there is a large amount of arbitrariness in the way the Hamiltonian from Eq. (3.3) is rearranged, for the purpose of introducing the bosonic field of Eq. (5.18). Different equivalent expressions for this starting Hamiltonian lead to functional integral representations which are

all valid, but eventually involve different fields, and correspond to different mean-field approximations. The choice of the auxiliary field representation, and its validity ultimately remains guided by the physics of the problem at hand[120]. The above derivation thus does not constitute a quantitative derivation of the spin-fermion model, but gives us a formal justification for the identification of the fluctuations of the auxiliary field $\boldsymbol{\chi}(\boldsymbol{r},t)$, with the real spin fluctuations of the system. In turn, this allows us to come back to a Hamiltonian representation of the system, in which we include the free fermions which live near the Fermi surface, spin fluctuations, and the interactions between these two degrees of freedom[129]:

$$\mathcal{H} = \sum_{\boldsymbol{k},\alpha} \boldsymbol{v}_k(\boldsymbol{k}-\boldsymbol{k}_F) c^\dagger_{\boldsymbol{k},\,\alpha} c_{\boldsymbol{k},\,\alpha} + \sum_{\boldsymbol{q}} \chi_0^{-1}(\boldsymbol{q}) \boldsymbol{S}_{\boldsymbol{q}} \boldsymbol{S}_{-\boldsymbol{q}} + g \sum_{\boldsymbol{q},\boldsymbol{k},\alpha,\beta} c^\dagger_{\boldsymbol{k}+\boldsymbol{q},\,\alpha} \tau_{\alpha\beta} c_{\boldsymbol{k},\,\beta} \cdot \boldsymbol{S}_{-\boldsymbol{q}}, \quad (5.28)$$

where g is the ($\boldsymbol{q}$-independent) coupling constant representing the strength of the interaction between fermionic spins and the collective degrees of freedom described by bosonic variables $\boldsymbol{S}_{\boldsymbol{q}}$, and $\chi_0^{-1}(\boldsymbol{q})$ is the static component of the bare spin susceptibility. In this framework, the spin fluctuations may be treated self-consistently, or considered as an input for the theory, and fitted from experimental data. In particular, neutron data can provide a suitable input for the spin fluctuation propagator.

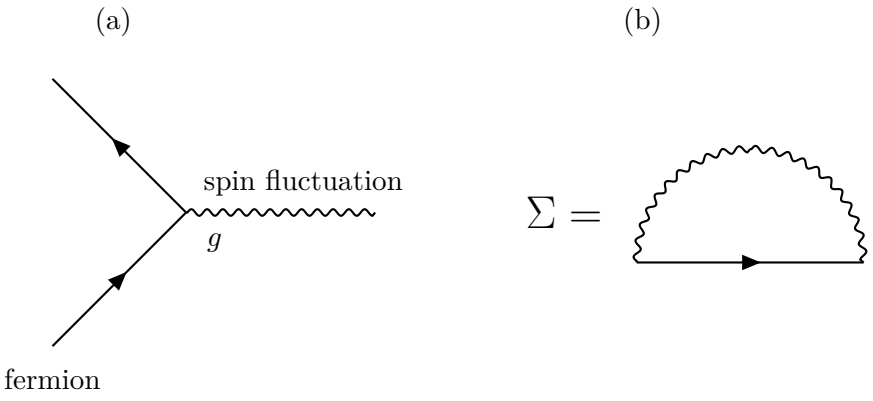

Figure 5.1: (a): Interaction vertex associated to the coupling between the fermionic spin and the spin fluctuations, with coupling constant g. (b) Diagrammatic representation of the equation for the self-energy within the spin-fermion model. The fermionic line represents the dressed fermionic Green's function.

This approach will be used in the study of the anomalies in the electronic dispersion of the cuprate superconductors, presented in Chapter 8. Starting from the interaction Hamiltonian $\sim g \sum_{\boldsymbol{q},\boldsymbol{k},\alpha,\beta} c^\dagger_{\boldsymbol{k}+\boldsymbol{q},\,\alpha} \tau_{\alpha\beta}\, c_{\boldsymbol{k},\,\beta} \cdot \boldsymbol{S}_{-\boldsymbol{q}}$, a diagrammatic perturbation approach can be used [130], as illustrated in Fig. 5.1. Writing the spin susceptibility in Matsubara frequencies as $\frac{1}{N}\chi_{\rm SF}(\boldsymbol{q}, i\hbar\nu)$, and neglecting vertex corrections, the evaluation of the diagram presented in panel (b) leads to the expression for the self-energy $\Sigma(\boldsymbol{k}, iE)$

$$\Sigma(\boldsymbol{k}, iE) = \frac{g^2}{\beta N} \sum_{\boldsymbol{k'},\, iE'} \chi_{\rm SF}\big(\boldsymbol{k}-\boldsymbol{k'},\, iE - iE'\big) \mathcal{G}\big(\boldsymbol{k'}, iE'\big). \quad (5.29)$$

Together with the expression for the fermionic propagator

$$\mathcal{G}(\boldsymbol{k}, iE) = [iE - (\epsilon_{\boldsymbol{k}} - \mu) - \Sigma(\boldsymbol{k}, iE)]^{-1}, \quad (5.30)$$

we obtain a self-consistent system of equations, which can be solved iteratively. In this framework, χ_{SF} and g are inputs of the theory. The form of χ_{SF} is inferred from neutron scattering data, and g is chosen so that other observables described by the model, e.g. the size of the superconducting gap, are consistent with experiment.

Chapter 6

Dynamical Mean Field Theory

The Dynamical Mean Field Theory (DMFT) is a technique whose development relied on the essential contributions by Metzner and Vollhardt [131], Metzner [132], Müller-Hartmann [133], Georges and Kotliar [100], and Jarrell [109]. In this chapter, we present the theoretical framework underlying this theory, which has been used to obtain the results on the physics of excitonic condensation presented in Chapter 9.

6.1 Introduction

DMFT has been developing rapidly since the first days of its introduction, and many reference articles, reviews and PhD thesis are available [132, 134–138]. The derivation we present here is called the "cavity" method, from the name of an approach extensively used in classical statistical mechanics. Georges et al. applied its concepts to the derivation of the DMFT equations [10]. This is by no means the only possible way to proceed, but has the advantage of providing a straightforward physical interpretation of the approach, and also of highlighting the links between the DMFT approach and other well-known mean field theories. Another popular approach is based on the expansion of the free energy and the correlation functions around the atomic limit. The latter was initiated by the pioneering work of Metzner and Vollhardt [131], who demonstrated the simplifications brought about by the $d \to \infty$ limit applied to the Hubbard model.

DMFT is a mean-field theory, and can be viewed as an extension of the well known mean field approach applied to the Ising model. For example, the mean-field approximation of the Ising model becomes exact in the limit of infinite coordination, and the same is true for DMFT. Intuitively, this can be understood because in the limit of infinite coordination, the neighbors of a given site are seen, from this site, as a continuous "bath", which indeed corresponds to a mean-field.

In the cavity method, a particular site of the lattice is singled out, e.g., site o, indexed by $i = 0$. The degrees of freedom of all the other sites are then integrated out, which allows the derivation of an effective Hamiltonian for site o. This Hamiltonian may be mapped onto a single-impurity Anderson model. The comparison is most easily expressed in the functional integral representation of these effective models. Thus, we first illustrate the way the non-desired degrees of freedom are integrated out in the framework of the Lagrangian representation of the physics of a few models, following the concepts developed in Sec. 5. We first examine the case of a non interacting system, in order to identify how the Green's function is present inside the Lagrangian formulation. Then, we derive effective models for the single impurity Anderson model and the Hubbard model in the limit of

infinite coordination, and demonstrate how they are related. This will allow us to develop a system of self-consistent equations, which can be iterated to find the solution of the problem at hand, provided the impurity problem can be solved. The numerical approach to the solution of the impurity problem will be the object of Sec. 7.

6.2 Lagrangian expression for selected models

6.2.1 Non-interacting system

As a preparation for the study of the Anderson and Hubbard models, it is useful to evaluate the action for a system of non-interacting particles described by a one-body Hamiltonian. In this section we follow the presentation by Negele and Orland [120].

For convenience, we choose a basis in which H_0 is diagonal. The discrete expression for the functional integral form of the partition function follows from Eq. (5.16):

$$\begin{aligned} H_0 &= \sum_\alpha \epsilon_\alpha a_\alpha^\dagger a_\alpha, \\ Z_0 &= \lim_{M\to\infty} \prod_\alpha \left[\prod_{k=1}^{n} \int d\phi_{\alpha,k}^* d\phi_{\alpha,k} e^{-\sum_{j,k=1}^{M} \phi_{\alpha,j}^* S_{jk}^{(\alpha)} \phi_{\alpha,k}} \right] \\ &= \lim_{M\to\infty} \prod_\alpha \det S^{(\alpha)}, \end{aligned} \tag{6.1}$$

where

$$S^{(\alpha)} = \begin{bmatrix} 1 & 0 & 0 & \cdots & 0 & a \\ -a & 1 & 0 & \ddots & 0 & 0 \\ 0 & -a & 1 & \ddots & 0 & 0 \\ 0 & 0 & -a & \ddots & 0 & 0 \\ \vdots & 0 & 0 & \ddots & 1 & 0 \\ \vdots & 0 & 0 & \ddots & -a & 1 \end{bmatrix}, \quad \phi_\alpha = \begin{bmatrix} \phi_{\alpha,1} \\ \phi_{\alpha,2} \\ \vdots \\ \phi_{\alpha,M}, \end{bmatrix} \tag{6.2}$$

$$a = 1 - \frac{\beta}{M}(\epsilon_\alpha - \mu),$$

with the convention that the time index increases with increasing row and column index.

The determinant of $S^{(\alpha)}$ may be evaluated by expanding by minors along the first row:

$$\begin{aligned} \lim_{M\to\infty} \det S^{(\alpha)} &= \lim_{M\to\infty} \left[1 + (-1)^{M-1} a (-a)^{M-1} \right] = \lim_{M\to\infty} \left[1 + a^M \right] \\ &= \lim_{M\to\infty} \left[1 + \left(1 - \frac{\beta(\epsilon_\alpha - \mu)}{M} \right)^M \right] \\ &= 1 + e^{-\beta(\epsilon_\alpha - \mu)}. \end{aligned} \tag{6.3}$$

Substitution into Eq. (6.1) yields the familiar expression for the partition function of a system of non-interacting particles:

$$Z_0 = \prod_\alpha \left(1 + e^{-\beta(\epsilon_\alpha - \mu)} \right).$$

Equipped with these results, we may turn to the evaluation of the single-particle Green's function for non-interacting particles, $\mathcal{G}_0$. Let τ_q correspond to the time $q\frac{\beta}{M}$, and τ_r correspond to the time $r\frac{\beta}{M}$, for integers q and r. Then,

$$\begin{aligned}
\mathcal{G}_0(\alpha\tau_q|\gamma\tau_r) &= -\left\langle T_\tau a_\alpha(\tau_q)a^\dagger_\gamma(\tau_r)\right\rangle \\
&= -\frac{1}{Z_0}\,\mathrm{Tr}\left[e^{-\beta(H-\mu N)}T_\tau a_\alpha(\tau_q)a^\dagger_\gamma(\tau_r)\right] \\
&= -\frac{1}{Z_0}\lim_{M\to\infty}\int\prod_\delta\prod_{k=1}^{M}d\phi^*_{\delta,k}d\phi_{\delta,k}e^{-\sum\limits_{j,k=1}^{M}\phi^*_{\delta,j}S^{(\delta)}_{jk}\phi_{\delta,k}}\phi_{\alpha,q}\phi^*_{\gamma,r} \\
&= -\delta_{\alpha\gamma}\frac{\int\prod\limits_k d\phi^*_k d\phi_k e^{-\sum\limits_{j,k=1}^{M}\phi^*_j S^{(\alpha)}_{jk}\phi_k}\phi_q\phi^*_r}{\int\prod\limits_k d\phi^*_k d\phi_k e^{-\sum\limits_{j,k=1}^{M}\phi^*_j S^{(\alpha)}_{jk}\phi_k}} \\
&= -\delta_{\alpha\gamma}\frac{\partial^2}{\partial J^*_q\partial J_r}\frac{\int\prod\limits_k d\phi^*_k d\phi_k e^{-\sum\limits_{j,k=1}^{M}\phi^*_j S^{(\alpha)}_{jk}\phi_k+\sum i(J^*_i\phi_i+\phi^*J_i)}}{\int\prod\limits_k d\phi^*_k d\phi_k e^{-\sum\limits_{j,k=1}^{M}\phi^*_j S^{(\alpha)}_{jk}\phi_k}}\Bigg|_{J=J^*=0} \\
&= -\delta_{\alpha\gamma}\frac{\partial^2}{\partial J^*_q\partial J_r}e^{\sum\limits_{j,k=1}^{M}J^*_j S^{(\alpha)^{-1}}_{jk}J_k}\Bigg|_{J=J^*=0} \\
&= -\delta_{\alpha\gamma}S^{(\alpha)^{-1}}_{qr},
\end{aligned} \tag{6.4}$$

where repeated use was made of Eq. (A.1).

The matrix S is defined in Eq. (6.2). It is straightforward to check that its inverse is given by the following expression:

$$S^{(\alpha)^{-1}} = \frac{1}{1+a^M}\begin{bmatrix} 1 & -a^{M-1} & -a^{M-2} & \cdots & -a \\ a & 1 & -a^{M-1} & \cdots & -a^2 \\ a^2 & a & 1 & \cdots & -a^3 \\ \vdots & \ddots & \ddots & \ddots & \vdots \\ a^{M-3} & \ddots & \ddots & \ddots & -a^{M-2} \\ a^{M-2} & a^{M-3} & \ddots & \ddots & -a^{M-1} \\ a^{M-1} & a^{M-2} & a^{M-3} & \cdots & 1 \end{bmatrix}. \tag{6.5}$$

For $q \geq r$, we have

$$\begin{aligned}
\lim_{M\to\infty} S_{qr}^{(\alpha)^{-1}} &= \lim_{M\to\infty} \frac{a^{q-r}}{1+a^M} \\
&= \lim_{M\to\infty} \left(1 - \frac{\beta}{M}(\epsilon_\alpha - \mu)\right)^{q-r} \left(1 - \frac{1}{\left(1 - \frac{\beta}{M}(\epsilon_\alpha - \mu)\right)^{-M} + 1}\right) \\
&= e^{-(\epsilon_\alpha-\mu)(\tau_q-\tau_r)}\left(1 - \frac{1}{e^{\beta(\epsilon_\alpha-\mu)}+1}\right) \\
&= e^{-(\epsilon_\alpha-\mu)(\tau_q-\tau_r)}(1-n_\alpha),
\end{aligned} \tag{6.6}$$

where n_α it the Fermi-Dirac distribution:

$$n_\alpha = \frac{1}{1+e^{\beta(\epsilon_\alpha-\mu)}}.$$

The result for $q \leq r$ is obtained similarly:

$$\begin{aligned}
\lim_{M\to\infty} S_{qr}^{(\alpha)^{-1}} &= \lim_{M\to\infty} -\frac{a^{M+q-r}}{1+a^M} \\
&= \lim_{M\to\infty} \left(1 - \frac{\beta}{M}(\epsilon_\alpha - \mu)\right)^{q-r} \left(\frac{-1}{\left(1 - \frac{\beta}{M}(\epsilon_\alpha - \mu)\right)^{-M} + 1}\right) \\
&= -e^{-(\epsilon_\alpha-\mu)(\tau_q-\tau_r)} n_\alpha.
\end{aligned} \tag{6.7}$$

With these results, the case in which creation and annihilation operators act at equal times need to be considered. Using the fact that the time-ordered product is defined to be equal to a normal ordered product at equal time, we find that the time-ordered product may be written $T_\tau\Big[a_\beta(\tau)a_\alpha^\dagger(\tau)\Big] = -a_\alpha^\dagger(\tau)a_\beta(\tau) = a_\beta(\tau)a_\alpha^\dagger(\tau) - \delta_{\alpha\beta}$, in which case the evolution operator gives rise to the term

$$\begin{aligned}
&|\phi_{k+1}\rangle\langle\phi_{k+1}|\, e^{-\epsilon H} a_\alpha\, |\phi_k\rangle\langle\phi_k|\, a_\beta^\dagger e^{-\epsilon H}\, |\phi_{k-1}\rangle\langle\phi_{k-1}| \dots \\
&\qquad = |\phi_{k+1}\rangle\, e^{-\epsilon H\left(\phi_{k+1}^*,\phi_k\right)} \phi_{\alpha,k}\phi_{\beta,k}^* e^{-\epsilon H(\phi_k^*,\phi_{k-1})}\, \langle\phi_{k-1}| \dots,
\end{aligned}$$

where ϕ_α and ϕ_β are evaluated at equal times. Thus, following the derivation of Eq. (6.4), $\Big\langle T_\tau a_\alpha(\tau)a_\alpha^\dagger(\tau)\Big\rangle = S_{r,r}^{-1} - 1 = -n_\alpha$.

Combining the obtained results, the single-particle Green's function can be written as

$$\begin{aligned}
\mathcal{G}_0\big(\alpha\tau|\alpha'\tau'\big) &= -\Big\langle T_\tau a_\alpha(\tau)a_{\alpha'}^\dagger(\tau')\Big\rangle \\
&= -\delta_{\alpha\alpha'} e^{-(\epsilon_\alpha-\mu)(\tau-\tau')}\big\{\theta\big(\tau-\tau'-\eta\big)(1-n_\alpha) - \theta\big(\tau-\tau'+\eta\big)n_\alpha\big\},
\end{aligned} \tag{6.8}$$

where η is a positive infinitesimal which allows the correct treatment of the case $\tau = \tau'$. With this expression, it is easily verified that

$$-\sum_{\alpha_2}\left[\delta_{\alpha_1\alpha_2}(\partial_{\tau_2} - \mu) + \langle\alpha_1|H_0|\alpha_2\rangle\right]\mathcal{G}_0(\alpha_2\tau_2|\alpha_3\tau_3) = \delta_{\alpha_1\alpha_2}\delta(\tau_2-\tau_3).$$

Thus, for a non-interacting system, we get

$$\mathcal{G}_0^{-1}(\alpha_1\tau_1|\alpha_2\tau_2) = -[\delta_{\alpha_1\alpha_2}(\partial_{\tau_1} - \mu) + \langle\alpha_1|H_0|\alpha_2\rangle]\delta(\tau_1 - \tau_2).$$

Identifying the relevant terms of the expression above with those of Eq. (5.18), and using the fact that the diagonal basis of the non-interacting Hamiltonian has been used, we find that the action for the non-interaction system may be written as

$$\begin{aligned} S[\phi^*_\alpha(\tau),\, \phi_\alpha(\tau)] &= \int_0^\beta d\tau\, L(\phi^*_\alpha(\tau),\, \phi_\alpha(\tau)) \\ &\equiv -\int_0^\beta d\tau \int_0^\beta d\tau' \left[\sum_\alpha \phi^*_\alpha(\tau)\mathcal{G}_0^{-1}\big(\alpha;\tau-\tau'\big)\phi_\alpha(\tau')\right], \end{aligned} \tag{6.9}$$

where $L(\phi^*_\alpha(\tau),\, \phi_\alpha(\tau))$ is the imaginary time Lagrangian for the model.

6.2.2 Single impurity Anderson model

The Hamiltonian of the single impurity Anderson model, given by Eqs. (3.6-3.7), can be written as:

$$\begin{aligned} H &= H_\mu + H_U + H_{\text{bath}} + H_{\text{mix}}, \\ H_\mu &= -\mu \sum_\sigma \hat{n}_\sigma, \\ H_U &= U\hat{n}_\uparrow\hat{n}_\downarrow, \\ H_{\text{mix}} &= \sum_{\boldsymbol{k}\sigma} V_{\boldsymbol{k}\sigma} c^\dagger_\sigma a_{\boldsymbol{k}\sigma} + \text{H.c.}, \\ H_{\text{bath}} &= \sum_{\boldsymbol{k}\sigma} \epsilon_{\boldsymbol{k}} a^\dagger_{\boldsymbol{k}\sigma} a_{\boldsymbol{k}\sigma}, \end{aligned} \tag{6.10}$$

where the operators $\hat{n}_\sigma$ and $c^{(\dagger)}_\sigma$ act on the impurity site, whose Hilbert space is spanned by the four states $|0\rangle, |\uparrow\rangle, |\downarrow\rangle, |\uparrow\downarrow\rangle$. We introduce the local part of the Hamiltonian

$$H_{\text{loc}} = H_\mu + H_U,$$

which describes the on site interaction, and the influence of the chemical potential, on the impurity site. The impurity is coupled to a bath described by H_{bath}, via the terms present in H_{mix}.

As presented in Sec. 5.2.1, we may represent the system with the help of a path integral which involves the action along all the possible paths. In the case of the Hamiltonian of Eq. (6.10), the expression derived in Eq. (5.18) takes the form

$$\begin{aligned} S &= \int_0^\beta d\tau \sum_\alpha (\phi^*_\alpha \partial_\tau \phi_\alpha + H(\phi^*_\alpha, \phi_\alpha)) \\ &= \int_0^\beta d\tau \sum_\alpha [\phi^*_\alpha(\partial_\tau - \mu)\phi_\alpha + H_U(\phi^*_\alpha, \phi_\alpha) + H_{\text{mix}}(\phi^*_\alpha, \phi_\alpha) + H_{\text{bath}}(\phi^*_\alpha, \phi_\alpha)]. \end{aligned}$$

In this expression, the bath operators, even though they are coupled to the impurity site operators, appear only in quadratic terms, and may thus be integrated out, leaving us with the impurity site operators, on which we wish to focus. The terms coming from $H_{\rm mix}(\phi^*,\phi)$ and $H_{\rm bath}(\phi^*,\phi)$ can be handled if we use the expression for a Gaussian integral over Grassmann variables, given in Eq. (A.1), with $A_{ij}\equiv\delta_{ij}(\partial_\tau-\epsilon_j)$, and $J\equiv V_l\phi_0$, and $(\phi^*_{0\uparrow},\phi_{0\uparrow},\phi^*_{0\downarrow},\phi_{0\downarrow})$ the four Grassmann generators associated with the impurity site. The term $\det A$ coming from the expression for the Gaussian integral reduces to an additive term $S_{\rm bath}$ in the action, which we can drop in the partition function expression, since it is tantamount to a shift in the free energy. With this, we obtain:

$$
\begin{aligned}
S &= S_{\rm eff}+S_{\rm bath},\\
Z &= \int\prod_\sigma \mathcal{D}\phi^*_{0\sigma}\mathcal{D}\phi_{0\sigma}e^{-S_{\rm eff}},\\
S_{\rm eff} &= \int_0^\beta d\tau\left(\sum_\sigma\phi^*_{0\sigma}\left[(\partial_\tau-\mu)+\sum_{lm}V_l^*\Big[(\partial_\tau-\epsilon_l)^{-1}\Big]_{lm}V_m\right]\phi_{0\sigma}+H_U(\phi^*_{0\uparrow},\phi^*_{0\downarrow},\phi_{0\uparrow},\phi_{0\downarrow})\right)\\
&= \int_0^\beta d\tau\left(\sum_\sigma\phi^*_{0\sigma}\left[(\partial_\tau-\mu)+\sum_{l}V_l^*\Big[(\partial_\tau-\epsilon_l)^{-1}\Big]_{ll}V_l\right]\phi_{0\sigma}+H_U(\phi^*_{0\uparrow},\phi^*_{0\downarrow},\phi_{0\uparrow},\phi_{0\downarrow})\right),
\end{aligned}
$$

where the diagonal nature of the bath Hamiltonian was used to obtain the last line.

The non interacting part of this action has the form obtained in Eq. (6.9), with the following form of the inverse bare propagator:

$$
\begin{aligned}
\mathcal{G}_0^{-1}(i\omega_n)^{\rm AM} &= i\omega_n+\mu-\int_{-\infty}^{+\infty}d\omega\frac{\Delta(\omega)}{i\omega_n-\omega},\\
\text{where } \Delta(\omega)&\equiv\sum_{l\sigma}|V_l|^2\delta(\omega-\epsilon_l).
\end{aligned}
\tag{6.11}
$$

We recognize in the term $\Delta(\omega)$ above the expression for the quantity $\Delta_d(\omega)$ of Eq. (3.12), obtained by the equation of motion method applied to the Anderson model.

Considering that any problem may be studied in its Lagrangian or Hamiltonian representation, the above expression is helpful, insofar as it establishes the correspondence between the parameters of the Hamiltonian representation of the single impurity Anderson model (the sets of ϵ_l and V_l), and the parameters of its Lagrangian representation (the form of the bare propagator $\mathcal{G}_0^{-1}(i\omega_n)$ determining $S_{\rm eff}$).

6.2.3 Hubbard model

The Hamiltonian of the Hubbard model, Eq. (3.2) can be written as:

$$
\begin{aligned}
H &= H_0+\Delta H+H^{(o)},\\
H_0 &= U\hat n_{0\uparrow}\hat n_{0\downarrow}-\mu\sum_\sigma c^\dagger_{0\sigma}c_{0\sigma},\\
\Delta H &= -\sum_{\langle i\rangle,\sigma}t_{i0}\Big(c^\dagger_{0\sigma}c_{i\sigma}+c^\dagger_{i\sigma}c_{0\sigma}\Big),\\
H^{(o)} &= -\sum_{\langle i\neq0,j\neq0\rangle,\sigma}t_{ij}\Big(c^\dagger_{i\sigma}c_{j\sigma}+\text{H. c.}\Big)+U\sum_{i\neq0}\hat n_{i\uparrow}\hat n_{i\downarrow}-\mu\sum_{i\neq0\sigma}c^\dagger_{i\sigma}c_{i\sigma},
\end{aligned}
\tag{6.12}
$$

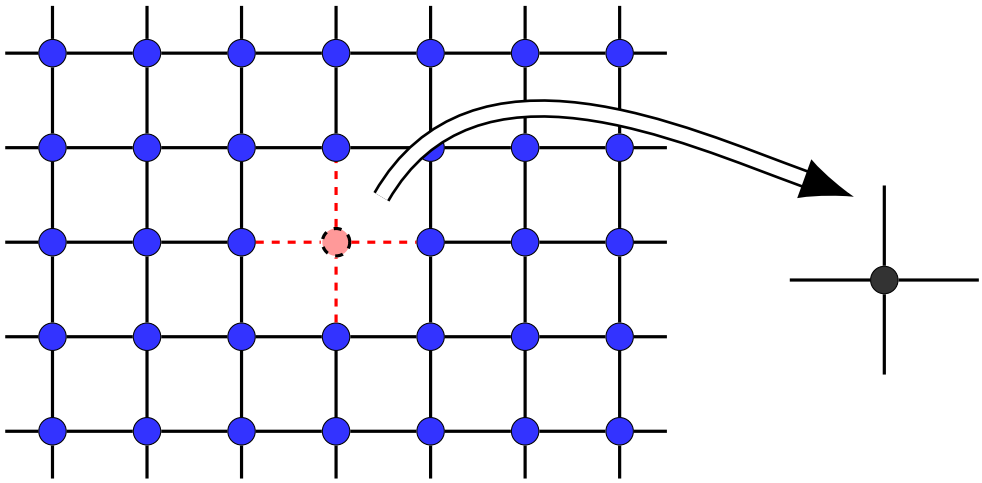

Figure 6.1: In this schematic representation, the original lattice point of view is shown on the left. One site (in red) is singled out, then removed, creating a cavity in the lattice. The single site is then considered as an impurity, while the remainder of the sites are viewed as a bath, whose electrons hop into, or out from, the impurity.

where the hopping terms entering ΔH are those connecting the site 0 with its nearest neighbors, and we assume a grand-canonical ensemble with the chemical potential μ. This splitting of the Hamiltonian corresponds to the situation depicted in Fig. 6.1, in which one site, with index 0, is singled out. We consider the terms of the Hamiltonian which contain only operators acting on the site 0 (H_0), those which contain only operators acting on sites different from the site 0 ($H^{(o)}$, the cavity Hamiltonian), and those which connect the site 0 with other sites (ΔH).

As discussed in Sec. 5.2.1 and above, we may represent the system with the help of a path integral. Using the Hamiltonian of Eq. (6.12), and the splitting it introduces, the expression derived in Eq. (5.18) takes the form

$$
\begin{aligned}
S = S_0 + \Delta S + S^{(o)} &= \int_0^\beta d\tau \sum_\alpha (\phi^*_\alpha \partial_\tau \phi_\alpha + H(\phi^*_\alpha, \phi_\alpha)), \\
S_0 &= \int_0^\beta d\tau \left[\sum_\sigma \phi^*_{0\sigma}(\partial_\tau - \mu)\phi_{0\sigma} + H_U(\phi^*_{0\uparrow}, \phi^*_{0\downarrow}, \phi_{0\uparrow}, \phi_{0\downarrow}) \right], \\
\Delta S &= -\int_0^\beta d\tau \left[\sum_{i\sigma} t_{i0}(\phi^*_{i\sigma}\phi_{0\sigma} + \phi^*_{0\sigma}\phi_{i\sigma}) \right], \\
S^{(o)} &= \int_0^\beta d\tau \Bigg[\sum_{i\neq 0,\,\sigma} \phi^*_{i\sigma}(\partial_\tau - \mu)\phi_{i\sigma} \\
&\quad - \sum_{i\neq 0,\, j\neq 0,\,\sigma} t_{ij}\left(\phi^*_{i\sigma}\phi_{j\sigma} + \phi^*_{j\sigma}\phi_{i\sigma}\right) + \sum_{i\neq 0} H_U(\phi^*_{i\uparrow}, \phi^*_{i\downarrow}, \phi_{i\uparrow}, \phi_{i\downarrow}) \Bigg],
\end{aligned}
\tag{6.13}
$$

From this expression, we wish to build an effective action, by explicitly integrating all

degrees of freedom other than those of the site 0:

$$\frac{1}{Z_{\text{eff}}} e^{-S_{\text{eff}}\left[\phi^*_{0\uparrow},\phi^*_{0\downarrow},\phi_{0\uparrow},\phi_{0\downarrow}\right]} \equiv \frac{1}{Z}\int \prod_{i\neq 0,\sigma} \mathcal{D}\phi^*_{i\sigma}\mathcal{D}\phi_{i\sigma} e^{-S\left[\phi^*_{i\sigma},\phi_{i\sigma}\right]}. \tag{6.14}$$

In order to achieve this, we use an approach inspired by the seminal work of Metzner [132]. In that work, Metzner considers the Hubbard Hamiltonian starting from the atomic limit, and treats the kinetic energy terms as the perturbation. We use a similar functional expansion, applied to the part of the exponent that mixes the site 0 with the other sites, which proceeds as follows:

$$\begin{aligned}
&\int \prod_{i\neq 0,\sigma} \mathcal{D}\phi^*_{i\sigma}\mathcal{D}\phi_{i\sigma} e^{-S\left[\phi^*_{i\sigma},\phi_{i\sigma}\right]} \\
&= \int\limits_{\phi_{i\sigma}(\beta)=-\phi_{i\sigma}(0)} \mathcal{D}[\phi^*_{i\sigma},\,\phi_{i\sigma}]_{i\neq 0} \exp\left\{-\int_0^\beta d\tau \left[\sum_{i\neq 0,\sigma} \phi^*_{i\sigma}\left(\frac{\partial}{\partial\tau}\right)\phi_{i\sigma} + H^{(o)}[\phi^*_{i\sigma},\,\phi_{i\sigma}]\right]\right\} \\
&\times \exp\left\{-\int_0^\beta d\tau \left[\sum_{i\sigma} t_{i0}(\phi^*_{i\sigma}\phi_{0\sigma} + \phi^*_{0\sigma}\phi_{i\sigma})\right]\right\} \\
&\times \exp\left\{-S_0\left[\phi^*_{0\uparrow},\phi^*_{0\downarrow},\phi_{0\uparrow},\phi_{0\downarrow}\right]\right\},
\end{aligned} \tag{6.15}$$

in which the part of the integral to be explicitly integrated reads

$$\begin{aligned}
I = &\int\limits_{\phi_{i\sigma}(\beta)=-\phi_{i\sigma}(0)} \mathcal{D}[\phi^*_{i\sigma},\,\phi_{i\sigma}]_{i\neq 0} \exp\left\{-\int_0^\beta d\tau \left[\sum_{i\neq 0\sigma} \phi^*_{i\sigma}\left(\frac{\partial}{\partial\tau}\right)\phi_{i\sigma} + H^{(o)}[\phi^*_{i\sigma},\,\phi_{i\sigma}]\right]\right\} \\
&\times \exp\left\{-\int_0^\beta d\tau \left[\sum_{i\sigma} t_{i0}(\phi^*_{i\sigma}\phi_{0\sigma} + \phi^*_{0\sigma}\phi_{i\sigma})\right]\right\}.
\end{aligned} \tag{6.16}$$

In this expression, we recognize the very definition of the thermal average of the quantity in the last line [120], for the system described by the cavity Hamiltonian $H^{(o)}$:

$$I = \left\langle e^{-\int_0^\beta d\tau \sum_{i\sigma} t_{i0}\left(\phi^*_{i\sigma}\phi_{0\sigma}+\phi^*_{0\sigma}\phi_{i\sigma}\right)} \right\rangle_{(o)} \tag{6.17}$$

At this point, the aforementioned functional expansion may be carried out, applied to the exponential in the bracket [132]. We introduce $\eta_{i\sigma} \equiv t_{i0}\phi_{0\sigma}$ and obtain

$$I = \sum_{n=1}^{\infty} I_n, \tag{6.18}$$

with the n^{th} order term of this expansion given by

$$I_n \equiv \frac{(-1)^n}{n!} \sum_{\substack{i_1\ldots i_n,\\ j_1\ldots j_n,\\ \sigma_1\ldots\sigma_n}} \int_0^\beta \left(\prod_{i=1}^n d\tau_i\right) \eta^*_{i_1\sigma_1}\ldots\eta^*_{i_n\sigma_n}\eta_{j_1\sigma_1}\ldots\eta_{j_n\sigma_n} \left\langle \phi^*_{i_1\sigma_1}\ldots\phi^*_{i_n\sigma_n}\phi_{j_1\sigma_1}\ldots\phi_{j_n\sigma_n}\right\rangle_{(o)}. \tag{6.19}$$

We have used the fact that an integral over Grassmann variables is non zero only if each of the variables, over which the integration is carried out, is present in the integrand. By definition, the ensemble average $\left\langle \phi^*_{i_1\sigma_1} \dots \phi^*_{i_n\sigma_n} \phi_{j_1\sigma_1} \dots \phi_{j_n\sigma_n} \right\rangle_{(o)}$ is the n-particle Green's function of the cavity system:

$$\begin{aligned} \mathcal{G}^{(o)}(j_1\tau_1\sigma_1,\, j_2\tau_2\sigma_2,\, \dots,\, j_n\tau_n\sigma_n | i_1\tau'_1\sigma_1,\, i_2\tau'_2\sigma_2,\, \dots,\, i_n\tau'_n\sigma_n) \equiv \\ \left\langle \phi^*_{i_1\sigma_1}(\tau'_1) \dots \phi^*_{i_n\sigma_n}(\tau'_n) \phi_{j_1\sigma_1}(\tau_1) \dots \phi_{j_n\sigma_n}(\tau_n) \right\rangle_{(o)}, \end{aligned} \tag{6.20}$$

evaluated for $\tau'_i = \tau_i$, $\sigma_i = \sigma'_i$. At this point, we can introduce the decomposition of the Green's function in terms of cumulants (connected Green's functions) $C^{(o)}_m$. Each term of the sums involved in such a decomposition corresponds to a partition of $(1, \dots, n, 1', \dots, n')$ in subsets containing equal numbers of primed and unprimed variables [120], e.g.:

$$\begin{aligned} G^{(o)}_1(1|1') &= C^{(o)}_1(1|1'), \\ G^{(o)}_2(1,2|1',2') &= C^{(o)}_2(1,2|1',2') + C^{(o)}_1(1|1')C^{(o)}_1(2|2') - C^{(o)}_1(1|2')C^{(o)}_1(2|1'). \end{aligned} \tag{6.21}$$

In these expressions, the sign attached to each product is determined by the parity of the permutation of the primed variables with respect to the unprimed variables.

At this point, the limit of infinite dimension leads to a crucial simplification: it can be shown [131] that in this limit, the hopping needs to be properly scaled, lest the kinetic energy diverges. More precisely, the hopping parameter needs to be adjusted as $t_{ij} \propto \left(1/\sqrt{d}\right)^{|i-j|}$, where $|i-j|$ is the Manhattan distance between i and j for the cubic lattice). The insight of Georges and coworkers is that this scaling, applied to the connected Green's functions appearing in Eq. (6.19), considerably simplifies the expression [10]: for $n = 1$, $C^{(o)}_1(1|1') \propto \left(1/\sqrt{d}\right)^{|i-j|}$, $\eta_{i\sigma} \propto \left(1/\sqrt{d}\right)^{|i|}$, while the number of terms in the sum has a $\left(d^{|i-j|}\right)^2$ dependence (there are $\simeq d^s$ sites at a given Manhattan distance s from a fixed site for large d). This means that the $n = 1$ term from Eq. (6.19) is of order 1. A detailed study of the combined scaling of the terms for $n > 1$ shows that they decay as $1/d$ or faster. Therefore, Eq. (6.19) simplifies to

$$I = \sum_{ij\sigma} \int_0^\beta d\tau\ \eta^*_{i\sigma}\eta_{j\sigma} \left\langle \phi^*_{i\sigma}\phi_{j\sigma} \right\rangle_{(o)} = \sum_{ij\sigma} \int_0^\beta \int_0^\beta d\tau\ d\tau'\ t_{i0}t_{j0}\phi^*_{0\sigma} G^{(o)}_{ij,\sigma}(\tau')\delta(\tau - \tau')\phi_{0\sigma}. \tag{6.22}$$

Noting that for $i, j \neq 0$,

$$\int_{\substack{\phi_{0\sigma}(\beta) \\ = -\phi_{0\sigma}(0)}} \mathcal{D}[\phi^*_{0\sigma},\, \phi_{0\sigma}] \eta^*_{i\sigma}\eta_{j\sigma} \left\langle \phi^*_{i\sigma}\phi_{j\sigma} \right\rangle_{(o)} = \int_{\substack{\phi_{0\sigma}(\beta) \\ = -\phi_{0\sigma}(0)}} \mathcal{D}[\phi^*_{0\sigma},\, \phi_{0\sigma}] \exp\Big\{ \eta^*_{i\sigma}\eta_{j\sigma} \left\langle \phi^*_{i\sigma}\phi_{j\sigma} \right\rangle_{(o)} \Big\}, \tag{6.23}$$

we obtain from Eq. (6.14) and Eq. (6.15)

$$\begin{aligned} S_{\text{eff}} &= \sum_{ij\sigma} \int_0^\beta \int_0^\beta d\tau \; d\tau' \; t_{i0} t_{j0} \phi^*_{0\sigma} G^{(o)}_{ij,\sigma}(\tau') \delta(\tau - \tau') \phi_{0\sigma} + S_0\left[\phi^*_{0\uparrow}, \phi^*_{0\downarrow}, \phi_{0\uparrow}, \phi_{0\downarrow}\right] \\ &= \sum_\sigma \int_0^\beta d\tau \; \left\{ \left(\int_0^\beta d\tau' \; \phi^*_{0\sigma} \left[\partial_\tau - \mu + \sum_{ij} t_{i0} t_{j0} G^{(o)}_{ij,\sigma}(\tau') \delta(\tau - \tau') \right] \phi_{0\sigma} \right) \right. \\ &\qquad \left. + H_U(\phi^*_{0\uparrow}, \phi^*_{0\downarrow}, \phi_{0\uparrow}, \phi_{0\downarrow}) \right\} \\ &\equiv \sum_\sigma \int_0^\beta d\tau \; \left\{ \left(- \int_0^\beta d\tau' \; \phi^*_{0\sigma} \left[\mathcal{G}_0^{-1}(\tau')^{\text{IDHM}} \delta(\tau - \tau') \right] \phi_{0\sigma} \right) + H_U(\phi^*_{0\uparrow}, \phi^*_{0\downarrow}, \phi_{0\uparrow}, \phi_{0\downarrow}) \right\}. \end{aligned} \tag{6.24}$$

The non interacting part of this action has the form obtained in Eq. (6.9), where the following form for the inverse bare propagator (IDHM stands for "infinite dimensional Hubbard model") is used:

$$\mathcal{G}_0^{-1}(i\omega_n)^{\text{IDHM}} = i\omega_n + \mu - \sum_{ij} t_{i0} t_{j0} G^{(o)}_{ij,\sigma}(i\omega_n). \tag{6.25}$$

This expression is helpful, but involves $G^{(o)}_{ij,\sigma}(i\omega_n)$, which is still not known. For a general lattice, it is possible to use an expansion of the Green's function for the full Hamiltonian in powers of the hopping matrix elements [10]. This allows to establish a relation that first appeared (without formal justification) in a work by Hubbard [139]:

$$G^{(o)}_{ij,\sigma}(i\omega_n) = G_{ij,\sigma}(i\omega_n) - \frac{G_{i0\sigma}(i\omega_n) G_{0j\sigma}(i\omega_n)}{G_{00\sigma}(i\omega_n)}, \tag{6.26}$$

where $G_{ij,\sigma}(i\omega_n)$ denotes the Green's function for the Hubbard model including the complete lattice.

In Appendix B, we introduce the quantity

$$\tilde{D}(\xi) \equiv \int_{-\infty}^{+\infty} d\epsilon \; D(\epsilon) \frac{1}{\xi - \epsilon}, \tag{6.27}$$

as well as the self-energy $\Sigma(i\omega_n)$, assumed to be k-independent (an assumption which has to be proven valid on its own by power counting in $1/d$ [10]), and show that Eq. (6.26) leads to

$$\mathcal{G}_0^{-1}(i\omega_n)^{\text{IDHM}} = \Sigma(i\omega_n) + \frac{1}{\tilde{D}(i\omega_n + \mu - \Sigma(i\omega_n))}. \tag{6.28}$$

We may now employ Dyson's equation [127] applied to the lattice and apply the DMFT approximation, which consists in the identification of the self-energy of the lattice with that of the impurity:

$$\Sigma(i\omega_n) \underbrace{=}_{\substack{\text{DMFT} \\ \text{approximation}}} \Sigma_{\text{lattice}}(i\omega_n) \equiv \mathcal{G}_0^{-1}(i\omega_n)^{\text{IDHM}} - G^{-1\,\text{IDHM}}(i\omega_n) \tag{6.29}$$

to obtain

$$G^{\mathrm{IDHM}}(i\omega_n) = \tilde{D}(i\omega_n + \mu - \Sigma(i\omega_n)) = \int_{-\infty}^{+\infty} d\epsilon \; \frac{D(\epsilon)}{i\omega_n + \mu - \epsilon - \Sigma(i\omega_n)} \\ = \sum_{\mathbf{k}\in \mathrm{BZ}} \frac{1}{i\omega_n + \mu - \epsilon_{\mathbf{k}} - \Sigma(i\omega_n)} \tag{6.30}$$

This crucial result expresses the fact that one can identify the impurity Green's function with the momentum-averaged lattice Green's function. The latter quantity depends only on the known lattice dispersion, and on the (momentum-independent) self-energy of the impurity. This is the self-consistency condition, which can be used to solve the problem iteratively.

This result holds for a lattice in the limit of infinite coordination, a crucial ingredient used in three occasions during the derivation. First, it lead to the simplification of the expression for the action, which is limited to the $n = 1$ contribution in Eq.(6.19). Second, it was used to relate the Green's function for the cavity Hamiltonian and that for the full Hamiltonian in Eq. (6.26). Third, it is a necessary ingredient in order to prove that the self-energy is k-independent.

A comparison of the $d \to \infty$ limit versus $d = 1$ and $d = 3$ was done by Metzner and Vollhardt [131]. They compared the second order contribution to the correlation energy in the Hubbard model, defined as

$$E_2 = \frac{LU^2}{(2\pi)^{3d}} \int d\boldsymbol{k} d\boldsymbol{k'} d\boldsymbol{q} \frac{n^0_{\boldsymbol{k}\uparrow} n^0_{\boldsymbol{k'}\downarrow} \left(1 - n^0_{\boldsymbol{k}+\boldsymbol{q}\uparrow}\right)\left(1 - n^0_{\boldsymbol{k'}-\boldsymbol{q}\downarrow}\right)}{\epsilon_{\boldsymbol{k}} + \epsilon_{\boldsymbol{k'}} - \epsilon_{\boldsymbol{k}+\boldsymbol{q}} - \epsilon_{\boldsymbol{k'}+\boldsymbol{q}}}, \tag{6.31}$$

where the integrations extend over the Brillouin zone, $n^0_{\boldsymbol{k}\sigma\equiv 1}$ for $|\boldsymbol{k}| < k_{F\sigma}$ and 0 elsewhere, and L is the number of lattice sites. The result is shown in Fig. 6.2, and shows that the $d = \infty$ limit is a reasonable approximation to the $d = 3$ situation in this case. While in no way conclusive of the general validity or quality of the $d \to \infty$ limit, it shows that it may be an approach worth exploring, at least in the situation where $d = 3$.

6.3 Self-consistency loop

At this point we are in a position to devise a self-consistent scheme for solving the many-body problem represented by the Hubbard model in the limit of infinite dimensions. At step p, we assume that a trial self-energy $\Sigma_p(i\omega_n)$ is known for the isolated site (the process can be initialized for the initial step $p = 0$ with $\Sigma_p(i\omega_n) \equiv 0$, for lack of a better candidate). Given this trial function, we use Eq. (6.30), and obtain the lattice Green's function at iteration p (note the change of notation, from G^{IDHM} to G_{lat}, following the DMFT convention which highlights the back and forth movement between the "lattice" and the "impurity" points of view, illustrated in Fig. 6.3):<

$$G_{lat,p}(i\omega_n) = \sum_{\mathbf{k}\in \mathrm{BZ}} \frac{1}{i\omega_n + \mu - \epsilon_{\mathbf{k}} - \Sigma_p(i\omega_n)}, \tag{6.32}$$

Given $G_{lat,p}(i\omega_n)$ and $\Sigma_p(i\omega_n)$, we obtain the effective non-interacting Green's function of the Anderson model, $\mathcal{G}^{-1}_{0,p}(i\omega_n)$, using Eq. (6.29). In order to close the self-consistent loop, the most numerically challenging step remains to be executed: solve the Anderson

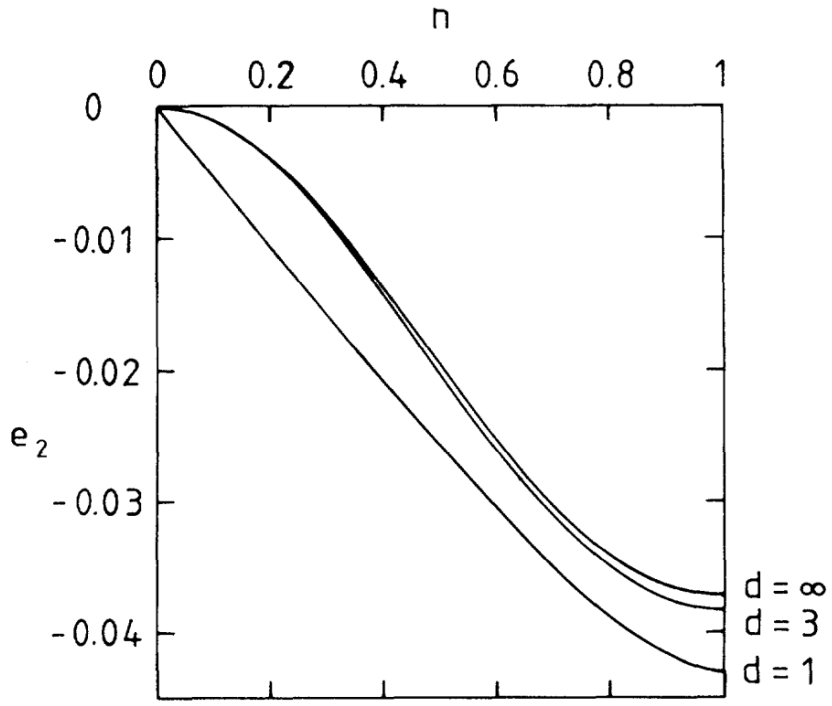

Figure 6.2: Second-order contribution to the correlation energy $e_2 \equiv E_2/\left[LU^2/|\bar{\epsilon_0}(\frac{1}{2},\frac{1}{2})|\right]$ versus density, for lattice dimensions $d = 1, 3$, and ∞. $\bar{\epsilon_0}(n_\uparrow, n_\downarrow)$ is the kinetic energy of the non interacting particles for arbitrary densities $n_\uparrow$, $n_\downarrow$. Reprinted figure with permission from Ref. [131].

model, i.e., calculate its Green's function, knowing $\mathcal{G}^{-1}_{0,p}(i\omega_n)$. Different numerical schemes have been developed in recent years to this end. In Sec. 7, we cover this problematic in some detail, and present a recently introduced numerical scheme which gives access to the Green's function for the Anderson model in Matsubara frequencies, i.e. solves the following model

$$\sum_\sigma \int_0^\beta d\tau \left(- \int_0^\beta d\tau' \; \phi^*_{0\sigma} \left[\mathcal{G}_0^{-1}(\tau')\delta(\tau - \tau') \right] \phi_{0\sigma} \right) + H_U(\phi^*_{0\uparrow}, \phi^*_{0\downarrow}, \phi_{0\uparrow}, \phi_{0\downarrow}). \tag{6.33}$$

Equipped with this tool, we obtain the impurity Green's function $G_p(i\omega_n)$ and can use Dyson's equation to obtain a new estimate for the self-energy of the impurity:

$$\Sigma_{p+1}(i\omega_n) = \mathcal{G}^{-1}_{0,p}(i\omega_n) - G_p(i\omega_n). \tag{6.34}$$

This process is illustrated in Fig. 6.3. It can be iterated until it reaches convergence, i.e. until $\|\Sigma_p - \Sigma_{p+1}\| < \epsilon$, where $\|\ldots\|$ denotes a suitably chosen norm over functions, and ϵ is a suitably chosen convergence criterion. Experience has shown that this convergence is remarkably robust. Far away from phase transitions, convergence is quick and can be achieved in a few tens of iterations.

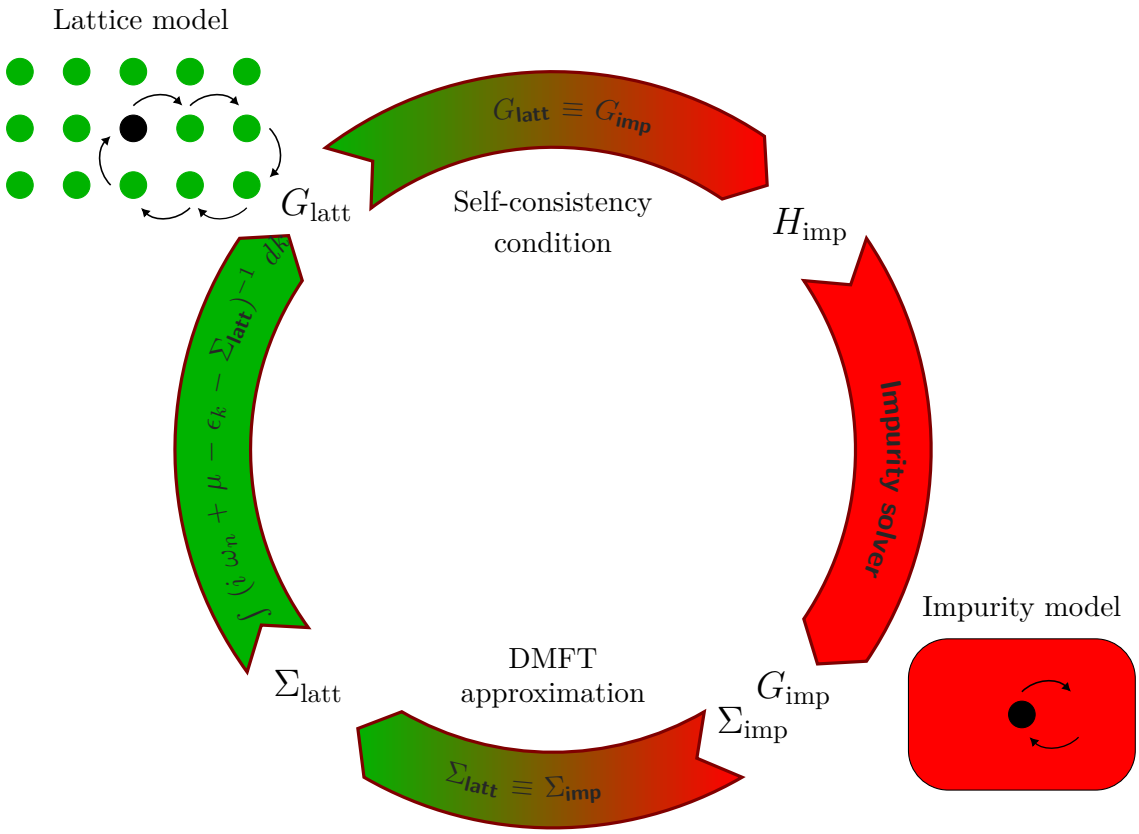

Figure 6.3: The DMFT self-consistency loop. On the right-hand side, the system is considered from the point of view of an impurity in a bath of conduction electrons whose characteristics are known. On the left-hand side, the problem is viewed as a lattice whose self-energy is known.

Chapter 7

Quantum impurity solvers

7.1 Introduction

The iterative approach developed in Sec. 6 relies on our ability to compute the self-energy of a local many-body problem, as shown in Eq (6.33). Compared with the initial situation which involved a full lattice, this is a significant simplification, insofar as the interacting system of interest now has a small size. Nevertheless, the impurity remains coupled to a bath with an infinite number of degrees of freedom, which makes the resolution of the question highly non-trivial.

The importance of this problem has led to the development of a variety of techniques to tackle it. The most natural approach consists in discretizing the bath levels, and using exact diagonalization. Nevertheless, in such frameworks which approximate the system by using discrete levels, the exponential growth of the dimension of the Hilbert space of the impurity with the number of discrete levels severely limits their accuracy. The need for computer memory has limited the size of the studied systems to typically some tens of sites, with one non degenerate orbital per site [140]. The convergence of these approaches towards the exact solution of the many-body problem is the subject of ongoing research, including the use of configuration interaction approximations [141–145].

Quantum Monte Carlo techniques have become the method of choice for solving these quantum field theories. One of their most desirable traits is the flexibility with which they can be adapted to the various forms that the impurity problem can take. In the following we will describe the details of this approach. We will first review the basics of Monte Carlo sampling, before we describe the details of the algorithms employed in the context of the impurity model.

7.2 Monte Carlo sampling of partition functions

In this section we introduce the basics of Monte Carlo sampling for partition functions. We rely on the presentations by Gull [137], Krauth [146], and Landau and Binder [147].

7.2.1 Monte Carlo basics

Quantum Monte Carlo is a broad term which actually covers different philosophies. The kind of numerical technique we are interested in is a variant of the so-called path integral method. This approach relies on the introduction of the interaction representation of the problem at hand: the Hamiltonian H is split into two parts, $H = H_a + H_b$. This

representation is commonly used to separate the roles played by the interacting and the non-interacting terms in the Hamiltonian, but in the present context, various decompositions will lead to different sampling algorithms, each with its own specificities. Time-dependent operators in this representation are defined as

$$O(\tau) = e^{\tau H_a} O e^{-\tau H_a}. \tag{7.1}$$

Within this framework, we may consider the partition function Z, written as

$$\begin{aligned} Z &= \mathrm{Tr}\left[e^{-\beta H_a} A(\beta)\right], \\ A(\beta) &= e^{\beta H_a} e^{-\beta H}. \end{aligned} \tag{7.2}$$

The operator A is such that

$$\begin{aligned} \frac{\mathrm{d}A}{\mathrm{d}\beta} &= -H_b(\beta) A(\beta), \\ A(\beta) &= T_\tau e^{-\int_0^\beta d\tau H_b(\tau)}. \end{aligned} \tag{7.3}$$

We can insert Eq. (7.2) into the expression for the partition function, and expand it in powers of $H_b(\tau)$:

$$\begin{aligned} Z &= \mathrm{Tr}\left[T_\tau e^{-\beta H_a} e^{-\int_0^\beta d\tau H_b(\tau)}\right] \\ &= \sum_{k=0}^{\infty} (-1)^k \int_0^\beta d\tau_1 \ldots \int_{\tau_{k-1}}^\beta d\tau_k \, \mathrm{Tr}\left[e^{-\beta H_a} H_b(\tau_k) H_b(\tau_{k-1}) \ldots H_b(\tau_1)\right], \end{aligned} \tag{7.4}$$

in which, when considering an impurity problem, the trace is carried out over all impurity and bath states. This kind of expressions is well suited to the use of Monte Carlo integration techniques: the infinite sum of integrals of Eq. (7.4) may be considered as a sum of terms equal to unity, with a weight given by the trace. This weight is a function of the set of imaginary times $(\tau_1, \ldots, \tau_k)$, and each such set of imaginary times can be viewed as a Monte Carlo configuration. The Monte Carlo approach then consists in sampling this infinite set of configurations in an efficient way, instead of trying to consider all of them, until a satisfactory approximation is reached.

A standard example of the application of Monte Carlo techniques to statistical physics is the evaluation of the partition function for the Ising model, on a finite lattice of N sites:

$$\begin{aligned} Z &= \sum_{x \in \mathcal{C}} e^{-\beta H_I(x)}, \\ H_I(x) &= J \sum_{\langle ij \rangle} S_i(x) S_j(x), \end{aligned} \tag{7.5}$$

where x is a configuration of the system: $x = \{\pm 1, \ldots, \pm 1\}$, so that the expression for partition function is a sum over 2^N terms, which makes its explicit evaluation for large N impractical. This is the kind of situations in which Monte Carlo shows its full potential: instead of evaluating each term of the sum, a fraction of all the terms are sampled in order to obtain an approximate value of the full sum. All the effort needs to go into a smart choice of the terms to be sampled, and of the way these terms are generated, so that the algorithm is efficient, and that the error is controlled and small.

In the simplest case, elements x_i are chosen uniformly inside the configuration space $\mathcal{C}$, in which case we can use the relation

$$\langle f \rangle \equiv \frac{1}{\Omega} \int f(x) dx = \lim_{N \to \infty} \frac{1}{N} \sum_{i=1}^{N} f(x_i), \tag{7.6}$$

with Ω the volume of $\mathcal{C}$. The approximation on the right hand side of Eq. (7.6) converges to the exact result, with an error proportional to $\frac{1}{\sqrt{N}}$, independently of the dimension of the space $\mathcal{C}$. This is the great strength of Monte Carlo based approaches, which are particularly well suited for the evaluation of high dimensional integrals.

7.2.2 Importance sampling

The question of generating the configurations which are included in the sampling of the exact observable we are after is the central issue in the elaboration of a Monte Carlo algorithm. In this respect, two approaches exist. The first one is called direct sampling, in which configurations are determined directly, without reference to a closeby pre-determined configuration. The second one is Markov chain Monte Carlo, described in some details in Sec. 7.2.3, where a new configuration is generated by a modification applied to a known configuration considered earlier.

When a method for generating configurations directly exists (as is the case for the Ising model), then the question of choosing an efficient sampling is raised. Considering for example the Ising model with negative J in the limit of low temperatures, where a ferromagnetic order is present, we immediately see that generating all configurations uniformly is not efficient, because most of the configurations have a high energy, and contribute very little to the partition function. Instead, it would be much more efficient to sample configurations proportionally to their contribution to the partition function. This is what is called importance sampling.

Let us imagine we can come up with a direct sampling algorithm which generates configurations x with probability $p(x)$ in phase space. Eq. (7.6) then becomes

$$\begin{aligned} \langle f \rangle = \frac{1}{\Omega} \int \frac{f(x)}{p(x)} p(x) dx = \lim_{N \to \infty} \frac{1}{N} \sum_{i=1}^{N} \frac{f(x_i)}{p(x_i)}, \\ \int_{\mathcal{C}} p(x) dx = 1. \end{aligned} \tag{7.7}$$

Using this transformation, the error of the Monte Carlo estimation of the integral becomes

$$\Delta = \sqrt{\frac{\mathrm{Var}(f/p)}{N}}. \tag{7.8}$$

Thus, if we can somehow choose p such that it is larger for configurations where f is also large (i.e., such that the distribution of p is similar to that of f), then the error is much reduced. This can be intuitively understood by considering that the terms with larger contributions are sampled more frequently, leading to a more efficient algorithm.

Formally, when considering an observable A, the quantity to be evaluated may be

written as

$$\begin{aligned} \langle A \rangle_\rho &\equiv \frac{1}{Z} \int_C A(x)\rho(x)dx, \\ Z &= \int_C \rho(x)dx. \end{aligned} \tag{7.9}$$

Importance sampling in this case leads to

$$\langle A \rangle_\rho = \frac{1}{Z} \int_C A(x)\rho(x)\frac{p(x)}{p(x)}dx = \lim_{N\to\infty} \frac{\sum_{j=1}^{N} A(x_j)\frac{\rho(x_j)}{p(x_j)}}{\sum_{j=1}^{N} \frac{\rho(x_j)}{p(x_j)}} \tag{7.10}$$

7.2.3 Metropolis algorithm

In practice, only simple systems lend themselves to direct sampling, in particular if such sampling needs to follow a non trivial distribution for the purpose of importance sampling implementation. In such cases, Markov chain Monte Carlo is usually the best option. In this framework, at each step of the sampling, a new configuration x_{k+1} is generated from a previous configuration x_k, by the application of some transformation. The nature of this transformation determines a matrix of transition probabilities between two configurations x and y, denoted W_{xy}. It is possible to show that the following set of conditions is sufficient, for this transformation to generate a valid Monte Carlo algorithm (i.e., an algorithm which produces configurations with the desired distribution $p(x)$) [146]:

- Irreducibity: the system cannot be split into independent subparts, within which the Markov chain algorithm would be trapped with no possibility of reaching another subpart.
- Aperiodicity: The Markov chain does not return in a finite time and with probability 1 to an already sampled configuration.
- Detailed balance: the transition matrix respects

$$\frac{W_{xy}}{W_{yx}} = \frac{p_y}{p_x}, \tag{7.11}$$

  for all configurations x and y.

The first two conditions are relatively straightforward to respect, but the last one needs more care. For this purpose, a popular approach is to use the Metropolis algorithm [148]. Two probabilities are introduced: the a priori proposal probability W_{prop}, and the acceptance probability W_{acc}, such that $W_{xy} = W_{\text{prop}}(x \to y)W_{\text{acc}}(x \to y)$, so that the detailed balance condition becomes

$$\begin{aligned} &\frac{W_{\text{prop}}(x \to y)W_{\text{acc}}(x \to y)}{W_{\text{prop}}(y \to x)W_{\text{acc}}(y \to x)} = \frac{p(y)}{p(x)} \\ \Leftrightarrow &\frac{W_{\text{acc}}(x \to y)}{W_{\text{acc}}(y \to x)} = \frac{p(y)W_{\text{prop}}(y \to x)}{p(x)W_{\text{prop}}(x \to y)}, \end{aligned} \tag{7.12}$$

with a form reminiscent of usual conservation laws. Metropolis suggested that this could be easily satisfied by choosing the acceptance probability adequately (the a priori proposal probability being given by the chosen algorithm) as follows:

$$W_{\text{acc}}(x \to y) = \min\left(1, \frac{p(y)W_{\text{prop}}(y \to x)}{p(x)W_{\text{prop}}(x \to y)}\right). \tag{7.13}$$

7.3 Monte Carlo approach to the impurity problem

This field was recently thoroughly reviewed by Gull and coworkers [140], and we follow their exposure in the following. The use of Quantum Monte Carlo techniques for the solution of the impurity problem dates back to the pioneering work of Hirsch and Fye [149], who had the idea to apply a Hubbard-Stratonovich transformation to each time slice of the functional integral. This technique transforms the problem at hand into a non interacting fermion problem at each time-step, so that the calculation of a trace over a 2^M-dimensional space is required, for each configuration of the relevant Ising variables (with M the number of time steps). This was the state of the art Monte Carlo approach until the design of continuous time solvers, which have become the most used solvers by practitioners in recent years.

All Monte Carlo approaches to the solution of the impurity problem are based on the functional integral formulation of the problem in imaginary time. After a time step $\Delta\tau = \beta/N$ has been chosen, complete sets of states are inserted at the discretization points, and the limit $\Delta\tau \to 0$ is taken. In spite of the development of many schemes aimed at handling this last point, the time step extrapolation to 0 remains an issue. The main goal of the solver is indeed the determination of the Green's function, which drops rapidly as τ is increased from 0, and possesses discontinuous derivatives at $\tau = 0$ and $\tau = \beta$, which need to be evaluated precisely. This means that the extrapolation to $\Delta\tau = 0$ needs to be very precise, while the low energy behavior of interest, which is described for imaginary times around the value $\tau \simeq \beta/2$, also needs to be known with precision. As a consequence, the number of grid points in imaginary time becomes very large in case of a regular time discretization, especially for low temperatures.

The continuous-time approaches, such as the hybridization expansion described further, have the advantage of not requiring any such discretization of the imaginary time axis. The idea behind this technique is to sample the terms of a diagrammatic expansion of the expression for the partition function, instead of evaluating the contributions from complete sets of states. In spite of the lack of massive computational power at the time, the very first approaches along these lines date back to the sixties, with the works of Handscomb [150], later generalized as the stochastic series expansion [151]. These results for quantum magnets rely on a Taylor expansion of the partition function in powers of βH. The more modern techniques are based on the insights of Prokof'ev and coworkers [152–154], and Beard and Wiese [155], whose efforts led to the elimination of all time discretization errors in the context of unfrustrated bosonic lattice models.

In spite of these advances, this success could not be extended to fermion systems in a straightforward manner. The reason for this is that in bosonic systems, all diagrams considered by the approaches described above have the same sign, which is not the case for fermion problems. This issue is referred to as the sign problem [156]. Its severity restricted for a time the use of continuous time Monte Carlo approach for fermion systems to special cases, where the sign problem is not present. However, it turned out that the impurity problem, unlike the full lattice problem, exhibits a much less severe sign problem when approached using the continuous time Monte Carlo techniques. Together

with the mapping of the infinite dimensional Hubbard model onto the Anderson model As was shown in Chapter 6, this sparked a renewed interest in these techniques, which allowed a rapid progress and a number a breakthroughs, in particular three main types of new expansions: a weak-coupling approach [157, 158], a complementary hybridization expansion expansion [11, 159], and the auxiliary-field formulation [160], see Ref [134] for a comparative analysis of their performance.

With these new tools in hand, DMFT was used to study many systems, from model Hamiltonians to real materials (within the framework of LDA + DMFT). Four-point correlation functions have also been used for the investigation of susceptibilities and phase boundaries, or in relation with the newly developed extensions of DMFT, aimed at taking spatial correlations into account (DΓA, dual fermion) [161–164].

7.3.1 Sampling the partition function to finite order

We now illustrate the principle behind the Monte Carlo sampling of continuous-time expansions of the partition function, before we describe the details of the algorithm used to obtain the results of the present work.

It was shown in Eq. (7.4) that the partition function may be written in the form

$$Z = \sum_{k=0}^{\infty} \int \dots \int_0^\beta d\tau_1 \dots d\tau_k p_k(\tau_1, \dots, \tau_k), \tag{7.14}$$

which may be interpreted as a summation over configurations up to infinite order with the weight $p_k(\tau_1, \dots, \tau_k)$. Let us consider the first order terms for simplicity. The unique term of order 0 is 1, while at order 1, the sole term to be considered is

$$Z_1 = \int_0^\beta d\tau_1 p_1(\tau_1). \tag{7.15}$$

This can easily be sampled using Monte Carlo, for instance by using a uniform distribution for τ_1^j, and evaluating

$$Z_1 = \lim_{N\to\infty} \frac{1}{N} \sum_{j=1}^{N} p_1(\tau_1^j). \tag{7.16}$$

We could similarly evaluate the order 2 term, as

$$Z_2 = \lim_{N\to\infty} \frac{1}{N} \sum_{j=1}^{N} p_2(\tau_1^j, \tau_2^j), \tag{7.17}$$

where (τ_1, τ_2) are uniformly distributed in $(0, \beta)$. A naive approach then consists in choosing a cutoff order k_{max}, and evaluating all orders of the summation up to this cutoff.

The problem with this is that there is a systematic and uncontrolled error introduced by the choice of the cutoff. The insight of Prokof'ev and coworkers [152] was to show that such series can be sampled exactly, without suffering from the truncation error. The principle of their approach is to use a Markov chain Monte Carlo algorithm in the phase space containing all orders, and to use the Metropolis algorithm to switch between configurations, of all possible orders. The weight of the very large orders is suppressed by the relevant combinatorial factors, so that the only remaining error is the statistical Monte Carlo error which scales as $1/\sqrt{N}$ with N the number of Monte Carlo samples.

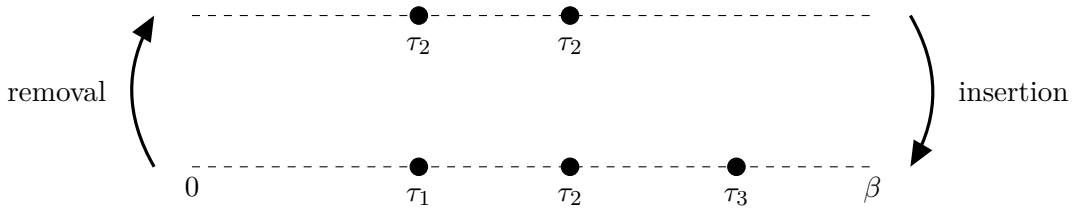

Figure 7.1: Illustration of an elementary step, raising (top to bottom transition) or lowering (bottom to top transition) the order of the current configuration, in a schematic continuous-time Markov chain Monte Carlo sampling algorithm.

7.3.2 Sampling the partition function to infinite order

In this section we detail the principle leading to the sampling of the partition function including all orders, and follow the presentation in Ref. [137]. The configuration space we choose to work with contains all configurations, of all orders up to infinity:

$$\mathcal{C} = \{\{\}, \{\tau_1\}, \{\tau_1, \tau_2\}, \ldots, \{\tau_1, \tau_2, \ldots, \tau_k\}, \ldots\}, \tag{7.18}$$

with τ_i continuous variables, such that $\tau_1 < \tau_2 < \ldots < \tau_k$. Assuming that all weights are real and positive, and that the partition function is finite, the weight of each configuration may be normalized into the probability distribution $p(\{\tau_i\})/Z$. A Markov chain Monte Carlo approach can then be implemented as follows: starting from some configuration x_k, we choose to lower (through the removal of a single imaginary time variable τ_j in x_k) or increase (through the insertion of a single imaginary time variable τ_{n+1} in x_k, assumed to have order n) the order of the current configuration, in order to obtain a new configuration. Moves that conserve the order of the configuration are also considered, such as the modification of the value of one single variable $\tau_i \in x_k$. The principle of a raising/lowering step in the Markov chain Monte-Carlo algorithm is illustrated in Fig. 7.1.

It is trivial to ensure that aperiodicity and irreducibility are respected in this framework. The last sufficient condition that has to be met, for such a process to be a valid algorithm, is detailed balance. For this, we employ the Metropolis algorithm as follows. Let us consider an order-raising step, and its corresponding order-lowering step, connecting two configurations, $x = \{\tau_1, \tau_2, \ldots, \tau_k\}$, and $y = \{\tau_1, \tau_2, \ldots, \tau_k, \tau_{k+1}\}$. The configuration y is obtained from x by the insertion of the additional vertex τ_{k+1}. In this case we have, as introduced above,

$$\begin{aligned} W_{xy} &= W_{\text{prop}}(x \to y) W_{\text{acc}}(x \to y), \\ W_{yx} &= W_{\text{prop}}(y \to x) W_{\text{acc}}(y \to x). \end{aligned} \tag{7.19}$$

The proposal probability $W_{\text{prop}}(x \to y)$ is equal to the probability of picking τ_{k+1} as the imaginary time value of the vertex to be added to the configuration x, that is

$$W_{\text{prop}}(x \to y) = \frac{d\tau}{\beta}, \tag{7.20}$$

where an infinitesimal quantity $d\tau$ has been introduced. On the other hand, $W_{\text{prop}}(y \to x)$ is given by the probability to pick τ_{k+1} as the vertex to be removed, among those that make up the configuration y. Therefore,

$$W_{\text{prop}}(y \to x) = \frac{1}{k+1}. \tag{7.21}$$

Application of the Metropolis algorithm Eq. (7.13) indicates that the acceptance ratio for the $x \to y$ and $y \to x$ moves need to be implemented as:

$$\begin{aligned} W_{\text{acc}}(x \to y) &= \min\left(1, \frac{p(y) W_{\text{prop}}(y \to x)}{p(x) W_{\text{prop}}(x \to y)}\right) \\ &= \min\left(1, \frac{1}{k+1} \frac{\beta}{d\tau} \frac{p(y)}{p(x)}\right). \end{aligned} \tag{7.22}$$

We note that the order of y is higher than the order of x by one unit, so that in practice, $\frac{p(y)}{p(x)} \propto d\tau$, so that the infinitesimal introduced above disappears, providing us with a finite acceptance probability. A caveat to observe is that in all derivations above, it was assumed that $p(x)$ is a real positive number. The extension of this derivation to the general case is straightforward if this condition is not satisfied, but may lead the Monte Carlo procedure to converge very slowly or not at all, depending of the severity of the sign problem which may occur.

We will now describe the continuous time hybridization expansion algorithm developed by Werner, Millis, Troyer, and coworkers [11, 159], which implements the approach just described: an analytic expansion is chosen for the partition function, the corresponding values of $p(x)$ are found, and the acceptance ratios are deduced, which allow for a numerical sampling of the partition function, or other observables, following Eq. (7.10).

7.4 The hybridization expansion continuous-time solver

In this section, we follow the presentation of Ref. [137] and Ref. [140]. The hybridization expansion algorithm proceeds from Eq. (7.4), applied to the Anderson model of Eq. (6.10), with

$$\begin{aligned} H_a &\equiv H_{\text{bath}} + H_{\text{loc}}, \\ H_b &\equiv H_{\text{mix}}. \end{aligned} \tag{7.23}$$

7.4.1 Expansion of the partition function

From the expression $H_{\text{mix}} = \sum_{\boldsymbol{k}\sigma} \left[V_{\boldsymbol{k}\sigma} c_\sigma^\dagger a_{\boldsymbol{k}\sigma} + V_{\boldsymbol{k}\sigma}^* a_{\boldsymbol{k}\sigma}^\dagger c_\sigma \right] \equiv \tilde{H}_{\text{mix}}^\dagger + \tilde{H}_{\text{mix}}$, we note that each term in the sum creates and annihilates an electron on the impurity, respectively, so that in this expansion, only even powers of H_{mix}, and among those, only terms with equal numbers of occurrences of $\tilde{H}_{\text{mix}}$ and $\tilde{H}_{\text{mix}}^\dagger$, can yield a nonzero contribution to the trace.

The partition function may thus be written

$$\begin{aligned} Z &= \sum_{k=0}^{\infty} \int_0^\beta d\tau_1 \dots \int_{\tau_{k-1}}^\beta d\tau_k \int_0^\beta d\tau'_1 \dots \int_{\tau'_{k-1}}^\beta d\tau'_k \\ &\qquad \mathrm{Tr}\left[T_\tau e^{-\beta H_a} \tilde{H}_{\mathrm{mix}}(\tau_k)\tilde{H}^\dagger_{\mathrm{mix}}(\tau'_k)\dots\tilde{H}_{\mathrm{mix}}(\tau_1)\tilde{H}^\dagger_{\mathrm{mix}}(\tau'_1)\right] \\ &= \sum_{k=0}^{\infty} \int_0^\beta d\tau_1 \dots \int_{\tau_{k-1}}^\beta d\tau_k \int_0^\beta d\tau'_1 \dots \int_{\tau'_{k-1}}^\beta d\tau'_k \times \sum_{\substack{j_1,j_2,\dots,j_k \\ j'_1,j'_2,\dots,j'_k}} \sum_{\substack{\boldsymbol{p_1},\boldsymbol{p_2},\dots,\boldsymbol{p_k} \\ \boldsymbol{p'_1},\boldsymbol{p'_2},\dots,\boldsymbol{p'_k}}} V^*_{\boldsymbol{p_1}j_1} V_{\boldsymbol{p'_1}j'_1} \dots V^*_{\boldsymbol{p_k}j_k} V_{\boldsymbol{p'_k}j'_k} \\ &\qquad \times \mathrm{Tr}\left[T_\tau e^{-\beta H_a} a^\dagger_{\boldsymbol{p}_k}(\tau_k) c_{j_k}(\tau_k) c^\dagger_{j'_k}(\tau'_k) a_{\boldsymbol{p}'_k}(\tau'_k) \dots a^\dagger_{\boldsymbol{p}_1}(\tau_1) c_{j_1}(\tau_1) c^\dagger_{j'_1}(\tau'_1) a_{\boldsymbol{p}'_1}(\tau'_1)\right]. \end{aligned} \tag{7.24}$$

In this expression, bath and impurity operators can be separated, to yield

$$\begin{aligned} Z =& \sum_{k=0}^{\infty} \int_0^\beta d\tau_1 \dots \int_{\tau_{k-1}}^\beta d\tau_k \int_0^\beta d\tau'_1 \dots \int_{\tau'_{k-1}}^\beta d\tau'_k \times \sum_{\substack{j_1,j_2,\dots,j_k \\ j'_1,j'_2,\dots,j'_k}} \sum_{\substack{\boldsymbol{p_1},\boldsymbol{p_2},\dots,\boldsymbol{p_k} \\ \boldsymbol{p'_1},\boldsymbol{p'_2},\dots,\boldsymbol{p'_k}}} V_{\boldsymbol{p_1}j_1} V^*_{\boldsymbol{p'_1}j'_1} \dots V_{\boldsymbol{p_k}j_k} V^*_{\boldsymbol{p'_k}j'_k} \\ &\times \mathrm{Tr}_c\left[T_\tau e^{-\beta H_{\mathrm{loc}}} c_{j_k}(\tau_k) c^\dagger_{j'_k}(\tau'_k) \dots c_{j_1}(\tau_1) c^\dagger_{j'_1}(\tau'_1)\right] \\ &\times \mathrm{Tr}_a\left[T_\tau e^{-\beta H_{\mathrm{bath}}} a^\dagger_{\boldsymbol{p}_k}(\tau_k) a_{\boldsymbol{p}'_k}(\tau'_k) \dots a^\dagger_{\boldsymbol{p}_1}(\tau_1) a_{\boldsymbol{p}'_1}(\tau'_1)\right]. \end{aligned} \tag{7.25}$$

In this expression, the bath operators are non interacting, and their time evolution is given by H_a, which does not include any coupling between the impurity and the bath. The trace over the bath operators can therefore be computed exactly. For this purpose we introduce the bath partition function

$$Z_{\mathrm{bath}} = \mathrm{Tr}\, e^{-\beta H_{\mathrm{bath}}} = \prod_\sigma \prod_{\boldsymbol{k}} \left(1 + e^{-\beta\epsilon_{\boldsymbol{k}}}\right), \tag{7.26}$$

and we consider the contribution of such a term to the first order term in Eq. (7.25). We find:

$$\begin{aligned} &\frac{1}{Z_{\mathrm{bath}}} \sum_{\boldsymbol{p}} V_{\boldsymbol{p}\sigma} V^*_{\boldsymbol{p}\sigma}\, \mathrm{Tr}_a\left[e^{-\beta H_{\mathrm{bath}}} a^\dagger_{\boldsymbol{p}}(\tau) a_{\boldsymbol{p}}(\tau')\right] \\ &= -\sum_{\boldsymbol{p}} |V_{\boldsymbol{p}\sigma}|^2 \mathcal{G}_{\mathrm{bath}}(\boldsymbol{p}\tau|\boldsymbol{p}\tau') \\ &= \sum_{\boldsymbol{p}} \frac{|V_{\boldsymbol{p}\sigma}|^2}{1+e^{-\beta\epsilon_{\boldsymbol{p}}}} \times \begin{cases} e^{-(\tau-\tau')\epsilon_{\boldsymbol{p}}} & \text{for } \tau \le \tau' \\ -e^{-(\beta-(\tau-\tau'))\epsilon_{\boldsymbol{p}}} & \text{for } \tau' < \tau, \end{cases} \end{aligned} \tag{7.27}$$

where Eqs. (6.4-6.7) were used to obtain the last line. We can at this point introduce the hybridization function Δ,

$$\Delta_{lm}(\tau) = \sum_{\boldsymbol{p}} \frac{V^*_{\boldsymbol{p}l} V_{\boldsymbol{p}m}}{1+e^{-\beta\epsilon_{\boldsymbol{p}}}} \times \begin{cases} e^{-\tau\epsilon_{\boldsymbol{p}}} & \text{for } \tau \le 0 \\ -e^{-(\beta-\tau)\epsilon_{\boldsymbol{p}}} & \text{for } 0 < \tau, \end{cases} \tag{7.28}$$

so that for an arbitrary product of operators or expansion order, application of Wick's theorem yields

$$\frac{1}{Z_{\text{bath}}}\,\text{Tr}_a\Bigg[T_\tau e^{-\beta H_{\text{bath}}} \sum_{\substack{\boldsymbol{p_1},\boldsymbol{p_2},\ldots,\boldsymbol{p_k}\\ \boldsymbol{p'_1},\boldsymbol{p'_2},\ldots,\boldsymbol{p'_k}}} V_{\boldsymbol{p_1}j_1}V^*_{\boldsymbol{p'_1}j'_1}\ldots V_{\boldsymbol{p_k}j_k}V^*_{\boldsymbol{p'_k}j'_k}\,a^\dagger_{\boldsymbol{p}_k}(\tau_k)a_{\boldsymbol{p}'_k}(\tau'_k)\ldots a^\dagger_{\boldsymbol{p}_1}(\tau_1)a_{\boldsymbol{p}'_1}(\tau'_1)\Bigg] = \det\boldsymbol{\Delta}, \tag{7.29}$$

Where $\boldsymbol{\Delta}$ is a $k\times k$ matrix with elements $\Delta_{lm}=\Delta_{j_l j_m}(\tau_l-\tau_m)$. The hybridization function thus defined is antiperiodic and is related to the bare Green's function of the effective action $\mathcal{G}_0^{-1}(i\omega_n)^{\text{AM}}$ introduced in Eq. (6.11) via $\Delta_{j_l j_m}(i-i\omega_n)=(i\omega_n+\mu)\delta j_l j_m-\mathcal{G}^{-1}_{0\,j_l j_m}(i\omega_n)^{\text{AM}}$.

With this notation, the partition function in the framework of this expansion reads

$$\begin{aligned} Z =& Z_{\text{bath}}\sum_{k=0}^{\infty}\int_0^\beta d\tau_1\ldots\int_{\tau_{k-1}}^\beta d\tau_k\int_0^\beta d\tau'_1\ldots\int_{\tau'_{k-1}}^\beta d\tau'_k \\ &\times\sum_{\substack{j_1,j_2,\ldots,j_k\\ j'_1,j'_2,\ldots,j'_k}}\text{Tr}_c\left[T_\tau e^{-\beta H_{\text{loc}}}c_{j_k}(\tau_k)c^\dagger_{j'_k}(\tau'_k)\ldots c_{j_1}(\tau_1)c^\dagger_{j'_1}(\tau'_1)\right]\det\boldsymbol{\Delta}. \end{aligned} \tag{7.30}$$

This general expression can simplify depending on the symmetries of the considered Hamiltonian. For example, if the bath is diagonal in some flavor index j (e.g. spin, site, orbit), with N different varieties of this flavor, then $\boldsymbol{\Delta}$ is block-diagonal and Eq. (7.30) simplifies to

$$\begin{aligned} Z =& Z_{\text{bath}}\sum_{k_1,\ldots,k_N=0}^{\infty}\prod_{j=1}^{N}\int_0^\beta d\tau_1\ldots\int_{\tau^j_{k_j-1}}^\beta d\tau^j_{k_j}\int_0^\beta d\tau'^j_1\ldots\int_{\tau'^j_{k_j-1}}^\beta d\tau'^j_{k_j} \\ &\times\text{Tr}_c\left[T_\tau e^{-\beta H_{\text{loc}}}\prod_{j=1}^{N}c_j\left(\tau^j_{k_j}\right)c^\dagger_j\left(\tau'^j_{k_j}\right)\ldots c_j\left(\tau^j_1\right)c^\dagger_j\left(\tau'^j_1\right)\right]\prod_{j=1}^{N}\det\boldsymbol{\Delta}_j. \end{aligned} \tag{7.31}$$

7.4.2 Case of density-density interactions

In the specific case of the two-band Hubbard model introduced in Eq. (4.1), a frequently employed approximation is to consider only the so-called density-density interactions. This consists in setting $\gamma\equiv 0$ in Eq. (4.1). In this case, the local Hamiltonian H_{loc} is diagonal in the occupation number basis. As a consequence, it is possible to represent the time evolution of the impurity by a collection of segments, which represent the status (occupied or unoccupied), of each of the fermionic flavors. This situation is illustrated in Fig. 7.2 The trace of a configuration over the local Hamiltonian, which enters Eq. (7.30), is written as

$$W_{\text{loc}}=\text{Tr}_c\left[T_\tau e^{-\beta H_{\text{loc}}}c_{j_k}(\tau_k)c^\dagger_{j'_k}(\tau'_k)\ldots c_{j_1}(\tau_1)c^\dagger_{j'_1}(\tau'_1)\right]. \tag{7.32}$$

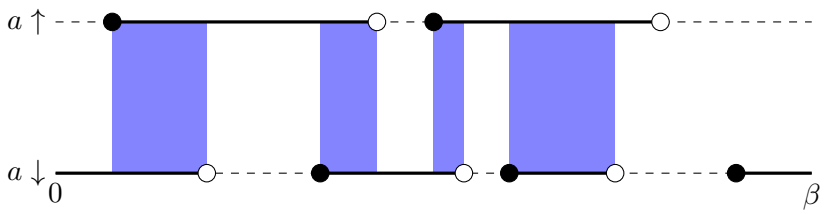

Figure 7.2: Illustration of a configuration of order $k = 5$ for the Anderson model with one orbital (a) and two spins. The solid (empty) circles represent the action of a creation (annihilation) operator. The thick segments denote the imaginary times when the flavor is occupied, the thin sections denote the imaginary times when the flavor is not occupied. The colored blue areas help visualize the regions where the orbital is doubly occupied.

For illustration, in the case of the single orbital Anderson model of Eq. (6.10), the local Hamiltonian in the occupation number basis is given by

$$\begin{pmatrix} 0 & 0 & 0 & 0 \\ 0 & -\mu & 0 & 0 \\ 0 & 0 & -\mu & 0 \\ 0 & 0 & 0 & U-2\mu \end{pmatrix}, \tag{7.33}$$

so that the number in Eq. (7.32) can be easily determined with the help of:

- the lengths of the segments present in the configuration for each flavor j, whose combined length is denoted L_j (segments represented in Fig. 7.2 by the thick lines),
- the length of the overlaps between the segments, which represent the simultaneous occupation of orbitals i and j, denoted as O_{ij} (overlaps represented in Fig. 7.2 by the shaded areas).

In terms of these quantities, Eq. (7.32) becomes

$$W_{\text{loc}} = s e^{\mu \sum_j L_j} e^{-\sum_{i<j} U O_{ij}}, \tag{7.34}$$

where s is a sign depending on the operator sequence. The case where there are no operators for a given flavor need to be handled separately in the code, as completely full or empty lines on the $[0, \beta)$ imaginary time interval.

The algorithm can therefore be split in three parts:

- Update the segment configuration, using a Markov chain Monte Carlo algorithm in the space of segment configurations of all orders, so that configurations are generated with the weight that they contribute to the partition function Z.
- Compute the determinant of the associated matrix $\mathbf{\Delta}$.
- Compute W_{loc}, from the length and overlaps of the segments in the configuration.

7.4.3 Updates

In this section we describe how Monte Carlo updates are executed on segment configurations, for the case of density-density interactions introduced in Sec. 7.4.2.

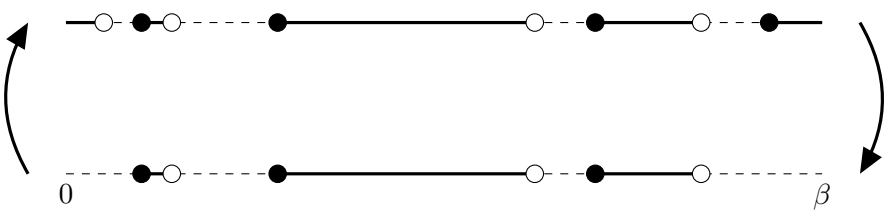

Figure 7.3: . Illustration of the segment insertion/removal step in the segment implementation of the CT-HYB solver. The symbols are defined in Fig. 7.2.

Illustration: segment insertion/removal

For illustration of the method, we consider a configuration $x_k = \{(\tau_1^s, \tau_1^e), \ldots, (\tau_k^s, \tau_k^e)\}$ containing k segments, and try to insert a new segment $s_{k+1} = (\tau_{k+1}^s, \tau_{k+1}^e)$, to obtain configuration y_{k+1}, as illustrated in Fig. 7.3. An orbital for insertion is chosen randomly with uniform probability among all orbitals. Then, and τ_{k+1}^s is chosen randomly with uniform probability in the interval $[0, \beta)$. The move is rejected if τ_{k+1}^s lies on an existing segmented, and accepted otherwise. If the move is accepted, τ_{k+1}^e is drawn randomly in the interval $[\tau_{k+1}^s, \tau_{k+1}^{s'}]$, where $\tau_{k+1}^{s'}$ is the starting time of the next segment on the chosen orbital. The reverse move is the removal of a segment, which needs to be picked among the $k+1$ available segments in y_{k+1}.

The proposal probabilities for the insertion and the inverse move are thus given by:

$$\begin{aligned} W_{\text{prop}}(x_k \to y_{k+1}) &= \frac{d\tau^2}{\beta l_{\max}}, \\ W_{\text{prop}}(y_{k+1} \to x_k) &= \frac{1}{k+1}. \end{aligned} \tag{7.35}$$

Using $p(x_k) \propto \left(\frac{d\tau}{\beta}\right)^{2k}$, the Metropolis algorithm leads to the following acceptance ratios for the proposed moves:

$$W_{\text{acc}}(x_k \to y_{k+1}) = \min\left(1, \frac{1}{k+1}\frac{l_{\max}}{\beta}\frac{\det \mathbf{\Delta}(y_{k+1}) W_{\text{loc}}(y_{k+1})}{\det \mathbf{\Delta}(x_k) W_{\text{loc}}(x_k)}\right). \tag{7.36}$$

Other kinds of updates are easily considered, and improve the statistics of the algorithm. Among those are the insertion/removal of anti-segments, which consist in annihilator-creator pairs, in place of the creator-annihilator pairs which make up a segment. Shifts of one or of both ends of segments or antisegments are also considered in order to improve the efficiency of the sampling.

The acceptance probabilities introduced above involve the computation of ratios of determinants of squares matrices which differ by the insertion/removal of one column and one row. Fast algorithms allow the efficient computation of the ratios of such determinants, provided the inverse of $\mathbf{\Delta}$ is readily available. This is why this inverse is stored in the implementation of the algorithm, rather that $\mathbf{\Delta}$ itself. The details for these fast update formulas are provided in Appendix C.

7.4.4 Accumulation formulas: Green's function

The most straightforward way to measure observables in the described framework is to use Eq. (7.10). We now present the procedure followed in our implementation of the algorithm

(based on a modification of the open source implementation provided by the project Alps v2.0 [165]) for the evaluation of the Green's function $G(\tau,\tau') = -\left\langle c(\tau)c^\dagger(\tau')\right\rangle$. The series to average for the calculation of this observable is the following:

$$\begin{aligned} G_{lm}(\tau_l,\tau_m) = -Z_{\text{bath}} \sum_{k=0}^{\infty} \int_0^\beta d\tau_1 \cdots \int_{\tau_{k-1}}^\beta d\tau_k \int_0^\beta d\tau'_1 \cdots \int_{\tau'_{k-1}}^\beta d\tau'_k \\ \times \sum_{\substack{j_1,j_2,\cdots,j_k \\ j'_1,j'_2,\cdots,j'_k}} \text{Tr}_c \left[T_\tau e^{-\beta H_{\text{loc}}} c_l(\tau_l) c_m^\dagger(\tau_m) c_{j_k}(\tau_k) c_{j'_k}^\dagger(\tau'_k) \cdots c_{j_1}(\tau_1) c_{j'_1}^\dagger(\tau'_1) \right] \det \mathbf{\Delta}_k, \end{aligned} \tag{7.37}$$

where the operator $c_l(\tau_l)c_m^\dagger(\tau_m)$ has been introduced inside the trace, so that its expected value is obtained as a result of the sampling procedure.

This shows that the configurations for the evaluation of the Green's functions can be thought of as configurations for the evaluation of the partition function, with the addition of one creation and one annihilation operators. Equivalently, these can be thought of as configurations for the evaluation of the partition function, with no hybridization line connecting $c_l(\tau_l)$ and $c_m^\dagger(\tau_m)$. In practice, the estimator for $G_{lm}(\tau_l,\tau_m)$ is obtained by identifying a pair of creation and annihilation operators in a configuration for the evaluation of the partition function, and removing the hybridization line between them. Following this, we need to evaluate the determinant of the matrix $\mathbf{\Delta}_{k-1}^{\tau_l,\,\tau_m}$, where $\mathbf{\Delta}_{k-1}^{\tau_l,\,\tau_m}$ is defined as the matrix $\mathbf{\Delta}_k$, from which the column s_l and the row s_m (corresponding to the operators c_l and $c_m^\dagger$) are removed.

Let us define $p_Z(\{(\tau_1^s,\tau_1^e),\ldots,(\tau_k^s,\tau_k^e)\})$ as the weight of the configuration

$$\mathcal{C}_Z \equiv \{(\tau_1^s,\tau_1^e),\ldots,(\tau_k^s,\tau_k^e)\},$$

used for the sampling of the partition function Z. In the same fashion, let us introduce p_G as the weight associated to the configuration $\mathcal{C}_G\big(\{(\tau_1^s,\tau_1^e),\ldots,(\tau_{k-1}^s,\tau_{k-1}^e),(\tau_m,\tau_l)\}\big)$, used for the sampling of the Green's function G. The configuration $\mathcal{C}_G$ is defined as the configuration $\mathcal{C}_Z$, in which the hybridization line between τ_l and τ_m has been removed. Following Eq. (7.30), we have

$$\begin{aligned} &p_Z(\{(\tau_1^s,\tau_1^e),\ldots,(\tau_k^s,\tau_k^e)\}) \equiv W_{\text{loc}} \det \mathbf{\Delta} \\ &= \text{Tr}_c \left[T_\tau e^{-\beta H_{\text{loc}}} c_{j_k}(\tau_k) c_{j'_k}^\dagger(\tau'_k) \ldots c_{j_1}(\tau_1) c_{j'_1}^\dagger(\tau'_1) \right] \det \mathbf{\Delta}. \end{aligned} \tag{7.38}$$

The definition of W_{loc} Eq. (7.32) shows that its value is not modified by the removal of a hybridization line. On the other hand, the hybridization matrix $\mathbf{\Delta}$ becomes $\mathbf{\Delta}_{k-1}^{\tau_l,\,\tau_m}$. The contribution of the determinant is therefore not the same. One can show, using the expansion in minors of the inverse matrix [140], that the resulting ratio of weights reads

$$\frac{p_G(\{(\tau_1^s,\tau_1^e),\ldots,(\tau_m,\tau_l)\})}{p_Z\big(\{(\tau_1^s,\tau_1^e),\ldots,(\tau_k^s,\tau_k^e)\}\big)} = \frac{\det \mathbf{\Delta}_{k-1}^{\tau_l,\,\tau_m}}{\det \mathbf{\Delta}_k} = (\mathbf{\Delta})^{-1}_{s_m,s_l} \equiv M_{s_m,s_l}. \tag{7.39}$$

This observation can be expressed more formally, as was demonstrated by Boehnke et al. [166]. As was stated above, we can express the partition function, or any function f

over the configuration space (the Green's function is the one we will focus on):

$$\begin{aligned} Z &= \sum_{\mathcal{C}} p(\mathcal{C}), \\ \langle f(\mathcal{C}) \rangle &= \frac{1}{Z} \sum_{\mathcal{C}} p(\mathcal{C}) f(\mathcal{C}). \end{aligned} \tag{7.40}$$

For a given pair (l, m) of orbitals, and a given pair of imaginary times (τ_1, τ_2) the corresponding matrix element of the Green's function is obtained from the following choice for f:

$$f(\mathcal{C}) \equiv G_{lm}(\tau_1, \tau_2) = -\frac{1}{Z} \frac{\partial Z}{\partial \Delta_{ml}(\tau_1, \tau_2)}. \tag{7.41}$$

Eq. (7.32) shows that W_{loc} does not depend on the hybridization matrix, so that the dependence of Z with respect to Δ_{ml} is explicitly given by Eq. (7.38), and is governed by the dependence of $\det \mathbf{\Delta}$ on $\Delta_{ml}(\tau_1, \tau_2)$.

In order to find the expression for this dependence, We can introduce the Grassmann integral representation of $\det \mathbf{\Delta}$:

$$\begin{aligned} \det \mathbf{\Delta} &= \int \prod_i d\eta_i d\eta_i^* e^{\sum\limits_{ij} \eta_i^* \Delta_{ij} \eta_j} \\ \Rightarrow \frac{\partial \det \mathbf{\Delta}}{\partial \Delta_{ml}} &= \int \prod_i d\eta_i d\eta_i^* (\eta_m^* \eta_l) e^{\sum\limits_{ij} \eta_i^* \Delta_{ij} \eta_j}. \end{aligned} \tag{7.42}$$

In Sec. A, we present a derivation of Eq. (A.3), which can easily be modified to show that

$$\int \prod_i d\eta_i d\eta_i^* (\eta_m^* \eta_l) e^{\sum\limits_{ij} \eta_i^* \Delta_{ij} \eta_j} = \det \mathbf{\Delta} \times M_{lm}. \tag{7.43}$$

In the following, we make the dependence of $\mathbf{\Delta}$ on the configuration $\mathcal{C} \equiv (n, \{\lambda_j, \lambda'_j, \tau_j, \tau'_j\})$ explicit. In this notation, λ'_j (λ_j) is the flavor of the creation (annihilation) operator with index j, which acts at imaginary time τ'_j (τ_j), and n is the order of the configuration. Using this notation, the matrix elements of $\mathbf{\Delta}(\mathcal{C})$ are given by:

$$\begin{aligned} \Delta(\mathcal{C})_{ij} &\equiv \Delta_{\lambda_i, \lambda'_j}(\tau_i - \tau'_j) \\ \Rightarrow \frac{\partial p(\mathcal{C})}{\partial \Delta_{ml}(\tau_2, \tau_1)} &= \frac{p(\mathcal{C})}{\det \mathbf{\Delta}(\mathcal{C})} \sum_{\alpha,\beta=1}^{n} \frac{\partial \det \mathbf{\Delta}(\mathcal{C})}{\partial \Delta(\mathcal{C})_{\beta\alpha}} \frac{\partial \Delta(\mathcal{C})_{\beta\alpha}}{\partial \Delta_{ml}(\tau_2, \tau_1)} \\ = p(\mathcal{C}) \sum_{\alpha,\beta=1}^{n} M(\mathcal{C})_{\beta\alpha} \frac{\partial \Delta(\mathcal{C})_{\beta\alpha}}{\partial \Delta_{ml}(\tau_2, \tau_1)} &= p(\mathcal{C}) \sum_{\alpha,\beta=1}^{n} M(\mathcal{C})_{\beta\alpha} \delta\big(\tau_1 - \tau'_\alpha\big) \delta(\tau_2 - \tau_\beta) \delta_{\lambda'_\alpha, l} \delta_{\lambda_\beta, m}. \end{aligned} \tag{7.44}$$

This leads to the accumulation formula for the Green's function, in imaginary time [11, 159]:

$$G_{lm}(\tau_1, \tau_2) = -\left\langle \sum_{\alpha,\beta=1}^{n} M(\mathcal{C})_{\beta\alpha} D(\mathcal{C})^{\alpha\beta}_{lm,\, \tau_1 \tau_2} \right\rangle, \tag{7.45}$$

where $D(\mathcal{C})^{\alpha\beta}_{lm,\,\tau_1\tau_2} \equiv \delta(\tau_1 - \tau'_\alpha)\delta(\tau_2 - \tau_\beta)\delta_{\lambda'_\alpha,l}\delta_{\lambda_\beta,m}$. This estimate can be binned into as fine a time grid as desired. The terminology "continuous time" solver is due to the fact that the performance of the algorithm does not depend on the finesse of the time mesh.

Efficient estimators for the density, the double occupancy, the potential energy, and in general, for any observable which commutes with the local Hamiltonian, are easily available, e.g.:

$$\begin{aligned} E_{\text{pot}} &= \sum_{i<j} U_{ij} D_{ij}, \\ D_{ij} &= \langle n_i n_j \rangle_{\text{MC}} . \end{aligned} \tag{7.46}$$

The average occupation n_j of flavor j is given by the associated total length of the segments associated to this flavor in the given configuration, L_j: $n_j = \langle L_j/\beta \rangle$. Double occupancies are related to the overlaps introduced in Eq.(7.34): $D_{ij} = \langle O_{ij}/\beta \rangle$. Since overlaps and lengths of segments are computed at every step for the determination of the acceptance ratio, such observables can be obtained at essentially no additional computational cost.

Similar formulas are available for the measurement of the two-particle Green's function [166]. From this estimate of the Green's function, the self-energy may be evaluated by application of Dyson's equation. It is also possible to sample the Green's function in Matsubara frequency directly, and so-called improved estimators have been developed, which greatly improve the high-frequently noise of these estimators at high frequency [167, 168]. Recently, the so-called worm algorithm was developed for the sampling of one-particle and two-particle quantities [169]. In this framework, the importance sampling is adapted to the quantity being evaluated (one- or two-particle Green's function), instead of using the weights of the configurations as they contribute to the partition function, as in the scheme just described. The formulas for the improved estimators have been derived for worm sampling as well [170].

Chapter 8

Main kink in the electronic dispersion of cuprate superconductors: role of the upper branch of the hour-glass magnetic spectrum

8.1 Introduction

The kink at 50–80 meV in the electronic dispersion along the Brillouin zone diagonal (i.e., from $(0,0)$ to (π,π)) of high-T_c cuprate superconductors [25, 29, 30, 40, 42, 43, 171, 172] has been the object of intense scrutiny by the scientific community since it was first reported. Understanding of the kink may be of importance in the context of the quest for the mechanism of high temperature superconductivity. Unfortunately, a satisfactory understanding has not yet been achieved. While there is a broad (yet not unanimous [15, 27, 173–175]) consensus that the kink is due to an interaction with bosonic excitations, the nature of the latter excitations remains controversial. It is debated whether they are of lattice [30, 39, 176–182] (phonon), magnetic [34, 40, 41, 183–194] (spin fluctuation), or more complex [44, 195–199] origin [36].

Regarding the magnetic scenario, it has been claimed for some time that the kink reflects the coupling of the charged quasiparticles to the resonance mode observed by neutron scattering [31, 200, 201]. In a more recent study by Dahm and coworkers [202], however, it was strongly suggested that in underdoped YBCO $YBa_2Cu_3O_{6.6}$, the kink is due to the upper branch of the hourglass dispersion of spin fluctuations, rather than to the resonance mode. This has opened the question of how the influence of the resonance mode and that of the upper branch cooperate, under which conditions the former is the dominant one, and under which the latter.

A relevant piece of information was recently reported by Plumb et al. [45]. These authors have shown that in nearly optimally doped $Bi_2Sr_2CaCu_2O_{8+\delta}$ (Bi2212), the energy of the kink decreases as a function of the angle between the Fermi surface cut and the Brillouin zone diagonal, from about 65 meV at the node (i.e., at the diagonal), to about 55 meV roughly one-third of the way to the antinode. In addition, when going from the node to the antinode, the kink and also the underlying structures of the quasiparticle self-

energy sharpen dramatically. These trends of the kink energy and sharpness have been compared with simple estimates for several phonon modes and for the upper branch of the hourglass of spin fluctuations, and the greatest similarity has been found for the latter.

The aims of the present study are (a) to address the angular dependence of the kink using the fully selfconsistent version of the Eliashberg equations employed in previous studies by some of the authors [203, 204], and the same inputs (band structure and spin susceptibility) as in Ref. [202], and to find out whether the model is capable of accounting for—in addition to the nodal dispersion—the trends reported recently by Plumb et al. (b) To clarify the interplay between the roles of the resonance mode and of the upper branch of the hourglass in the formation of the kink.

The rest of the paper is organized as follows. In Sec. 8.2 we summarize the equations employed in the calculations, present important computational details and discuss our choice of the values of the input parameters. Our results are presented in Secs. 8.3 and 8.4. In Subsection 8.3.1, we address qualitative aspects of the nodal kink, among others the role played by the kurtosis of the resonance mode of the spin susceptibility. In Subsection 8.3.2, we provide a detailed account of the relation between the energy and the shape of the nodal kink, and the structures of the quasiparticle self-energy. In particular, we highlight the effect of the magnitude of the coupling constant on the properties of the kink. In Sec. 8.4 we address the evolution of the kink when going from the node to the antinode. First (in Subsec. 8.4.1), we use the effective self-energy approach of Ref. [45] and then (in Subsec. 8.4.2) our own approach based on an approximate relation between the properties of the kink and those of the quantity $S(\boldsymbol{k}, E) \equiv \Sigma_0(\boldsymbol{k}, E) + \phi(\boldsymbol{k}, E)$. Here $\Sigma_0(\boldsymbol{k}, E)$ and $\phi(\boldsymbol{k}, E)$ are the τ_0 component of the self-energy and the anomalous self-energy, respectively. In Sec. 8.5 we compare our results with the experimental data of Refs. [202] and [45]. It is shown that a minor modification of the input parameter values brings the renormalized (nodal) Fermi velocity and the energy of the nodal kink close to the experimental values for YBCO [202]. The calculated magnitude of the slope of the angular dependence of the kink energy is only slightly larger than that of Bi2212 [45]. We make a prediction concerning the angular dependence of the kink energy in underdoped YBCO and provide a possible qualitative interpretation of the difference between the kink in underdoped YBCO and that in Bi2212.

8.2 Spin-fermion model based calculations

Within the spin-fermion model [33, 36, 129, 188, 205, 206], the self-energies $\widehat{\Sigma}_A(\boldsymbol{k}, \mathrm{i}E_n)$ and $\widehat{\Sigma}_B(\boldsymbol{k}, \mathrm{i}E_n)$ of the antibonding and bonding bands of a bilayer cuprate superconductor, such as Bi2212 or YBCO, are given by [34]:

$$\widehat{\Sigma}_{A/B} = g^2 \big[\chi^o_{\mathrm{SF}} * \widehat{\mathcal{G}}_{B/A} + \chi^e_{\mathrm{SF}} * \widehat{\mathcal{G}}_{A/B} \big]. \tag{8.1}$$

Here g is the coupling constant, whose dependence on $\boldsymbol{k}$ is neglected, $\chi^o_{\mathrm{SF}}(\boldsymbol{q}, \mathrm{i}\omega_n)$ and $\chi^e_{\mathrm{SF}}(\boldsymbol{q}, \mathrm{i}\omega_n)$ are the odd and even components of the spin susceptibility [201], respectively, and the symbol $\chi_{\mathrm{SF}} * \widehat{\mathcal{G}}$ stands for

$$\frac{1}{\beta N} \sum_{\boldsymbol{k'}, \mathrm{i}E'_n} \chi_{\mathrm{SF}}(\boldsymbol{k} - \boldsymbol{k'}, \mathrm{i}E_n - \mathrm{i}E'_n) \times \widehat{\mathcal{G}}(\boldsymbol{k'}, \mathrm{i}E'_n). \tag{8.2}$$

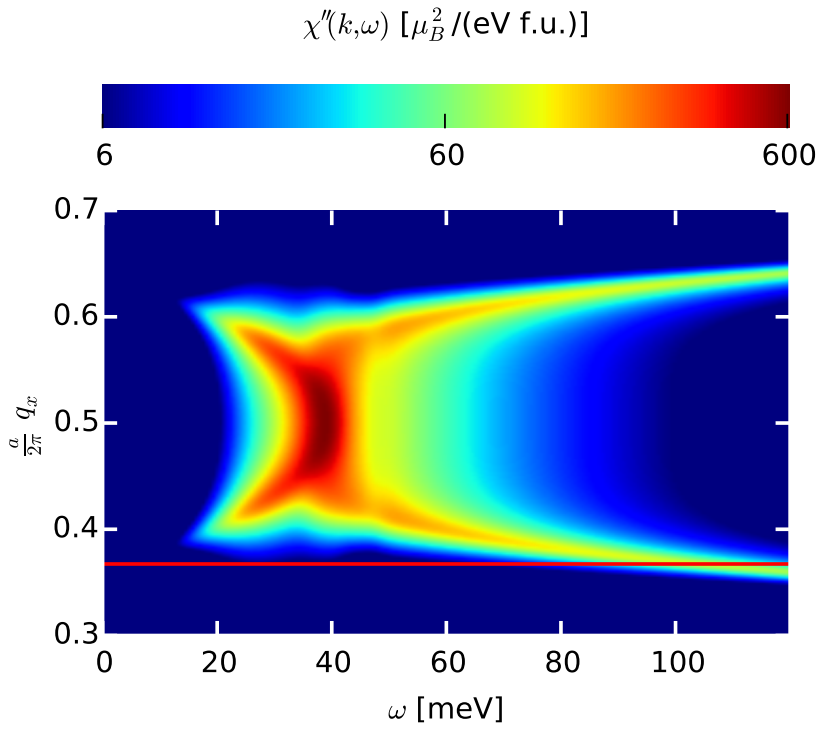

Figure 8.1: Cut of the spin excitation spectrum $\chi''(\boldsymbol{q},\omega)$ along the nodal axis, calculated using the set of parameter values S_1. The solid red line corresponds to the position of the vector $\boldsymbol{Q}_0$ shown in Fig. 8.2. Reprinted figure with permission from Ref. [209].

Further, $\widehat{\mathcal{G}}_{A/B}(\boldsymbol{k}, \mathrm{i}E_n)$ are the Nambu propagators of the renormalized electronic quasiparticles:

$$\widehat{\mathcal{G}}_{A/B}(\boldsymbol{k}, \mathrm{i}E_n) = \frac{1}{\mathrm{i}E_n\widehat{\tau}_0 - (\epsilon_{\boldsymbol{k}}^{A/B} - \mu)\widehat{\tau}_3 - \widehat{\Sigma}_{A/B}(\boldsymbol{k}, \mathrm{i}E_n)}, \tag{8.3}$$

where $\widehat{\tau}_0$ and $\widehat{\tau}_3$ are the Pauli matrices, $\epsilon_{\boldsymbol{k}}^A$ and $\epsilon_{\boldsymbol{k}}^B$ are the bare dispersion relations of the two bands, and μ is the chemical potential. We have considered only the odd channel (i.e., only the term with χ^o_{SF} in Eq. (8.1)). This channel has been demonstrated [34] to be the dominant one, in particular because χ^e_{SF} does not exhibit a pronounced resonance mode [207]. A broadening factor δ is used in the analytic continuation of the propagators to the real axis ($\mathrm{i}E_n \to E + \mathrm{i}\delta$), $\delta = 1\,\mathrm{meV}$.

The input parameters of the model are the imaginary component χ'' (the indices are omitted for simplicity) of the spin susceptibility, the dispersion relations $\epsilon_{\boldsymbol{k}}^{A/B}$, the chemical potential μ, and the coupling constant g. For all of them except for g, and except otherwise stated, we have used the parametrization published in Ref. [202], that is based on fits of the neutron [208] and photoemission data of underdoped $YBa_2Cu_3O_{6.6}$. The spin susceptibility exhibits the hourglass shape with the resonance mode at $q = (\pi/a, \pi/a)$, illustrated in Figure 8.1 by a cut of the spectrum of $\chi''(\boldsymbol{q},\omega)$ along the nodal axis. The Fermi surfaces corresponding to the dispersion relations $\epsilon_{\boldsymbol{k}}^A$ and $\epsilon_{\boldsymbol{k}}^B$ are shown in Fig. 8.2. The distances from the Γ point to the Fermi surfaces, along the Brillouin zone diagonal and expressed in units of $\frac{\pi}{a}\sqrt{2}$, are $k^A_{F,N} = 0.342$, and $k^B_{F,N} = 0.393$. The calculations are done for $T = 20\,\mathrm{K}$.

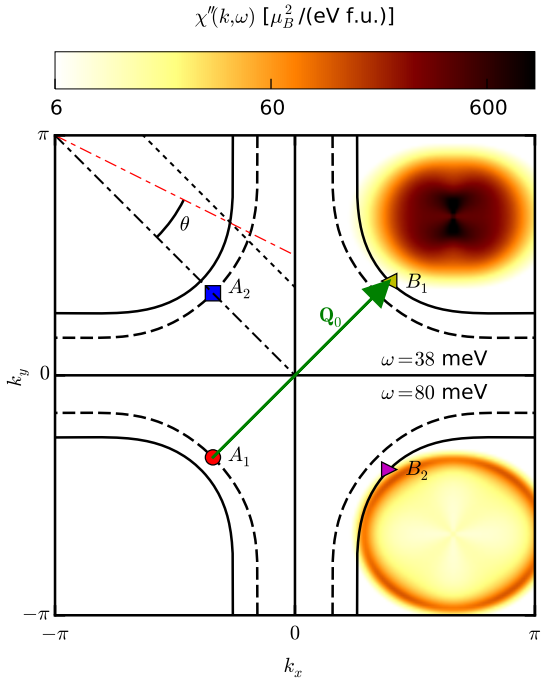

Figure 8.2: The Fermi surfaces for the antibonding (dashed line), and bonding (solid line) bands, obtained using the set of parameter values S_1. The solid green arrow represents the interband scattering vector $\boldsymbol{Q_0}$. The red dashed-dotted line (the nearby dashed line) indicates an example of the Fermi surface cut used in Subsec. 8.4.1 (8.4.2). Also shown are two (suitably shifted) constant energy cuts of the spin susceptibility. The one shown in the upper right quadrant corresponds to $\chi''(\boldsymbol{k}-\boldsymbol{k}_{A_1},\omega=38\,\text{meV})$, the one shown in the bottom right quadrant to $\chi''(\boldsymbol{k}-\boldsymbol{k}_{A_2},\omega=80\,\text{meV})$. Reprinted figure with permission from Ref. [209].

Finally, we address the coupling constant g. In Ref. [202], the magnitude of the superconducting gap Δ_{SC} was fixed ($\Delta_{\text{SC}}=30\,\text{meV}$), so that the value of the coupling constant g could be obtained by imposing that the value of the calculated renormalized Fermi velocity be consistent with the angle resolved photoemission (ARPES) data. This choice leads to a high value of the superconducting transition temperature T_{c} of 174 K. In the present work, the iterative solution of Eqs. (8.1) and (8.3) has been performed in a fully self-consistent manner, along the lines of Refs. [203, 204]. The renormalized dispersions are adjusted at each iteration, following the approach developed in Refs. [202, 210], in such a way that the renormalized Fermi surfaces are fixed and match the ARPES profiles used as inputs. Within this framework, Δ_{SC} is not constrained, so that its dependence on g has allowed us to fix the value of g by requiring that $\Delta_{\text{SC}}=30\,\text{meV}$. The resulting value of g of 1.0 eV is considerably smaller than that of Ref. [202] (the coupling constant of the latter reference $\bar{U}$ is connected to our g by $\bar{U}=g\sqrt{\frac{2}{3}}$, and the value of $\bar{U}$ used therein corresponds to $g=1.95\,\text{eV}$). The renormalization of the nodal Fermi velocity is weaker and the value of T_{c} lower with this smaller value of g. The set of parameter values just introduced is the main set used throughout the paper, and is referred to as set S_1.

The calculations have been performed using the fast Fourier transform algorithm, taking

full advantage of the symmetries of the system. We have used a grid of 256×256 points in the Brillouin zone and a cutoff of 4 eV to limit the number of Matsubara frequencies. We have checked, by varying the density of the grid and the cutoff, that these values are sufficient.

8.3 The kink in the dispersion relation along the nodal axis

8.3.1 Role of the upper branch of χ''

The solid blue line in Fig. 8.3 represents the electronic dispersion along the nodal axis for the bonding band. For a given energy, the associated value of k is obtained as the root of the real part of the denominator of Eq. (8.3). It coincides with the value of k corresponding to the maximum of the spectral function for the given energy. The dashed line connects the quasiparticle peak at k_F and the maximum of the spectral function corresponding to the high energy cutoff of 250 meV. The kink is smooth and broad, with a relatively small amplitude. The discrepancy between this profile and the result of Ref. [202] is mainly due to the lower value of g used in the present study, as discussed in detail in Subsec. 8.3.2.

The position and the profile of the kink can be understood in terms of a combination of the geometrical features of the Fermi surfaces and those of the spin susceptibility spectrum. Consider a scattering process whereby an electron from the bonding band, of quasimomentum $\boldsymbol{k}$ and energy E, is scattered to the antibonding band, quasimomentum $\boldsymbol{k} - \boldsymbol{q}$ and energy $E - \omega$, while a spin excitation of quasimomentum $\boldsymbol{q}$ and energy ω is emitted (an example with $\boldsymbol{k} = \boldsymbol{k}_{B_1}$ and $\boldsymbol{q} = \boldsymbol{Q}_0 \equiv \boldsymbol{k}_{B_1} - \boldsymbol{k}_{A_1}$ is shown in Fig. 8.2). The process can occur with a considerable probability only if the momentum $\boldsymbol{q}$ is such that $\chi''(\boldsymbol{q}, \omega)$ is significant. Let us consider scattering processes along the direction of the Brillouin zone diagonal, from the region around $\boldsymbol{k}_{B_1}$ to the region around $\boldsymbol{k}_{A_1} = \boldsymbol{k}_{B_1} - \boldsymbol{Q}_0$. Figure 8.2 shows that such processes have a negligible probability for $\omega \simeq 40$ meV (see the constant energy cut shown in the upper right quadrant of Fig. 8.2). The contribution of the resonance mode to the quasiparticle self-energy $\widehat{\Sigma}^B_{|\boldsymbol{k}=\boldsymbol{k}_{B_1}}$ can thus be expected to be negligible, and the nodal dispersion to be almost unaffected by the presence of the resonance mode. For $\omega \simeq 80$ meV – the energy of the crossing point of the red line and the upper branch of the hourglass in Fig. 8.1 –, however, the probability is considerable (see the constant energy cut in the lower right quadrant of Fig. 8.2). The nodal dispersion can thus be expected to be strongly influenced by the coupling to spin excitations of the upper branch. Indeed, the calculated spectrum of $\mathrm{Im}\left\{\widehat{\Sigma}^B_{|\boldsymbol{k}=\boldsymbol{k}_{B_1}}\right\}$, shown in Fig. 8.5, does not exhibit any significant feature around 40 meV due to the resonance mode. Instead, it displays a steep onset around 80 meV due to the upper branch.

The kink itself (defined as the minimum of the second derivative of the dispersion) is located at a higher energy of about 130 meV. The difference is due to two facts. (a) The kink energy corresponds to the energy of the maximum of the real part of the self-energy (connected to its imaginary part through the Kramers-Kronig relation). This maximum is located at an energy higher than that of the onset of the imaginary part. This issue is discussed in detail in Subsec. 8.3.2. (b) The self-energy is k-dependent and in the region of k-space around the kink (where $|\boldsymbol{k}| < k^B_{F,N}$), its imaginary part sets on at a higher energy than for k close to $k^B_{F,N}$. This can be inferred from Figure 8.1: the energy of the crossing point of the upper branch of χ'' with a fixed q horizontal line increases when the magnitude of q decreases. The impact of the k-dependence of the self-energy on the energy of the kink is quantitatively assessed in Subsec. 8.3.2. The validity of the simple relation

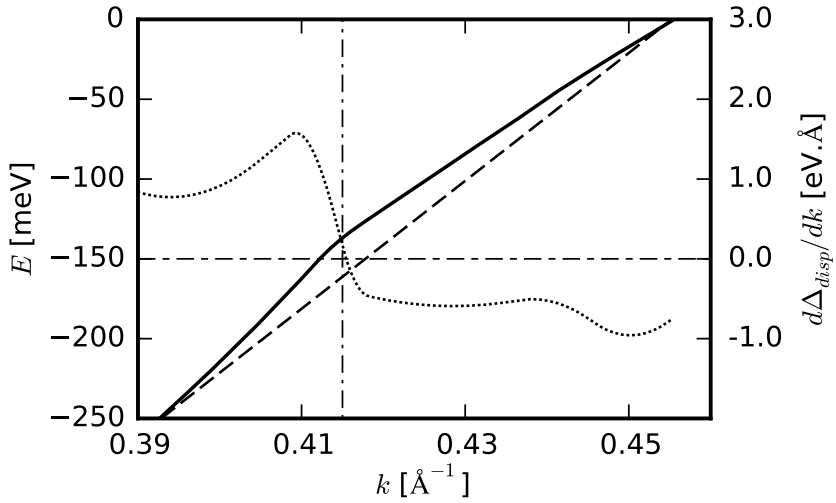

Figure 8.3: Dispersion relation along the Brillouin zone diagonal for the bonding band. The solid line represents the renormalized dispersion. The dashed line represents a linear approximation to the bare dispersion. The dotted line is the derivative of the difference Δ_{disp} between the renormalized dispersion and the bare dispersion. The vertical dash-dotted line is a guide to the eye. The calculations have been performed using the set of parameter values S_1. Reprinted figure with permission from Ref. [209].

between the kink energy and the boson energy has been examined, in a different context, by Schachinger and Carbotte [211].

The above analysis confirms the conclusions of Ref. [202] regarding the origin of the kink. However, it additionally reveals that the presence of the upper branch *per se* is not a sufficient condition for it to play the prominent role in the formation of the nodal kink. Another necessary condition is the simultaneous occurrence of a low kurtosis [212] of $\chi''(\boldsymbol{q}, \omega_{\mathrm{res}})$ (where ω_{res} is the frequency of the resonance mode) and of a relatively small value of $|\boldsymbol{Q}_0|$. Only under these conditions is the contribution of the resonance mode negligible. A higher kurtosis of $\chi''(\boldsymbol{q}, \omega_{\mathrm{res}})$ or a larger value of $|\boldsymbol{Q}_0|$ would allow the contribution of the resonance to be large enough and dominate that of the high-energy branch. This effect was confirmed by separate calculations of the respective contributions of the resonance mode and of the upper branch/continuum for various shapes of the spectrum of χ''.

The low kurtosis exhibited by $\chi''(\boldsymbol{q}, \omega_{\mathrm{res}})$ is illustrated in Fig. 8.4, which displays $\chi''_{\mathrm{int}}(q) = \int_0^{40\,\mathrm{meV}} \chi''(q, \omega) d\omega$ as a function of q for $\boldsymbol{q}$ along the Brillouin zone diagonal. The figure allows us to assess the q-space distribution of the spectral weight of low energy spin fluctuations including the resonance mode. The solid green line, corresponding to the spectrum of χ'' used in the present study, exhibits a broad peak and thin tails, both characteristic of a distribution with low kurtosis. The dashed blue line corresponds to the form of the spin susceptibility used by two of the present authors in previous studies [203, 213, 214] (the MBC form in the following). It possesses a higher kurtosis, with both a narrower peak and fatter tails. Finally, the black dash-dotted line represents the susceptibility profile used by Eschrig et al. in their thorough analysis of the dispersion anomalies within the spin-fermion model [186] (see also Ref. [188]). It also displays a relatively high kurtosis. The vertical red dashed line sits at the position of the interband vector $\boldsymbol{Q}_0$. It

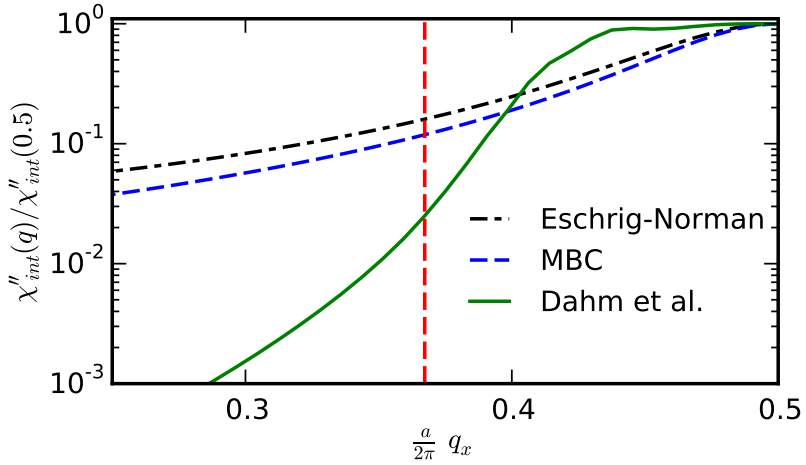

Figure 8.4: The quantity χ''_{int}, defined in the text, as a function of q_x along the Brillouin zone diagonal. The three lines correspond to the three profiles of $\chi''(\boldsymbol{q},\omega)$ discussed in the text. The vertical red dashed line indicates the position of the interband vector $\boldsymbol{Q_0}$. Reprinted figure with permission from Ref. [209].

can be seen that both for the MBC profile and for the Eschrig-Norman one, $\chi''_{\mathrm{int}}(|\boldsymbol{Q}_0|)$ is significant, approximately an order of magnitude larger than the corresponding value for the present spectrum of χ''. This has a direct impact on the magnitude of the contribution of the resonance mode to the quasiparticle self-energy. Note, that the spectrum of χ'' used here was obtained from a fit to experimental inelastic neutron scattering data, while the other two spectra (MBC and Eschrig-Norman) are based on assumptions about the q-dependence. The considerations here are complementary to those of a previous work by Chubukov and Norman [185], where the weakening of the effect of the resonance on the near nodal dispersion has been addressed using an analytical approach.

8.3.2 Impact of the magnitude of the coupling constant

In this subsection, we examine the link between the kink in the nodal dispersion and the features of the fermionic self-energy. Using Eq. (8.3), we find that the renormalized velocity v for a quasimomentum k along the nodal axis is given by:

$$v(\bar{\epsilon}_k) = \frac{v_0(\bar{\epsilon}_k) + \partial_k \Sigma'(k,\bar{\epsilon}_k)}{1 - \partial_E \Sigma'(k,\bar{\epsilon}_k)}, \tag{8.4}$$

where v_0 is the bare velocity and $\bar{\epsilon}_k$ the renormalized dispersion. The known form of the bare velocity allows one to approximate $v_0(\bar{\epsilon}_k)$ by its value at the Fermi surface, v_{F_0}. Moreover, it is usually assumed that the momentum dependence of the self-energy is weak [188], so that the term $\partial_k \Sigma'(k,\bar{\epsilon}_k)$ in Eq. (8.4) can be neglected, and the term $\partial_E \Sigma'(k,\bar{\epsilon}_k)$ replaced with $\partial_E \Sigma'(k=k_F,\bar{\epsilon}_k)$. With these approximations, the energy dependence of v is determined by the renormalization factor $Z(\bar{\epsilon}_k) = 1 - \partial_E \Sigma'(k=k_F,\bar{\epsilon}_k)$, and the energy of the kink coincides with the energy of the extremum of $\Sigma'(k=k_F,\bar{\epsilon}_k)$. In the following, we quantitatively assess the impact of the momentum dependence of the self-energy on the kink energy and shape, and identify two qualitatively distinct regimes.

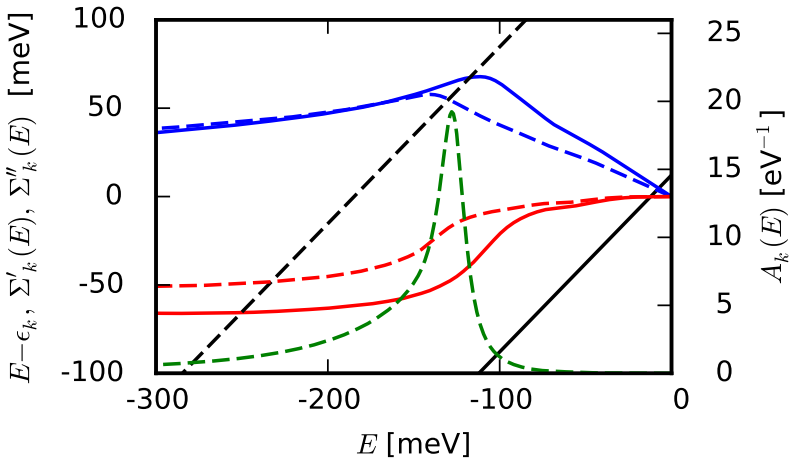

Figure 8.5: Graphical solution of the equation for the quasiparticle energy $\bar{\epsilon}_k$, for two different values of k along the nodal axis: $k = k^B_{F,\,N}$ and k_{kink} (i.e., the value of quasimomentum for which the nodal kink occurs), and the corresponding spectra of the real and imaginary parts of the self-energy, and of the spectral function $A_k(E)$. The calculations have been performed using the set of parameter values S_1. The solid lines correspond to $k = k^B_{F,\,N}$, the dashed lines to $k = k_{\mathrm{kink}}$. The black lines represent the linear functions $E - \epsilon_k - \mu$, the red lines the imaginary parts of the self-energy, whose real parts are shown in blue. The green line represents the spectral function for k_{kink}. Reprinted figure with permission from Ref. [209].

Figure 8.5 illustrates the relationship between the energy of the kink and the energies of the features of the self-energy, for the set of parameter values S_1. It shows the graphical solution of the equation for the quasiparticle energy $\bar{\epsilon}_k$, for two values of k along the nodal axis: $k^B_{F,\,N}$ and k_{kink} (the value of quasimomentum at which the kink occurs). Also shown are the corresponding spectra of the real and imaginary components of the normal self-energy, and for k_{kink}, in addition, the normal spectral function $A_k(E)$. The spectral function for $k^B_{F,\,N}$ possesses a sharp quasiparticle peak at $E = 0$. For each of the two values of k, $\bar{\epsilon}_k$ is determined as the energy of the crossing between the corresponding black line (representing $E - \epsilon_k + \mu$) and the corresponding blue line (representing $\mathrm{Re}\{\Sigma(k, E)\}$). The energies of the crossing points coincide with those of the quasiparticle peaks of $A_k(E)$, as expected. It can be seen that $\Sigma''_{k=k^B_{F,\,N}}$ sets on at around 80 meV as discussed in Sec. 8.3.1, and that the maximum of its Kramers-Kronig transform $\Sigma'_{k=k^B_{F,\,N}}$ occurs at a higher energy (approximately 110 meV) due to the finite width of the step in $\Sigma''_{k=k^B_{F,\,N}}$. Finally, the aforementioned assumption of weak momentum dependence of the self-energy can be seen to be valid: even though the energy of the maximum of $\Sigma'_{k=k_{\mathrm{kink}}}$ is higher than that of the maximum of $\Sigma'_{k=k^B_{F,\,N}}$ by $\Delta_{\mathrm{kink}} \simeq 20$ meV, the shapes of the profiles are qualitatively very similar. In particular, a sharp maximum is present in both profiles. This explains why the energy of the kink is only slightly (by Δ_{kink}) higher than that of the maximum of $\Sigma'_{k=k^B_{F,\,N}}$, and why the kink is relatively sharp.

It is worth contrasting these findings with the results of the fully self-consistent approach with the value of the coupling constant g of 1.95 eV (as in Ref. [202]) in place of

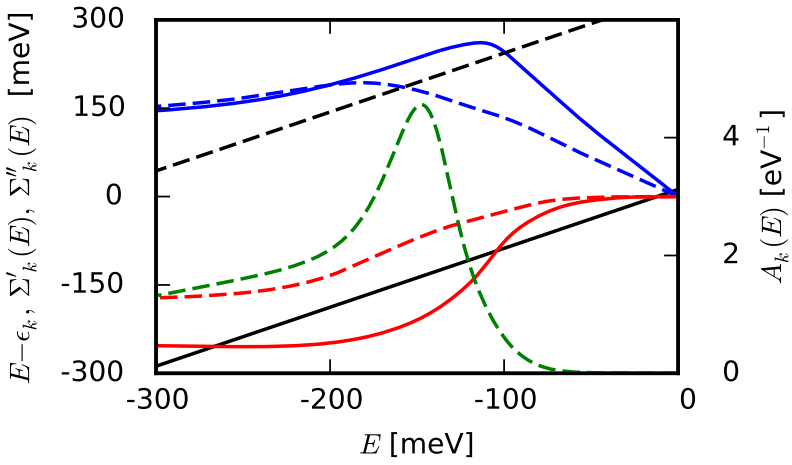

Figure 8.6: The same quantities as in Fig. 8.5, calculated with the same input parameter values, except for $g = 1.95\,\mathrm{eV}$, consistent with Ref. [202]. Notice the change in the scale of the left axis, compared with Fig. 8.5. Reprinted figure with permission from Ref. [209].

$g = 1.0\,\mathrm{eV}$. Figure 8.6 illustrates the properties of the system in this case. The large value of the coupling constant induces much larger magnitudes of the real and imaginary parts of the self-energy than in the former case. Thus, the maximum value of $\Sigma'_{k=k^B_{F,\,N}}$ is much larger, and the distance between $k^B_{F,\,N}$ and k_{kink} as well. Figure 8.6 shows that over such a broad k-interval, the quasimomentum dependence of $\Sigma'(k, E)$ may no longer be considered to be weak. The flattening of Σ' as k moves away from the Fermi surface (expected irrespective of the chosen set of parameter values) is large enough for the profile to change qualitatively. In particular, the pronounced maximum of Σ' disappears before the $E - \epsilon_k + \mu$ line reaches it. Therefore, the position and the shape of this extremum at $k^B_{F,\,N}$ are not the critical factors determining the energy and the shape of the kink anymore. Instead, the dependence of the self-energy on k has a substantial impact on the profile of the kink. In terms related to Eq. (8.4), this means that the weak momentum approximation breaks down.

The interpretation of the formation of the kink therefore differs qualitatively between the former and the latter case. In the low-g regime, the energy of the kink is approximately given by the energy of the maximum of $\Sigma'(k^B_{F,\,N}, \bar{\epsilon}_k)$, and the kink is sharp. In the high-g regime, the kink is made smoother by the influence of the momentum dependence of Σ'.

8.4 The kink in the dispersion relation away from the nodal axis

Having analyzed the behavior of the kink in the dispersion relation along the Brillouin zone diagonal, we now proceed to examine how the situation evolves away from the nodal axis, as a function of the angle θ between the direction of the Fermi surface cut and the diagonal (for a definition of θ, see Fig. 8.2).

8.4.1 Effective self-energy approach

First, we follow the approach introduced by Plumb et al. [45]. Figure 8.7 shows a heat map of $\mathrm{Re}\{\Sigma_{\mathrm{eff}}(\theta, E)\}$, the real part of the effective self-energy defined by Eq. (1) of Ref. [45], and used in order to track the angular dependence of the kink [45]. For the convenience of the reader, the definition of $\Sigma_{\mathrm{eff}}(\theta, E)$ will be restated here. Denote the inverse of the renormalized dispersion relation for a given value of θ by $\bar{k}(\theta, E)$. Then we define $\mathrm{Re}\{\Sigma_{\mathrm{eff}}(\theta, E)\} \equiv \bar{\epsilon}_{k=\bar{k}(\theta,E)} - \epsilon_{k=\bar{k}(\theta,E)}$. In the present work, we have followed the approach of Ref. [45], and approximated the bare dispersion by a straight line connecting the quasiparticle peak at k_F and the maximum of the spectral function corresponding to the high energy cutoff of 200 meV. The heat map has been obtained by an interpolation of the results for a discrete set of θ-values. For each of these values, the red circle indicates the energy of the maximum of $\mathrm{Re}\{\Sigma_{\mathrm{eff}}\}$, coinciding with the energy $\Omega_{\mathrm{kink}}(\theta)$ of the kink in the fermionic dispersion.

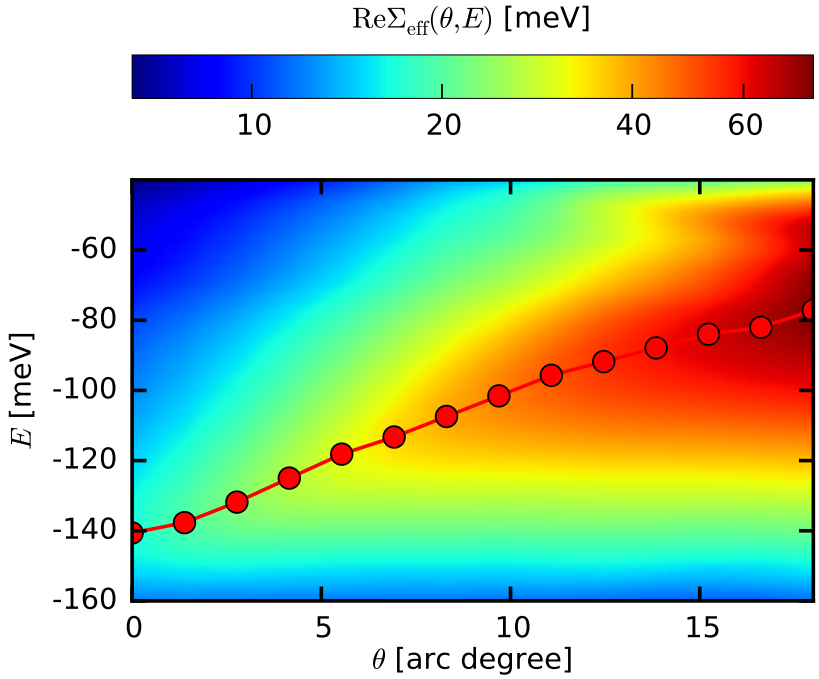

Figure 8.7: Heat map of the real part of the effective self-energy $\Sigma_{\mathrm{eff}}(\theta, E)$ defined in the text, calculated using the set of parameter values S_1. For each of the selected values of θ, the red circle represents the energy of the maximum of $\mathrm{Re}\{\Sigma_{\mathrm{eff}}(\theta, E)\}$, which coincides with the energy of the kink. Reprinted figure with permission from Ref. [209].

The most striking aspect of the result is the strong angular dependence of Ω_{kink}. With increasing θ, Ω_{kink} decreases and the intensity and the sharpness of the kink increase. Both observations are in qualitative agreement with the experimental findings of Ref. [45]. These trends can be understood in terms of the interplay between the fermionic dispersion and the bosonic spectrum, discussed for the case of $\theta = 0°$ in Sec. 8.3.1. As the Fermi surface cut moves away from the nodal axis, the modulus of the interband scattering vector along the $(\pi/a, \pi/a)$ direction increases. As a consequence, the section of χ'' which contributes most to the scattering, changes. As Fig. 8.1 shows, the spectral weight of the constant-q cut of the upper branch of χ'' increases, and the energy of the maximum decreases as q

increases towards 0.5 from below. The profile of the self-energy can be expected to follow the same trend, which indeed occurs in Fig. 8.7.

Following this analysis, we are in a position to conjecture that for large values of θ, the contribution of the resonance mode to the scattering becomes large, and eventually dominates the profile. This should be accompanied by a change of sign of the slope of $\Omega_{\rm kink}(\theta)$ at a critical angle θ_c. Simple geometrical considerations based on Fig. 8.2 provide $\theta_c \simeq 28°$. The coupling to the resonance mode has been put forward as the source of the dispersion anomalies in earlier spin-fermion model based studies [186, 188]. Within the framework of these studies, however, the scattering mechanism does not exhibit a very strong angular dependence, given the high kurtosis of the resonance mode. A more precise analysis of the situation, presented in Sec. 8.4.2, shows that θ_c is larger than 20°, and that for $\theta > \theta_c$, the effective self-energy approach introduced above does not provide reliable estimates of the kink energy.

Note finally that the scenario outlined above is – from the qualitative point of view – analogous to the one proposed by Hong et al. [197]. These authors have also argued that the observed complex structure of the quasiparticle self-energy and its evolution when going from the nodal cut to the antinodal one is determined by the presence of two independent contributions: that of a resonance mode and the one of a separate branch of bosonic excitations.

8.4.2 Relation between the kink and the features of the quasiparticle self-energy

Here we present a different approach to determine the angular dependence of the kink energy, based on a numerical procedure for estimating the roots of the real part of the denominator of the Green's function (8.3). This method is particularly well suited to the study of the kink for larger values of θ. For numerical reasons we use here slightly different Fermi surface cuts than in Subsec.8.4.1. The present ones are parallel to the Brillouin zone diagonals. For an example of the two types of cuts, see Fig. 8.2.

The 2×2 self-energy matrix can be expressed in terms of the Pauli matrices:

$$\widehat{\Sigma}(\boldsymbol{k}, E) \equiv \Sigma_0(\boldsymbol{k}, E)\hat{\tau_0} + \xi(\boldsymbol{k}, E)\hat{\tau_3} + \phi(\boldsymbol{k}, E)\hat{\tau_1},$$

and the Nambu propagator as

$$\begin{aligned} \widehat{G}(\boldsymbol{k}, E) &= \left[\widehat{G}_0^{-1}(\boldsymbol{k}, E) - \widehat{\Sigma}(\boldsymbol{k}, E)\right]^{-1} \\ &= \frac{\big[E - \Sigma_0(\boldsymbol{k}, E)\big]\hat{\tau_0} + \widetilde{\epsilon}(\boldsymbol{k}, E)\hat{\tau_3} + \phi(\boldsymbol{k}, E)\hat{\tau_1}}{\big[E - \Sigma_0(\boldsymbol{k}, E)\big]^2 - \widetilde{\epsilon}(\boldsymbol{k}, E)^2 - \phi(\boldsymbol{k}, E)^2}. \end{aligned}$$

We have dropped the band index for simplicity, and $\widetilde{\epsilon}(\boldsymbol{k}, E)$ stands for $\epsilon(\boldsymbol{k}, E) - \mu + \xi(\boldsymbol{k}, E)$. The normal component of the propagator is given by

$$G(\boldsymbol{k}, E) = \frac{E - \Sigma_0(\boldsymbol{k}, E) + \widetilde{\epsilon}(\boldsymbol{k}, E)}{\big[E - \Sigma_0(\boldsymbol{k}, E)\big]^2 - \widetilde{\epsilon}(\boldsymbol{k}, E)^2 - \phi(\boldsymbol{k}, E)^2}. \tag{8.5}$$

The approach we introduce here is most easily pictured as an extension of Sec. 8.3.2 and Fig. 8.5 to the case where $\phi(\boldsymbol{k}, E)$ is finite. Provided the quasiparticle is well defined, its energy E is equal to the root of the real part of the denominator, i.e., to the solution of the following equation in E, parametrized by $\boldsymbol{k}$:

$$\mathrm{Re}\big\{\big[(E - S(\boldsymbol{k}, E))\,(E - D(\boldsymbol{k}, E)) - \widetilde{\epsilon}(\boldsymbol{k}, E)^2\big]\big\} = 0, \tag{8.6}$$

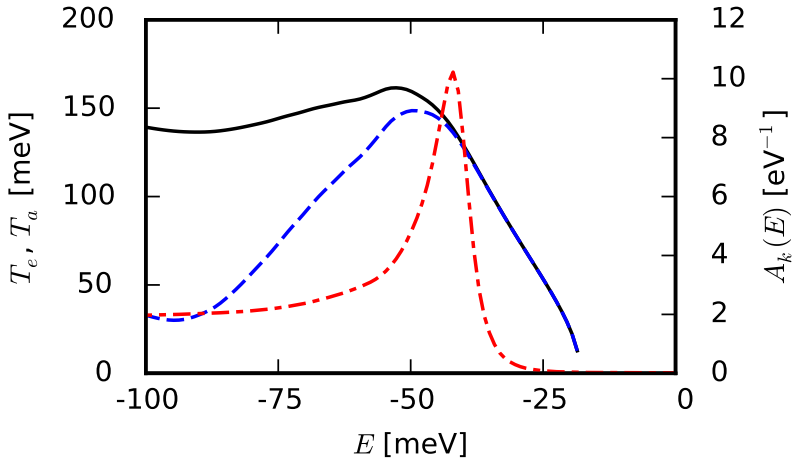

Figure 8.8: Comparison of the expression from Eq. (8.6), $T_{\rm e} \equiv \left(\mathrm{Re}\{[(E-S(\boldsymbol{k},E))\,(E-D(\boldsymbol{k},E))]\}\right)^{1/2}$ (black solid line) with its approximation $T_{\rm a} \equiv \left(\mathrm{Re}\{[E-S(\boldsymbol{k},E)]\}\,\mathrm{Re}\{[E-D(\boldsymbol{k},E)]\}\right)^{1/2}$ used in Eq. (8.7) (dashed blue line), for $k = k_{\rm kink}$ corresponding to the cut defined by $\theta = 26.9°$. The dashed-dotted line represents the spectral function $A_k(E)$. The calculations have been performed using the set of parameter values S_1. Reprinted figure with permission from Ref. [209].

where $S(\boldsymbol{k},E) \equiv \Sigma_0(\boldsymbol{k},E) \pm \phi(\boldsymbol{k},E)$ and $D(\boldsymbol{k},E) \equiv \Sigma_0(\boldsymbol{k},E) \mp \phi(\boldsymbol{k},E)$. The upper (lower) sign is used if $\mathrm{Re}\{\Sigma_0(\boldsymbol{k},E)\}$ and $\mathrm{Re}\{\phi(\boldsymbol{k},E)\}$ have the same (opposite) signs (recall that $\mathrm{Re}\{\phi(\boldsymbol{k},E)\}$ possesses d-wave symmetry, while $\mathrm{Re}\{\Sigma_0(\boldsymbol{k},E)\}$ is positive in the momentum-energy section we are considering). Assuming that the imaginary parts of $E-S(\boldsymbol{k},E)$ and $E-D(\boldsymbol{k},E)$ are small compared to their real parts, we may approximate Eq. (8.6) by:

$$\mathrm{Re}\{[(E-S(\boldsymbol{k},E))]\} \simeq \frac{\mathrm{Re}\left\{\left[\widetilde{\epsilon}(\boldsymbol{k},E)^2\right]\right\}}{\mathrm{Re}\{[(E-D(\boldsymbol{k},E))]\}}. \tag{8.7}$$

The validity of this assumption is related to that of the quasiparticle picture, for an illustration, see Fig. 8.8.

For $\theta = 0°$, $S(\boldsymbol{k},E) = D(\boldsymbol{k},E) = \Sigma_0(\boldsymbol{k},E)$ and Eq. (8.7) reduces to the simple equation determining the quasiparticle energy employed in Sec. 8.3, $\mathrm{Re}\{[E-\Sigma_0(\boldsymbol{k},E)-\widetilde{\epsilon}(\boldsymbol{k},E)]\} = 0$.

For large values of θ, where the gap is fully developed, $\Sigma_0(\boldsymbol{k},E)$ and $\phi(\boldsymbol{k},E)$ have comparable magnitudes. As a consequence, $\mathrm{Re}\{[E-S(\boldsymbol{k},E)]\}$ and $\mathrm{Re}\{[E-D(\boldsymbol{k},E)]\}$ exhibit very different profiles, while both remain weakly k-dependent along a fixed cut. This is illustrated by Fig. 8.9. One can see that the profile of $\mathrm{Re}\{[E-D(k,E)]\}_{|\theta=26.9°}$ is approximately linear, contrasting with the peaked shape of $\mathrm{Re}\{[E-S(k,E)]\}_{|\theta=26.9°}$. The former profile, close to linear, emerges as the difference between two similarly peaked functions $\Sigma_0(\boldsymbol{k},E)$ and $\phi(\boldsymbol{k},E)$ (plus the linear function E). The similarity is due to the fact that both functions result from the convolution in Eq. (8.2). The latter profile represents the sum of the two functions (plus the linear function E), and therefore exhibits a peaked shape reminiscent of the similar shape of both functions.

The expressions entering Eq. (8.7) can be interpreted in simple terms. The one on the left hand side displays a peak whose magnitude increases with increasing θ as a consequence

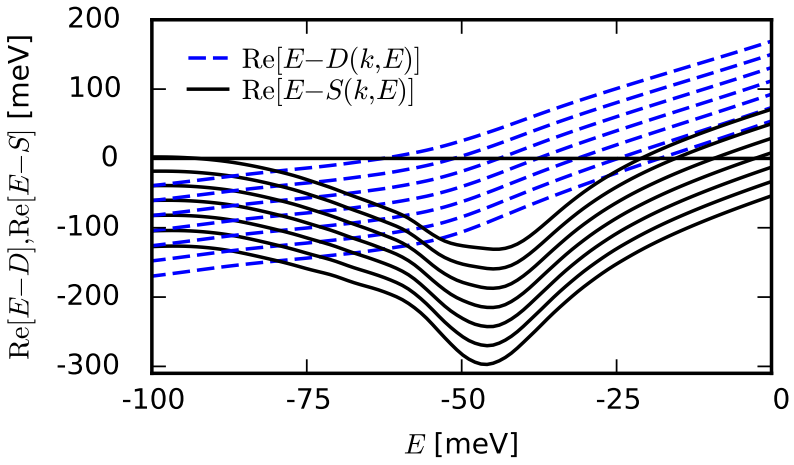

Figure 8.9: Profiles of the terms $\mathrm{Re}\{[E - D(k, E)]\}$ and $\mathrm{Re}\{[E - S(k, E)]\}$ entering Eq. (8.7), for $\theta = 26.9°$ and for a set of values of the quasimomentum k, calculated using the set of parameter values S_1. The lowest curves correspond to the Fermi surface. The quasimomentum k differs by $\Delta k = \pi/128$ from one curve to the next. For readability, each curve is shifted by 20 meV with respect to the previous one as k moves away from the Fermi surface. Reprinted figure with permission from Ref. [209].

of the lengthening of the interband scattering vector, and of the corresponding increase of the spectral weight of the section of χ'' which contributes to the scattering processes. The term on the right-hand side of Eq. (8.7) involves the inverse of an approximately linear expression. For fixed values of θ and $\boldsymbol{k}$, the value of this expression at the origin equals $|\,\mathrm{Re}\{\phi(\boldsymbol{k}, E = 0)\}|$. These observations allow us to interpret the profile of the right-hand side of Eq. (8.7) as that of a hyperbola-like function, with the origin of the E-axis displaced by $-|\,\mathrm{Re}\{\phi(\boldsymbol{k}, E = 0)\}| \simeq -|\,\mathrm{Re}\{\phi(\boldsymbol{k} = \boldsymbol{k}_F(\theta), E = 0)|\} = \Delta_{\mathrm{SC}}(\theta)$, as illustrated in Fig. 8.10. As $\boldsymbol{k}$ moves away from the Fermi surface, a family of hyperbola-like functions ("hyperbolas" in the following) is generated, with a multiplicative factor $\mathrm{Re}\big\{\big[\widetilde{\epsilon}(\boldsymbol{k}, E)^2\big]\big\}$ applied to the y-axis. The right-hand side of Eq. (8.7) thus evolves from a very sharp hyperbola, for $k \to k_F(\theta)$, to a smooth hyperbola, for large values of $|k - k_F(\theta)|$.

This analysis shows that the left-hand (right-hand) side term of Eq. (8.7), indexed by (k, θ), is strongly (weakly) dependent on θ, but weakly (strongly) dependent on k. In other words, Eq. (8.7) allows us to disentangle the sensitivities of the quantities of interest with respect to k and θ. At this point, noticing that neither $\mathrm{Re}\{\widetilde{\epsilon}(\boldsymbol{k}, E)\}$ nor $D(\boldsymbol{k}, E)$ exhibit a pronounced kink, we are in a position to conclude that the origin of the kink in the fermionic dispersion lies in the kink exhibited by the left hand side of Eq. (8.7), $\mathrm{Re}\{[(E - S(\boldsymbol{k}, E))]\}$. The position of the kink can now be reliably evaluated by exploring the smooth quantity $\mathrm{Re}\{[(E - S(\boldsymbol{k}, E))]\}$ defined on the fine energy mesh.

The approach detailed below has been used to obtain the profile of $\Omega_{\mathrm{kink}}(\theta)$ displayed in Fig. 8.11: For each selected value of θ, the momentum dependence of the self-energy is examined. We then define $k_0(\theta)$ as the value of k on the computational k-mesh, along the considered θ-cut (recall that the k-space cuts we use in this subsection have the advantage of matching the geometry of the computational k-mesh), which is closest to $k_{\mathrm{kink}}(\theta)$. This process is illustrated in Fig. 8.10. Given a value of θ, $k_0(\theta)$ is the value of k, such that

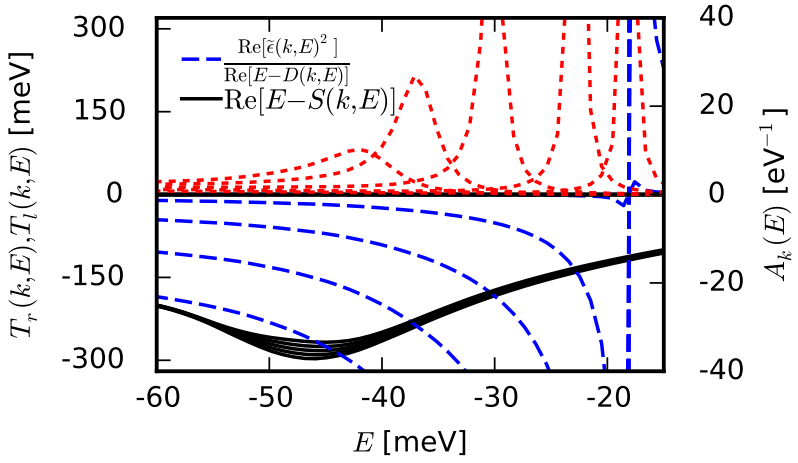

Figure 8.10: Profiles of both sides of Eq. (8.7) and of the quasiparticle spectral function $A_k(E)$ for $\theta = 26.9°$ and for a set of values of the quasimomentum k, calculated using the set of parameter values S_1. As in Fig. 8.9, the quasimomentum k differs by $\Delta k = \pi/128$ from one curve to the next. The set of dashed blue (solid black) lines represents the term $T_r(\boldsymbol{k}, E) \equiv \mathrm{Re}\{[\tilde{\epsilon}(\boldsymbol{k}, E)^2]\}/\mathrm{Re}\{[(E - D(\boldsymbol{k}, E))]\}$ (the term $T_l(\boldsymbol{k}, E) \equiv \mathrm{Re}\{[(E - S(\boldsymbol{k}, E))]\}$). Note that the energies of the peaks of the spectral function (dotted red line) coincide with those of the crossing points of the corresponding blue and black lines. Reprinted figure with permission from Ref. [209].

the dashed line representing $\mathrm{Re}\{[\tilde{\epsilon}(\boldsymbol{k}, E)^2]\}/\mathrm{Re}\{[(E - D(\boldsymbol{k}, E))]\}$ crosses the solid line representing $\mathrm{Re}\{[(E - S(\boldsymbol{k}, E))]\}$ close to its extremum. Once k_0 is fixed, we obtain the energy of the kink as that of the extremum of $\mathrm{Re}\{S(\boldsymbol{k}_0, E)\}$ (we have checked that in the present context the two energies coincide). As discussed above, in the $\theta \to 0$ limit, this method for estimating the energy of the kink is equivalent to the one used in Sec. 8.3.2 , but there is one caveat: for small values of θ, the gap is small, so that the kink in $E - S(\boldsymbol{k}, E)$ is weak and may not always dominate the very weak kink in $E - D(\boldsymbol{k}, E)$. As a consequence, for small values of θ, the former method may be more accurate in estimating the energy of the kink.

It can be seen in Fig. 8.11 that the present $\Omega_{\mathrm{kink}}(\theta)$ is close to the result shown in Sec. 8.4.1. The main discrepancies appear in the $\theta \to 0$ region (discussed above), and for large values of θ. The latter arise because the kink becomes so intense, and sharp in momentum space, that the former method, based on interpolations of the renormalized dispersion in k-space, does not provide a precise estimate of the kink energy.

The increased extent of the accessible θ-domain allows for a confirmation of the conjecture exposed in Sec. 8.4.1, related to the role of the resonance mode. Figure 8.11 clearly shows that the slope of $\Omega_{\mathrm{kink}}(\theta)$ changes sign at $\theta_c \simeq 23°$. We argued in Sec. 8.4.1 that if the kink is due to the upper branch of χ'', then the slope of $\Omega_{\mathrm{kink}}(\theta)$ must be negative. This is the trend observed for $\theta < \theta_c$. Conversely, if the resonance mode is the dominant source of scattering, the θ-dependence of $\Omega_{\mathrm{kink}}(\theta)$ is determined mainly by that of $\Delta_{\mathrm{SC}}(\theta)$ and $\Omega_{\mathrm{kink}}(\theta)$ must therefore display a positive slope close to that of $\Delta_{\mathrm{SC}}(\theta)$. This is what we observe in the $\theta > \theta_c$ region of Fig. 8.11, where the profile of $\Omega_{\mathrm{kink}}(\theta)$ follows that of $\omega_{\mathrm{res}} + \Delta_{\mathrm{SC}}(\theta)$, represented by the solid white line. The fact that the $\Omega_{\mathrm{kink}}(\theta)$ line is located

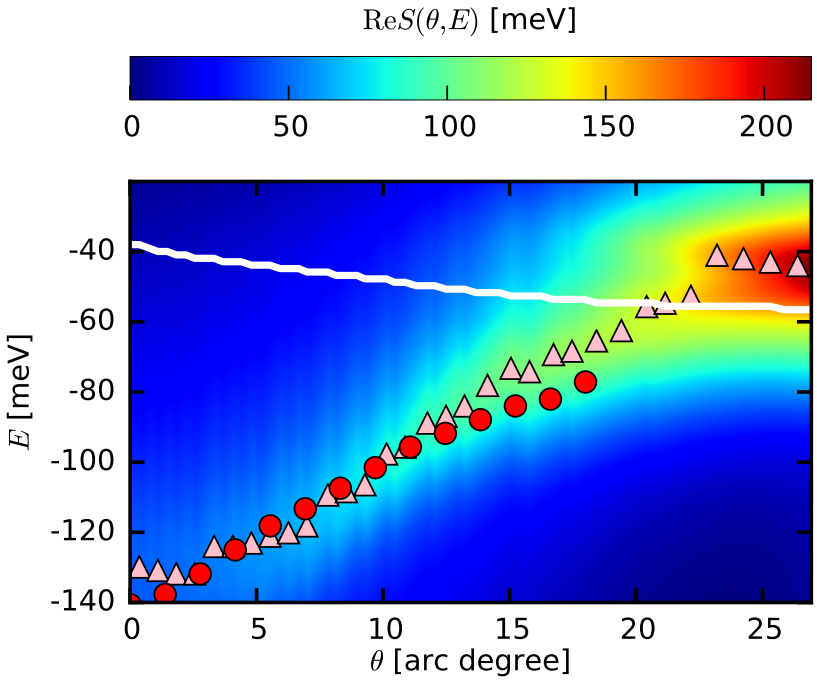

Figure 8.11: Heat map of the real part of the quantity $S(\boldsymbol{k}, E)$ defined in the text, calculated using the set of parameter values S_1. For each of the selected values of θ, the pink triangle represents the energy of the extremum of $\mathrm{Re}\{S(\boldsymbol{k}, E)\}$, which coincides with Ω_{kink}, as discussed in the text. The solid white line represents the expression $\omega_{\mathrm{res}} + \Delta_{\mathrm{SC}}(\theta)$. The solid red circles, displayed for comparison, are taken from Fig. 8.7. Reprinted figure with permission from Ref. [209].

somewhat above the $\omega_{\mathrm{res}} + \Delta_{\mathrm{SC}}(\theta)$ line is likely due to the influence of the lower branch of χ''. The discontinuity of $\Omega_{\mathrm{kink}}(\theta)$ at $\theta = \theta_c$ is an artifact related to the method for the numerical determination of $\Omega_{\mathrm{kink}}(\theta)$.

Finally, we note the remarkable similarity between the background of the heat map shown in Fig. 8.11 and the profile of the upper branch of χ'' displayed in Fig. 8.1, arising from the selfenergy-χ'' relation (8.1). It illustrates the major role played by the upper branch of χ'' in the formation of the angular dependence of $\Omega_{\mathrm{kink}}(\theta)$ in the near nodal region.

8.5 Comparison with experimental data

The main trend of Subsection 8.4.1, i.e. the decrease of $|\Omega_{\mathrm{kink}}|$ when going from the nodal cut to the antinodal one, is consistent with the experimental findings of Ref. [45]. Our results provide support for the conjecture that the decrease is associated with the dispersion of the upper branch of the hourglass. The calculated value of the energy of the nodal kink ($\simeq 130\,\mathrm{meV}$), however, is much higher than that of underdoped YBCO reported in Ref. [202] (80 meV). In addition, the calculated magnitude of the slope of $\Omega_{\mathrm{kink}}(\theta)$ (3.5 meV per arc degree) is much higher than the experimental value of Bi2212 reported in Ref. [45] (0.8 meV per arc degree). Finally, the renormalized Fermi velocity of 2.8 eVÅ on the nodal axis (see Fig. 8.3), is much larger than the experimental value of underdoped YBCO of

1.8 eVÅ. This discrepancy is connected with the fact that the value of g used in the set S_1 is much smaller than that of Ref. [202].

Based on our interpretation of the origin of the kink, it is possible to understand the influence of the model parameters on the profile of $\Omega_{\rm kink}(\theta)$. We are also well equipped to find out which adjustments are necessary in order to reconcile the results of the calculations with the experimental data. It can be expected that $\Omega_{\rm kink}(\theta = 0)$ decreases with increasing interband distance $|\boldsymbol{Q}_0|$ (see Fig. 8.2 for a definition), but that it is not very sensitive to the doping level or the bonding-antibonding splitting (provided that $|\boldsymbol{Q}_0|$ and the Fermi velocity are kept fixed). Our analysis also indicates that a widening of the upper branch of the hourglass should lead to a shift of $\Omega_{\rm kink}(\theta = 0)$ towards lower energies and to a reduction of the slope of $\Omega_{\rm kink}(\theta)$. Finally, reducing the bandwidth of the bare dispersion should induce a lowering of the renormalized Fermi velocity. We have checked these trends by performing calculations of the same type as described in sections 8.3 and 8.4 for many different sets of values of the input parameters.

As an example, and an illustration of the sensitivity of the results of the calculations to the input parameter values, we present below results of our calculations obtained using a set of parameter values (S_2 in the following), where some of the values have been modified along the lines of the previous paragraph. The values of $k^A_{F,\,N}$ and $k^B_{F,\,N}$ are increased to 36.0% and 40.7% of $\pi\sqrt{2}/a$, respectively. This shift applied to the band structure leaves the system well within the limits given by published experimental values: the values of $k^A_{F,\,N}$ and $k^B_{F,\,N}$ remain smaller than 41%, the common value of the two parameters reported in Ref. [215]. Furthermore, the corresponding increase in the magnitude of $|\boldsymbol{Q}_0|$ is small, so that the resonance mode does not participate in the scattering along the nodal cut, and the qualitative features of Fig. 8.2 are conserved. The bandwidth of the bare dispersion is reduced by 40%, so that the value of the renormalized Fermi velocity is close to the experimental one, and we set $g = 0.8$ eV, so that the maximum value of the gap remains unchanged at 30 meV. Finally, the upper branch of χ'' is made wider, so as to further reduce the value of $\Omega_{\rm kink}(\theta = 0)$ and the slope of the profile of $\Omega_{\rm kink}$.

Figure 8.12 displays the renormalized dispersion calculated using the set of parameter values S_2. It can be seen that the kink is much more pronounced. As expected, the energy of the kink (ca 90 meV) and the renormalized Fermi velocity (ca 1.5 eVÅ) are considerably lower than in Fig. 8.3, and close to the experimental values of Ref. [202].

The corresponding angular dependence of $\Omega_{\rm kink}$ is shown in Fig. 8.13. It can be seen that the magnitude of the slope of $\Omega_{\rm kink}$ is reduced to only 1.1 meV per arc degree, reasonably close to the experimental value for Bi2212 [45]. The value of θ_c of Fig. 8.13 (ca 26°) is higher than that of Fig. 8.11. The difference is mainly due to that between the bare dispersion relations of S_1 and those of S_2. The interpretation exposed at the end of Sec. 8.4 still applies. Based on this interpretation and the above discussion we can make a prediction concerning the angular dependence of $\Omega_{\rm kink}$ in underdoped YBCO. We predict that there exists a critical value θ_c, such that for $\theta < \theta_c$ ($\theta > \theta_c$), $\Omega_{\rm kink}(\theta)$ is a decreasing (weakly increasing) function. The minimum $\Omega_{\rm kink}(\theta_c)$ of $\Omega_{\rm kink}$ is determined by $\Delta_{\rm SC}(\theta_c)$ and by the lower branch of χ''. A value in the range from 40 meV to 60 meV can be expected. This prediction could be tested in ARPES experiments.

Finally we address, in light of our findings, the $\Omega_{\rm kink}(\theta)$ line for nearly optimally doped Bi2212 reported in Ref. [45], which was one of our starting points. The energy of the nodal kink in Bi2212 of ca 65 meV is roughly 15 meV lower than that of underdoped YBCO and 25 meV lower than our result shown in Fig. 8.13. The magnitude of the slope of $\Omega_{\rm kink}$ in Bi2212 is only slightly smaller than that of our calculations. The difference may be caused

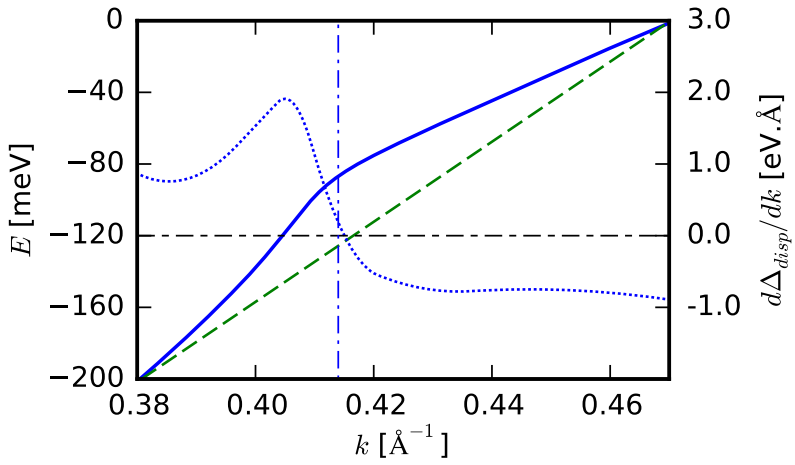

Figure 8.12: The same quantities as in Fig. 8.3. The calculations have been performed using the set of parameter values S_2. Reprinted figure with permission from Ref. [209].

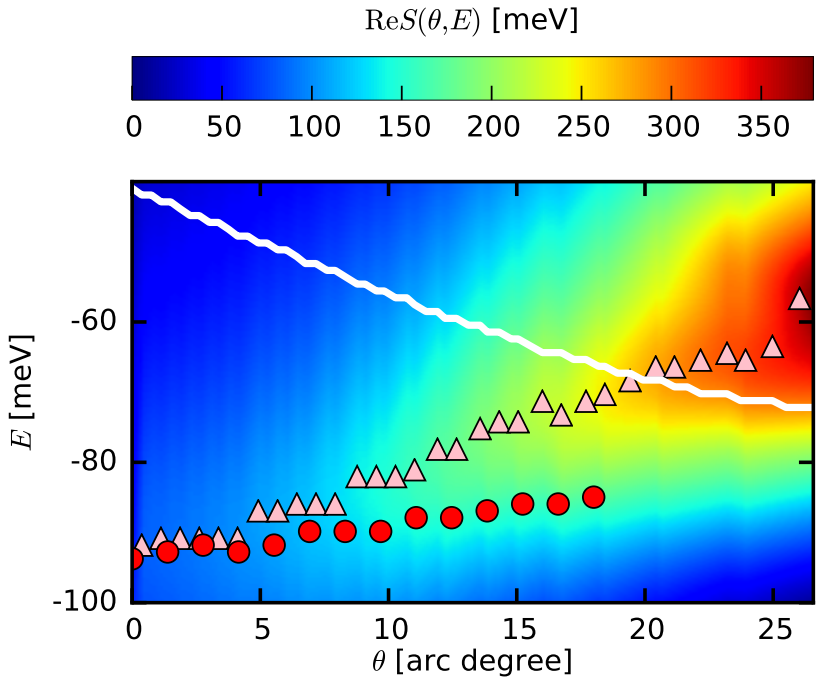

Figure 8.13: The same quantities as in Fig. 8.11, calculated using the set of input parameter values S_2. The apparent steps in the pink triangle profile are due to the reduced energy range of the E-axis, and the discretization of the energy mesh. Reprinted figure with permission from Ref. [209].

by a difference in the Fermi surfaces and/or by a difference in χ''. Since the magnitude of the internodal distance, $|\boldsymbol{Q}_0|$, of optimally doped Bi2212 is almost the same as that of underdoped YBCO, it appears that some difference in χ'' plays the crucial role. Note that the neutron scattering data of optimally doped Bi2212 [216] reveal a fairly high kurtosis of $\chi''(q,E)_{|E=42\,\mathrm{meV}}$ [see Fig. 2 (c) of Ref. [216]], and that the higher energy cuts of $\chi''(q,E)$ shown in Figs. 2(a) and 2(b) of Ref. [216] are considerably wider than those of underdoped YBCO. In particular, the values of χ'' for $q = 0.19$ r.l.u. (corresponding to $|\boldsymbol{Q}_0|$ of Fig. 8.1) and $\omega = 42\,\mathrm{meV}$, $54\,\mathrm{meV}$ and $66\,\mathrm{meV}$ in Figs. 2 (c), (b) and (a) of Ref. [216], are all significant, and of a comparable magnitude. Motivated by this observation and by the large width of the nodal kink in Bi2212 (see Fig. 1 (d) of Ref. [45]), we propose the following qualitative interpretation of the angular dependence of Ω_{kink} in Bi2212: we suggest that the nodal kink is not determined by a single narrow cut through the upper branch of the hourglass, as in the case of underdoped Y-123 (see Fig. 1), but rather by a broad band of χ'' ranging from ca $40\,\mathrm{meV}$ to ca $100\,\mathrm{meV}$. Even the $42\,\mathrm{meV}$ cut contributes because of the high kurtosis. With increasing θ, lower energy segments of χ'' become more influential, for the same reasons as discussed in Sec. 8.4.1, and as a consequence, the energy of the kink slighly decreases.

Chapter 9

Spontaneous Spin Textures in Multiorbital Mott Systems

In this chapter, we present the recent results on the two-dimensional Hubbard model in the intermediate coupling regime, published in Ref. [102]. We also provide some preliminary results which extend the conclusions of Ref. [102]: in Sec. 9.5, we present an innovative algorithm which allows to account for a finite in-plane magnetic field, in the segment implementation of the continuous-time hybridization expansion impurity solver, even though the local Hamiltonian is not diagonal in the occupation number basis.

9.1 Introduction

The manipulation of spin polarization by controlling charge currents and vice versa has attracted considerable attention due to applications in spintronic devices. A major role is played by spin-orbit coupling in non-centrosymmetric systems. As originally realized by Dresselhaus and Rashba [217], spin-orbit coupling in a non-centrosymmetric crystal lifts the degeneracy of the Bloch states at a given $\mathbf{k}$-point and locks their momenta and spin polarizations together, giving rise to a spin texture in reciprocal space. This leads to a number of phenomena such as spin-torques in ferro- [218, 219] and anti-ferromagnets [220, 221], topological states of matter, or spin textures in the reciprocal space, which may generate a spin galvanic effect [222]. For a review, see Ref. [223]. Electronic correlations can also provide a coupling between spin polarization and charge currents on their own, e.g. via effective magnetic fields acting on electrons moving through a non-coplanar spin background [224, 225]. Wu and Zhang [226] proposed that spin-orbit coupling can be generated dynamically in analogy to the breaking of relative spin-orbit symmetry in ^{3}He [227]. Subsequently, an effective field theory of spin-triplet Fermi surface instabilities with high orbital partial wave was developed in Ref. [228]. Here, we present a spontaneous formation of a $\mathbf{k}$-space spin texture, similar to the effect of Rashba-Dresselhaus spin-orbit coupling, in centrosymmetric bulk systems with no intrinsic spin-orbit coupling. The spin texture is a manifestation of excitonic magnetism, that has been proposed to take place in some strongly correlated materials [53, 229]. The basic ingredient is a crystal built of atoms with quasi-degenerate singlet/triplet ground states. Under suitable conditions a spin-triplet exciton condensate [48, 104] is formed, which may adopt a variety of thermodynamic phases with diverse properties [101]. Several experimental realizations of excitonic magnetism have already been discussed in the literature [119, 230–233].

9.2 Model

We use the dynamical mean-field theory to study the minimal model of an excitonic magnet: the two-orbital Hubbard Hamiltonian at half-filling introduced in Eq. (4.1). The parameters Δ and J are balanced such that the energy difference between the atomic low-spin and high-spin states is smaller or comparable to the kinetic energy gain due to the electron delocalization. The numerical simulations using continuous-time quantum Monte-Carlo impurity solver [159, 165, 234] were performed with the density-density approximation for the interaction ($\gamma = 0$), which effectively introduces a magnetic easy axis in the present model. Analytic mean-field calculations as well as preliminary DMFT computations performed with a version of the model which respects SU(2) symmetry [101] show only quantitative differences (e.g. reduction of the transition temperature). The spectral functions were obtained using the maximum entropy method [235].

9.2.1 Computational details

The DMFT calculations were performed for the same parameters as in Ref. [119]: $U = 4$, $J = 1$, $U' = U - 2J$, $\Delta = 3.4$, $t_a = 0.4118$, $t_b = -0.1882$, $V_1 = \pm V_2 = 0.05$, $\gamma = 0$ (density-density approximation). Energies are expressed in eV in the following, and temperatures in K. We used the hybridization-expansion continuous time quantum Monte-Carlo impurity solver [159], modified to treat real off-diagonal hybridization functions. The spectra were obtained with maximum entropy analytic continuation [235] of the self-energy. For the off-diagonal elements, the spectral function of which is not positive definite, we used the ansatz $S(\omega) = S_+(\omega) - S_-(\omega)$, where $S_+(\omega)$ and $S_-(\omega)$ are positive definite. We checked that $S(\omega)$ obtained this way depends only weakly on the default model (while S_+ and S_- strongly depend on the default model).

Studies [53, 116, 118, 119, 236, 237] performed without cross-hopping (i.e. using $V_{1,2} = 0$) revealed the formation of the exciton condensate below a critical temperature, which decreases with doping away from half-filling. In the strong-coupling limit the ground state wave function of a uniform condensate can be approximated by a product of local functions $\Pi_i |C_i\rangle$, where each $|C\rangle$ has the form

$$|C\rangle = \left[s b^\dagger_\uparrow b^\dagger_\downarrow + \xi_1 a^\dagger_\uparrow b^\dagger_\uparrow + \tfrac{\xi_0}{\sqrt{2}} (a^\dagger_\uparrow b^\dagger_\downarrow + a^\dagger_\downarrow b^\dagger_\uparrow) + \xi_{-1} a^\dagger_\downarrow b^\dagger_\downarrow \right] |\mathrm{v}\rangle. \tag{9.1}$$

This form describes a local hybrid between low-spin and high-spin states with amplitudes s, ξ_1, ξ_0, and ξ_{-1}, which provides a useful analytic reference for interpretation of the numerical results.

In the DMFT calculations, the thermodynamic phases can be characterized by the order parameter $\boldsymbol{\phi}^{(i)} = \sum_{\alpha\beta} \boldsymbol{\sigma}_{\alpha\beta} \left\langle a^\dagger_{i\alpha} b_{i\beta} \right\rangle$, where $\boldsymbol{\sigma}$ is the vector of the Pauli matrices. In addition, we evaluate the spin moment per atom $\mathbf{M}$ as well as the spin density in the direct space $\mathbf{m}(\mathbf{r})$ and in the reciprocal space $\mathbf{m}_\mathbf{k} = \sum_{\alpha\beta} \boldsymbol{\sigma}_{\alpha\beta} \langle a^\dagger_{\mathbf{k}\alpha} a_{\mathbf{k}\beta} + b^\dagger_{\mathbf{k}\alpha} b_{\mathbf{k}\beta} \rangle$.

9.2.2 Results of calculations

In Fig. 9.1 we show the phase diagrams obtained for the Hamiltonian Eq. (4.1), as functions of temperature T and hole doping n_h away from half-filling, corresponding to $n = 2$. We choose the hopping parameters so that $t_a t_b < 0$, which leads to a uniform $\boldsymbol{\phi}$-order. Note that on a bipartite lattice the $t_a t_b > 0$ case with a staggered $\boldsymbol{\phi}$-order can be mapped on the $t_a t_b < 0$ by the gauge transformation $a_i \to (-1)^i a_i$ [101]. Fig. 9.2 shows the details

of the computational results, and displays all the points where actual computations were carried out.

We consider two cross-hopping patterns at this point: $V_1 = V_2$ (referred to as "even") and $V_1 = -V_2$ (referred to as "odd"). The two corresponding phase diagrams share the general features inherited from the similar system with no cross-hopping studied in Ref. [119]. These include the polar state with no ordered moment at low doping levels, and a doping-induced transition to a different excitonic phase. The thermodynamic phase can be distinguished by several criteria. In the ferromagnetic condensate (FMEC), the order parameter has the form $\boldsymbol{\phi} = \boldsymbol{x} + i\boldsymbol{x}'$, with non-collinear real vectors $\boldsymbol{x}$ and $\boldsymbol{x}'$. This combination generates a finite uniform polarization $M_\perp$ perpendicular to $\boldsymbol{\phi}$.

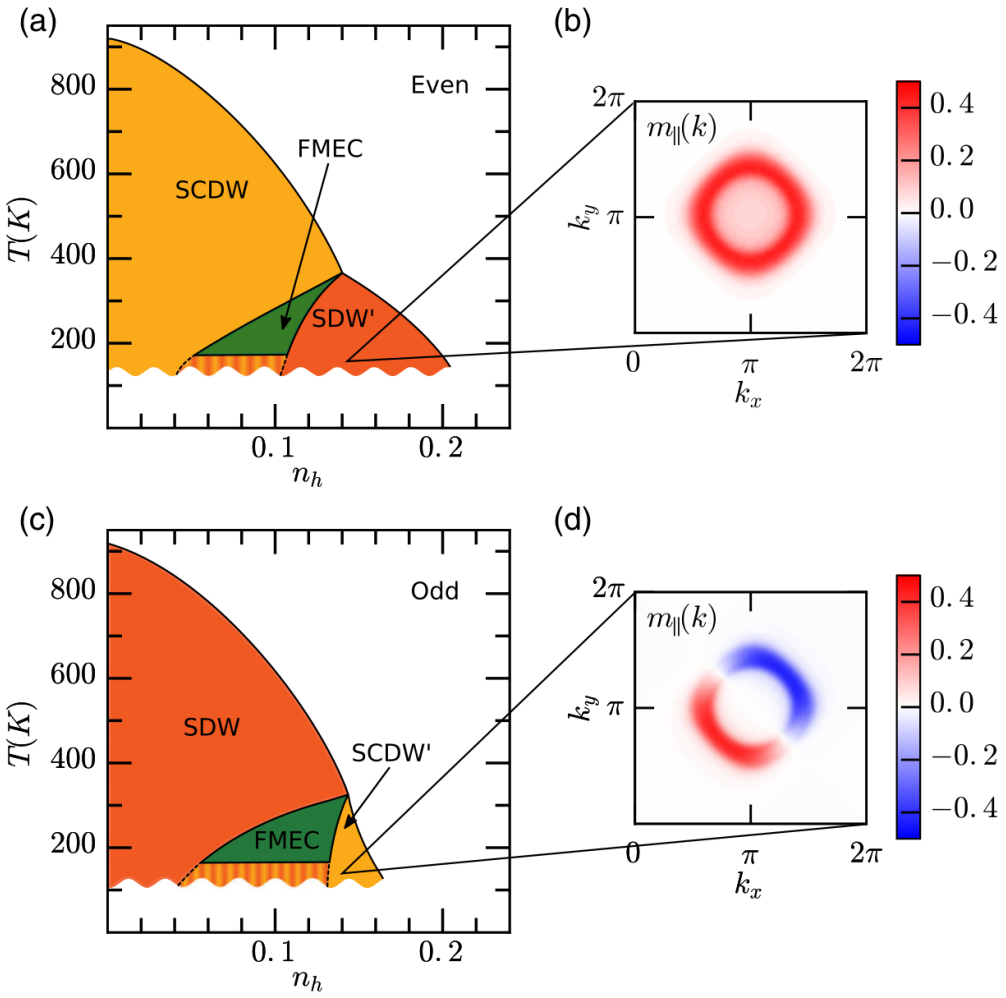

Figure 9.1: Panels (a) and (c): Phase diagrams in the doping-temperature plane for even and odd cross hopping, respectively. Full lines mark continuous transitions, dotted lines mark the boundaries of phase coexistence regions. Panels (b) and (d): Spin textures, as observed at the indicated points of the phase diagrams in units of $\mu_B(a_0/2\pi)^2$, obtained for $n_h = 0.14$, T =193 K. Reprinted figure with permission from Ref. [102].

The order parameter in the polar condensate can be written as $\boldsymbol{\phi} = e^{i\varphi}\boldsymbol{x}$, with a real vector $\boldsymbol{x}$, and an arbitrary scalar phase φ. The polar condensates can be further dis-

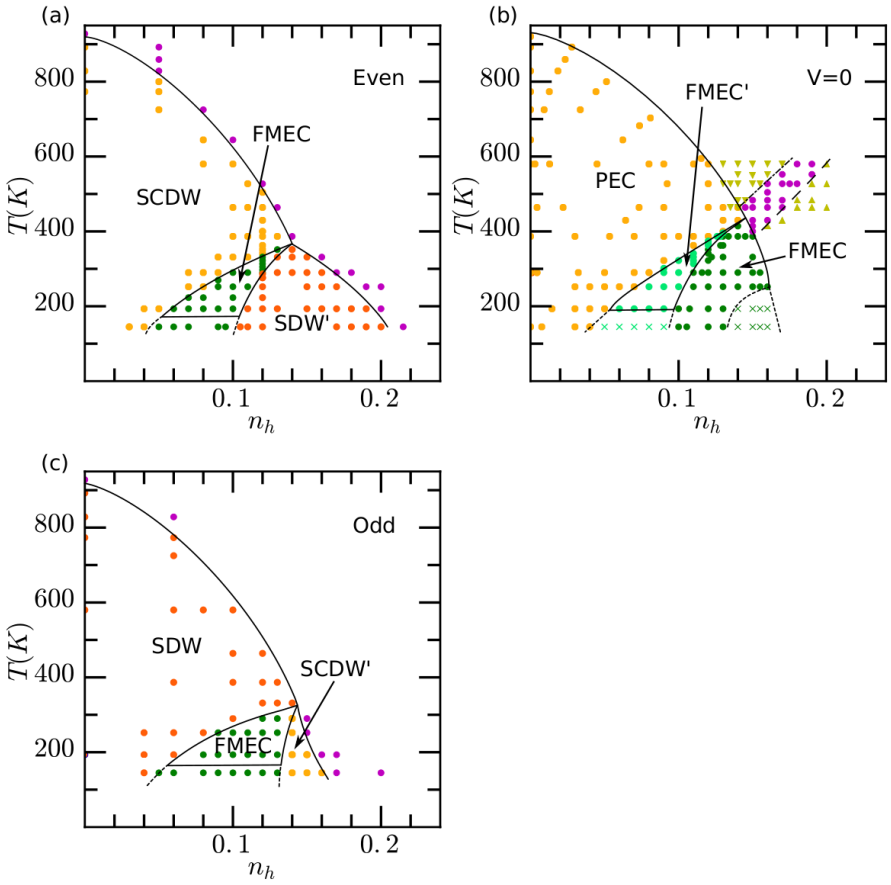

Figure 9.2: The input data for the Fig. 9.1. The dots indicate the points at which actual calculations were performed. Reprinted figure with permission from Ref. [102].

tinguished by their time-reversal symmetry, into the spin-density-wave (SDW) and spin-current-density-wave (SCDW) types, introduced by Halperin and Rice [48]. The spin-density wave order corresponds to the case of a pure real $\boldsymbol{\phi}$. It breaks time-reversal symmetry, and gives rise to a finite intra-atomic spin polarization $\mathbf{m}(\mathbf{r})$. The spin-current-density wave order corresponds to a pure imaginary $\boldsymbol{\phi}$, and preserves time-reversal symmetry. It gives rise to an intra-atomic spin current with $\mathbf{m}(\mathbf{r}) = 0$. The preference of the undoped system for SDW or SCDW ordering on a given bond is controlled by the sign of $t_a t_b V_1 V_2$, and follows the rules given in Ref. [53]. Finally, we distinguish the polar phases into primed and unprimed species. The spin(current)-polarization in the unprimed phases is purely local, a fact reflected by $\mathbf{m}_\mathbf{k} = 0$. The primed phases are characterized by the appearance of $\mathbf{k}$-space spin textures, $\mathbf{m}_\mathbf{k} \neq 0$, which, in the case of the SCDW' phase, correspond to global spin currents. The characteristics for the different phases are summarized in Table 9.1.

9.3 Interpretation: double-exchange mechanism

The observation of the spontaneous spin textures in the primed phases is our central result. It can be understood by invoking the generalized double-exchange mechanism, recently used by Chaloupka and Khaliullin to study ruthenates [238]. In a manner analogous to the

Table 9.1: The characteristics of the different condensate phases: $M_\perp$ ($M_\parallel$) is the magnetic moment per atom perpendicular (parallel) to the order parameter $\boldsymbol{\phi}$; $\mathbf{m}(\mathbf{r})$ ($\mathbf{m}_\mathbf{k}$) is the spin density in direct (reciprocal) space. The symbol ✓/0 means that both cases may be realized, as explained in the main text.

Condensate state	$M_\perp$	$M_\parallel$	$\mathbf{m}(\mathbf{r})$	$\mathbf{m}_\mathbf{k}$	$\mathrm{Re}\,\boldsymbol{\phi}$	$\mathrm{Im}\,\boldsymbol{\phi}$
FMEC	✓	✓/0	✓	✓	✓	✓
SDW	0	0	✓	0	✓	0
SCDW	0	0	0	0	0	✓
SDW'	0	✓/0	✓	✓	✓	0
SCDW'	0	0	0	✓	0	✓

well-known Zener double-exchange [239] in manganites, the exciton condensate acts as a filter for propagation of doped carriers. The stable phase is determined by the competition between the kinetic energy of doped carriers and the energy difference between possible condensates.

In the strong coupling limit, the propagation of a single electron through the condensate with order parameter $\boldsymbol{\phi}^{(i)}$ can be described by an effective Hamiltonian, as we now show. In the strong-coupling limit, the on-site Hilbert space can be restricted to the states

$$\begin{aligned}
&|\emptyset\rangle = b_\uparrow^\dagger b_\downarrow^\dagger |\mathrm{v}\rangle, \\
&|1\rangle = a_\uparrow^\dagger b_\uparrow^\dagger |\mathrm{v}\rangle, |0\rangle = \tfrac{1}{\sqrt{2}}(a_\uparrow^\dagger b_\downarrow^\dagger + a_\downarrow^\dagger b_\uparrow^\dagger)|\mathrm{v}\rangle, |-1\rangle = a_\downarrow^\dagger b_\downarrow^\dagger |\mathrm{v}\rangle, \\
&|\uparrow\rangle = b_\uparrow^\dagger |\mathrm{v}\rangle, |\downarrow\rangle = b_\downarrow^\dagger |\mathrm{v}\rangle,
\end{aligned} \tag{9.2}$$

where the bottom row corresponds to the doped hole states.

The wave function of the uniform condensate can be written approximately as a product of local functions $\Pi_i |C_i\rangle$ with

$$\begin{aligned}
&|C_i\rangle = s|\emptyset_i\rangle + \xi_{-1}^{(i)}|-1_i\rangle + \xi_0^{(i)}|0_i\rangle + \xi_1^{(i)}|1_i\rangle, \\
&s^2 + |\xi_1^{(i)}|^2 + |\xi_0^{(i)}|^2 + |\xi_{-1}^{(i)}|^2 = 1.
\end{aligned} \tag{9.3}$$

Since the overall phase of $|C\rangle$ is physically irrelevant, we are free to assume that s is purely real. It is also at times convenient to use the following Cartesian representation:

$$\begin{pmatrix} \xi_x \\ \xi_y \\ \xi_z \end{pmatrix} = \begin{pmatrix} \xi_{-1} - \xi_1 \\ -i(\xi_{-1} + \xi_1) \\ \sqrt{2}\xi_0 \end{pmatrix}. \tag{9.4}$$

In case the model respects the SU(2) symmetry, the spin rotations act as SO(3) transformations on the real and imaginary parts of $\boldsymbol{\xi}$. It is therefore always possible to make at least one of its Cartesian components zero. The density-density interaction, used in the numerical simulations, introduces an easy axis anisotropy which enforces the vanishing component to be ξ_0. For $\xi_0 = 0$ the relations between the order parameter $\boldsymbol{\phi}$ and the expansion coefficients in Eq. (9.3) read:

$$\begin{aligned}
\phi_+^{(i)} &= \langle C_i | a_{i\uparrow}^\dagger b_{i\downarrow} | C_i \rangle = -s\xi_1^{(i)*} \\
\phi_-^{(i)} &= \langle C_i | a_{i\downarrow}^\dagger b_{i\uparrow} | C_i \rangle = s\xi_{-1}^{(i)*} \\
\phi_0^{(i)} &= \langle C_i | a_{i\uparrow}^\dagger b_{i\uparrow} - a_{i\downarrow}^\dagger b_{i\downarrow} | C_i \rangle = \sqrt{2} s \xi_0^{(i)*}.
\end{aligned} \tag{9.5}$$

9.3.1 The undoped case

The ground state of the undoped system is determined by the second-order processes in hopping [101]. The most important of these processes were discussed in Sec. 4, Fig. (4.6). Their representation is repeated in Fig. 9.3 for convenience. The numerical results can be understood by looking at the signs of the different contributions to the variational energy $\langle CC|H|CC\rangle$ on the nearest-neighbor bonds:

$$\begin{aligned}
\left\langle C_iC_j|H^{(i)}|C_iC_j\right\rangle &\sim t_at_bs^2\,\mathrm{Re}(\xi_1^{(j)^*}\xi_1^{(i)}+\xi_{-1}^{(j)^*}\xi_{-1}^{(i)})\\
\left\langle C_iC_j|H^{(ii)}|C_iC_j\right\rangle &\sim -(t_a^2+t_b^2)\left(|\xi_1^{(i)}|^2|\xi_{-1}^{(j)}|^2+|\xi_{-1}^{(i)}|^2|\xi_1^{(j)}|^2\right)\\
\left\langle C_iC_j|H^{(iii)}|C_iC_j\right\rangle &\sim -V_1V_2s^2\,\mathrm{Re}\left(\xi_1^{(j)}\xi_{-1}^{(i)}+\xi_{-1}^{(j)}\xi_1^{(i)}\right).
\end{aligned} \tag{9.6}$$

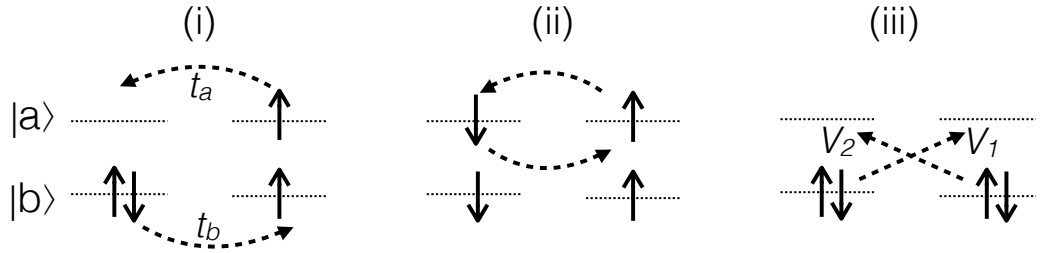

Figure 9.3: Nearest-neighbor hopping processes in the undoped system with marked amplitudes t_a and t_b and cross-hopping $V_1 = \pm V_2$: (i) hopping of high-spin boson, (ii) superexchange between high-spin states, (iii) pair creation/annihilation due to cross-hopping. Reprinted figure with permission from Ref. [102].

The term $H^{(i)}$, which drives the phase transition and selects the uniform order for $t_at_b < 0$, does not distinguish between the excitonic phases. The term $H^{(ii)}$, arising from nearest-neighbor anti-ferromagnetic exchange, favors the PEC phase with $|\xi_1| = |\xi_{-1}|$. These first two processes do not distinguish the phase of the complex order parameter.

The pair-creation term $H^{(iii)}$, on the other hand, is sensitive to the phase $\boldsymbol{\phi}$. However, for real $V_{1,2}$, it is sensitive only to the total phase of $\xi_1\xi_{-1}$, and selects its value to be either 0 or π, depending on the sign of V_1V_2. Both of the corresponding states can be realized with purely real $\xi_1 = \xi_{-1}$ or $\xi_1 = -\xi_{-1}$. Using real $\xi_{1,-1}$ is tantamount, at least on the level of states of the form (9.3), to selecting a specific direction for $\boldsymbol{\xi}$ among the possible degenerate choices. This will be shown to correspond to a choice for the direction of the spin polarization. For even cross-hopping $V_1 = V_2$, $H^{(iii)}$ selects the SCDW state, $\xi_1 = \xi_{-1}$ ($\phi_+ = -\phi_-$), while for the odd cross-hopping $V_1 = -V_2$, it selects the SDW state, $\xi_1 = -\xi_{-1}$ ($\phi_+ = \phi_-$).

9.3.2 The doped case

When the system is doped, the low-energy Hilbert space contains additional states $|\uparrow\rangle$ and $|\downarrow\rangle$, which give rise to additional exchange processes between the bosonic and fermionic excitations. These additional processes are shown in Figs. 9.4 and 9.5.

Effective Hamiltonian

The simplest way to account for these processes in the low doping regime is to compute the matrix elements describing the propagation of the doped carriers on the condensate

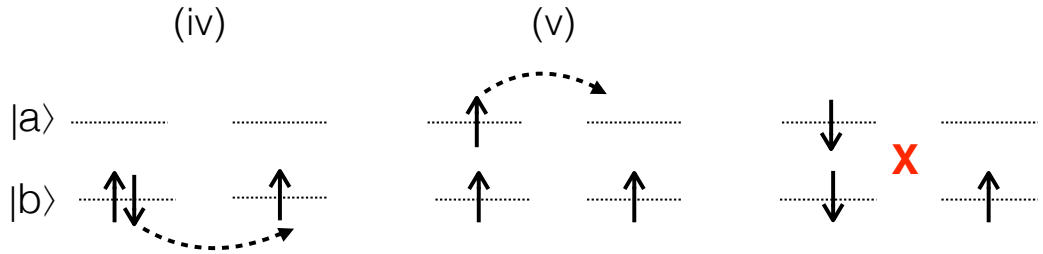

Figure 9.4: Nearest-neighbor processes allowing the propagation of doped holes in the system without cross-hopping: (iv) spin-independent hole propagation, (v) spin-dependent hole propagation. Reprinted figure with permission from Ref. [102].

background. This approach is well known from the treatment of double-exchange interaction and was recently applied in a context similar to our model [238]. For the sake of completeness we evaluate the matrix elements for general $\boldsymbol{\xi}$.

The contribution from hopping within the b-band, process (iv), reads

$$\langle \sigma_i C_j | H^{(iv)} | C_i \sigma_j \rangle = -t_b s^2. \tag{9.7}$$

The contribution from hopping within the a-band, process (v), is spin-dependent and reads

$$\begin{aligned}
\langle \uparrow_i C_j | H^{(v)} | C_i \uparrow_j \rangle &= -t_a \left({\xi_1^{(j)}}^* \xi_1^{(i)} + \frac{1}{2} {\xi_0^{(j)}}^* \xi_0^{(i)} \right) \\
\langle \downarrow_i C_j | H^{(v)} | C_i \downarrow_j \rangle &= -t_a \left({\xi_{-1}^{(j)}}^* \xi_{-1}^{(i)} + \frac{1}{2} {\xi_0^{(j)}}^* \xi_0^{(i)} \right) \\
\langle \uparrow_i C_j | H^{(v)} | C_i \downarrow_j \rangle &= -\frac{t_a}{\sqrt{2}} \left({\xi_{-1}^{(j)}}^* \xi_0^{(i)} + {\xi_0^{(j)}}^* \xi_1^{(i)} \right) \\
\langle \downarrow_i C_j | H^{(v)} | C_i \uparrow_j \rangle &= -\frac{t_a}{\sqrt{2}} \left({\xi_1^{(j)}}^* \xi_0^{(i)} + {\xi_0^{(j)}}^* \xi_{-1}^{(i)} \right).
\end{aligned} \tag{9.8}$$

The cross-hopping processes, Fig. 9.5, give rise to

$$\begin{aligned}
\langle \uparrow_i C_j | H^{(vi)} | C_i \uparrow_j \rangle &= \frac{V_1^{(ji)}}{\sqrt{2}} s {\xi_0^{(j)}}^*, \\
\langle \downarrow_i C_j | H^{(vi)} | C_i \downarrow_j \rangle &= -\langle \uparrow C | H^{(vi)} | C \uparrow \rangle, \\
\langle \uparrow_i C_j | H^{(vi)} | C_i \downarrow_j \rangle &= V_1^{(ji)} s {\xi_{-1}^{(j)}}^*, \\
\langle \downarrow_i C_j | H^{(vi)} | C_i \uparrow_j \rangle &= -V_1^{(ji)} T s {\xi_1^{(j)}}^*,
\end{aligned} \tag{9.9}$$

and

$$\begin{aligned}
\langle \uparrow_i C_j | H^{(vii)} | C_i \uparrow_j \rangle &= \frac{V_2^{(ji)}}{\sqrt{2}} s \xi_0^{(i)}, \\
\langle \downarrow_i C_j | H^{(vii)} | C_i \downarrow_j \rangle &= -\langle \uparrow C | H^{(vi)} | C \uparrow \rangle, \\
\langle \uparrow_i C_j | H^{(vii)} | C_i \downarrow_j \rangle &= -V_2^{(ji)} s \xi_1^{(i)}, \\
\langle \downarrow_i C_j | H^{(vii)} | C_i \uparrow_j \rangle &= V_2^{(ji)} s \xi_{-1}^{(i)}.
\end{aligned} \tag{9.10}$$

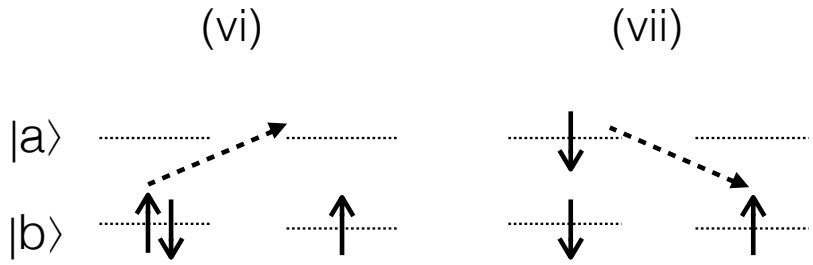

Figure 9.5: Additional spin-flip hopping of doped holes due to cross-hopping. Reprinted figure with permission from Ref. [102].

The dynamics of the doped hole is thus described by an effective single-band Hamiltonian

$$\begin{aligned} H_{\text{eff}} &= \sum_{ij} h_{\alpha\beta}^{(ij)} \tilde{b}_{i\alpha}^{\dagger} \tilde{b}_{j\beta}, \\ \text{with} \quad h_{\alpha\beta}^{(ij)} &= \langle \alpha_i C_j | H | C_i \beta_j \rangle \end{aligned} \tag{9.11}$$

being the effective hopping on bond ij. Using the Cartesian representation Eq. (9.4), the effective hopping can be expressed in a compact form:

$$\begin{aligned} \bar{h}^{(ij)} = &- \left(t_b s^2 + t_a \left(1 - s^2 \right) \right) \bar{I} \\ &+ \frac{t_a}{4} i \left(\boldsymbol{\xi}^{(j)^*} \wedge \boldsymbol{\xi}^{(i)} \right) \cdot \bar{\boldsymbol{\sigma}} \\ &+ \frac{1}{2} \left(V_1^{(ji)} s \boldsymbol{\xi}^{(j)^*} + V_2^{(ji)} s \boldsymbol{\xi}^{(i)} \right) \cdot \bar{\boldsymbol{\sigma}}, \end{aligned} \tag{9.12}$$

where the bar denotes 2×2 matrices. The density-density interaction imposes the constraint $\xi_0 = 0$, in which case the above equation reduces to

$$\bar{h}^{(ij)} = \begin{pmatrix} -t_b s^2 - t_a \xi_1^{(j)^*} \xi_1^{(i)} & V_1^{(ji)} s \xi_{-1}^{(j)^*} - V_2^{(ji)} s \xi_1^{(i)} \\ -V_1^{(ji)} s \xi_1^{(j)^*} + V_2^{(ji)} s \xi_{-1}^{(i)} & -t_b s^2 - t_a \xi_{-1}^{(j)^*} \xi_{-1}^{(i)} \end{pmatrix}. \tag{9.13}$$

The Hamiltonian H_{eff} contains the usual spin-preserving hopping and two 'magnetic' terms proportional to ξ and ξ^2. The 'magnetic' terms correspond to spin-dependent hopping that can be viewed as 'magnetic' fields acting on the bonds, which give rise to 'magnetic' fields acting locally in reciprocal space. With $i\boldsymbol{\xi}^* \wedge \boldsymbol{\xi}$ being the magnetic polarization of the condensate [101, 104], the ξ^2-term is analogous to the Zener double-exchange interaction [239]. The magnetic polarization is perpendicular to the order parameter and is not sensitive to the phase of $\boldsymbol{\xi}$.

The ξ-linear term appears only for non-zero cross hopping. It gives rise to a polarization parallel to $\boldsymbol{\xi}$. In a similar fashion with the treatment of the undoped case, we can show that the mean-field ground-state energy can be minimized by a purely real $\xi_{1,2}$. The kinetic energy of the doped carriers (eigenvalues of $H_{\text{eff}}(\mathbf{k})$) depends only on the amplitude of the off-diagonal elements of H_{eff}. For $\xi_0 = 0$, it is proportional to $V_1^2|\xi_{-1}|^2 + V_2^2|\xi_1|^2 - 2V_1V_2\,\text{Re}(\xi_1\xi_{-1})$.

Competition between the phases

The effective Hamiltonian H_{eff} may be rewritten as

$$\begin{aligned} H_{\text{eff}} =& \sum_{\langle ij \rangle} \left(t_s \delta_{\alpha\beta} + \frac{1}{2} \mathbf{B}^{(ij)} \cdot \boldsymbol{\sigma}_{\alpha\beta} \right) \tilde{b}^{\dagger}_{i\alpha} \tilde{b}_{j\beta} + \text{h.c.}, \\ &\text{with} \\ \mathbf{B}^{(ij)} =& \frac{i t_a}{2 s^2} \left(\boldsymbol{\phi}^{(j)} \wedge \boldsymbol{\phi}^{(i)*} \right) + V_1^{(ji)} \boldsymbol{\phi}^{(j)} + V_2^{(ji)} \boldsymbol{\phi}^{(i)*}, \end{aligned} \tag{9.14}$$

where $t_s = -t_b s^2 - t_a \left(1 - s^2\right)$ and s^2 is the low-spin fraction in the condensate. In general, the **B**-fields depend on the site indices as indicated in the brackets - in the studied 'odd' and 'even' models, the site indices are obsolete. The ϕ-quadratic term in (9.14) describes the standard double-exchange interaction of the doped particle with the uniform background with spin polarization $\mathbf{M}_{\perp} = -i \left(\boldsymbol{\phi}^* \wedge \boldsymbol{\phi} \right) / s^2$.

Qualitatively, at low doping the anti-ferromagnetic interactions between the high-spin states dominate, making the system a polar condensate with spin-independent hopping. For higher doping, the FMEC state allows the doped carriers to gain kinetic energy, via process (v). For some critical doping, this kinetic energy gain of the doped carriers in the FMEC state outweighs the energy cost generated by the high-spin high-spin exchange energy, process (ii), and the system adopts the FMEC state.

Quantitatively, the ϕ-linear term in Eq. (9.14) dominates if the system is close enough to the normal-phase boundary, but it appears in the condensate phase only for finite cross-hopping . We have shown above that the minimization of the bond energy leads to a situation where $\boldsymbol{\phi}$ is either purely real or purely imaginary depending on the relative sign of V_1 and V_2. For each of these situations, the strong coupling calculations [53] show that the V_1 and V_2 contributions in (9.14) cancel out, $V_1 \boldsymbol{\phi} + V_2 \boldsymbol{\phi}^* = 0$, for $\boldsymbol{\phi}$ that minimizes the bond energy. On a bipartite lattice, where all bonds can be satisfied simultaneously, the ϕ-linear term vanishes globally, allowing the SDW and SCDW phases at finite doping, as can be seen in Fig. 9.1.

When the kinetic energy gain of the doped particles overcomes the interactions selecting the condensate type in the undoped system, the ϕ-linear term in Eq. (9.14) becomes finite. It has the form of an exchange field acting on bonds or equivalently acting locally in the reciprocal space, which for the two hopping patterns considered so far reads

$$\mathbf{B}_{\mathbf{k}} = 4 V_1 \boldsymbol{\phi} \begin{cases} \cos k_x + \cos k_y & \text{SDW'} \\ i(\sin k_x + \sin k_y) & \text{SCDW'} \end{cases} \tag{9.15}$$

More generally, the form of $\mathbf{B}_{\mathbf{k}}$ reflects the symmetry of the cross-hopping pattern. The s-wave symmetry of our even cross-hopping therefore leads to an s-wave texture, Fig. 9.1, with a finite $M_{\parallel}$. Apart from a strong radial localization, the shape of $\mathbf{m}_{\mathbf{k}}$ is not qualitatively different from the approximately constant $\mathbf{m}_{\mathbf{k}}$ of a normal local moment ferromagnet. However, a d-wave cross-hopping, with V's along the x and y directions having opposite sings, produces a d-wave texture, shown in Fig. 9.6, and $M_{\parallel} = 0$. We point out that without doping the s- and d-wave systems are identical, in the strong-coupling limit, since the cross-hopping enters as a product $V_1 V_2$ on each bond [53].

The SCDW' phase is characterized by a purely imaginary $\boldsymbol{\phi}$, which gives rise to a **k**-odd exchange field in Eq. (9.15). The odd cross-hopping pattern can be thought of as having $p_x + p_y$ symmetry, which is imprinted in the spin texture, shown in the panel (b) of Fig. 9.1.

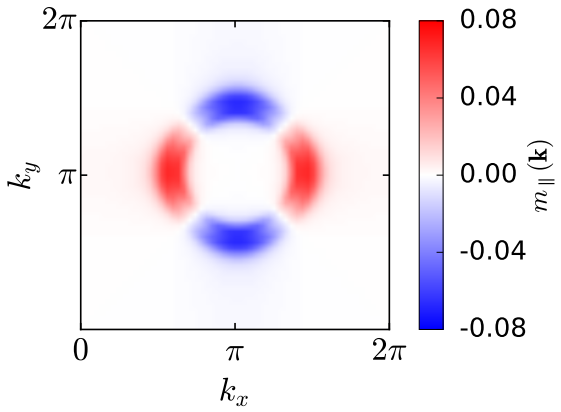

Figure 9.6: The d-wave spin texture in the SDW' phase of a model with even cross-hopping of opposite signs along the x and y axes. Obtained for $n_h = 0.16$, and T=193 K. Reprinted figure with permission from Ref. [102].

There is not only no net polarization ($\mathbf{M} = 0$), but the polarization is zero in every point ($\mathbf{m}(\mathbf{r}) = 0$), reflecting the time-reversal invariance of the SCDW' state.

In Fig. 9.7 we analyze the spin texture in the SCDW' state in detail. The frequency-resolved contributions to $\mathbf{m}_\mathbf{k}$ in the panels (c) and (d) of Fig. 9.7 reveal that the spin polarization comes from a narrow energy range around the Fermi level. The spectral functions exhibit rather sharp quasi-particle bands around the Fermi level, resembling the band structure of a non-interacting system. The spin density, on the other hand, is quite different from that of a non-interacting system. It cannot be associated with particular quasi-particle bands, but rather lives on their tails in sharply defined regions of the Brillouin zone. In Fig. 9.8 we show the $\mathbf{k}$-resolved spectral function from Fig. 4 of the article over the full energy range.

The shape of the spin texture in the SCDW' state is determined by the model parameters. The Weiss field in the SCDW and SCDW' phases, which generates local intra-atomic spin currents, can be viewed as a spontaneously generated spin-orbit coupling. The corresponding 'spin-orbit' splitting is approximately $(U - 2J)|\phi|$ thus can be as large as lower units of eV. Only in the SCDW' phase does the spontaneous spin-orbit coupling extend to the inter-atomic scale. The equivalent of the Rashba/Dresselhaus spin-orbit coupling is found from Eq. (9.15), having a maximum largest amplitude, in the (1,1) direction, of $4V_1|\phi|a_0$. With $|\phi| \sim 0.2 - 0.4$ (the maximum theoretical value is $1/\sqrt{2}$), the present cross-hopping of 50 meV, and a lattice constant a_0 of a few Å, the effective Rashba/Dresselhaus spin-orbit constant is of the order 1×10^{-11} eV m.

9.4 Realization

In order to support the SDW' or SCDW' states, we need the following:

1. The material must exhibit spin-triplet polar exciton condensation.
2. The local order must generate a spin-dependent hopping in Eq. (9.15).
3. The spin-dependent hopping must generate spin polarization or spin currents.

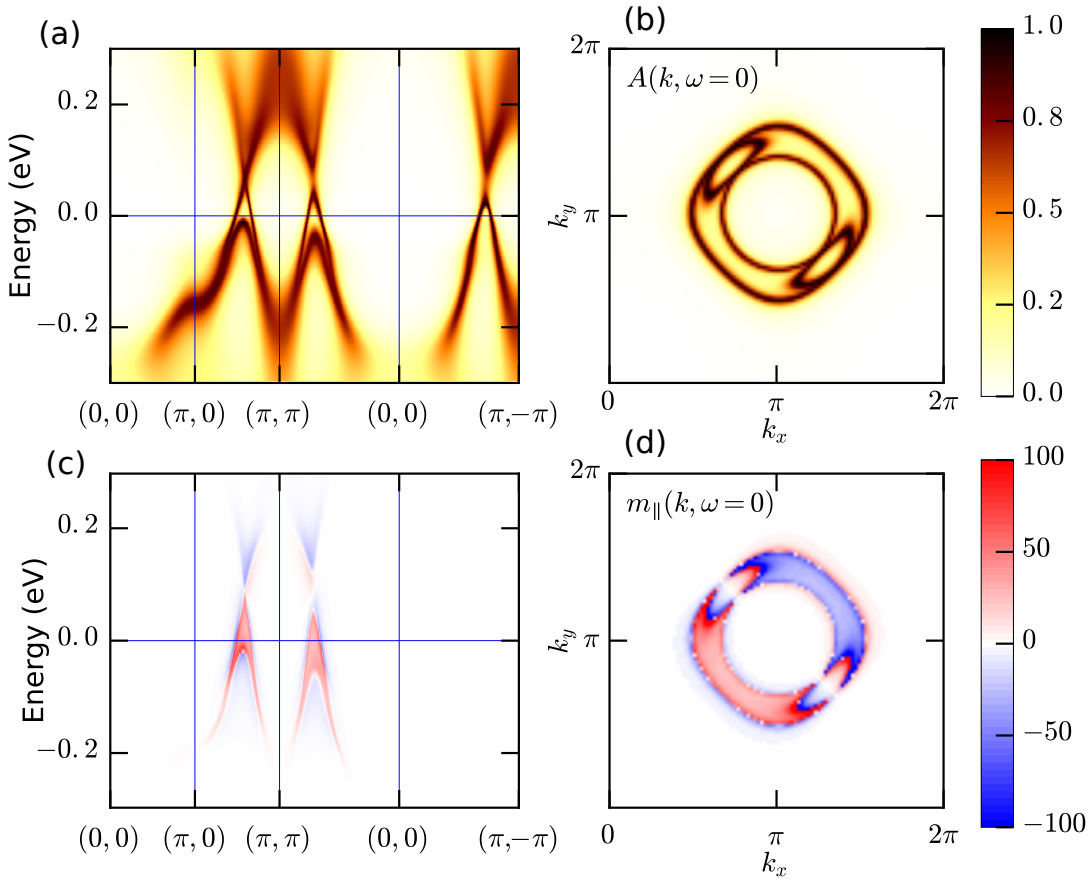

Figure 9.7: One-particle spectral density in the SCDW' phase for the same parameters as Fig. 9.1, panels (c) and (d). Panel (a): total spectral density $A(\mathbf{k},\omega)$ along high-symmetry lines in the Brillouin zone. Panel (b): Fermi surface $A(\mathbf{k},\omega=0)$. Panel (c): in-plane magnetization spectral density $m_\parallel(\mathbf{k},\omega)$ along the same lines as in panel (a). Panel (d): in-plane magnetization density at the Fermi level $m_\parallel(\mathbf{k},\omega=0)$ in units of $\mu_B.(\frac{a_0}{2\pi})^2\mathrm{eV}^{-1}$. Reprinted figure with permission from Ref. [102].

Transition metal perovskites are the most discussed candidates for excitonic magnetism [118, 229, 231]. The singlet-triplet quasi-degeneracy favorable for (i) is typically realized with the d^6 configuration, placed in an octahedral geometry (Fe^{2+}, Co^{3+}, Ni^{4+}), the d^8 configuration in a square planar geometry (Ni^{2+}), or the d^4 configuration in a octahedral geometry with strong spin-orbit coupling (Ru^{4+}, Os^{4+}, Rh^{5+}, Ir^{5+}). We thus focus on models built upon d-orbitals.

It is quite straightforward to construct the 'even' (or d-wave) model and thus the SDW' state from orbitals of the same parity. We focus on the more difficult 'odd' model and the SCDW' state. Here we have two options. First, we use the fact that only the in-plane parity is relevant. We can start with a lattice of $3z^2-r^2$ (or x^2-y^2) and $z(x+y)$ orbitals. Breaking the $z \leftrightarrow -z$ symmetry, e.g., by using an appropriate substrate, leads to the desired 'odd' cross-hopping pattern.

The second option is to build the model upon x^2-y^2 and xy orbitals, with more than one atom in the unit cell. In this case, the conditions (ii) and (iii) become distinct. For

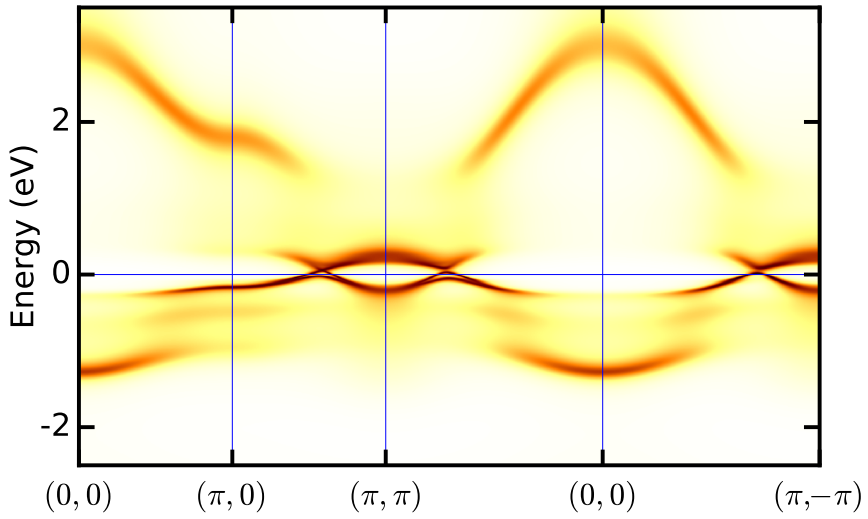

Figure 9.8: The spectral function over the full relevant energy range, for the same values of the parameters as in Fig. 9.6. Reprinted figure with permission from Ref. [102].

example, one can obtain $V_1 V_2 < 0$ on each bond by tilting the orbitals (oxygen octahedral in real perovskite). However, the corresponding pattern of $\mathbf{B}^{(ij)}$ has alternating signs and does not give rise to a finite $\mathbf{m}_\mathbf{k}$. In order to create the desired cross-hopping pattern, the inversion center at the atomic site has to be removed. In Fig. 9.9 we show an example of such hopping pattern in an Emery-like model. The diagonal hopping amplitudes t_a and t_b are both negative. The cross-hopping (V_1, V_2), induced via tilted oxygen orbitals (induced for example by a substrate with the appropriate texture), follows the $(++), (--), (++), ...$ pattern along both the x and the y directions. These suggestions are obviously not the only ways to realize the hopping patterns favoring the SCDW' phase.

The most advanced experimental realization of the triplet-excitonic condensation is arguably found in Ca_2RuO_4 [231], described by the model of Khaliullin [229], which is equivalent to the strong coupling limit of the present model for a special choice of parameters. While the double-exchange mechanism is active also in ruthenates [238], static spin textures were not reported. Since the equivalents of cross- and diagonal hopping in ruthenates originate from the same $t_{2g} \to t_{2g}$ process, their ratio is fixed and close to one. This is quite different from the present parameters with small cross-hopping.

Finally, we point out that **k**-space spin textures are accessible in cold atoms experiments, where the two-orbital model may be sufficiently simple to realize.

9.5 Spin-galvanic effect

As highlighted in Sec. 9.3, intra-cell spin textures are generated in the SCDW' phase of the condensate. It is natural, in this situation, to try and exploit the asymmetry in the spin texture, in order to generate macroscopic spin currents, thus achieving a realization of the spin-galvanic effect. One way to do this is to apply an in-plane static homogeneous magnetic field, parallel to the order parameter. Taking into account the interaction of the magnetization with the field, and assuming that the direction of the order parameter remains finite along the magnetic field, an imbalance between the up and down spins, with

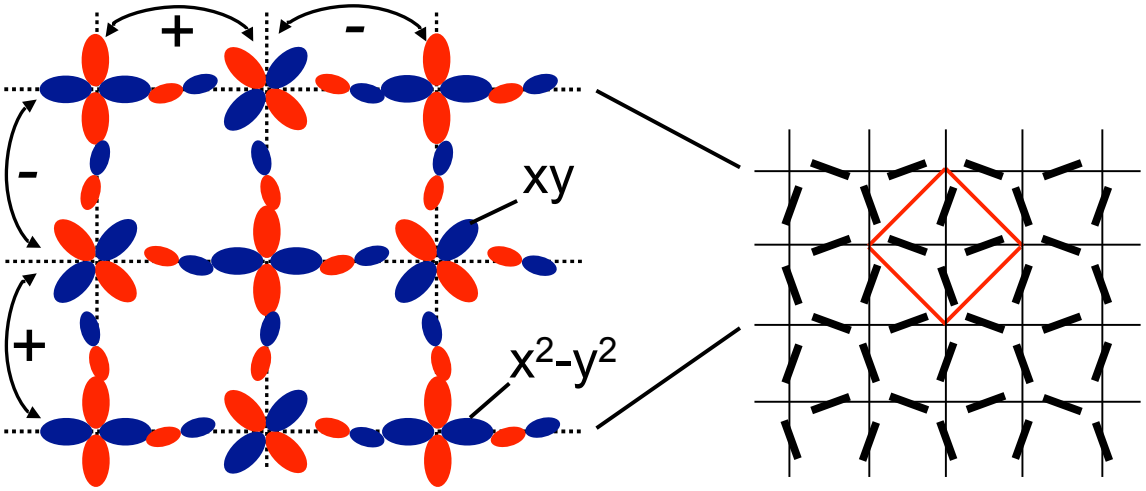

Figure 9.9: A cartoon view of the orbital pattern (left) that gives rise to $t_a, t_b > 0$ and $V_1 = V_2$ on each bond with alternating signs between bonds (only half of the orbitals is shown for sake of clarity). Zoomed out view of the texture on the ligand sublattice (right). The red square in the right panel marks the crystallographic unit cell. The model can be transformed to the "odd" cross-hopping case with a single-atom unit cell by sublattice transformation $a_i \to (-1)^i a_i$. Reprinted figure with permission from Ref. [102].

quantization axis along the magnetic field, should occur. Combined with the spin texture reported in Fig. 9.1, this could generate global spin currents in the material.

In this respect, a numerical challenge needs to be addressed: in the presence of the in-plane magnetic field, the local Hamiltonian is no longer diagonal in the occupation number basis, so that the efficient segment version of the hybridization expansion continuous-time impurity solver cannot be used as is. In the present section, we present a novel approach to the segment implementation of the continuous-time hybridization expansion solver. This is inspired by a recent work by Steiner, Nomura, and Werner [240], who developed a similar modification in order to account for the non density-density terms of the Coulomb interaction.

9.5.1 Algorithm

In DMFT, the lattice problem is replaced by the self-consistent solution of a two-orbital quantum impurity model. We consider an in-plane magnetic field B along the x-axis. In this framework, a term of the form $-\boldsymbol{B} \cdot \boldsymbol{\sigma} = -B\sigma_x$ has to be added to the local Hamiltonian. We follow the approach by Steiner, Nomura, and Werner: the local Hamiltonian is split

into a density-density part, diagonal in occupation number, and the rest:

$$\begin{aligned} H &= H_{\text{dens}} + \sum_{\alpha} H_{\alpha,B} + \sum_{\alpha} H^{\dagger}_{\alpha,B} + H_{\text{bath}} + H_{\text{hyb}} + H^{\dagger}_{\text{hyb}}, \\ H_{\text{dens}} &= \frac{\Delta}{2} \sum_{\sigma} \left(n^a_\sigma - n^b_\sigma \right) - \mu \sum_{\alpha,\sigma} n_{\alpha,\sigma} \\ &\quad + U \sum_{\alpha} n_{\alpha,\uparrow} n_{\alpha,\downarrow} + U' \sum_{\sigma\sigma'} n^a_\sigma n^b_{\sigma'} - J \sum_{\sigma} n^a_\sigma n^b_\sigma, \\ H_{\text{bath}} &= \sum_{\boldsymbol{k},\sigma} \epsilon_{\boldsymbol{k}} d^{\dagger}_{\boldsymbol{k},\sigma} d_{\boldsymbol{k},\sigma}, \\ H_{\text{hyb}} &= \sum_{\boldsymbol{k},\alpha,\sigma} c^{\dagger}_{\alpha,\sigma} V_{\boldsymbol{k},\alpha,\sigma} d_{\boldsymbol{k},\sigma}, \\ H_{\alpha,B} &= B \cdot c^{\dagger}_{\alpha,\downarrow} c_{\alpha,\uparrow} \equiv B \cdot Q_\alpha, \end{aligned} \tag{9.16}$$

where $\alpha \in \{a, b\}$.

We follow the derivation leading to Eq. (13) of Ref. [11], considering the fact that the hybridization matrix is not assumed to be diagonal in our framework:

$$\begin{aligned} Z = &\sum_{k=0}^{\infty} \int_0^\beta d\tau_1 \dots \int_{\tau_{k-1}}^\beta d\tau_k \int_0^\beta d\tau'_1 \dots \int_{\tau'_{k-1}}^\beta d\tau'_k \\ &\times \operatorname{Tr}\left[T_\tau e^{-\beta(H_{\text{bath}}+H_{\text{dens}})} \tilde{H}_{j_k}(\tau_k) \tilde{H}^{\dagger}_{j'_k}(\tau'_k) \dots \tilde{H}_{j_1}(\tau_1) \tilde{H}^{\dagger}_{j'_1}(\tau'_1) \right], \end{aligned} \tag{9.17}$$

where $\tilde{H}_j(\tau)$ is either $H_{\text{hyb}}(\tau)$ or $H_{\alpha,\text{B}}(\tau)$.

The total number of creation operators in each term of the expansion must be equal to the total number of annihilation operators. By construction, each $H_{\alpha,\,B}$ term introduces creation and annihilation operators in pairs in any of these terms. The remaining creation and annihilation operators are brought by the H_{hyb} part of the Hamiltonian. It thus follows that the creation/annihilation operators introduced in each term of the expansion by H_{hyb} also come in pairs (possibly acting on different orbitals, if we consider moves which introduce broken segments, i.e. single insertion of $H_{\alpha,\,B}$ and not only $H^{\dagger}_{\alpha,\,B} H_{\alpha,\,B}$ pairs). Their contribution can thus be evaluated in the usual way by means of the determinant of the hybridization matrix. It also follows that we can use a modified version of the segment representation:

$$\begin{aligned} Z = &\sum_{\{n_{\alpha,\sigma}=0\}}^{\infty} \sum_{n_b=0}^{\infty} \sum_{n_{\bar{b}}=0}^{\infty} \left(\prod_{\alpha,\sigma} \int_0^\beta d\tau_{h_1} \dots \int_{\tau_{h_{n_{\alpha,\sigma}-1}}}^\beta d\tau_{h_{n_{\alpha,\sigma}}} \int_0^\beta d\tau'_{h_1} \dots \int_{\tau'_{h_{n_{\alpha,\sigma}-1}}}^\beta d\tau'_{h_{n_{\alpha,\sigma}}} \right) \\ &\times \int_0^\beta d\tau_{b_1} \dots \int_{\tau_{b_{n_b}-1}}^\beta d\tau_{b_{n_b}} \int_0^\beta d\tau'_{\bar{b}_1} \dots \int_{\tau'_{\bar{b}_{n_{\bar{b}}-1}}}^\beta d\tau'_{\bar{b}_{n_{\bar{b}}}} \times \operatorname{Tr}\Bigg[T_\tau e^{-\beta(H_{\text{bath}}+H_{\text{dens}})} \\ &\left(\prod_{\alpha,\sigma} \sum_{\substack{j_{h_1},\dots,j_{h_{n_{\alpha,\sigma}}} \\ j'_{h_1},\dots,j'_{h_{n_{\alpha,\sigma}}}}} \sum_{\substack{\boldsymbol{p_{h_1}},\dots,\boldsymbol{p_{h_{n_{\alpha,\sigma}}}} \\ \boldsymbol{p'_{h_1}},\dots,\boldsymbol{p'_{h_{n_{\alpha,\sigma}}}}}} V^*_{\boldsymbol{p_{h_1}} j_{h_1}} V_{\boldsymbol{p'_{h_1}} j'_{h_1}} \dots V^*_{\boldsymbol{p_{h_{n_{\alpha,\sigma}}}} j_{h_{n_{\alpha,\sigma}}}} V_{\boldsymbol{p'_{h_{n_{\alpha,\sigma}}}} j'_{h_{n_{\alpha,\sigma}}}} \end{aligned}$$

$$
\begin{aligned}
&\times d^\dagger_{\boldsymbol{p}_{h_{n_{\alpha,\sigma}}}}\left(\tau_{h_{n_{\alpha,\sigma}}}\right) c_{j_{h_{n_{\alpha,\sigma}}}}\left(\tau_{h_{n_{\alpha,\sigma}}}\right) c^\dagger_{j'_{h_{n_{\alpha,\sigma}}}}\left(\tau'_{h_{n_{\alpha,\sigma}}}\right) d_{\boldsymbol{p}'_{h_{n_{\alpha,\sigma}}}}\left(\tau'_{h_{n_{\alpha,\sigma}}}\right) \\
&\dots d^\dagger_{\boldsymbol{p}_{h_1}}(\tau_{h_1}) c_{j_{h_1}}(\tau_{h_1}) c^\dagger_{j'_{h_1}}\left(\tau'_{h_1}\right) d_{\boldsymbol{p}'_{h_1}}\left(\tau'_{h_1}\right)\Bigg) \\
&\times Q_{l_{b_{n_b}}}\left(\tau_{b_{n_b}}\right)\dots Q_{l_{b_1}}(\tau_{b_1}) Q^\dagger_{l'_{\bar{b}_{n_{\bar{b}}}}}\left(\tau'_{\bar{b}_{n_{\bar{b}}}}\right)\dots Q^\dagger_{l'_{\bar{b}_1}}\left(\tau'_{\bar{b}_1}\right)\Bigg] B^{(n_{\bar{b}}+n_b)} \\
&= Z_{\text{bath}} \sum_{\{n_{\alpha,\sigma}=0\}}^{\infty} \sum_{n_b=0}^{\infty} \sum_{n_{\bar{b}}=0}^{\infty} \left(\prod_{\alpha,\sigma} \int_0^\beta d\tau_{h_1} \dots \int_{\tau_{h_{n_{\alpha,\sigma}-1}}}^\beta d\tau_{h_{n_{\alpha,\sigma}}} \int_0^\beta d\tau'_{h_1} \dots \int_{\tau'_{h_{n_{\alpha,\sigma}-1}}}^\beta d\tau'_{h_{n_{\alpha,\sigma}}} \right) \\
&\times \int_0^\beta d\tau_{b_1} \dots \int_{\tau_{b_{n_b-1}}}^\beta d\tau_{b_{n_b}} \int_0^\beta d\tau'_{\bar{b}_1} \dots \int_{\tau'_{\bar{b}_{n_{\bar{b}}-1}}}^\beta d\tau'_{\bar{b}_{n_{\bar{b}}}} \operatorname{Tr}_c \Big[T_\tau e^{-\beta H_{\text{dens}}} \\
&\left(\prod_{\substack{\alpha,\sigma \\ j_{h_1},\dots,j_{h_{n_{\alpha,\sigma}}} \\ j'_{h_1},\dots,j'_{h_{n_{\alpha,\sigma}}}}} \sum c_{j_{h_{n_{\alpha,\sigma}}}}\left(\tau_{h_{n_{\alpha,\sigma}}}\right) c^\dagger_{j'_{h_{n_{\alpha,\sigma}}}}\left(\tau'_{h_{n_{\alpha,\sigma}}}\right) \dots c_{j_{h_1}}(\tau_{h_1}) c^\dagger_{j'_{h_1}}\left(\tau'_{h_1}\right) \right) \\
&\times Q_{l_{b_{n_b}}}\left(\tau_{b_{n_b}}\right) \cdots Q_{l_{b_1}}(\tau_{b_1}) Q^\dagger_{l'_{\bar{b}_{n_{\bar{b}}}}}\left(\tau'_{\bar{b}_{n_{\bar{b}}}}\right) \cdots Q^\dagger_{l'_{\bar{b}_1}}\left(\tau'_{\bar{b}_1}\right)\Big] B^{(n_{\bar{b}}+n_b)} \det \boldsymbol{\Delta}^{\tau_{\{n_{\alpha,\sigma}\}},\, \tau'_{\{n_{\alpha,\sigma}\}}}_{j_{\{n_{\alpha,\sigma}\}},\, j'_{\{n_{\alpha,\sigma}\}}} s_{\{n_{\alpha,\sigma}\}} s_{T_\tau},
\end{aligned}
$$

where $s_{\{n_\alpha,\sigma\}}$ is a sign determined by the signature of the permutation which permutes the c operators taking part in the hybridization from their time-ordered sequence (smallest τ to the right) into the alternating order $\dots c_{j_{h_1}}(\tau_{h_1}) c^\dagger_{j'_{h_1}}\left(\tau'_{h_1}\right)$, and s_{T_τ} compensating for a possible sign change produced by the time ordering of all the operators.

The computation of the trace can be executed as in the usual segment implementation of CT-HYB in the density-density approximation. Note that the local configuration and the hybridization matrix are no longer in a one-to-one correspondence: the local configuration contains $2 \times \sum_{\alpha,\sigma} n_{\alpha,\sigma} + n_b + n_{\bar{b}}$ operators, while the hybridization matrix only has $\sum_{\alpha,\sigma} n_{\alpha,\sigma}$ rows and $\sum_{\alpha,\sigma} n_{\alpha,\sigma}$ columns. Another specificity to keep in mind is that Q_α and $Q^\dagger_\alpha$ have to come in pairs in case of diagonal hybridization matrix, which implies $n_b = n_{\bar{b}}$. Conversely, if the hybridization matrix has off-diagonal matrix elements, then this does not need to be respected. In terms of diagrams in Fig 9.10, this means that we can have an odd number of dashed vertical lines, or, stated differently, that we can have "dangling" broken segments without a partner, as represented close to $\tau = \beta$ on the b orbital.

9.5.2 Updates

In order to evaluate the partition function in the presence of a magnetic field, we propose to generate segment configurations in a Markov chain Monte Carlo process, such that the configurations are generated following their contribution to the partition function. We use all commonly employed updates of the usual segment implementation, i.e., segment/anti-segment insertion/removal, and shift of the operators which contribute to the hybridization (i.e., those represented by a circle in Fig 9.10).

In addition, we consider the addition/removal of intra-orbital spin flips, i.e. insertions of

- insertion and removal of $Q_\alpha(\tau_s)Q_\alpha^\dagger(\tau_s')$, $\tau_s > \tau_s'$,
- insertion and removal of $Q_\alpha^\dagger(\tau_s')Q_\alpha(\tau_s)$, $\tau_s' > \tau_s$.

The insertion/removal of "dangling segments", i.e. insertion or removal of isolated $Q_\alpha(\tau_s)$ or $Q_\alpha^\dagger(\tau_s)$ operators is relevant in the case of non-diagonal hybridization functions and needs to be considered (see the broken segment on the $|b\downarrow\rangle$ orbital, for τ close to β in Fig 9.10).

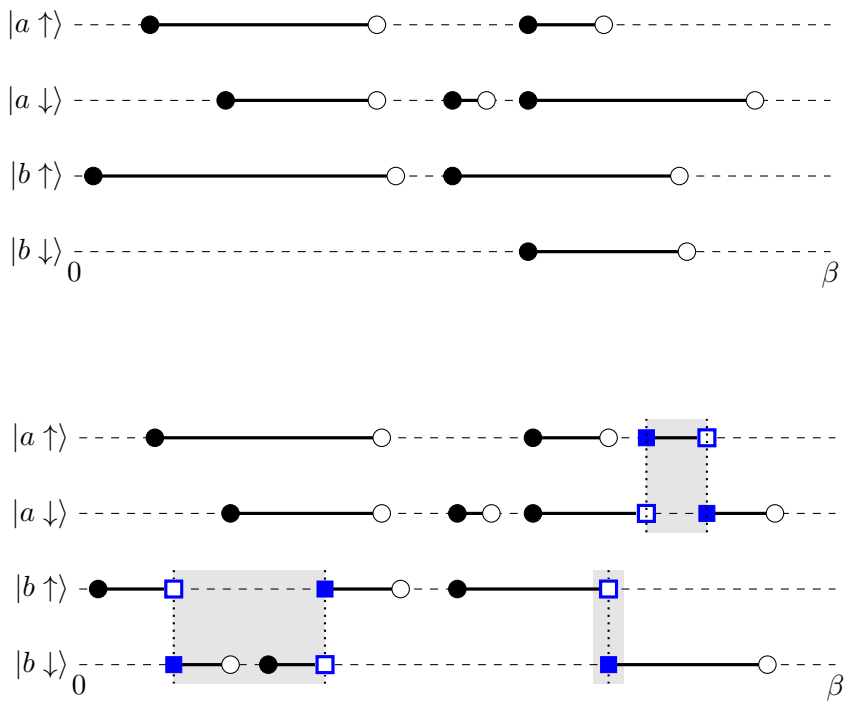

Figure 9.10: Upper panel: Initial configuration in the absence of magnetic field. Lower panel: The same configuration, modified by the insertion of spin-flip segments, following the action of the magnetic field.

9.5.3 Sampling

The insertion of an intra-orbital spin-flip is only possible if the impurity is in the appropriate state, e.g. the $|\uparrow, *\rangle$ state for an insertion of $Q_1^\dagger(\tau' s)Q_1(\tau_s)$, $\tau_s' > \tau_s$. We now examine this specific case in detail. The other possibilities (different values of α, and permutation of times/operators) can be deduced in a straightforward manner. First, we generate a random imaginary time τ_s and check whether the local state at τ_s is appropriate, i.e. of the kind $|\uparrow, *\rangle$. If it is not the case, the move is rejected. Otherwise, the length $l_{\max}$, defined as the distance in imaginary time between τ_s and the earliest occurrence of any operator on the $|1\uparrow\rangle$ or $|1\downarrow\rangle$ spin-orbital configuration lines, is calculated. The imaginary time τ_s' is then chosen randomly in the interval $[\tau_s, \tau_s + l_{\max}]$.

For the removal of a $Q_1^\dagger(\tau' s)Q_1(\tau_s)$, $\tau_s' > \tau_s$, a Q_1 operator acting acting at imaginary time τ_s is picked at random among the n_b^1 in the current configuration. Its $Q_1^\dagger$ partner

(the next-occurring one in imaginary time, acting on the same orbital and same spin) is identified, and τ_s' is defined as the imaginary time where it acts. If there is no other operator acting on any of the $|1\uparrow\rangle$ or $|1\downarrow\rangle$ orbitals in the imaginary time interval $[\tau_s, \tau_s']$, then the removal is accepted with the probability given below. Otherwise the move is rejected.

We define $l \equiv \tau' - s - \tau_s$, so that acceptance probabilities read:

$$\begin{aligned}
R_{Q_\alpha^\dagger Q_\alpha}(n_b \to n_b+1, n_{\bar{b}} \to n_{\bar{b}}+1) &= B^2 \frac{\beta l_{\max}}{n_b+1} e^{J(\Delta_{\text{overlap}\downarrow\downarrow} - \Delta_{\text{overlap}\uparrow\uparrow})}, \\
R_{Q_\alpha Q_\alpha^\dagger}(n_b \to n_b+1, n_{\bar{b}} \to n_{\bar{b}}+1) &= B^2 \frac{\beta l_{\max}}{n_{\bar{b}}+1} e^{-J(\Delta_{\text{overlap}\downarrow\downarrow} - \Delta_{\text{overlap}\uparrow\uparrow})}, \\
R_{Q_\alpha^\dagger Q_\alpha}(n_b \to n_b-1, n_{\bar{b}} \to n_{\bar{b}}-1) &= B^2 \frac{n_b}{\beta l_{\max}} e^{-J(\Delta_{\text{overlap}\downarrow\downarrow} - \Delta_{\text{overlap}\uparrow\uparrow})}, \\
R_{Q_\alpha Q_\alpha^\dagger}(n_b \to n_b-1, n_{\bar{b}} \to n_{\bar{b}}-1) &= B^2 \frac{n_{\bar{b}}}{\beta l_{\max}} e^{J(\Delta_{\text{overlap}\downarrow\downarrow} - \Delta_{\text{overlap}\uparrow\uparrow})},
\end{aligned} \tag{9.18}$$

where the R_{AB} notation implies that the B operator has the smaller time argument. $\Delta_{\text{overlap }\sigma\sigma}$ is defined as the difference between the total overlap between segments in orbitals 1σ and 2σ in the new configuration, minus the total overlap between segments in orbitals 1σ and 2σ in the old configuration. We note that the acceptance probability of lowering (increasing) the spin of a given orbital depends on the spin state of the other orbital, and is asymmetric if the other orbital is not fully occupied, illustrating the crucial role of Hund's coupling in the context of the transitions between these configurations.

Chapter 10

Summary and outlook

The thesis has addressed ordered phases of two classes of strongly correlated materials: the superconducting phase of high-temperature cuprate superconductors, and the excitonic-condensate phase of the two-dimensional Hubbard model. The functional integral formalism introduced in Chapter 5 was used to justify the spin-fermion model of high-temperature cuprate superconductors, to derive the equations of the Dynamical Mean-Field Theory (in Chapter 6), and to introduce an efficient numerical approach to the Anderson impurity model, based on Monte Carlo sampling (in Chapter 7).

The main results we obtained concern (*i*) the influence of the upper branch of the hour-glass magnetic spectrum on the electronic dispersion in the superconducting state of cuprates, and (*ii*) the spontaneous emergence of spin textures in multiorbital Mott systems. They are presented in Chapter 8 and Chapter 9, respectively. The renormalization of the electronic dispersion in cuprates has been studied using the spin-fermion model and the spin textures in multiorbital Mott systems using the Dynamical Mean-Field Theory.

Impact of the upper branch of the magnetic spectrum on the electronic dispersion

We have investigated the effect of the upper branch of the hour-glass magnetic spectrum on the electronic dispersion of high-T_c cuprate superconductors using the fully self-consistent version of the phenomenological model, where charged planar quasiparticles are coupled to spin fluctuations. A key ingredient of this study, as compared to previous works, is that a realistic input band structure and a realistic input spin susceptibility, both introduced in a recent study by Dahm et al. [Nat. Phys. **5**, 217 (2009)] have been used. The following results have been obtained:

- We have confirmed the finding by Dahm et al., that the energy of the nodal kink is determined, for the present values of the input parameters, by the upper branch of the magnetic spectrum.
- We have further demonstrated that the position and the shape of the kink depend strongly on the strength of the charge-spin coupling. For low (but still realistic) values of the coupling constant, the position of the kink can be estimated using the common approximation, where the quasimomentum dependence of the self-energy along the Fermi surface cut is neglected. The kink is weak but sharp. For high values of the coupling constant, however, the dependence of the self-energy on the quasimomentum plays an important role. The kink is less sharp, but has a larger amplitude.

- We have shown that the kurtosis of the resonance mode of the spin susceptibility in the quasimomentum space has a major influence on the mechanism of the fermionic scattering. If the kurtosis is low (high), as in the present study (as in several previous studies), the effect of the resonance mode in the near-nodal region of the Brillouin zone is weak (large), and the upper branch of the hour-glass (the resonance mode) plays the major role in the formation of the nodal kink.

- The calculated energy of the kink decreases as a function of the angle θ between the Fermi surface cut and the nodal direction. This result is in qualitative agreement with recent experimental results by Plumb et al. [New J. Phys. **15**, 113004 (2013)].

- Based on our interpretation of the formation of the kink, we have been able to modify the values of the input parameters in such a way that both the renormalized (nodal) Fermi velocity and the energy of the nodal kink are close to the experimental values for underdoped YBCO reported by Dahm et al. The calculated magnitude of the slope of the angular dependence of the kink energy is close to that of optimally doped Bi2212 reported by Plumb et al.

- We predict that there exists a critical value θ_c such that the energy of the kink is a decreasing (weakly increasing) function of θ for $\theta < \theta_c$ ($\theta > \theta_c$), and provide a possible qualitative interpretation for the difference between the kink in underdoped YBCO and that in optimally doped Bi2212.

These results call for additional experiments, which could confirm the latter prediction. The continuous development of ARPES techniques make this a possibility in the near future.

Spontaneous Spin Textures in Multiorbital Mott Systems

We have investigated excitonic condensation in the two-band Hubbard model, away from half-filling, on the hole-doped side of the phase diagram. The key ingredient, relative to previous studies, is the use of a finite hopping between different orbitals on nearest neighbor sites (the so-called cross-hopping). Both patterns of the cross-hopping compatible with the symmetries of the system have been considered: even and odd. The following numerical results were obtained, using single-site DMFT:

- We confirmed the existence of three different kinds of order below the critical temperature, which were reported in a previous work by Kuneš [Phys. Rev. B **90**, 235140 (2014)]: a ferromagnetically ordered phase (FMEC), a spin-current density wave (SCDW) phase, and a spin-density wave (SDW) phase.

- We were able to further distinguish the polar phases (SCDW and SDW) into two species: in the presence of odd (even) cross-hopping, the magnetization in the SDW (SCDW) phase is purely local, while the other polar phase, SCDW (SDW) exhibits a $\boldsymbol{k}$-space spin texture.

We then used a strong coupling approach, recently derived by Kuneš and Augustinský [Phys. Rev. B **89**, 115134 (2014)], which allowed us to interpret the emergence of the different phases with increasing doping as a result of a mechanism analogous to the Zener double exchange. Finally, we pointed out a few real compounds in which these effects could be realized.

Outlook

The present work represents an important step in clarifying the interplay between the upper branch of the magnetic spectrum and the resonance mode, and the way it gives rise to structures in the momentum-dependent self-energy, but it also opens further questions. In particular, the validity of the usual approach to the extraction of the self-energy from experimental data (the so-called effective self-energy approach) should be further examined. Its results should be compared with those obtained from a model-based approach to the momentum-dependent self-energy.

Another issue to consider, after the origin of the kink has been linked to the high-energy branch of the magnetic spectrum, is the evolution of the kink with temperature. The magnetic spectrum exhibits a strong temperature dependence, in particular as far as the resonance mode around the critical temperature is concerned. It would be worthwhile to find out whether the experimental observations of the temperature dependence of the kink and those of the magnetic spectrum also fit together within the spin-fluctuation based model.

Concerning the excitonic condensation in the Hubbard model, the challenges ahead are related to those of the DMFT technique. In particular, it will be interesting to investigate the behavior of two-particle quantities close to and above the critical temperature. The static susceptibilities have been calculated in previous works by Kuneš [Phys. Rev. B **83**, 085102 (2011)] and Kuneš and Augustinský [Phys. Rev. B **89**, 115134 (2014)], clearly showing the proximity of the excitonic instability. The dynamic susceptibility remains to be studied. Furthermore, the condensation should be addressed within more realistic models, respecting the full rotational invariance of the Coulomb interaction, and including all the five transition metal d-orbitals. This still represents an algorithmic and numerical challenge.

Appendix A

Gaussian integrals over the Grassmann algebra

In this appendix, we derive the value of the Gaussian integral over Grassmann variables. As an introduction, we recall the result for an integral over real variables:

$$\frac{1}{(2\pi)^{\frac{n}{2}}}\int dx_1\dots dx_n e^{-\frac{1}{2}x_iA_{ij}x_j+x_iJ_i}=[\det A]^{-\frac{1}{2}}e^{\frac{1}{2}J_iA^{-1}_{ij}J_j}, \tag{A.1}$$

where A is a real symmetric definite positive matrix, and summation over repeated indices is assumed. A similar identity holds for a Gaussian integral over complex variables, in the form:

$$\int\prod_{i=1}^{n}\frac{dx_i^*dx_i}{2i\pi}e^{-x_i^*H_{ij}x_j+J_i^*x_i+J_ix_i^*}=[\det H]^{-1}e^{J_i^*H^{-1}_{ij}J_j}, \tag{A.2}$$

where H is a Hermitian matrix.

We would like to calculate a similar Gaussian integral, and show the following result holds, when the integral is carried out over Grassmann variables:

$$\int\prod_{i=1}^{n}d\eta_j^*d\eta_j e^{-\eta_i^*H_{ij}\eta_j+\zeta_i^*\eta_i+\zeta_i\eta_i^*}=\det H\exp\left[\zeta_i^*H^{-1}_{ij}\zeta_j\right], \tag{A.3}$$

where H is Hermitian, $\{\eta_i,\eta_i^*,\zeta_i^*,\zeta_i\}$ are Grassmann variables, and summation over repeated indices is assumed. The derivation below follows the presentation by Orland and Negele in Ref. [120].

We first consider a Gaussian integral involving a single pair of conjugate Grassmann variables:

$$\int d\xi^*d\xi e^{-\xi^*a\xi}=\int d\xi^*d\xi(1-\xi^*a\xi)=a. \tag{A.4}$$

Thus, if we can bring the multivariable Grassmann integral Eq. (A.3) into diagonal form, then we may use this relation and expect to obtain the product of eigenvalues, i.e. the determinant of H, in the numerator of the result (instead of the denominator, which is the result for complex variables).

In order to do this, we derive the law for linear transformations of Grassmann variables: Given a polynomial P,

$$I=\int d\zeta_1^*d\zeta_1\dots d\zeta_n^*d\zeta_nP(\zeta^*,\zeta)=\left|\frac{\partial(\eta^*,\eta)}{\partial(\zeta^*,\zeta)}\right|\int d\eta_1^*d\eta_1\dots d\eta_n^*d\eta_n\times P(\zeta^*(\eta^*,\eta),\zeta^*(\eta^*,\eta)). \tag{A.5}$$

For this, we introduce the notation

$$\begin{aligned}(\zeta_1^*, \zeta_2^*, \ldots, \zeta_n^*, \zeta_n, \zeta_{n-1}, \ldots, \zeta_1) &\equiv \left(\tilde{\zeta}_1, \tilde{\zeta}_2^*, \ldots, \tilde{\zeta}_{2n}^*\right) \\ (\eta_1^*, \eta_2^*, \ldots, \eta_n^*, \eta_n, \eta_{n-1}, \ldots, \eta_1) &\equiv (\tilde{\eta}_1, \tilde{\eta}_2^*, \ldots, \tilde{\eta}_{2n}^*),\end{aligned} \tag{A.6}$$

and write

$$\tilde{\zeta}_i = M_{ij}\tilde{\eta}_j. \tag{A.7}$$

The only non-vanishing contributions to Eq. (A.5) come from the term in the polynomial which contains each $\tilde{\zeta}_i$ as a factor once, and once only. This term can be written as $p\prod_{i=1}^{2n}\tilde{\zeta}_i$. With this, we obtain

$$I = \int d\zeta_1^* d\zeta_1 \ldots d\zeta_n^* d\zeta_n p \prod_{i=1}^{2n}\tilde{\zeta}_i = J\int d\eta_1^* d\eta_1 \ldots d\eta_n^* d\eta_n p \prod_{i=1}^{2n}\left(\sum_j M_{ij}\tilde{\eta}_j\right), \tag{A.8}$$

in which J needs to be evaluated. The left-hand side yields $p(-1)^n$. For the right-hand side, we note that the only non-zero contributions arise from the $(2n)!$ distinct permutations P of the variables $\{\tilde{\eta}\}$ generated by the product. Thus,

$$\begin{aligned} I = p(-1)^n &= Jp\int d\eta_1^* d\eta_1 \ldots d\eta_n^* d\eta_n \prod_{i=1}^{2n}\left(\sum_j M_{ij}\tilde{\eta}_j\right) \\ &= Jp\int d\eta_1^* d\eta_1 \ldots d\eta_n^* d\eta_n \sum_P \prod_i M_{iP(i)}\tilde{\eta}_{P(i)} \\ &= Jp\sum_P \prod_i M_{iP(i)}(-1)^P \int d\eta_1^* d\eta_1 \ldots d\eta_n^* d\eta_n \tilde{\eta}_1\tilde{\eta}_2 \ldots \tilde{\eta}_{2n} \\ &= Jp\det M(-1)^n,\end{aligned} \tag{A.9}$$

so that

$$J = (\det M)^{-1} = \left|\frac{\partial(\tilde{\eta})}{\partial\left(\tilde{\zeta}\right)}\right| = \left|\frac{\partial(\eta^*, \eta)}{\partial(\zeta^*, \zeta)}\right|, \tag{A.10}$$

which proves Eq. (A.5) for a general linear transformation. Equipped with this relation, we diagonalize H via the unitary transformation U and define the following transformations:

$$\begin{aligned}\rho_i &= \eta_i - H_{ij}^{-1}\zeta_i, \\ \rho_i^* &= \eta_i^* - H_{ij}^{-1}\zeta_i^*, \\ \xi_i &= U_{ij}^{-1}\rho_j, \\ \xi_i^* &= U_{ij}^{-1*}\rho_j^*.\end{aligned} \tag{A.11}$$

We can use Eq. (A.4), and the fact that all involved Jacobians are unity, to get

$$\begin{aligned}
&\int \prod_{i=1}^{n} d\eta_j^* d\eta_j e^{-\eta_i^* H_{ij} \eta_j + \zeta_i^* \eta_i + \zeta_i \eta_i^* - \zeta_i^* H_{ij}^{-1} \zeta_j} \\
&\qquad = \int \prod_{i=1}^{n} d\rho_i^* d\rho_i e^{-\rho_i^* H_{ij} \rho_j} \\
&\qquad = \int \prod_{i=1}^{n} d\xi_i^* d\xi_i e^{-\sum\limits_i h_i \xi_i^* \xi_i} \\
&\qquad = \prod_{m=1}^{n} h_m = \det H,
\end{aligned} \tag{A.12}$$

which proves Eq. (A.3).

Appendix B

Link between cavity and full Green's function in DMFT

Equation 6.25 yields (the spin index is dropped for readability)

$$\begin{aligned}\mathcal{G}_0^{-1}(i\omega_n)^{\mathrm{IDHM}} &= i\omega_n + \mu - \sum_{ij} t_{i0}t_{j0}\left(G_{ij}(i\omega_n) - \frac{G_{i0}(i\omega_n)G_{0j}(i\omega_n)}{G_{00}(i\omega_n)}\right) \\ &= i\omega_n + \mu - \sum_{ij} t_{i0}t_{j0}G_{ij}(i\omega_n) + \frac{\left(\sum_i t_{i0}G_{i0}(i\omega_n)\right)^2}{G_{00}(i\omega_n)},\end{aligned} \tag{B.1}$$

In order to make progress, we use the known form of the Fourier transform of the Green's function $G_{ij}(i\omega_n)$ (introducing the momentum dependence explicitly in the notation, and assuming a momentum-independent self-energy, an assumption which has to be justified on its own by power counting in $1/d$ [10]):

$$\begin{aligned}G(\mathbf{k}, i\omega_n) &= \frac{1}{i\omega_n + \mu - \epsilon_{\mathbf{k}} - \Sigma(i\omega_n)} = \frac{1}{\xi(i\omega_n) - \epsilon_{\mathbf{k}}}, \\ \xi(i\omega_n) &\equiv i\omega_n + \mu - \Sigma(i\omega_n), \\ \epsilon_{\mathbf{k}} &\equiv \sum_j t_{ij} e^{-i\mathbf{k}(\mathbf{r}_i - \mathbf{r}_j)}, \forall i.\end{aligned} \tag{B.2}$$

We also introduce the density of states

$$D(\epsilon) = \sum_{\mathbf{k}\in \mathrm{BZ}} \delta(\epsilon - \epsilon(\mathbf{k})). \tag{B.3}$$

With these notations, we may express $G_{ij}(i\omega_n)$ as the inverse Fourier transform of $G(\mathbf{k}, i\omega_n)$, t_{i0} as the inverse Fourier transform of $\epsilon_{\mathbf{k}}$, and insert the expressions into the

last two terms of the right-hand side of Eq. (B.1), which become:

$$\begin{aligned}\sum_{ij} t_{i0}t_{j0}G_{ij}(i\omega_n) - \frac{\left(\sum_i t_{i0}G_{i0}(i\omega_n)\right)^2}{G_{00}(i\omega_n)} &= \sum_{\mathbf{k}\in \mathrm{BZ}} \frac{\epsilon_{\mathbf{k}}^2}{\xi(i\omega_n)-\epsilon_{\mathbf{k}}} - \frac{\left[\sum_{\mathbf{k}\in \mathrm{BZ}} \frac{\epsilon_{\mathbf{k}}}{\xi(i\omega_n)-\epsilon_{\mathbf{k}}}\right]^2}{\sum_{\mathbf{k}\in \mathrm{BZ}} \frac{1}{\xi(i\omega_n)-\epsilon_{\mathbf{k}}}} \\ &= \int_{-\infty}^{+\infty} d\epsilon\ D(\epsilon)\frac{\epsilon^2}{\xi(i\omega_n)-\epsilon} - \frac{\left[\int_{-\infty}^{+\infty} d\epsilon\ D(\epsilon)\frac{\epsilon}{\xi(i\omega_n)-\epsilon}\right]^2}{\int_{-\infty}^{+\infty} d\epsilon\ D(\epsilon)\frac{1}{\xi(i\omega_n)-\epsilon}}.\end{aligned} \tag{B.4}$$

Moreover, we notice that $t_{00} = \sum_{\mathbf{k}\in \mathrm{BZ}} \epsilon_{\mathbf{k}} = 0$, and introduce $\tilde{D}(\xi) \equiv \int_{-\infty}^{+\infty} d\epsilon\ D(\epsilon)\frac{1}{\xi-\epsilon}$, so that

$$\begin{aligned}&\int_{-\infty}^{+\infty} d\epsilon\ D(\epsilon)\frac{\epsilon}{\xi(i\omega_n)-\epsilon} = -1 + \xi(i\omega_n)\tilde{D}(\xi(i\omega_n)), \\ &\int_{-\infty}^{+\infty} d\epsilon\ D(\epsilon)\frac{\epsilon^2}{\xi(i\omega_n)-\epsilon} = \int_{-\infty}^{+\infty} d\epsilon\ D(\epsilon)\epsilon\left(-1+\frac{\xi(i\omega_n)}{\xi(i\omega_n)-\epsilon}\right) \\ &= \xi(i\omega_n)\int_{-\infty}^{+\infty} d\epsilon\ D(\epsilon)\frac{\epsilon}{\xi(i\omega_n)-\epsilon} = \xi(i\omega_n)\Big[-1+\xi(i\omega_n)\tilde{D}(\xi(i\omega_n))\Big],\end{aligned} \tag{B.5}$$

and Eq. (B.4) simplifies to

$$\sum_{ij} t_{i0}t_{j0}G_{ij}(i\omega_n) - \frac{\left(\sum_i t_{i0}G_{i0}(i\omega_n)\right)^2}{G_{00}(i\omega_n)} = \xi(i\omega_n) - \frac{1}{\tilde{D}(\xi(i\omega_n))}. \tag{B.6}$$

Inserting this expression into Eq. (B.1), we obtain

$$\mathcal{G}_0^{-1}(i\omega_n)^{\mathrm{IDHM}} = \Sigma(i\omega_n) + \frac{1}{\tilde{D}(i\omega_n+\mu-\Sigma(i\omega_n))}. \tag{B.7}$$

Appendix C

Fast update formulas

The fast-update formulas are a generalization of the Shermann-Morrison formula [241], which provides a way of efficiently calculating the inverse of a matrix $\boldsymbol{B}$, in the case where $\boldsymbol{B}$ differs only slightly from matrix $\boldsymbol{A}$, whose inverse is known:

$$\begin{aligned} \boldsymbol{A} &\to \boldsymbol{A}^{-1} \\ \boldsymbol{A} + \underline{u} \otimes \underline{v} \to (\boldsymbol{A} + \underline{u} \otimes \underline{v})^{-1} &= \boldsymbol{A}^{-1} - \frac{\left(\boldsymbol{A}^{-1} \cdot \underline{u}\right) \otimes \left(\underline{v} \cdot \boldsymbol{A}^{-1}\right)}{1+\lambda}, \\ \lambda &= \underline{v} \cdot \boldsymbol{A}^{-1} \underline{u}. \end{aligned} \tag{C.1}$$

This method allows the computation of the inverse of a matrix with N^2 operations instead of N^3, for a matrix of dimension N. As discussed in Sec. 7.4, in the actual implementations of the hybridization expansion solver, the inverse of the hybridization matrix $\boldsymbol{M}_k = \boldsymbol{\Delta}_k^{-1}$, for a configuration of order k, is stored and manipulated. This section follows the presentation by Kiss [242]

C.1 Segment insertion

Let us consider the case of a Monte Carlo step in which a segment is added to the current configuration of order k, associated to annihilation operator i and creation operator j. Accordingly, a row i and a column j are added to the initial matrix $\boldsymbol{\Delta}_k$, which becomes

$$\boldsymbol{\Delta}_k = \begin{pmatrix} . & . & 0 & . \\ . & . & 0 & . \\ 0 & 0 & 1 & 0 \\ . & . & 0 & . \end{pmatrix}, \tag{C.2}$$

such that the determinant $\det \boldsymbol{\Delta}_k$ is not changed. We may then modify the values of the new row and column, by their known values (deduced, in the framework of DMFT, from the values of the hybridization function at this stage of the self-consistent procedure), $\bar{\Delta}_{i1}, \bar{\Delta}_{i2}, \ldots, \bar{\Delta}_{ik+1}$ for row i, and $\bar{\Delta}_{1j}, \bar{\Delta}_{2j}, \ldots, \bar{\Delta}_{k+1j}$ for column j, in order to obtain the matrix $\boldsymbol{\Delta}_{k+1}^{+ij}$. We consider this latter transformations in two separate steps.

Step 1

In this step, the j^{th} column of $\boldsymbol{\Delta}_k$ is modified by means of the transformation $(\boldsymbol{\Delta}_k)_{nj} \to \bar{\Delta}_{nj}, \forall n \in \{1, 2, \ldots, k+1\}$. The matrix thus obtained is denoted by δ_{k+1}^{+ij}. This is equivalent

to a transformation of $\mathbf{\Delta}_k$ as described in Eq. (C.1) for A, with the following values for the vectors $\underline{u}$ and $\underline{v}$:

$$\begin{aligned} \underline{u} : u_n &= \bar{\Delta}_{nj} - (\mathbf{\Delta}_k)_{nj}, \\ \underline{v} : v_n &= \begin{cases} 1 & \text{if } n = j \\ 0 & \text{otherwise} \end{cases}, \end{aligned} \tag{C.3}$$

The value of the corresponding parameter λ is given by:

$$\lambda = \sum_l \left(\mathbf{\Delta}_k^{-1}\right)_{jl} \Big(\bar{\Delta}_{lj} - (\mathbf{\Delta}_k)_{lj}\Big) = \left(\mathbf{\Delta}_k^{-1}\right)_{ji} \Big(\bar{\Delta}_{ij} - (\mathbf{\Delta}_k)_{ij}\Big) = \bar{\Delta}_{ij} - 1 \equiv \lambda_I - 1. \tag{C.4}$$

For ease of notation we introduce the row vector $\underline{R}$ and column vector $\underline{L}$, defined as:

$$\begin{aligned} R_t &= \sum_{l=1}^{k} \bar{\Delta}_{il} (M_k)_{lt}, \\ L_s &= \sum_{l=1}^{k} (M_k)_{sl} \bar{\Delta}_{lj}. \end{aligned} \tag{C.5}$$

Using Eq. (C.1), we find

$$\begin{aligned} M'_{nm} &= \left(\mathbf{\Delta}_k^{-1}\right)_{nm} - \frac{1}{1+\lambda} \left(\sum_l \left(\mathbf{\Delta}_k^{-1}\right)_{nl} \Big(\bar{\Delta}_{lj} - (\mathbf{\Delta}_k)_{lj}\Big) \right) \left(\mathbf{\Delta}_k^{-1}\right)_{jm} \\ &= (\boldsymbol{M}_k)_{nm} - \frac{1}{\lambda_I} \left(\sum_l (\boldsymbol{M}_k)_{nl} \bar{\Delta}_{lj} - \left(\mathbf{\Delta}_k^{-1} \mathbf{\Delta}_k\right)_{nj} \right) (\boldsymbol{M}_k)_{jm} \\ &= (\boldsymbol{M}_k)_{nm} - \frac{1}{\lambda_I} \left(\sum_l (\boldsymbol{M}_k)_{nl} \bar{\Delta}_{lj} - \delta_{nj} \right) (\boldsymbol{M}_k)_{jm} \\ &= \begin{cases} (\boldsymbol{M}_k)_{nm} & \text{if } n \neq j \text{ and } m \neq i \\ -\dfrac{1}{\lambda_I} \left(\sum\limits_l (\boldsymbol{M}_k)_{nl} \bar{\Delta}_{lj} \right) = -\dfrac{1}{\lambda_I} L_n & \text{if } n \neq j \text{ and } m = i \\ \dfrac{1}{\lambda_I} & \text{if } n = j \text{ and } m = i. \end{cases}, \end{aligned} \tag{C.6}$$

Step 2

In this step δ_{k+1}^{+ij} is transformed into $\mathbf{\Delta}_{k+1}^{+ij}$, by the following replacements affecting its i^{th} row: $(\mathbf{\Delta}_k)_{in} \to \bar{\Delta}_{in}, \forall n \in \{1, 2, \ldots, k+1\}$. In this case, with the notations of Eq. (C.1), we have:

$$\begin{aligned} \underline{u} : u_n &= \begin{cases} 1 & \text{if } n = i, \\ 0 & \text{otherwise.} \end{cases} \\ \underline{v} : v_n &= \bar{\Delta}_{in} - (\mathbf{\Delta}_k)_{in}, \end{aligned} \tag{C.7}$$

while the λ parameter becomes:

$$\begin{aligned} \lambda &= \sum_l \big(\bar{\Delta}_{il} - (\mathbf{\Delta}_k)_{il}\big) \left(\left(\delta_{k+1}^{+ij}\right)^{-1} \right)_{li} = \sum_l \big(\bar{\Delta}_{il} - (\mathbf{\Delta}_k)_{il}\big) M'_{li} \\ &- \frac{1}{\lambda_I} \sum_{ll'} \big(\bar{\Delta}_{il} - (\mathbf{\Delta}_k)_{il}\big) (\boldsymbol{M}_k)_{ll'} \bar{\Delta}_{l'j} = -\frac{1}{\lambda_I} \sum_{ll'} \bar{\Delta}_{il} (\boldsymbol{M}_k)'_{ll'} \bar{\Delta}_{l'j} \equiv \lambda_{II} - 1, \end{aligned} \tag{C.8}$$

where use was made of Eq. (C.6).

Application of Eq. (C.1) with these initial quantities thus leads to:

$$M''_{nm} = M'_{nm} - \frac{1}{\lambda_{II}}\left[M'_{ni}\cdot\sum_l\left(\bar{\Delta}_{il} - (\boldsymbol{\Delta}_k)_{il}\right)M'_{lm}\right], \tag{C.9}$$

which simplifies to:

- if $n \neq j$ and $m \neq i$:

$$\begin{aligned} M''_{nm} &= M_{nm} - \frac{1}{\lambda_{II}}\left[-\frac{1}{\lambda_I}\left(\sum_l (\boldsymbol{M}_k)_{nl}\bar{\Delta}_{lj}\right)\right]\cdot\sum_l\left(\bar{\Delta}_{il} - (\boldsymbol{\Delta}_k)_{il}\right)(\boldsymbol{M}_k)_{lm}] \\ &= M_{nm} + \frac{1}{\lambda_{II}\lambda_I}\left(\sum_l (\boldsymbol{M}_k)_{nl}\bar{\Delta}_{lj}\right)\cdot\left(\sum_l \bar{\Delta}_{il}(\boldsymbol{M}_k)_{lm}\right) = M_{nm} + \frac{1}{\lambda_{II}\lambda_I}L_n R_m. \end{aligned} \tag{C.10}$$

- if $n \neq j$ and $m = i$:

$$\begin{aligned} M''_{ni} &= -\frac{1}{\lambda_I}L_n - \frac{1}{\lambda_{II}}\left[M'_{ni}\cdot\sum_l\left(\bar{\Delta}_{il} - (\boldsymbol{\Delta}_k)_{il}\right)M'_{li}\right] \\ &= -\frac{1}{\lambda_I}L_n - \frac{1}{\lambda_{II}}\left[M'_{ni}\cdot(\lambda_{II}-1)\right] = -\frac{1}{\lambda_I}L_n - \frac{1}{\lambda_{II}}\left[-\frac{1}{\lambda_I}L_n\cdot(\lambda_{II}-1)\right] \\ &= -\frac{L_n}{\lambda_I\lambda_{II}}. \end{aligned} \tag{C.11}$$

- if $n = j$ and $m \neq i$:

$$\begin{aligned} M''_{jm} &= 0 - \frac{1}{\lambda_{II}}\left[\frac{1}{\lambda_I}\cdot\sum_l\left(\bar{\Delta}_{il} - (\boldsymbol{\Delta}_k)_{il}\right)M'_{lm}\right] = -\frac{1}{\lambda_I\lambda_{II}}\cdot\sum_l\left(\bar{\Delta}_{il}(\boldsymbol{M}_k)_{lm}\right) \\ &= -\frac{R_m}{\lambda_I\lambda_{II}}. \end{aligned} \tag{C.12}$$

- if $n = j$ and $m = i$:

$$\begin{aligned} M''_{ji} &= \frac{1}{\lambda_I} - \frac{1}{\lambda_{II}}\left[\frac{1}{\lambda_I}\cdot\sum_l\left(\bar{\Delta}_{il} - (\boldsymbol{\Delta}_k)_{il}\right)M'_{li}\right] = \frac{1}{\lambda_I} - \frac{1}{\lambda_I\lambda_{II}}(\lambda_{II}-1) \\ &= \frac{1}{\lambda_I\lambda_{II}}. \end{aligned} \tag{C.13}$$

Therefore, The inverse of the fully transformed matrix is given in block form as:

$$\boldsymbol{M}_{k+1} = \left(\begin{array}{c|c|c} \boldsymbol{N} & -\underline{L}^{(i)}/\lambda^+ & \boldsymbol{N} \\ \hline -\underline{R}^{(j)}/\lambda^+ & 1/\lambda^+ & -\underline{R}^{(j)} \\ \hline \boldsymbol{N} & -\underline{L}^{(i)}/\lambda^+ & \boldsymbol{N} \end{array}\right), \tag{C.14}$$

where

$$\begin{aligned} N_{ts} &= (\boldsymbol{M}_k)_{ts} + L_t^{(i)}R_s^{(j)}/\lambda^+ \\ \lambda^+ &\equiv \lambda_I\lambda_{II} = \bar{\Delta}_{ij} - \sum_{st}\bar{\Delta}_{sj}(\boldsymbol{M}_k)_{ts}\bar{\Delta}_{it}. \end{aligned} \tag{C.15}$$

The relation between the inverse of a matrix, and its cofactors and determinant provides us with the relation:

$$\begin{aligned}(\boldsymbol{M}_k)_{ji} &= (-1)^{i+j}\frac{\det \boldsymbol{\Delta}_{(k-1),\neq ij}}{\det \boldsymbol{\Delta}_k} \\ \Rightarrow \det \boldsymbol{\Delta}^{(ij)}_{k+1}(\boldsymbol{M}_{k+1})_{ji} &= (-1)^{i+j}\det \boldsymbol{\Delta}_k,\end{aligned} \tag{C.16}$$

so that the ratio of determinants, which enters the acceptance ratio of the Markov chain in the CT-HYB algorithm can be evaluated as

$$\frac{\det \boldsymbol{\Delta}^{(ij)}_{k+1}}{\det \boldsymbol{\Delta}_k} = (-1)^{i+j}\frac{1}{(\boldsymbol{M}_{k+1})_{ji}} = (-1)^{i+j}\lambda^+. \tag{C.17}$$

C.2 Segment removal

This is the case where the i^{th} row and j^{th} column of $\boldsymbol{\Delta}_k$ are erased, to generate $\boldsymbol{\Delta}_{(k-1),\neq ij}$. In this case, an approach similar to that developed for the study of the insertion of a segment gives the matrix elements of the $\boldsymbol{M}_{k-1}$ as:

$$\begin{aligned}(\boldsymbol{M}_{k-1})_{st} &= (\boldsymbol{M}_k)_{st} - \frac{(\boldsymbol{M}_k)_{si}(\boldsymbol{M}_k)_{jt}}{\lambda^-}, \\ \lambda^- &\equiv (\boldsymbol{M}_k)_{ji}.\end{aligned} \tag{C.18}$$

The determinant ratio comes out as follows:

$$\frac{\det\left(\boldsymbol{\Delta}_{k-1}\right)_{(\neq ij)}}{\det \boldsymbol{\Delta}_k} = (-1)^{i+j}(\boldsymbol{M}_k)_{ji} = (-1)^{i+j}\lambda^-. \tag{C.19}$$

C.3 Segment shift

C.3.1 Shift of a creation time

In this section we consider a move consisting in the shift of a vertex of the configuration, associated with a creation operator, e.g. with column j of the matrix $\boldsymbol{\Delta}_k$. In this case, the j^{th} column of $\boldsymbol{\Delta}_k$ is transformed, following $(\boldsymbol{\Delta}_k)_{nj} \to \bar{\Delta}_{nj}, \forall n \in \{1, 2, \ldots, k\}$. This corresponds, in the formulation of Eq. (C.1), to

$$\begin{aligned}\underline{u} : u_n &= \bar{\Delta}_{nj} - (\boldsymbol{\Delta}_k)_{nj}, \\ \underline{v} : v_n &= \begin{cases} 1 & \text{if } n = j, \\ 0 & \text{otherwise.}\end{cases}\end{aligned} \tag{C.20}$$

The corresponding value for the parameter λ is given by:

$$\begin{aligned}\lambda &= \sum_l \left(\boldsymbol{\Delta}_k^{-1}\right)_{jl}\Big(\bar{\Delta}_{lj} - (\boldsymbol{\Delta}_k)_{lj}\Big) = \sum_l \left(\boldsymbol{\Delta}_k^{-1}\right)_{jl}\bar{\Delta}_{lj} - \sum_l \left(\boldsymbol{\Delta}_k^{-1}\right)_{jl}(\boldsymbol{\Delta}_k)_{lj} \\ &= \sum_l (\boldsymbol{M}_k)_{jl}\bar{\Delta}_{lj} - 1 \equiv \lambda_I - 1.\end{aligned} \tag{C.21}$$

Using Eq. (C.1), we get the matrix elements for the inverse of the updated matrix:

$$\begin{aligned} M'_{nm} &= \left(\boldsymbol{\Delta}_k^{-1}\right)_{nm} - \frac{1}{1+\lambda}\left(\sum_l \left(\boldsymbol{\Delta}_k^{-1}\right)_{nl}\left(\bar{\Delta}_{lj} - (\boldsymbol{\Delta}_k)_{lj}\right)\right)\left(\boldsymbol{\Delta}_k^{-1}\right)_{jm} \\ &= (\boldsymbol{M}_k)_{nm} - \frac{1}{\lambda_I}\left(\sum_l (\boldsymbol{M}_k)_{nl}\bar{\Delta}_{lj} - \left(\boldsymbol{\Delta}_k^{-1}\boldsymbol{\Delta}_k\right)_{nj}\right)(\boldsymbol{M}_k)_{jm} \\ &= (\boldsymbol{M}_k)_{nm} - \frac{1}{\lambda_I}\left(\sum_l (\boldsymbol{M}_k)_{nl}\bar{\Delta}_{lj} - \delta_{nj}\right)(\boldsymbol{M}_k)_{jm} \\ &= \begin{cases} (\boldsymbol{M}_k)_{nm} - \dfrac{1}{\lambda_I}\left[\sum_l (\boldsymbol{M}_k)_{nl}\bar{\Delta}_{lj}\right](\boldsymbol{M}_k)_{jm} & \text{if } n \neq j. \\ (\boldsymbol{M}_k)_{jm} - \dfrac{1}{\lambda_I}\left[\sum_l (\boldsymbol{M}_k)_{jl}\bar{\Delta}_{lj} - 1\right](\boldsymbol{M}_k)_{jm} & \\ = (\boldsymbol{M}_k)_{jm}\left[1 - \dfrac{\lambda_I - 1}{\lambda_I}\right] = \dfrac{(\boldsymbol{M}_k)_{jm}}{\lambda_I} & \text{if } n = j. \end{cases} \end{aligned} \tag{C.22}$$

C.3.2 Shift of an annihilation time

In this case, a vertex associated with an annihilation operator, e.g. with row i of the matrix $\boldsymbol{\Delta}_k$, is shifted. In this case, the i^{th} row of $\boldsymbol{\Delta}_k$ is transformed, following $(\boldsymbol{\Delta}_k)_{in} \to \bar{\Delta}_{in}, \forall n \in \{1, 2, \ldots, k\}$. This corresponds, in the formulation of Eq. (C.1), to

$$\begin{aligned} \underline{u} : u_n &= \begin{cases} 1 & \text{if } n = i. \\ 0 & \text{otherwise.} \end{cases} \\ \underline{v} : v_n &= \bar{\Delta}_{in} - (\boldsymbol{\Delta}_k)_{in}. \end{aligned} \tag{C.23}$$

The corresponding value for the parameter λ is given by:

$$\lambda = \sum_l \left(\bar{\Delta}_{il} - (\boldsymbol{\Delta}_k)_{il}\right)\left(\boldsymbol{\Delta}_k^{-1}\right)_{li} = \sum_l \bar{\Delta}_{il}\left(\boldsymbol{\Delta}_k^{-1}\right)_{li} - 1 = \sum_l \bar{\Delta}_{il}(\boldsymbol{M}_k)_{li} - 1 \equiv \lambda_{II} - 1. \tag{C.24}$$

Using Eq. (C.1), we get the matrix elements for the inverse of the updated matrix:

$$\begin{aligned} M'_{nm} &= \left(\boldsymbol{\Delta}_k^{-1}\right)_{nm} - \frac{1}{1+\lambda}\left(\boldsymbol{\Delta}_k^{-1}\right)_{ni}\left[\sum_l \left(\bar{\Delta}_{il} - (\boldsymbol{\Delta}_k)_{il}\right)\left(\boldsymbol{\Delta}_k^{-1}\right)_{lm}\right] \\ &= (\boldsymbol{M}_k)_{nm} - \frac{1}{\lambda_{II}}(\boldsymbol{M}_k)_{ni}\left[\sum_l \bar{\Delta}_{il}(\boldsymbol{M}_k)_{lm} - \delta_{im}\right] \\ &= \begin{cases} (\boldsymbol{M}_k)_{nm} - \dfrac{1}{\lambda_{II}}(\boldsymbol{M}_k)_{ni}\left[\sum_l \bar{\Delta}_{il}(\boldsymbol{M}_k)_{lm}\right] & \text{if } m \neq i. \\ (\boldsymbol{M}_k)_{nm} - \dfrac{1}{\lambda_{II}}(\boldsymbol{M}_k)_{ni}\left[\sum_l \bar{\Delta}_{il}(\boldsymbol{M}_k)_{lm} - 1\right] = \dfrac{(\boldsymbol{M}_k)_{ni}}{\lambda_{II}} & \text{if } m = i. \end{cases} \end{aligned} \tag{C.25}$$

Appendix D

High-frequency expansion formulas

The type of impurity solver which we have used [140, 159], implemented in a freely available open source package [165], takes as input the hybridization function in imaginary time, and delivers as output the Green's function in imaginary time or Matsubara frequency, as well as the self-energy in imaginary frequency. The implementation of the self-consistency condition thus requires the calculation of Fourier transforms, and in particular, that of the hybridization function F from imaginary time to Matsubara frequency. It is essential that the high-frequency behavior of the hybridization function be correctly captured in this process, because such behavior determines the accuracy of $F(\tau)$ for small values of τ, and as a consequence, all important quantities such as the discontinuity of this function at $\tau = 0$. With this in mind, the objective of this appendix is to work out the relations between the asymptotic expressions for the Green's function, that for the self-energy, and that for the hybridization function.

D.1 Green's function

D.1.1 Analytic expressions for the tails

For an introduction to the formalism of the temperature Green's functions in many-body physics, we refer the reader to the work by Mahan on the subject [127]. The Green's function is defined a $\boldsymbol{G}(\tau) = G_{ij}(\tau) = -\left\langle T_\tau \hat{c}_j(\tau)\hat{c}_i^\dagger(0)\right\rangle$, where the (i,j) subscripts designate flavors, i.e. spin-orbital indices. The fermionic commutation relations imply that $\boldsymbol{G}(\tau)$ is antiperiodic, $\boldsymbol{G}(-\tau) = -\boldsymbol{G}(\beta-\tau)$, and discontinuous at $\tau = 0$. Such antiperiodic function may be Fourier transformed, in which case only odd Matsubara frequencies contribute:

$$\boldsymbol{G}(\tau) = \frac{1}{\beta}\sum_{n=-\infty}^{+\infty} e^{-i\omega_n\tau}\boldsymbol{G}(i\omega_n), \tag{D.1}$$

where $\omega_n \equiv \dfrac{(2n+1)\pi}{\beta}$. The reciprocal relation involves an integral over the period in imaginary time:

$$\boldsymbol{G}(i\omega_n) = \int_0^\beta e^{i\omega_n\tau}\boldsymbol{G}(\tau)d\tau. \tag{D.2}$$

It is a powerful feature of the continuous-time quantum Monte-Carlo scheme, that it is able to sample the relation (D.2) in a direct and efficient way [167], thus avoiding any issue related to the discretization of the integral.

In the course of the determination of the self-consistency condition in the system though, an accurate evaluation of the expression on the right-hand side of Eq. (D.1) is critical, e.g. when evaluating the hybridization function $\boldsymbol{F}(\tau)$ (whose behavior close for $\tau \to 0$ needs to be properly described), or the occupation matrix, defined by $\boldsymbol{n} \equiv n_{ij} = \left\langle c_i^\dagger c_j \right\rangle = \left\langle T_\tau c_i^\dagger(0) c_j(0) \right\rangle = \delta_{ij} + \boldsymbol{G}(\tau = 0^+)$. The challenge in this respect is that we need to evaluate a series, whose numerical representation is truncated for $n > N_{\max}$, but for which the contribution of the high-n terms is all-important.

In order to tackle this issue, it is convenient to use the high-frequency expansion form of $\boldsymbol{G}(i\omega_n)$, obtained from (D.2) after repeated integration by parts:

$$\boldsymbol{G}(i\omega_n) = \int_0^\beta e^{i\omega_n \tau} \boldsymbol{G}(\tau) d\tau \tag{D.3}$$

$$= \frac{-\boldsymbol{G}(\beta) - \boldsymbol{G}(0)}{i\omega_n} - \frac{-\boldsymbol{G}'(\beta) - \boldsymbol{G}'(0)}{(i\omega_n)^2} + \frac{-\boldsymbol{G}''(\beta) - \boldsymbol{G}''(0)}{(i\omega_n)^3} - \dots \tag{D.4}$$

$$= \sum_{k \geqslant 1} \frac{\boldsymbol{c}_k}{(i\omega_n)^k}, \tag{D.5}$$

with

$$\boldsymbol{c}_k = (-1)^k (\boldsymbol{G}^{(k-1)}(\beta) + \boldsymbol{G}^{(k-1)}(0)). \tag{D.6}$$

This form is very helpful, because by inserting (D.5) into (D.1), $\boldsymbol{G}(\tau)$ is expressed as the infinite sum of the Fourier transforms of each of the individual orders of the high-frequency expansion:

$$\boldsymbol{G}(\tau) = \frac{1}{\beta} \sum_{k \geqslant 1} \sum_{n=-\infty}^{+\infty} e^{-i\omega_n \tau} \frac{\boldsymbol{c}_k}{(i\omega_n)^k}. \tag{D.7}$$

For any value of k, $T_k(\tau) \equiv \sum_{n=-\infty}^{+\infty} e^{-i\omega_n \tau} \frac{1}{(i\omega_n)^k}$ may be evaluated analytically, using standard Matsubara frequency summation techniques [127]. For the first four orders we obtain

$$T_1(\tau) \equiv \frac{1}{\beta} \sum_{n=-\infty}^{+\infty} \frac{e^{-i\omega_n \tau}}{i\omega_n} = -\frac{1}{2}, \tag{D.8}$$

$$T_2(\tau) \equiv \frac{1}{\beta} \sum_{n=-\infty}^{+\infty} \frac{e^{-i\omega_n \tau}}{(i\omega_n)^2} = -\frac{2\tau - \beta}{4}, \tag{D.9}$$

$$T_3(\tau) \equiv \frac{1}{\beta} \sum_{n=-\infty}^{+\infty} \frac{e^{-i\omega_n \tau}}{(i\omega_n)^3} = \frac{\tau(\beta - \tau)}{4}, \tag{D.10}$$

$$T_4(\tau) \equiv \frac{1}{\beta} \sum_{n=-\infty}^{+\infty} \frac{e^{-i\omega_n \tau}}{(i\omega_n)^4} = \frac{(\beta - 2\tau)(\beta^2 + 2\beta\tau - 2\tau^2)}{48}. \tag{D.11}$$

Provided the coefficients $\boldsymbol{c}_k$ are known, this allows the first terms of the series (D.7) to be evaluated analytically, while the remaining orders, which converge much faster, may be safely computed numerically by a truncated summation. A choice has to be made concerning the maximum order $k_{\max}$ to be analytically evaluated. This choice depends

on the knowledge of the c_k coefficients, as well as on the nature of the quantity being transformed. Our implementation uses $k_{\max} = 3$. We then compute

$$\begin{aligned}
\boldsymbol{G}(\tau) &= \sum_{k\geqslant 1} \boldsymbol{c}_k T_k(\tau) \\
&= \sum_{k=1}^{k_{\max}} \boldsymbol{c}_k T_k(\tau) + \sum_{k>k_{\max}} \boldsymbol{c}_k \sum_{n=-\infty}^{+\infty} \frac{e^{-i\omega_n\tau}}{(i\omega_n)^k} \\
&\simeq \sum_{k=1}^{k_{\max}} \boldsymbol{c}_k T_k(\tau) + \sum_{k>k_{\max}} \boldsymbol{c}_k \sum_{n=-N_{\max}}^{+N_{\max}} \frac{e^{-i\omega_n\tau}}{(i\omega_n)^k} \\
&= \sum_{k=1}^{k_{\max}} \boldsymbol{c}_k \left[T_k(\tau) - \sum_{n=-N_{\max}}^{+N_{\max}} \frac{e^{-i\omega_n\tau}}{(i\omega_n)^k} \right] + \sum_{k\geqslant 1} \boldsymbol{c}_k \sum_{n=-N_{\max}}^{+N_{\max}} \frac{e^{-i\omega_n\tau}}{(i\omega_n)^k} \\
&= \underbrace{\sum_{k=1}^{k_{\max}} \boldsymbol{c}_k \left[T_k(\tau) - \sum_{n=-N_{\max}}^{+N_{\max}} \frac{e^{-i\omega_n\tau}}{(i\omega_n)^k} \right]}_{\text{analytic tail adjustment}} + \underbrace{\sum_{n=-N_{\max}}^{+N_{\max}} e^{-i\omega_n\tau} \boldsymbol{G}(i\omega_n)}_{\text{naive numerical summation}} .
\end{aligned} \tag{D.12}$$

The last pending issue in this program for an accurate evaluation of Eq. (D.5) is the determination of the values of the $\boldsymbol{c}_k$ matrices. It is worth noting that this splitting of a sum over Matsubara frequencies into a naive numerical summation term, and an analytic tail adjustment term, may be carried out on any expression whose high-frequency asymptotic expression is known analytically. This is routinely used in our implementation for the self-energy, the hybridization function (the relevant high-frequency expansion coefficients are derived further below), and the product function $\boldsymbol{\Sigma}(i\omega_n)\boldsymbol{G}(i\omega_n)$, which is involved in the determination of the interaction energy on the lattice.

D.1.2 Coefficients of the high-frequency expansion

In order to evaluate the the coefficients of the high-frequency (HF) expansion of the Green's function, we consider the Green's function defined as:

$$\big(\boldsymbol{G}(\boldsymbol{R}', \tau'; \boldsymbol{R}, \tau)\big)_{ij} = G_{ij}(\boldsymbol{R}', \tau'; \boldsymbol{R}, \tau) = -\left\langle T_\tau \hat{c}_j(\boldsymbol{R}', \tau') \hat{c}_i^\dagger(\boldsymbol{R}, \tau) \right\rangle , \tag{D.13}$$

where the (i, j) subscripts designate flavors, i.e. spin-orbital indices, and where we have explicitly introduced the dependence of the creation and annihilation operators on site $\boldsymbol{R}$. Whenever no explicit dependence is specified for the creation/annihilation operator, it is understood that we are considering such operator in direct space, at the origin of the direct lattice and of imaginary time: $\hat{c}_i^{(\dagger)} \equiv \hat{c}_i^{(\dagger)}(\boldsymbol{R} = \boldsymbol{0}, \tau = 0)$. Within the framework of DMFT, the dynamics of the quantum impurity is described by the local Green's function $\boldsymbol{G}(\tau) \equiv \boldsymbol{G}(\boldsymbol{R}, \tau; \boldsymbol{R}, 0)$, $\forall \boldsymbol{R} \in \mathcal{L}$, where $\mathcal{L}$ is the direct lattice.

The multiple derivatives of the Green's function with respect to τ, which appear in Eq. (D.4) may be expressed in terms of commutators and anticommutators involving the corresponding local Hamiltonian (6.10), and the creation/annihilation operators. Note that, while we are considering a form of the Coulomb interaction restricted to density-density terms, no assumption is made concerning the value of the cross-orbital hoppings, which may be finite. Therefore, the impurity Green's function is not diagonal, but only block diagonal, with the blocks defined as the blocks of orbitals coupled by the finite cross-hoppings.

In the following, we denote the creation and annihilation operators by $\hat{c}_k^{(\dagger)}$, where k is a flavor index, combining the orbital and spin quantum numbers. The site index is dropped for simplicity, since we are considering a local problem. With these notations, the local Hamiltonian in the grand-canonical ensemble may be written in a concise form (we follow the notation introduced in Ref. [140]; note the factor $\frac{1}{2}$, which differs from Eq. (6.10), due to the fact that the Hamiltonian (6.10) orders the orbitals):

$$\begin{aligned} \hat{K} &= \hat{K}_t + \hat{K}_U, \\ \hat{K}_t &= \sum_{ij} (t_{ij} - \mu\delta_{ij}) \hat{c}_i^\dagger \hat{c}_j, \\ \hat{K}_U &= \frac{1}{2} \sum_{i \neq j} U_{ij} \hat{n}_i \hat{n}_j, \end{aligned} \tag{D.14}$$

where $\hat{K}_t$ describes the hoppings inside the unit cell containing the impurity (i, j are flavor labels).

Eq. (D.6) then leads to:

$$c_1^{kl} = \left\langle \{\hat{c}_l, \hat{c}_k^\dagger\} \right\rangle, \tag{D.15}$$

$$c_2^{kl} = -\left\langle \left\{ [\hat{K}, \hat{c}_l], \hat{c}_k^\dagger \right\} \right\rangle, \tag{D.16}$$

$$c_3^{kl} = \left\langle \left\{ \left[\hat{K}, [\hat{K}, \hat{c}_l] \right], \hat{c}_k^\dagger \right\} \right\rangle. \tag{D.17}$$

The first term yields $\boldsymbol{c}_1 = \mathbb{1}$. The next terms require the evaluation of the commutators. In the case of density-density interaction, we may use

$$\begin{aligned} [\hat{c}_i^\dagger \hat{c}_j, \hat{c}_l] &= -\delta_{il} \hat{c}_j, \\ [\hat{n}_i \hat{n}_j, \hat{c}_l] &= -\delta_{il} \hat{c}_l \hat{n}_j - \delta_{jl} \hat{n}_i \hat{c}_l, \\ \left\{ \hat{c}_l \hat{n}_j, \hat{c}_k^\dagger \right\} &= \hat{c}_l \hat{c}_j^\dagger \delta_{jk} + \hat{n}_j \delta_{kl}, \\ \left\{ \hat{n}_j \hat{c}_l, \hat{c}_k^\dagger \right\} &= -\hat{c}_j^\dagger \hat{c}_l \delta_{jk} + \hat{n}_j \delta_{kl}, \\ \left\{ [\hat{n}_i \hat{n}_j, \hat{c}_l], \hat{c}_k^\dagger \right\} &= -\delta_{kl}(\delta_{il} \hat{n}_j + \delta_{jl} \hat{n}_i) + \delta_{jl} \delta_{ik} \hat{c}_i^\dagger \hat{c}_l - \delta_{il} \delta_{jk} \hat{c}_l \hat{c}_j^\dagger, \end{aligned}$$

in order to obtain

$$\begin{aligned} [\hat{K}_U, \hat{c}_l] &= -\frac{1}{2} \sum_{i \neq l} (U_{il} + U_{li}) \hat{n}_i \hat{c}_l, \\ \left\{ [\hat{K}_U, \hat{c}_l], \hat{c}_k^\dagger \right\} &= \frac{1}{2}(1 - \delta_{kl})(U_{kl} + U_{lk}) \hat{c}_k^\dagger \hat{c}_l - \frac{1}{2} \delta_{kl} \sum_{i \neq l} (U_{li} + U_{il}) \hat{n}_i. \end{aligned}$$

Furthermore

$$\begin{aligned} &[\hat{c}_i^\dagger \hat{c}_j, \hat{c}_l] = -\delta_{li} \hat{c}_j \Rightarrow \left[\hat{K}_t, \hat{c}_l \right] = -\sum_j (t_{lj} - \mu\delta_{lj}) \hat{c}_j \\ &\Rightarrow \left\{ \left[\hat{K}_t, \hat{c}_l \right], \hat{c}_k^\dagger \right\} = -t_{lk} + \mu\delta_{lk} \end{aligned}$$

Regrouping all the terms we obtain

$$\left\{[\hat{K},\hat{c}_l],\hat{c}_k^\dagger\right\} = -t_{lk} + \mu\delta_{lk} + \frac{1}{2}(1-\delta_{kl})(U_{kl}+U_{lk})\hat{c}_k^\dagger\hat{c}_l - \frac{1}{2}\delta_{kl}\sum_{i\neq l}(U_{li}+U_{il})\hat{n}_i,$$

and the expression for c_2^{kl} follows, using the fact that on-site orbitals are orthogonal, and noting $t_{kk} \equiv \epsilon_k + \Delta_k$:

$$c_2^{kl} = \begin{cases} -\mu + \epsilon_k + \Delta_k + \frac{1}{2}\sum_{i\neq k}(U_{ki}+U_{ik})\langle\hat{n}_i\rangle & \text{if } k = l. \\ -\frac{1}{2}(U_{kl}+U_{lk})\left\langle\hat{c}_k^\dagger\hat{c}_l\right\rangle & \text{if } k \neq l. \end{cases} \tag{D.18}$$

The off-diagonal term is finite in the presence of excitonic order.

D.2 Self-energy

The coefficients of the high-frequency expansion of the impurity self-energy may be determined, using the DMFT self-consistency condition:

$$\boldsymbol{G}(i\omega_n) = \frac{1}{N_s}\sum_{\boldsymbol{k}\in BZ}^{Ns}[i\omega_n + \mu - \boldsymbol{\Delta} - \boldsymbol{\epsilon}(\boldsymbol{k}) - \boldsymbol{\Sigma}(i\omega_n)]^{-1}.$$

We introduce the notations $\tilde{\boldsymbol{\mu}}(\boldsymbol{k}) = \mu - \boldsymbol{\Delta} - \boldsymbol{\epsilon}(\boldsymbol{k})$ for $\boldsymbol{k}$ a vector of the reciprocal space, and $\boldsymbol{\Sigma}(i\omega_n) = \boldsymbol{c}_{0,\Sigma} + \frac{\boldsymbol{c}_{1,\Sigma}}{(i\omega_n)} + \mathcal{O}\left(\frac{1}{(i\omega_n)^2}\right)$. If $\boldsymbol{\Sigma}$ is assumed to be diagonal (normal state) or 2×2 block-diagonal (excitonic condensate phase, in the $a_\uparrow b_\downarrow a_\downarrow b_\uparrow$ basis), then analytic expressions for the matrix elements of the matrix inverse are easily obtained. Each of these matrix elements can be expanded in powers of $\frac{1}{i\omega_n}$, leading to

$$\boldsymbol{G}(i\omega_n) = \frac{1}{i\omega_n}\left\{1 + \frac{1}{N_s}\sum_{\boldsymbol{k}\in BZ}\left[\frac{-\tilde{\boldsymbol{\mu}}(\boldsymbol{k}) + \boldsymbol{c}_{0,\Sigma}}{i\omega_n} + \frac{\boldsymbol{c}_{1,\Sigma} + [\tilde{\boldsymbol{\mu}}(\boldsymbol{k}) - \boldsymbol{c}_{0,\Sigma}]^2}{(i\omega_n)^2}\right]\right\} + \mathcal{O}\left(\frac{1}{(i\omega_n)^4}\right). \tag{D.19}$$

We can at this point identify the coefficients of the expansion of the local Green's function, in Eq (D.19), with the expression (D.5). In this way, we obtain the leading term of the expansion of the self-energy in the limit of high-frequency:

$$c_{0,\Sigma}^{kl} = \begin{cases} \sum_{i\neq k}(U_{ki}+U_{ik})\langle\hat{n}_i\rangle & \text{if } k = l, \\ -(U_{kl}+U_{lk})\left\langle\hat{c}_k^\dagger\hat{c}_l\right\rangle & \text{if } k \neq l, \end{cases} \tag{D.20}$$

which indicates that in the absence of orbital order, the high-frequency limit of the self-energy is diagonal, and equal to the value of the Hartree term of the Coulomb interaction energy.

D.3 Hybridization function

The hybridization function is defined as

$$\boldsymbol{F}(i\omega_n) = i\omega_n + \overline{\boldsymbol{\mu}} - \boldsymbol{\mathcal{G}_0}(i\omega_n)^{-1}, \tag{D.21}$$

with $\overline{\boldsymbol{\mu}} = \mu - \boldsymbol{\Delta} - \overline{\boldsymbol{\epsilon}}$. The high-frequency expansion for the bare Green's function of the lattice $\boldsymbol{\mathcal{G}_0}(i\omega_n)$ may be determined from Eq. (D.19), in which the self-energy term is set to zero:

$$\boldsymbol{\mathcal{G}_0}(i\omega_n) = \frac{1}{i\omega_n}\left\{1 - \frac{\overline{\boldsymbol{\mu}}}{i\omega_n} + \frac{\overline{\boldsymbol{\mu}^2}}{(i\omega_n)^2}\right\} + \mathcal{O}\left(\frac{1}{(i\omega_n)^4}\right), \tag{D.22}$$

where $\overline{\boldsymbol{\mu}^2} \equiv \dfrac{1}{N_s}\sum\limits_{\boldsymbol{k}\in BZ}\tilde{\boldsymbol{\mu}}(\boldsymbol{k})^2$. From Eq. (D.21) we thus obtain

$$\boldsymbol{F}(i\omega_n) = \frac{\overline{\boldsymbol{\mu}^2} - \overline{\boldsymbol{\mu}}^2}{i\omega_n} + \mathcal{O}\left(\frac{1}{(i\omega_n)^2}\right) = \frac{\overline{\boldsymbol{\epsilon}^2} - \overline{\boldsymbol{\epsilon}}^2}{i\omega_n} + \mathcal{O}\left(\frac{1}{(i\omega_n)^2}\right),$$

where use was made of the fact that $\mu - \boldsymbol{\Delta}$ is diagonal in flavor coordinates, and therefore commutes with $\boldsymbol{\epsilon}(\boldsymbol{k})$.

Bibliography

[1] N. F. Mott, Proc. Phys. Soc. Sect. A **62**, 416 (1949) (cit. on p. 1).

[2] Z.-A. Ren, G.-C. Che, X.-L. Dong, J. Yang, W. Lu, W. Yi, X.-L. Shen, Z.-C. Li, L.-L. Sun, et al., Europhysics Lett. **83**, 17002 (2008) (cit. on p. 1).

[3] Y. Kamihara, H. Hiramatsu, M. Hirano, R. Kawamura, H. Yanagi, T. Kamiya, and H. Hosono, J. Am. Chem. Soc. **128**, 10012 (2006) (cit. on p. 1).

[4] H. Takahashi, K. Igawa, K. Arii, Y. Kamihara, M. Hirano, and H. Hosono, Nature **453**, 376 (2008) (cit. on p. 1).

[5] Y. Kamihara, T. Watanabe, M. Hirano, and H. Hosono, J. Am. Chem. Soc. **130**, 3296 (2008) (cit. on p. 1).

[6] A. P. Drozdov, M. I. Eremets, I. A. Troyan, V. Ksenofontov, and S. I. Shylin, Nature **525**, 73 (2015) (cit. on p. 1).

[7] C. Heil and L. Boeri, Phys. Rev. B **92**, 060508 (2015) (cit. on p. 1).

[8] J. Hubbard, Proc. R. Soc. A Math. Phys. Eng. Sci. **276**, 238 (1963) (cit. on p. 2).

[9] N. F. Mott, Philos. Mag. **6**, 287 (1961) (cit. on pp. 2, 17).

[10] A. Georges, G. Kotliar, W. Krauth, and M. Rozenberg, Rev. Mod. Phys. **68**, 13 (1996) (cit. on pp. 2, 42, 61, 69, 70, 130).

[11] P. Werner and A. J. Millis, Phys. Rev. B **74**, 155107 (2006) (cit. on pp. 2, 79, 81, 87, 120).

[12] J. Bardeen, L. N. Cooper, and J. R. Schrieffer, Phys. Rev. **108**, 1175 (1957) (cit. on pp. 3, 17).

[13] J. R. Schrieffer, *Theory Of Superconductivity*, Perseus Books, 1999 (cit. on pp. 3, 17).

[14] J. G. Bednorz and K. A. Müller, Zeitschrift für Phys. B **64**, 189 (1986) (cit. on p. 3).

[15] P. W. Anderson, Science **316**, 1705 (2007) (cit. on pp. 3, 89).

[16] J. Bok, J. Prost, and F. Brochard-Wyart, *P.G. De Gennes' Impact on Science*, Series on Directions in Condensed Matter Physics, World Scientific Publishing, 2009 (cit. on pp. 3, 5).

[17] B. Keimer, S. A. Kivelson, M. R. Norman, S. Uchida, and J. Zaanen, Nature **518**, 179 (2015) (cit. on pp. 3, 4, 7, 9).

[18] A. S. Alexandrov, A. Bussmann-Holder, and H. Keller, *High Tc Superconductors and Related Transition Metal Oxides: Special Contributions in Honor of K. Alex Müller on the Occasion of his 80th Birthday*, 1st ed., Springer-Verlag Berlin Heidelberg, 2007 (cit. on pp. 3, 4).

[19] M. R. Norman and C. Pépin, Rep. Prog. Phys. **66**, 1547 (2003) (cit. on pp. 3, 4).

[20] P. A. Lee, N. Nagaosa, and X. G. Wen, Rev. Mod. Phys. **78** (2006) (cit. on p. 3).

[21] M. Hashimoto, I. M. Vishik, R.-H. He, T. P. Devereaux, and Z.-X. Shen, Nat. Phys. **10**, 483 (2014) (cit. on pp. 3, 6).

[22] C. W. Chu, J. Supercond. **7**, 1 (1994) (cit. on p. 4).

[23] J. Labbé and J. Bok, Europhysics Lett. **3**, 1225 (1987) (cit. on p. 4).

[24] J. Bok and J. Bouvier, Phys. C Supercond. **403**, 263 (2004) (cit. on p. 4).

[25] A. Damascelli, Z. Hussain, and Z. X. Shen, Rev. Mod. Phys. **75**, 473 (2003) (cit. on pp. 5, 6, 89).

[26] N. Ashcroft and N. Mermin, *Solid State Physics*, Holt, Rinehart and Winston, 1976 (cit. on p. 5).

[27] K. Byczuk, M. Kollar, K. Held, Y.-F. Yang, I. A. Nekrasov, T. Pruschke, and D. Vollhardt, Nat. Phys. **3**, 168 (2007) (cit. on pp. 5, 89).

[28] D. C. Peets, J. D. F. Mottershead, B. Wu, I. S. Elfimov, R. Liang, W. N. Hardy, D. A. Bonn, M. Raudsepp, N. J. C. Ingle, et al., New J. Phys. **9**, 28 (2007) (cit. on p. 8).

[29] T. Valla, A. V. Fedorov, P. D. Johnson, B. O. Wells, S. L. Hulbert, Q. Li, G. D. Gu, and N. Koshizuka, Science **285**, 2110 (1999) (cit. on pp. 8, 9, 89).

[30] A. Lanzara, P. Bogdanov, X. J. Zhou, S. A. Kellar, D. L. Feng, H. Eisaki, E. D. Lu, T. Yoshida, H. Eisaki, et al., Nature **412**, 510 (2001) (cit. on pp. 8, 9, 11, 89).

[31] J. Rossat-Mignod, L. P. Regnault, C. Vettier, P. Bourges, P. Burlet, J. Bossy, J. Y. Henry, and G. Lapertot, Phys. C Supercond. **185**, 86 (1991) (cit. on pp. 8, 10, 89).

[32] D. J. Scalapino, Phys. Rep. **250**, 329 (1995) (cit. on p. 9).

[33] D. J. Scalapino, Rev. Mod. Phys. **84**, 1383 (2012) (cit. on pp. 9, 55, 90).

[34] M. Eschrig and M. R. Norman, Phys. Rev. Lett. **89**, 277005 (2002) (cit. on pp. 9, 89–91).

[35] A. Abanov, A. V. Chubukov, M. Eschrig, M. R. Norman, and J. Schmalian, Phys. Rev. Lett. **89**, 177002 (2002) (cit. on p. 9).

[36] J. P. Carbotte, T. Timusk, and J. Hwang, Rep. Prog. Phys. **74**, 066501 (2011) (cit. on pp. 9, 89, 90).

[37] R. J. McQueeney, Y. Petrov, T. Egami, M. Yethiraj, G. Shirane, and Y. Endoh, Phys. Rev. Lett. **82**, 628 (1999) (cit. on p. 10).

[38] Y. Petrov, T. Egami, R. J. McQueeney, M. Yethiraj, H. A. Mook, and F. Dogan, cond-mat/0003414, 1 (2000) (cit. on p. 10).

[39] H. Iwasawa, J. F. Douglas, K. Sato, T. Masui, Y. Yoshida, Z. Sun, H. Eisaki, H. Bando, A. Ino, et al., Phys. Rev. Lett. **101**, 157005 (2008) (cit. on pp. 10, 12, 89).

[40] A. Kaminski, M. Randeria, J. C. Campuzano, M. R. Norman, H. Fretwell, J. Mesot, T. Sato, T. Takahashi, and K. Kadowaki, Phys. Rev. Lett. **86**, 1070 (2001) (cit. on pp. 10, 11, 13, 89).

[41] S. V. Borisenko, A. Kordyuk, V. B. Zabolotnyy, J. Geck, D. Inosov, A. Koitzsch, J. Fink, M. Knupfer, B. Büchner, et al., Phys. Rev. Lett. **96**, 117004 (2006) (cit. on pp. 11, 12, 14, 89).

[42] A. Gromko, A. V. Fedorov, Y.-D. Chuang, J. Koralek, Y. Aiura, Y. Yamaguchi, K. Oka, Y. Ando, and D. Dessau, Phys. Rev. B **68**, 174520 (2003) (cit. on pp. 12, 15, 89).

[43] T. Sato, H. Matsui, T. Takahashi, H. Ding, H.-B. Yang, S.-C. Wang, T. Fujii, T. Watanabe, A. Matsuda, et al., Phys. Rev. Lett. **91**, 157003 (2003) (cit. on pp. 13, 16, 89).

[44] J. He, W. Zhang, J. Bok, D. Mou, L. Zhao, Y.-Y. Peng, S. He, G. Liu, X. Dong, et al., Phys. Rev. Lett. **111**, 107005 (2013) (cit. on pp. 14–17, 89).

[45] N. C. Plumb, T. J. Reber, H. Iwasawa, Y. Cao, M. Arita, K. Shimada, H. Namatame, M. Taniguchi, Y. Yoshida, et al., New J. Phys. **15**, 113004 (2013) (cit. on pp. 15, 18, 89, 90, 98, 103, 104, 106, 125).

[46] D. Jérome, T. M. Rice, and W. Kohn, Phys. Rev. **158**, 462 (1967) (cit. on p. 17).

[47] B. I. Halperin and T. M. Rice, Rev. Mod. Phys. **40**, 755 (1968) (cit. on pp. 17, 20, 21, 40).

[48] B. I. Halperin and T. M. Rice, *Solid State Physics. Advances in Research and Applications*, ed. by F. Seitz, D. Turnbull, and H. Ehrenreich, vol. 21, Academic Press, 1968, 513 (cit. on pp. 17, 20, 107, 110).

[49] C. Cohen-Tannoudji, B. Diu, and F. Laloë, *Quantum mechanics*, Wiley, 1977 (cit. on p. 17).

[50] R. S. Knox, Collect. Excit. Solids **53**, 183 (1983) (cit. on p. 19).

[51] J. des Cloizeaux, J. Phys. Chem. Solids **26**, 259 (1964) (cit. on p. 19).

[52] V. Tugushev, Zh. Eksp. Teor. Fiz. **86**, 1282 (1984) (cit. on pp. 21, 22).

[53] J. Kuneš and P. Augustinský, Phys. Rev. B **89**, 115134 (2014) (cit. on pp. 21, 40, 41, 107, 108, 110, 115, 125).

[54] B. A. Volkov and Y. Kopaev, JETP Lett. **27**, 7 (1978) (cit. on p. 21).

[55] B. A. Volkov and Y. Kopaev, JETP Lett. **19**, 104 (1974) (cit. on p. 22).

[56] B. A. Volkov, Y. V. Kopaev, and A. I. Rusinov, Sov. Phys. JETP **41**, 952 (1975) (cit. on pp. 22, 23, 36).

[57] F. X. Bronold and H. Fehske, Phys. Rev. B **74**, 165107 (2006) (cit. on p. 23).

[58] B. Bucher, P. Steiner, and P. Wachter, Phys. Rev. Lett. **67**, 2717 (1991) (cit. on p. 23).

[59] D. P. Young, D. Hall, M. E. Torelli, Z. Fisk, J. L. Sarrao, J. D. Thompson, H.-R. Ott, S. B. Oseroff, R. G. Goddrich, et al., Nature **397**, 412 (1999) (cit. on pp. 23, 37).

[60] T. M. Rice, M. E. Zhitomirsky, and V. I. Anisimov, Nature **402**, 251 (1999) (cit. on p. 23).

[61] L. Balents and C. Varma, Phys. Rev. Lett. **84**, 1264 (2000) (cit. on p. 23).

[62] M. E. Zhitomirsky and T. M. Rice, Phys. Rev. B **62**, 1492 (2000) (cit. on p. 23).

[63] T. A. Gloor, M. E. Zhitomirsky, and T. M. Rice, Eur. Phys. J. B **21**, 491 (2001) (cit. on p. 23).

[64] D. Qian, D. Hsieh, L. Wray, E. Morosan, N. L. Wang, Y. Xia, R. J. Cava, and M. Z. Hasan, Phys. Rev. Lett. **98**, 117007 (2007) (cit. on p. 23).

[65] H. Cercellier, C. Monney, F. Clerc, C. Battaglia, L. Despont, M. G. Garnier, H. Beck, P. Aebi, L. Patthey, et al., Phys. Rev. Lett. **99**, 146403 (2007) (cit. on p. 23).

[66] C. Monney, H. Cercellier, F. Clerc, C. Battaglia, E. F. Schwier, C. Didiot, M. G. Garnier, H. Beck, P. Aebi, et al., Phys. Rev. B **79**, 045116 (2009) (cit. on p. 23).

[67] C. Monney, E. F. Schwier, M. G. Garnier, N. Mariotti, C. Didiot, H. Beck, P. Aebi, H. Cercellier, J. Marcus, et al., Phys. Rev. B **81**, 155104 (2010) (cit. on p. 23).

[68] C. Monney, C. Battaglia, H. Cercellier, P. Aebi, and H. Beck, Phys. Rev. Lett. **106**, 106404 (2011) (cit. on p. 23).

[69] J. van Wezel, P. Nahai-Williamson, and S. S. Saxena, Phys. Rev. B **81**, 165109 (2010) (cit. on p. 23).

[70] C. Monney, G. Monney, P. Aebi, and H. Beck, Phys. Rev. B **85**, 235150 (2012) (cit. on p. 23).

[71] B. Zenker, H. Fehske, H. Beck, C. Monney, and A. R. Bishop, Phys. Rev. B **88**, 075138 (2013) (cit. on p. 23).

[72] G. Monney, C. Monney, B. Hildebrand, P. Aebi, and H. Beck, Phys. Rev. Lett. **114**, 086402 (2015) (cit. on p. 23).

[73] H. Watanabe, K. Seki, and S. Yunoki, Phys. Rev. B **91**, 205135 (2015) (cit. on p. 23).

[74] Y. Wakisaka, T. Sudayama, K. Takubo, T. Mizokawa, M. Arita, H. Namatame, M. Taniguchi, N. Katayama, M. Nohara, et al., Phys. Rev. Lett. **103**, 026402 (2009) (cit. on p. 23).

[75] Y. Wakisaka, T. Sudayama, K. Takubo, T. Mizokawa, N. L. Saini, M. Arita, H. Namatame, M. Taniguchi, N. Katayama, et al., J. Supercond. Nov. Magn. **25**, 1231 (2012) (cit. on p. 23).

[76] K. Seki, Y. Wakisaka, T. Kaneko, T. Toriyama, T. Konishi, T. Sudayama, N. L. Saini, M. Arita, H. Namatame, et al., Phys. Rev. B **90**, 155116 (2014) (cit. on pp. 23, 24).

[77] K. Sugimoto, T. Kaneko, and Y. Ohta, Phys. Rev. B **93**, 041105 (2016) (cit. on p. 23).

[78] T. Yamada, K. Domon, and Y. Ono, J. Phys. Soc. Japan **85**, 053703 (2016) (cit. on p. 23).

[79] K. Domon, T. Yamada, and Y. Ono, J. Phys. Soc. Japan **85**, 065005 (2016) (cit. on p. 23).

[80] T. M. Rice, Phys. Rev. B **2**, 3619 (1970) (cit. on p. 23).

[81] E. Sonin, Solid State Commun. **25**, 253 (1978) (cit. on p. 23).

[82] E. Fawcett, Rev. Mod. Phys. **60**, 209 (1988) (cit. on p. 23).

[83] A. M. Gabovich, A. I. Voitenko, and M. Ausloos, Phys. Rep. **367**, 583 (2002) (cit. on p. 23).

[84] A. Sotnikov and J. Kuneš, Sci. Rep. **6**, 30510 (2016) (cit. on p. 23).

[85] A. Ikeda, T. Nomura, Y. H. Matsuda, A. Matsuo, K. Kindo, and K. Sato, Phys. Rev. B **93**, 220401 (2016) (cit. on p. 23).

[86] A. Ikeda, S. Lee, T. T. Terashima, Y. H. Matsuda, M. Tokunaga, and T. Naito, Phys. Rev. B **94**, 115129 (2016) (cit. on p. 23).

[87] T. Tatsuno, E. Mizoguchi, J. Nasu, M. Naka, and S. Ishihara, J. Phys. Soc. Japan **85**, 83706 (2016) (cit. on p. 23).

[88] A. D. K. Finck, J. P. Eisenstein, L. N. Pfeiffer, and K. W. West, Phys. Rev. Lett. **106**, 236807 (2011) (cit. on p. 23).

[89] L. Rademaker, J. van den Brink, J. Zaanen, and H. Hilgenkamp, Phys. Rev. B **88**, 235127 (2013) (cit. on pp. 23, 37).

[90] A. Kantian and D. S. L. Abergel, arXiv 1609.09080, 1 (2016) (cit. on p. 23).

[91] S. Banerjee, L. Register, E. Tutuc, D. Reddy, and A. MacDonald, IEEE Electron Device Lett. **30**, 158 (2009) (cit. on p. 23).

[92] K. Wu, L. Rademaker, and J. Zaanen, Phys. Rev. Appl. **2**, 054013 (2014) (cit. on p. 23).

[93] E. Fradkin, *Field Theories of Condensed Matter Systems*, Levant Books, 2006 (cit. on pp. 25, 27, 55).

[94] P. Fazekas, *Lecture Notes on Electron Correlation and Magnetism*, Series in modern condensed matter physics, World Scientific, 1999 (cit. on pp. 25, 26).

[95] E. Pavarini, E. Koch, J. van den Brink, and G. Sawatzky, *Quantum Materials: Experiments and Theory*, vol. 6, Modeling and Simulation, Forschungszentrum Jülich, 2016 (cit. on p. 25).

[96] P. W. Anderson, Science **235**, 1196 (1987) (cit. on p. 25).

[97] S. Doniach and E. Sondheimer, *Green's Functions for Solid State Physicists*, Imperial College Press, 1998 (cit. on p. 28).

[98] W. Jones and N. March, *Theoretical Solid State Physics*, Dover books on physics and chemistry vol. 2, Dover Publications, 1985 (cit. on p. 28).

[99] P. W. Anderson, Phys. Rev. **124**, 41 (1961) (cit. on pp. 28–32).

[100] A. Georges and G. Kotliar, Phys. Rev. B **45**, 6479 (1992) (cit. on pp. 33, 61).

[101] J. Kuneš, J. Phys. Condens. Matter **27**, 333201 (2015) (cit. on pp. 34, 41, 42, 44, 107, 108, 112, 114).

[102] J. Kuneš and D. Geffroy, Phys. Rev. Lett. **116**, 256403 (2016) (cit. on pp. 35, 107, 109, 110, 112–114, 116–119).

[103] E. Bascones, A. A. Burkov, and A. H. MacDonald, Phys. Rev. Lett. **89**, 86401 (2002) (cit. on p. 36).

[104] L. Balents, Phys. Rev. B **62**, 2346 (2000) (cit. on pp. 37–39, 41, 44, 107, 114).

[105] J. R. Schrieffer and P. A. Wolff, Phys. Rev. **149**, 491 (1966) (cit. on p. 40).

[106] S. B. Haley and P. Erdös, Phys. Rev. B **5**, 1106 (1972) (cit. on p. 41).

[107] M. Potthoff, M. Aichhorn, and C. Dahnken, Phys. Rev. Lett. **91**, 206402 (2003) (cit. on p. 42).

[108] T. Maier, M. Jarrell, T. Pruschke, and M. H. Hettler, Rev. Mod. Phys. **77**, 1027 (2005) (cit. on p. 42).

[109] M. Jarrell, Phys. Rev. Lett. **69**, 168 (1992) (cit. on pp. 42, 61).

[110] M. Jarrell, H. Akhlaghpour, and T. Pruschke, Phys. Rev. Lett. **70**, 1670 (1993) (cit. on p. 42).

[111] M. Ulmke, V. Janiš, and D. Vollhardt, Phys. Rev. B **51**, 10411 (1995) (cit. on p. 42).

[112] H. Park, K. Haule, and G. Kotliar, Phys. Rev. Lett. **107**, 137007 (2011) (cit. on p. 42).

[113] M. Capone, Science **296**, 2364 (2002) (cit. on p. 42).

[114] M. Capone, M. Fabrizio, C. Castellani, and E. Tosatti, Phys. Rev. Lett. **93**, 047001 (2004) (cit. on p. 42).

[115] A. Koga and P. Werner, Phys. Rev. B **91**, 085108 (2015) (cit. on p. 42).

[116] S. Hoshino and P. Werner, Phys. Rev. B **93**, 155161 (2016) (cit. on pp. 42, 108).

[117] T. I. Vanhala, J. E. Baarsma, M. O. J. Heikkinen, M. Troyer, A. Harju, and P. Törmä, Phys. Rev. B **91**, 144510 (2015) (cit. on p. 42).

[118] J. Kuneš and P. Augustinský, Phys. Rev. B **90**, 235112 (2014) (cit. on pp. 42–44, 108, 117).

[119] J. Kuneš, Phys. Rev. B **90**, 235140 (2014) (cit. on pp. 43, 45, 107–109, 125).

[120] J. Negele and H. Orland, *Quantum Many-particle Systems*, Advanced Books Classics, Westview Press, 2008 (cit. on pp. 46, 52, 59, 62, 68, 69, 127).

[121] A. Altland and B. Simons, *Condensed Matter Field Theory*, Cambridge University Press, 2006 (cit. on p. 46).

[122] F. Berezin, *The method of second quantization*, Pure and applied physics. A series of monographs and textbooks, Academic Press, 1966 (cit. on p. 47).

[123] P. A. M. Dirac, Phys. Zeitschrift der Sowjetunion **3**, 312 (1933) (cit. on p. 52).

[124] R. P. Feynman, Rev. Mod. Phys. **20**, 367 (1948) (cit. on p. 52).

[125] R. P. Feynman, Phys. Rev. **76**, 769 (1949) (cit. on p. 52).

[126] R. P. Feynman, Phys. Rev. **80**, 440 (1950) (cit. on p. 52).

[127] G. Mahan, *Many-Particle Physics*, Physics of Solids and Liquids, Springer, 1990 (cit. on pp. 54, 70, 137, 138).

[128] J. E. Hirsch, Phys. Rev. B **28**, 4059 (1983) (cit. on p. 56).

[129] A. Abanov, A. V. Chubukov, and J. Schmalian, Adv. Phys. **52**, 119 (2003) (cit. on pp. 59, 90).

[130] J. Chaloupka, *Microscopic Gauge-invariant Theory of the c-axis Infrared Response of Bilayer High-T c Cuprate Superconductors*,
PhD thesis, Masarykova univerzita, 2008 (cit. on p. 59).

[131] W. Metzner and D. Vollhardt, Phys. Rev. Lett. **62**, 324 (1989)
(cit. on pp. 61, 69, 71, 72).

[132] W. Metzner, Phys. Rev. B **43**, 8549 (1991) (cit. on pp. 61, 68).

[133] E. Müller-Hartmann, Zeitschrift für Phys. B **76**, 211 (1989) (cit. on p. 61).

[134] E. Gull, P. Werner, A. Millis, and M. Troyer, Phys. Rev. B **76**, 235123 (2007)
(cit. on pp. 61, 79).

[135] G. Kotliar and D. Vollhardt, Phys. Today **57**, 53 (2004) (cit. on p. 61).

[136] A. Georges, "Strongly Correlated Electron Materials: Dynamical Mean-Field Theory and Electronic Structure", *AIP Conf. Proc.* Vol. 715, 2004, AIP, 2004, 3
(cit. on p. 61).

[137] E. Gull, *Continuous-Time Quantum Monte Carlo Algorithms for Fermions*,
PhD thesis, 2008 (cit. on pp. 61, 74, 80, 81).

[138] J. Ferber, *Density Functional Theory and Dynamical Mean Field Theory : Applications to Correlated Electron Materials*,
PhD thesis, Goethe University of Frankfurt, 2012 (cit. on p. 61).

[139] J. Hubbard, Proc. R. Soc. A Math. Phys. Eng. Sci. **276**, 238 (1963) (cit. on p. 70).

[140] E. Gull, A. J. Millis, A. I. Lichtenstein, A. N. Rubtsov, M. Troyer, and P. Werner, Rev. Mod. Phys. **83**, 349 (2011) (cit. on pp. 74, 78, 81, 86, 137, 140).

[141] D. Zgid and G. K. Chan, J. Chem. Phys. **134**, 94115 (2011) (cit. on p. 74).

[142] D. Zgid, E. Gull, and G. K.-L. Chan, Phys. Rev. B **86**, 165128 (2012)
(cit. on p. 74).

[143] Y. Lu, M. Höppner, O. Gunnarsson, and M. W. Haverkort,
Phys. Rev. B **90**, 085102 (2014) (cit. on p. 74).

[144] G. H. Booth, A. J. W. Thom, and A. Alavi, J. Chem. Phys. **131**, 054106 (2009)
(cit. on p. 74).

[145] D. Cleland, G. H. Booth, and A. Alavi, J. Chem. Phys. **132**, 041103 (2010)
(cit. on p. 74).

[146] W. Krauth, *Statistical Mechanics: Algorithms and Computations*,
Oxford Master Series in Physics, Oxford University Press, UK, 2006
(cit. on pp. 74, 77).

[147] D. Landau and K. Binder,
A Guide to Monte Carlo Simulations in Statistical Physics,
Cambridge University Press, 2013 (cit. on p. 74).

[148] N. Metropolis, A. W. Rosenbluth, M. N. Rosenbluth, A. H. Teller, and E. Teller, J. Chem. Phys. **21**, 1087 (1953) (cit. on p. 77).

[149] J. E. Hirsch and R. M. Fye, Phys. Rev. Lett. **56**, 2521 (1986) (cit. on p. 78).

[150] D. C. Handscomb, Math. Proc. Cambridge Philos. Soc. **60**, 115 (1964)
(cit. on p. 78).

[151] A. W. Sandvik and J. Kurkijärvi, Phys. Rev. B **43**, 5950 (1991) (cit. on p. 78).

[152] N. V. Prokof'ev, B. V. Svistunov, and I. S. Tupitsyn,
J. Exp. Theor. Phys. Lett. **64**, 911 (1996) (cit. on pp. 78, 79).

[153] N. V. Prokof'ev, B. V. Svistunov, and I. S. Tupitsyn,
J. Exp. Theor. Phys. **87**, 310 (1998) (cit. on p. 78).

[154] N. V. Prokof'ev and B. V. Svistunov, Phys. Rev. Lett. **81**, 2514 (1998)
(cit. on p. 78).

[155] B. Beard and U.-J. Wiese, Nucl. Phys. B - Proc. Suppl. **53**, 838 (1997)
(cit. on p. 78).

[156] M. Troyer and U.-J. Wiese, Phys. Rev. Lett. **94**, 170201 (2005) (cit. on p. 78).

[157] A. N. Rubtsov and A. I. Lichtenstein, J. Exp. Theor. Phys. Lett. **80**, 61 (2004)
(cit. on p. 79).

[158] A. N. Rubtsov, V. V. Savkin, and A. I. Lichtenstein,
Phys. Rev. B **72**, 035122 (2005) (cit. on p. 79).

[159] P. Werner, A. Comanac, L. de'Medici, M. Troyer, and A. J. Millis,
Phys. Rev. Lett. **97**, 076405 (2006) (cit. on pp. 79, 81, 87, 108, 137).

[160] E. Gull, A. J. Millis, A. I. Lichtenstein, A. N. Rubtsov, M. Troyer, and P. Werner,
Europhysics Lett. **82**, 349 (2008) (cit. on p. 79).

[161] H. Kusunose, J. Phys. Soc. Japan **75**, 054713 (2006) (cit. on p. 79).

[162] A. Toschi, A. A. Katanin, and K. Held, Phys. Rev. B **75**, 045118 (2007)
(cit. on p. 79).

[163] A. N. Rubtsov, M. I. Katsnelson, and A. I. Lichtenstein,
Phys. Rev. B **77**, 033101 (2008) (cit. on p. 79).

[164] C. Slezak, M. Jarrell, T. Maier, and J. Deisz,
J. Phys. Condens. Matter **21**, 435604 (2009) (cit. on p. 79).

[165] B. Bauer, L. D. Carr, H. G. Evertz, A. Feiguin, J. Freire, S. Fuchs, L. Gamper,
J. Gukelberger, E. Gull, et al., J. Stat. Mech. Theory Exp. **2011**, P05001 (2011)
(cit. on pp. 86, 108, 137).

[166] L. Boehnke, H. Hafermann, M. Ferrero, F. Lechermann, and O. Parcollet,
Phys. Rev. B **84**, 075145 (2011) (cit. on pp. 86, 88).

[167] H. Hafermann, K. R. Patton, and P. Werner, Phys. Rev. B **85**, 205106 (2012)
(cit. on pp. 88, 137).

[168] H. Hafermann, P. Werner, and E. Gull,
Comput. Phys. Commun. **184**, 1280 (2013) (cit. on p. 88).

[169] P. Gunacker, M. Wallerberger, E. Gull, A. Hausoel, G. Sangiovanni, and K. Held,
Phys. Rev. B **92**, 155102 (2015) (cit. on p. 88).

[170] P. Gunacker, M. Wallerberger, T. Ribic, A. Hausoel, G. Sangiovanni, and K. Held,
Phys. Rev. B **94**, 125153 (2016) (cit. on p. 88).

[171] P. V. Bogdanov, A. Lanzara, S. A. Kellar, X. J. Zhou, E. D. Lu, W. J. Zheng,
G. Gu, J.-I. Shimoyama, K. Kishio, et al., Phys. Rev. Lett. **85**, 2581 (2000)
(cit. on p. 89).

[172] W. Zhang, G. Liu, L. Zhao, H. Liu, J.-Q. Meng, X.-L. Dong, W. Lu, J. S. Wen,
Z. J. Xu, et al., Phys. Rev. Lett. **100**, 107002 (2008) (cit. on p. 89).

[173] T. P. Devereaux, T. Cuk, Z. X. Shen, and N. Nagaosa, Phys. Rev. Lett. **93**, 117004 (2004) (cit. on p. 89).

[174] T. Cuk, F. Baumberger, D. H. Lu, N. Ingle, X. J. Zhou, H. Eisaki, N. Kaneko, Z. Hussain, T. P. Devereaux, et al., Phys. Rev. Lett. **93**, 117003 (2004) (cit. on p. 89).

[175] S. Park, Y. Cao, Q. Wang, M. Fujita, K. Yamada, S.-K. Mo, D. S. Dessau, and D. Reznik, Phys. Rev. B **88** (2013) (cit. on p. 89).

[176] G.-H. Gweon, T. Sasagawa, S. Y. Zhou, J. Graf, H. Takagi, D.-H. D.-H. Lee, and A. Lanzara, Nature **430**, 187 (2004) (cit. on p. 89).

[177] J. Lee, K. Fujita, K. McElroy, J. A. Slezak, M. Wang, Y. Aiura, H. Bando, M. Ishikado, T. Masui, et al., Nature **442**, 546 (2006) (cit. on p. 89).

[178] F. Giustino, M. L. Cohen, and S. G. Louie, Nature **452**, 975 (2008) (cit. on p. 89).

[179] D. Reznik, G. Sangiovanni, O. Gunnarsson, and T. P. Devereaux, Nature **455**, E6 (2008) (cit. on p. 89).

[180] M. Capone, C. Castellani, and M. Grilli, Adv. Condens. Matter Phys. **2010**, 920860 (2010) (cit. on p. 89).

[181] D. R. Garcia and A. Lanzara, Adv. Condens. Matter Phys. **2010**, 807412 (2010) (cit. on p. 89).

[182] I. M. Vishik, W. S. Lee, R.-H. He, M. Hashimoto, Z. Hussain, T. P. Devereaux, and Z.-X. Shen, New J. Phys. **12**, 105008 (2010) (cit. on p. 89).

[183] M. Norman, H. Ding, J. Campuzano, T. Takeuchi, M. Randeria, T. Yokoya, T. Takahashi, T. Mochiku, and K. Kadowaki, Phys. Rev. Lett. **79**, 3506 (1997) (cit. on p. 89).

[184] P. D. Johnson, T. Valla, A. V. Fedorov, Z. Yusof, B. O. Wells, Q. Li, A. R. Moodenbaugh, G. D. Gu, N. Koshizuka, et al., Phys. Rev. Lett. **87**, 177007 (2001) (cit. on p. 89).

[185] A. V. Chubukov and M. R. Norman, Phys. Rev. B **70**, 174505 (2004) (cit. on pp. 89, 95).

[186] M. Eschrig and M. R. Norman, Phys. Rev. B **67**, 144503 (2003) (cit. on pp. 89, 94, 99).

[187] D. Manske, *Theory of Unconventional Superconductors: Cooper-Pairing Mediated by Spin Excitations*, Physics and Astronomy Online Library, Springer, 2004 (cit. on p. 89).

[188] M. Eschrig, Adv. Phys. **55**, 47 (2006) (cit. on pp. 89, 90, 94, 95, 99).

[189] A. A. Kordyuk, S. V. Borisenko, V. B. Zabolotnyy, J. Geck, M. Knupfer, J. Fink, B. Büchner, C. T. Lin, B. Keimer, et al., Phys. Rev. Lett. **97**, 017002 (2006) (cit. on p. 89).

[190] V. B. Zabolotnyy, S. V. Borisenko, A. A. Kordyuk, J. Fink, J. Geck, A. Koitzsch, M. Knupfer, B. Büchner, H. Berger, et al., Phys. Rev. Lett. **96**, 037003 (2006) (cit. on p. 89).

[191] V. B. Zabolotnyy, S. V. Borisenko, A. A. Kordyuk, J. Geck, D. S. Inosov, A. Koitzsch, J. Fink, M. Knupfer, B. Büchner, et al., Phys. Rev. B **76**, 064519 (2007) (cit. on p. 89).

[192] T. Das, R. S. Markiewicz, and A. Bansil, Phys. Rev. B **85**, 144526 (2012) (cit. on p. 89).

[193] T. Das, R. S. Markiewicz, and A. Bansil, Adv. Phys. **63**, 151 (2014) (cit. on p. 89).

[194] A. Kordyuk and S. V. Borisenko, Low Temp. Phys. **32**, 298 (2006) (cit. on p. 89).

[195] J. H. Yun, J. Bok, H.-Y. Choi, W. Zhang, X. J. Zhou, and C. M. Varma, Phys. Rev. B **84**, 104521 (2011) (cit. on p. 89).

[196] W. Zhang, J. Bok, J. H. Yun, J. He, G. Liu, L. Zhao, H. Liu, J.-Q. Meng, X. Jia, et al., Phys. Rev. B **85**, 064514 (2012) (cit. on p. 89).

[197] S. Hong and H.-Y. Choi, J. Phys. Condens. Matter **25**, 365702 (2013) (cit. on pp. 89, 99).

[198] S. Hong, J. Bok, and H.-Y. Choi, Phys. C Supercond. **493**, 24 (2013) (cit. on p. 89).

[199] G. Mazza, M. Grilli, C. Di Castro, and S. Caprara, Phys. Rev. B **87**, 014511 (2013) (cit. on p. 89).

[200] H. F. Fong, B. Keimer, D. Reznik, D. L. Milius, and I. Aksay, Phys. Rev. B **54**, 6708 (1996) (cit. on p. 89).

[201] H. F. Fong, P. Bourges, Y. Sidis, L. P. Regnault, J. Bossy, A. Ivanov, D. L. Milius, I. A. Aksay, and B. Keimer, Phys. Rev. B **61**, 14773 (2000) (cit. on pp. 89, 90).

[202] T. Dahm, V. Hinkov, S. V. Borisenko, A. Kordyuk, V. B. Zabolotnyy, J. Fink, B. Büchner, D. J. Scalapino, W. Hanke, et al., Nat. Phys. **5**, 217 (2009) (cit. on pp. 89–94, 96, 97, 103, 104, 124, 125).

[203] J. Chaloupka and D. Munzar, Phys. Rev. B **76**, 214502 (2007) (cit. on pp. 90, 92, 94).

[204] B. Šopík, J. Chaloupka, A. Dubroka, C. Bernhard, and D. Munzar, New J. Phys. **17**, 053022 (2015) (cit. on pp. 90, 92).

[205] T. Moriya and K. Ueda, Adv. Phys. **49**, 555 (2000) (cit. on p. 90).

[206] K. Bennemann and J. Ketterson, *Superconductivity*, Springer-Verlag Berlin Heidelberg, 2008 (cit. on p. 90).

[207] P. Bourges, H. F. Fong, L. P. Regnault, J. Bossy, C. Vettier, D. L. Milius, I. Aksay, and B. Keimer, Phys. Rev. B **56**, R11439 (1997) (cit. on p. 91).

[208] V. Hinkov, B. Keimer, A. Ivanov, P. Bourges, Y. Sidis, and C. D. Frost, 19 (2010) (cit. on p. 91).

[209] D. Geffroy, J. Chaloupka, T. Dahm, and D. Munzar, Phys. Rev. B **93**, 144501 (2016) (cit. on pp. 91, 92, 94–98, 100–103, 105).

[210] T. Dahm and D. J. Scalapino, Phys. Rev. B **88**, 134509 (2013) (cit. on p. 92).

[211] E. Schachinger and J. P. Carbotte, Phys. Rev. B **80**, 094521 (2009) (cit. on p. 94).

[212] L. T. DeCarlo, Psychol. Methods **2**, 292 (1997) (cit. on p. 94).

[213] D. Munzar, C. Bernhard, and M. Cardona, Phys. C Supercond. **312**, 121 (1999) (cit. on p. 94).

[214] P. Cásek, C. Bernhard, J. Humlíček, and D. Munzar, Phys. Rev. B **72**, 134526 (2005) (cit. on p. 94).

[215] D. Fournier, G. Levy, Y. Pennec, J. L. McChesney, A. Bostwick, E. Rotenberg, R. Liang, W. N. Hardy, D. A. Bonn, et al., Nat. Phys. **6**, 905 (2010) (cit. on p. 104).

[216] G. Xu, G. D. Gu, M. Hucker, B. Fauqué, T. G. Perring, L. P. Regnault, and J. M. Tranquada, Nat. Phys. **5**, 642 (2009) (cit. on p. 106).

[217] G. Dresselhaus, Phys.Rev. **100**, 580 (1955) (cit. on p. 107).

[218] A. Manchon and S. Zhang, Phys. Rev. B **78**, 212405 (2008) (cit. on p. 107).

[219] H. Li, H. Gao, L. P. Zârbo, K. Výborný, X. Wang, I. Garate, F. Doğan, A. Čejchan, J. Sinova, et al., Phys. Rev. B **91**, 134402 (2015) (cit. on p. 107).

[220] J. Železný, H. Gao, K. Výborný, J. Zemen, J. Mašek, A. Manchon, J. Wunderlich, J. Sinova, and T. Jungwirth, Phys. Rev. Lett. **113**, 157201 (2014) (cit. on p. 107).

[221] P. Wadley, B. Howells, J. Elezny, C. Andrews, V. Hills, R. P. Campion, V. Novak, K. Olejnik, F. Maccherozzi, et al., Science **351**, 587 (2016) (cit. on p. 107).

[222] J. Wunderlich, A. C. Irvine, J. Sinova, B. G. Park, L. P. Zârbo, X. L. Xu, B. Kaestner, V. Novák, and T. Jungwirth, Nat. Phys. **5**, 675 (2009) (cit. on p. 107).

[223] A. Manchon, H. C. Koo, J. Nitta, S. M. Frolov, and R. A. Duine, Nat. Mater. **14**, 871 (2015) (cit. on p. 107).

[224] N. Nagaosa, X. Z. Yu, and Y. Tokura, Philos. Trans. R. Soc. A **370**, 5806 (2012) (cit. on p. 107).

[225] F. Jonietz, S. Muhlbauer, C. Pfleiderer, A. Neubauer, W. Munzer, A. Bauer, T. Adams, R. Georgii, P. Boni, et al., Science **330**, 1648 (2010) (cit. on p. 107).

[226] C. Wu and S.-C. Zhang, Phys. Rev. Lett. **93**, 036403 (2004) (cit. on p. 107).

[227] D. Vollhardt and P. Woelfle, *The Superfluid Phases Of Helium 3*, Taylor & Francis, 1990 (cit. on p. 107).

[228] C. Wu, K. Sun, E. Fradkin, and S.-C. Zhang, Phys. Rev. B **75**, 115103 (2007) (cit. on p. 107).

[229] G. Khaliullin, Phys. Rev. Lett. **111**, 197201 (2013) (cit. on pp. 107, 117, 118).

[230] G. Cao, T. F. Qi, L. Li, J. Terzic, S. J. Yuan, L. E. DeLong, G. Murthy, and R. K. Kaul, Phys. Rev. Lett. **112**, 056402 (2014) (cit. on p. 107).

[231] A. Jain, M. Krautloher, J. Porras, G. H. Ryu, D. P. Chen, D. L. Abernathy, J. T. Park, A. Ivanov, J. Chaloupka, et al., Arxiv **1510**, 07011v1 (2015) (cit. on pp. 107, 117, 118).

[232] T. Dey, A. Maljuk, D. V. Efremov, O. Kataeva, S. Gass, C. G. F. Blum, F. Steckel, D. Gruner, T. Ritschel, et al., Phys. Rev. B **93**, 014434 (2016) (cit. on p. 107).

[233] K. Pajskr, P. Novák, V. Pokorný, J. Kolorenč, R. Arita, and J. Kuneš, Phys. Rev. B **93**, 035129 (2016) (cit. on p. 107).

[234] A. Albuquerque, F. Alet, P. Corboz, P. Dayal, A. Feiguin, S. Fuchs, L. Gamper, E. Gull, S. Gürtler, et al., J. Magn. Magn. Mater. **310**, 1187 (2007) (cit. on p. 108).

[235] J. E. Gubernatis, M. Jarrell, R. N. Silver, and D. S. Sivia, Phys. Rev. B **44**, 6011 (1991) (cit. on p. 108).

[236] T. Kaneko and Y. Ohta, Phys. Rev. B **90**, 245144 (2014) (cit. on p. 108).

[237] T. Kaneko, B. Zenker, H. Fehske, and Y. Ohta, Phys. Rev. B **92**, 115106 (2015) (cit. on p. 108).

[238] J. Chaloupka and G. Khaliullin, Phys. Rev. Lett. **116**, 017203 (2016) (cit. on pp. 110, 113, 118).

[239] C. Zener, Phys. Rev. **82**, 403 (1951) (cit. on pp. 111, 114).

[240] K. Steiner, Y. Nomura, and P. Werner, Phys. Rev. B **92**, 115123 (2015) (cit. on p. 119).

[241] J. Sherman and W. J. Morrison, Ann. Math. Stat. **21**, 124 (1950) (cit. on p. 132).

[242] A. Kiss, *Note on the CT-QMC simulation method*, unpublished, 2009 (cit. on p. 132).

Publications

1. *Role of the upper branch of the hour-glass magnetic spectrum in the formation of the main kink in the electronic dispersion of high-Tc cuprate superconductors*
   D. Geffroy, J. Chaloupka, T. Dahm, and D. Munzar
   Phys. Rev. B **93**, 144501 (2016)

2. *Spontaneous Spin Textures in Multiorbital Mott Systems*
   J. Kuneš and D. Geffroy
   Phys. Rev. Lett. **116**, 256403 (2016)

3. *Excitonic structure and pumping power dependent emission blue-shift of type-II quantum dots*
   P. Klenovský, P. Steindl, and D. Geffroy
   Sc. Rep. **7**, 45568 (2017)

4. *Complex hybridization function: impact on the phase diagram of the excitonic condensation*
   D. Geffroy, A. Hariki, and J. Kuneš
   In preparation, to be submitted to J. Phys. Condens. Matter

Conference presentations

1. D. Geffroy and D. Munzar, *High T_c superconductors: the spin-fermion model approach*, IMPI Podzimní Škola, Brno (Czech Republic), 2013 (oral presentation).

2. D. Geffroy, J. Chaloupka, and D. Munzar, *Spin-fermion model of high-T_c cuprates: impact of the high energy branch of spin susceptibility*, 11^{th} International Conference on the Low Energy Electrodynamics in Solids (LEES'14), Loire Valley (France), 2014 (poster presentation).

3. D. Geffroy, J. Chaloupka, and D. Munzar, *Spin-fermion model of high-T_c cuprates: impact of the high energy branch of spin susceptibility*, 11^{th} International Conference on Materials and Mechanisms of Superconductivity and High Temperature Superconductors (M^2S-HTSC XI), Geneva (Switzerland), 2015 (poster presentation).

4. D. Geffroy, J. Chaloupka, and D. Munzar, *Main kink in the electronic dispersion of high-T_c cuprates: Role of the upper branch of the hour-glass magnetic spectrum*, 11^{th} International Conference on Spectroscopies in Novel Superconductors (SNS2016), Stuttgart/Ludwigsburg (Germany), 2016 (poster presentation).

5. J. Kuneš and D. Geffroy, *Spontaneous Spin Textures in Multiorbital Mott Systems*, 6^{th} Autumn School on Correlated Electrons: Quantum Materials: Experiments and Theory, Jülich (Germany), 2016 (poster presentation).